Integrating High-Precision U-Pb Geochronologic Data with Dynamic Models of Earth Processes

by

Terrence Blackburn
B.S., University of Kansas (2004)
M.Sc., University of Kansas (2006)

Submitted in partial fulfillment of the requirements for the degree of
Doctor of Philosophy
at the
MASSACHUSETTS INSTITUTE OF TECHNOLOGY

September 1, 2012

Author .....
Massachusetts Institute of Technology
September 1, 2012

Certified by .....
Samuel A. Bowring
Robert R. Shrock Professor of Geology
Earth, Atmospheric and Planetary Sciences, MIT
Thesis Supervisor

Accepted by .....
Rob van der Hilst
Department Head and Schlumberger Professor of Earth Sciences
Earth, Atmospheric and Planetary Sciences, MIT

Integrating High-Precision U-Pb Geochronologic Data with Dynamic Models of Earth Processes

by

Terrence Blackburn

Submitted to the Massachusetts Institute of Technology
on August 10, 2012, in partial fulfillment of the
requirements for the degree of
Doctor of Philosophy

Abstract

Radioisotopic dating can provide critical constraints for understanding the rates of tectonic, dynamic and biologic processes operating on our planet. Improving the interpretation and implementation of geochronologic data by coupling it with numerical modeling studies is the central theme of this thesis. Each chapter works to address a variety of problems in the Earth sciences. In each study, the interpretation of geochronologic data is aided with a numerical model that simulates the long-term behavior and/or initial conditions of the U-Pb system and provides an effective means of exploring the parameters that influence a calculated date. The record provided by geochronologic data is then coupled with models to quantitatively determine rates of geologic process on Earth. This approach permits geochronologic data to move beyond just establishing a relative time line of events. Using this dual modeling approach, Chapters 2-5 work to measure the long-term cooling and erosion rate of the lithosphere, specifically constraining the time scales and rate of transition between the stages of mountain belt formation and stability. Chapter six works to constrain the timing and duration of Central Atlantic Magmatic Province flood basalt volcanism and its relationship to the end Triassic mass extinction. The seventh and final chapter uses high precision U-Pb geochronology to evaluate the reliability of an Ar-Ar standard often used as a fluence monitor. The overall focus of this thesis has been to push the envelope of geochronologic precision and accuracy while coupling the data with modeling studies to yield new insight into Earth systems.

Thesis Supervisor: Samuel A. Bowring
Title: Professor of Geology, MIT

Contents

List of Figures

List of Tables

Chapter 1: Introduction

Measuring geologic time is of fundamental importance to understanding earth history. Without the temporal constraints provided by geochronology, specifically radio-isotopic dating, Earth scientists could not determine the rates of many physical, chemical and biologic processes essential to understanding our planet. The U-Pb system in particular has been employed to place constraints on everything from the age of the earliest forming solids in our solar system, to the timing and duration of mass extinction events that punctuate Earth history. Since the discovery of radioactivity and isotopes at the turn of the last century, the earliest applications of geochronology established a relatively broad timeline of events. However, until the 1960-70s, the level of possible precision on a single geochronologic date was often on the order of several percent and limited largely by inability to measure small samples sizes and eliminate open system behavior. In the past three decades there has been a rapid evolution of advancements in laboratory methods and data reduction protocols that have spurred ever-increasing levels of precision and accuracy at high spatial resolution. This in turn enables Earth scientists to approach new problems in tectonics, Earth history and dynamics.

Two new challenges arise from the increase in the precision and accuracy: first, the ability to interpret a high-precision geochronologic record relies on understanding the physical and/or chemical processes that have second-order influence on radio-isotopic systems. As specifically addressed in this thesis, this includes evaluating the influence of diffusive Pb-loss from these systems or the preferential exclusion of intermediate decay products from a crystallizing mineral. The future of high-precision geochronology will rely on providing ever more quantitative means to understand and correct for these processes. Second, in addition to using geochronology to establish a time line of Earth history, these data may be more fully exploited through integration with a physical model describing the rates of geological processes operating on Earth. Examples in this thesis include integrating U-Pb data with thermal models to describe the rate of lithospheric cooling, to using astronomically influenced models for cyclical

sediment accumulation within a basin. Coupling geochronologic data with these additional geologic or physical constraints permits us to evaluate and refine these models, and in doing so enhances our understanding of Earth processes. The underlying theme of this thesis has been to improve the implementation and interpretation of geochronologic data. Each of the following chapters provides an example on how coupling geochronologic data with numerical models can be used to approach different problems in the Earth sciences.

The purpose of the second chapter, entitled "U-Pb thermochronology: creating a temporal record of lithosphere thermal evolution" was to demonstrate how an enhanced record of long-term lithosphere cooling could be established by exploiting the dual decay scheme of the U-Pb system. Though thermochronology has for years been used to measure the time-scales and rates of cooling of the Earth's lithosphere, the conclusions drawn by these studies are often non-unique, with a large number of potential thermal histories that remain consistent with measured data. A high fidelity reconstruction of time-temperature paths for dated rocks can be produced by exploiting the U-Pb system's dual decay scheme, where parent isotopes ^{238}U and ^{235}U decay at different rates to daughter isotopes ^{206}Pb and ^{207}Pb, respectively. Coupling the dual isotopic system with diffusion's length scale dependency, which causes different crystal sizes to retain Pb over different time scales, results in a set of daughter isotopic compositions for a range of crystal sizes that is unique to the time-temperature history of the sample. I have employed this technique to demonstrate that Archean and Proterozoic lower crustal xenoliths, samples that resided at 25-50 km depths for billions of years, record a thermal history of long-term slow cooling. The contents of this second chapter have been published in the journal *Contributions to Mineralogy and Petrology* (Blackburn et al., 2011). Chapter 3 focuses on how the thermal history can be used to understand the relative contributions of heat transfer mechanisms, and in particular, advection/surface erosion, to the cooling history of the lithosphere over billion-year time scales.

Blackburn, T., Bowring, S., Schoene, B., Mahan, K., and Dudas, F., (2011), U-Pb thermochronology: creating a temporal record of lithosphere thermal evolution: *Contributions to Mineralogy and Petrology*, v.162, p 479-500.

The third chapter, entitled "An exhumation history of continents at billion year time-scales", has focused on constraining the times-scales and rate of lithosphere erosion using a combination of U-Pb thermochronology and thermal modeling. Present day models to explain the survival of ancient continental lithosphere require that the stable interiors of continental masses

are the same density as the underlying convecting mantle and thus experience minimal isostatic uplift and erosion over their history. The formation and growth of continental masses through mountain building processes, however, requires that the lithosphere's earliest history be characterized by rapid erosion of topographically high mountains. By reconstructing a continent's erosional history over billion year time-scales, we have produced a chronological record of the transition between these formation and stability stages that further provides a new understanding of the composition and density of the lithosphere, its relationship with the underlying mantle, and the forces operating to exhume the continents over the history of our planet. Because erosion of the Earth's surface enhances the rate of heat loss within the lithosphere, we can utilize the thermal history of lower crustal rocks, reconstructed using thermochronology, to produce a long-term erosional history for some of Earth's oldest and most stable structures. Combined with thermal models, the thermochronologic data record a sudden and early transition from rapid erosion to near zero erosion that then persists for billions of years. The long-term stability documented here implies the North American continent has experienced minimal uplift or burial over its lifetime, maintaining the present day stability and isostatic equilibrium over billion-year time scales. The contents of this chapter have previously been published in the journal *Science*:

Blackburn, T.J., Bowring, S.A., Perron, T., Mahan K., Dudas F., Barnhart, K. (2012) An exhumation history of continents over billion year time-scales, *Science*, v. 335, p 73-76.

The fifth chapter of this thesis will extrapolate this work to understand what processes cause the magnitude of isostatic uplift to abruptly transition between rapid erosion of topographically high mountains.

The fourth chapter, entitled "Zirconium in rutile speedometry: constraining lower crustal cooling rates and residence temperatures" describes the development of a high temperature speedometer, capable of constraining the rates of cooling through extremely high thermal windows (700-1000 °C) and thus greater depths within the Earth. This technique fills a critical gap between the time-scales of processes measured by high temperature geochronometers and low to moderate temperature thermochronologic systems. This study demonstrates that the rate of cooling between the high temperatures recorded by geothermometers (900-1000 °C) and the long-term residence temperatures for the lower crust, is extremely rapid (>300 °C/My). This suggests that the ultra high temperature terranes buried deeply during mountain building processes, cool rapidly through a combination of high erosion rates and conductive heat loss. The

Zr in rutile system is sensitive to the long-term holding temperature, and was thus exploited to provide a new and independent measure of long-term lower crustal temperatures. The contents of this chapter have previously been published in the journal *Earth and Planetary Science Letters*:

Blackburn, T.J., Bowring, S.A., Schoene B., Mahan K., (2012) Zirconium in rutile speedometry: constraining lower crustal cooling rates and residence temperatures., *Earth and Planetary Science Letters*, v. 317-318, p 231-240.

The fifth chapter, entitled "Sink to survive: The preservation of ancient mountain belts through crustal density changes" works to address how isostasy can control both the surface expression and erosional history of collisional mountain belts and yet after billions of years of isostatic uplift and erosion does not result in their complete destruction through erosion. The paper presents a compilation of low-temperature thermochronologic and cosmogenic nuclide data recording the rate of mountain belt erosion and its change through time. The data suggest that the rate of mountain belt erosion decreases dramatically ~300 My after the formation of a collisional orogen. The interpretation of this data is aided by a model designed to simulate the thermal, density and erosional history of an idealized mountain belt. Measured and modeled data indicate that erosion within a hot, low-density and topographically high mountain belt is rapid, while after several hundred million years of cooling, decreased lower crustal temperatures trigger metamorphic garnet growth, resulting the densification of the lower crust and a dramatic decrease in subsequent erosion. Though mountain belt erosion may vary with tectonic or climate setting, it is isostasy coupled with it's link to the thermal and density evolution of the crust that *dominantly* controls the long-term erosional history of the lithosphere and ultimately leads to the preservation of Earth's ancient mountain belts. This model not only explains the secular trends in erosion rate presented in this chapter, but also explains: 1) the lower crust's initially rapid cooling rates from high temperatures recorded by the Zr in rutile system (chapter 4), 2) the long-term slow cooling recorded by the U-Pb system (chapter 2-3) and 3) the time-scale of transition the rapid erosion and stability stages (chapter 3).

The sixth chapter, entitled "High-precision U-Pb zircon dating of Central Atlantic Magmatic Province" documents how high-precision zircon U-Pb dating of continental flood basalts can be used to evaluate the potential causal relationship between ~200 Ma flood basalts related to the opening of the Atlantic and the late Triassic extinction event just prior to the Triassic-Jurassic boundary. Flood basalt volcanism has often been suspected as the potential trigger to global biotic crisis through the volcanic emission of CO_2 or methane that can lead to

greenhouse conditions. Though the relative timing of the late Triassic extinction and Jurassic recovery is well defined in marine sedimentary sections, the restriction of flood basalts to terrestrial sedimentary sections has prevented a straight forward comparison between the timing of extinction and flood basalt eruptions. The data are also used to test the astrochronologic model for sediment accumulation in the Newark basin, and confirm the models reliability. The integration of high-precision geochronologic dates and the high-fidelity cyclostratagraphic model permit resolution of the late Triassic extinction at the < 100 ky level, and further permit that the very oldest flood basalt units erupt either prior to or synchronously with the extinction. In addition, our data constrain the duration of flood basalt eruption to < 650 ky and thus remain consistent with a causal relationship between the flood basalts and extinction event.

The seventh and final chapter, entitled "U-Pb geochronologic and thermochronologic time-temperature constraints of $^{40}Ar/^{39}Ar$ hornblende standard HB3gr" describes how a combination of U-Pb geo- and thermochronology can be used to evaluate the intercalibration between the U-Pb and $^{40}Ar/^{39}Ar$ geochronologic systems. A persistent bias between these mostly commonly used radioisotopic systems could be largely eliminated through recalibration of the ^{40}K decay constants and adoption of new high-precision dates for irradiation standards. The commonly used irradiation standard, HB3gr hornblende, separated from a granite pluton in the Llano uplift of Texas, is shown here to have experienced an episode of moderately slow cooling, resulting in a bias between $^{40}Ar/^{39}Ar$ hornblende and zircon U-Pb dates. Thermochronologic analyses coupled with Pb-diffusion models suggest Hb3gr experienced post-magmatic cooling rates on the order of 20-30 °C/Ma making the hornblende unsuitable for use as an irradiation standard for high precision $^{40}Ar/^{39}Ar$ studies and the rock a poor candidate for intercalibration studies.

In Chapters 2-5 involve the interpretation of U-Pb and Zr in rutile thermochronologic data using a combination of Pb/Zr diffusion models and thermal models to describe the long-term cooling history of the lithosphere. The focus of Chapter 6 is to refine the interpretation of high-precision U-Pb zircon geochronologic data through integration with the Astronomical Time Scale. While chapter 7 utilizes high-precision U-Pb geochronology to evaluate a potential standard for intercalibration of the U-Pb and $^{40}Ar/^{39}Ar$ systems. Though each thesis chapter addressed a distinct geologic question, the overarching theme of the thesis is the implementation and interpretation of geochronologic data through use of numerical modeling.

Chapter 2: U-Pb thermochronology: creating a temporal record of lithosphere thermal evolution

Blackburn, T., Bowring, S., Schoene, B., Mahan, K., and Dudas, F., (2011), U-Pb thermochronology: creating a temporal record of lithosphere thermal evolution: *Contributions to Mineralogy and Petrology*, v.162, p 479-500.

Abstract: A new approach to U-Pb accessory mineral thermochronology allows high-resolution time-temperature histories to be extracted from lower crustal xenoliths. The combination of the U-Pb system's dual decay scheme with the effects of temperature dependent Pb-diffusion can yield a time sensitive record of Pb production/diffusion within accessory phases. The difference in half-life for parent isotopes ^{238}U and ^{235}U results in the time-variable production of Pb isotopes ^{206}Pb and ^{207}Pb, while Pb diffusion can result in large variations in the time-scales at which Pb retention occurs between grains of different sizes. The combined effects of variable production rates between the two systems and diffusion result in data topologies on a concordia diagram that permit distinction between slow cooling and reheating t-T paths. In slowly cooled systems, the difference in time for Pb retention for grains of variable size yields a measure of partial retention zone (PRZ) residence time, and provides a robust measure of cooling rate through the PRZ. In Montana, three lower crustal xenoliths, each from a different depth, yield U-Pb rutile data that record a prolonged (>1 Ga) and slow cooling history towards a steady state geothermal gradient following the amalgamation of the terrain onto North America. The shallowest samples record the initial recovery of a conductive geothermal gradient and cool through the mineral PRZ at rates of <0.25 ºC/Ma over ~500 Ma. Deeper xenoliths record cooling at younger times over similar time scales and rates. This multi-depth thermal record provides a long-term record of lithosphere cooling and stabilization.

2.1 Introduction

Over the past 20 years thermochronologic techniques including U-Pb, Rb-Sr, K-Ar, $^{40}Ar/^{39}Ar$, fission track and (U-Th)/He systems have allowed earth scientists to accurately describe the time-temperature evolution of rock samples. The diffusive loss of daughter isotopes in these systems can be

quantified by volume-diffusion theory and exploited as a reliable method to yield temperature sensitive dates. Low-temperature (<400-60°C) thermochronometric systems, such as $^{40}Ar/^{39}Ar$ and (U-Th)/He have typically been applied to structural, tectonic and geomorphologic studies of the upper crust with the goal of constraining near-surface thermal histories. Reconstructing a samples thermal history can be used to quantify heat transfer mechanisms operating within the lithosphere, providing a time-dependent measure for this process.

In contrast to noble gas thermochronology, U-Pb accessory phase thermochronometry (minerals: apatite, titanite and rutile) allows estimates of cooling rates of rocks as they pass through moderate to high temperatures (400-800 °C) corresponding to thermal histories for rocks between 20 and 50 km depth. Most attempts to employ U-Pb thermochronometers have produced dates consistent with exhumation of post-peak metamorphic lower crustal terranes (Baldwin et al., 2004; Flowers et al., 2006; Mezger et al., 1989). Schmitz and Bowring (2003b), however, applied U-Pb accessory phase thermochronology to explore the thermal relaxation of ancient cratonic lithosphere by dating rutile, titanite and apatite from exhumed lower crustal xenoliths. Lower crustal xenoliths may preserve ancient cooling histories, from the high temperatures during and following igneous crystallization and/or metamorphism (700->1000 °C), to the low temperatures predicted for a steady state geotherm in the lower crust (ca 450-~500 °C). This history is initially recorded by high temperature geochronometers such as zircon or monazite, while cooling is recorded by moderate temperature thermochronometers apatite, rutile and titanite. Archean cratons are characterized by thick (>200 km) lithospheric mantle of depleted peridotite that effectively insulate the crust from thermal and tectonic perturbations (Jordan, 1988). Though the antiquity of the crust and keels is well established, the time-scales of cooling and stabilization of these cratons is poorly understood. U-Pb thermochronology of lower crustal xenoliths can be used to constrain the long-term thermal relaxation of these tectonic terranes, and potentially decipher the magnitude of heat transfer mechanisms operating over the history of a craton.

An additional contrast between U-Pb and noble gas thermochronology is the U-Pb system's dual decay scheme, where two parent isotopes, ^{238}U and ^{235}U, decay to daughter isotopes ^{206}Pb and ^{207}Pb respectively. The difference in decay rates between parent isotopes imposes a time-variant parent and daughter isotopic composition for any point in Earth's history. Volume diffusion behavior, in particular for slowly cooled systems, induces age gradients within single grains and among grains of varying size as a result of partial retention of radiogenic daughter and diffusion's length-scale dependency. This results in the retention of Pb between grains of different sizes over different time-scales, with each grain acquiring a unique parent-daughter ratio and daughter isotopic composition. The dual decay scheme can be exploited as two separate thermochronologic systems that when combined, can yield data that is unique to a particular cooling path. This is a distinct advantage over single isotope systems that are often plagued by

non-unique data sets in particular the ambiguity of potentially identical internal diffusion profiles and grain size-age relationships that can be produced by slow-cooling and reheating time-temperature (t-T) paths.

The purpose of this paper to is to: 1) outline new numerical and laboratory procedures for U-Pb thermochronology, 2) demonstrate how the U-Pb system's dual decay scheme can yield time sensitive information on Pb diffusion allowing for the determination of unique cooling paths, 3) show how duration in the Pb PRZ affects the topology of U-Pb data plotted on a concordia diagram, which in turn can provide a robust estimate of cooling rate and 4) demonstrate that an approach involving multiple xenolith samples from different depths can further be used to decipher thermal histories for the deep lithosphere.

2.2 U-Pb thermochronology

A major goal of radioisotopic thermochronology is to determine an accurate time-temperature history for a sample as it passes through the closure interval of different mineral-isotopic chronometers. Temperature sensitive U-Pb dates are the result of thermally activated volume diffusion of radiogenic Pb that is produced by the decay of U. In order to assign meaningful temperatures to U-Pb dates, we need a quantitative assessment of Pb diffusion behavior within the accessory minerals of interest (rutile, apatite, titanite). This behavior can be approximated by the 1-D diffusion-production equation:

$$\frac{\partial C}{\partial t} = D(T)\bullet\frac{\partial^2 C}{\partial r^2} + P \qquad (1)$$

where the change in concentration of an element (C) (in this case Pb) with time (t) is equal to the second order spatial derivative of the element concentration multiplied by a Diffusion constant (D), which is itself a function of temperature (T). A production term (P) accounts for the in-situ decay of radiogenically produced daughter. A successful solution to this equation will provide us with a book-keeping method for radiogenically produced ^{206}Pb and ^{207}Pb as it varies within a grain from diffusion (D) and decay of uranium (P) as a function of time.

The variability of both daughter production and daughter retention with temperature and time presents a significant complication in understanding the meaning of measured dates of whole mineral grains. The open vs. closed system behavior of elements in solids is dependent upon whether diffusion or production controls the budget of Pb within an accessory phase. Open system behavior occurs at higher temperatures when diffusion is fast enough to induce the loss of radiogenic daughter as quickly as it is produced by decay. Closed system behavior occurs at low temperatures when diffusive loss of Pb is so slow that all radiogenically produced Pb is effectively retained. The region of time-temperature space

between open and closed system behavior is defined as the Partial Retention Zone (PRZ), a region where both production and diffusion are operating at or a near a balance resulting in the partial retention of radiogenic daughter. Any measured U-Pb date, is a result of the daughter isotope gained since the time of system closure plus the daughter acquired in the PRZ. The partial retention of radiogenic daughter is controlled by three different variables, all simultaneously and independently operating to create a unique partial retention zone for a particular thermal history. These variables are: 1) temperature dependent diffusion of radiogenic daughter, 2) production of radiogenic daughter and 3) diffusion's length dependency. This first variable, the diffusion of radiogenic daughter, is controlled by the sample's time-temperature path and results in a unique PRZ for a specific t-T path. For example, fast cooling rates condense the values of diffusivity that may yield partial retention behavior and limit the effects of PRZ residence. Slow cooling, in contrast, results in prolonged time periods with an effective diffusivity that induces partial loss of daughter, yielding a PRZ that is unique to a cooling path. The second key variable, daughter production, will vary both in time as the activity of the parent isotope changes and between different radiometric system. For example, the difference in daughter production rates from the decay of ^{238}U and ^{235}U results in a unique PRZ for the ^{235}U-^{207}Pb and ^{238}U-^{206}Pb systems. Lastly, the length scale dependency of diffusion requires that radiogenic daughter that is produced within the cores of grains has a physically longer distance to travel than the daughter product produced at the edges. The difference in time-scales between Pb-retention in the core and rim of a grain leads to an apparent difference in the time of grain core vs. rim closure while simultaneously providing a temporal record of PRZ residence. For grains of variable size, this length scale-dependency will result in each individual grain size partially retaining Pb over different time periods which in turn results in each grain having its own unique PRZ. The ultimate goal of assigning a meaningful temperature to any measured thermochronometric date requires an understanding for how all of these variables contribute to affect the duration of PRZ residence. The most commonly used method for estimating PRZ residence and assigning a temperature to a measured thermochronologic date is the Dodson method (Dodson, 1973).

The Dodson method has been successfully applied to upper-crustal thermochronologic studies, but some of the models inherent assumptions are likely violated in the lower crust. These assumptions include: 1) a monotonic cooling path and 2) cooling through the PRZ occurs on time-scales far shorter than the half-lives of radioactive parent elements, allowing the solution to assume a linear production of radiogenic daughter. One characteristic of the U-Pb rutile and titanite data produced in this study as well as two previous studies of lower crustal xenoliths (Davis et al., 2003; Schmitz and Bowring, 2003a) are discordant arrays of U-Pb dates. Measurements of varying grain size yield dispersion in measured U-Pb dates of hundreds of millions of years, defining a curvilinear array on a concordia diagram. This extreme discordance indicates a loss of equilibrium within the U-Pb system that could potentially be interpreted as

the result of two different t-T paths: 1) reheating, violating the monotonic cooling history required to use Dodson's approach and 2) slow-cooling, which must consider radiogenic production over the hundreds of millions of years of potential PRZ residence. This requires that we utilize a solution to the diffusion-production equation that allows testing of both slow cooling and reheating time temperature paths, and that accounts for the production of specific Pb isotopes during prolonged residence within the PRZ.

2.2.1 Analytical solution to the diffusion equation

In the late 1950's and early 1960's as U-Pb zircon geochronology was being developed, volume diffusion theory and analytical solutions to the diffusion equation were derived in an effort to explain the loss of Pb and discordance observed in nearly all zircon measurements. Wetherill (1956) developed a graphical method using the concordia curve to determine both the timing of zircon crystallization and a secondary reheating event, potentially a reheating event, that he hypothesized induced the diffusive loss of Pb,. The topology of data predicted by the episodic Pb-loss model is a straight line connecting the U/Pb ratios corresponding to the time of initial system closure (t_1) and the time of system reset or partial reset (t_2) (Fig. 1a). In this model the variation in U/Pb ratios along this discordia line is due to volume-diffusion's dependence on diffusion domain (*a*). The smallest domains are most susceptible to loss and yield the youngest dates, while the larger domains are less susceptible to Pb loss and yield older dates.

Seeking an alternative mechanism for Pb-loss within zircons, Tilton (1960), suggested a model for the 'continuous' loss of Pb within zircons. This diffusion model assumed that zircon grains were continually losing lead between the time of system formation until the time of system closure. Tilton (1960) presented an analytical solution to the diffusion equation for both U-Pb systems and thus plotted on a U-Pb concordia diagram. This analytical solution is restricted to using a constant diffusivity, i.e. temperature sensitive diffusivity cannot be modeled. Results from this solution are plotted in Figure 1b (cross symbol). Start time in this sample calculation is 3000 Ma. Unlike the secondary Pb-loss event model, the modeled data define a curvilinear array between the time of system formation and the origin. The curvilinear diffusion trajectory curves asymptomatically as it approaches the origin. The asymptotic nature of the Pb diffusion trajectory as it approaches concordia is unique to continuous diffusion and will serve as a characteristic signature within real data sets.

Though the analytical solutions are restricted to a constant diffusivity, the difference in the data topology between the two models demonstrates how powerful the dual U-Pb system can be for monitoring time-variant Pb diffusion. The Wetherill and Tilton models for Pb loss are analogous to the end-member cases of reheating and slow cooling t-T paths, respectively. Below we will show how modeling reheating and slow cooling t-T paths within systems obeying temperature dependent diffusion will produce data topologies with the same distinguishable characteristics as the Wetherill and Tilton

models.

2.2.2 Numerical Solution to Diffusion equation

A more flexible solution to equation 1 by finite different methods can be used to calculate Pb concentration profiles for grains with variable temperature dependent diffusivity. A forward time, centered space solution to the diffusion equation provides a means to forward model synthetic U-Pb data for comparison to measured thermochronometric data (Schoene and Bowring, 2007). In general terms, the concentration of radiogenic daughter is solved for by assuming a time-temperature path, parent element distribution, and grain size. Both age and grain size can be accurately measured for each real grain that is dated. The key parameter space that remains to be explored is the t-T path. In this exploratory study we assume a homogenous distribution of parent elements. By forward calculation of the Pb concentrations for a series of grain sizes, we can create a synthetic data set that includes the predicted Pb diffusion profile, grain size vs. age curve, and data topology in U-Pb concordia space, for any pre assumed t-T path. The correct time temperature path is qualitatively deduced by how synthetic data compare to measured thermochronometric dates. The accuracy of the finite-difference solution has been evaluated by comparing results (at a constant T) to the analytical solution developed by Tilton (1960). Figure 1b shows the results of a comparison of constant diffusivity between the finite difference (circles) and analytical solutions (cross). The U/Pb values produced by the numerical solution agree with no more than 0.4% deviation from the analytical solution.

2.3 Data Topology

2.3.1 Resolving a unique cooling path

The nearly identical data produced by both slow cooling and reheating has long been noted and debated in thermochronology (Heizler, 2002; Hodges and Bowring, 1995; Schoene and Bowring, 2007). In past studies, geological considerations and the magnitude of local and regional thermal events have been used to decide between slow-cooling and reheating t-T paths (Hodges and Bowring 1995). Ambiguity in a rock's cooling path arises from the possibility that data from internal diffusion profiles and grain size-age relationships may be produced from either slow-cooling or reheating time-temperature paths. The finite difference solution to the diffusion equation can be used to demonstrate how the dual decay scheme can be employed to distinguish between continuous diffusion in a slow cooling system and Pb-loss during some secondary event. Figure 2 shows the modeled U-Pb results from both reheating and slow cooling time-temperature paths. The Pb diffusion profiles (Fig. 2a) and grain size-age relationships (Fig. 2b) produced by the two t-T paths (fig 2 inset) are nearly identical and are beyond resolution of any

analytical technique. The same t-T paths shown in the figure 2 inset are used to produce U/Pb ratios for both the ^{238}U and ^{235}U decay schemes and are plotted in U-Pb concordia space (fig 2c); the topologies are distinguishable for each t-T path. The slow-cooling modeled data define curvilinear arrays that become asymptotic near the lower intercept and are easily distinguishable from the straight-line of the reheating t-T path. The topology of data exhibited by a single sample will be an important tool to deciphering cooling paths for the case study region presented below. In the following sections we will explore why each t-T path results in the data topologies and how we can exploit these data trends to further interpret a samples t-T path.

Interpreting thermochronologic data on a concordia diagram also allows users to extract cooling rates from samples that do not exhibit perfect single domain behavior. In a grain size vs. age plot (fig 2c), an internal fast diffusion pathway (grain cracks, defects or inter-growths) would yield a younger measured date and thus 'fall' off an array of data points. On a concordia diagram this data would still lie on the diffusion trajectory, however the data would have lower $^{206}Pb/^{238}U$ and $^{207}Pb/^{235}U$ ratios than well-behaved single domain grains of the same size. Mixing two separate diffusion domains that have experienced the same thermal history will always plot on the diffusion trajectory as a mixture between the domain sizes (Tilton, 1960).

2.3.2 Slow Cooling : Relationship between internal Pb profiles and whole grain U-Pb dates

Diffusion is a length-scale dependent process. As such, radiogenic daughter that is produced within the cores of grains has a physically longer distance to travel than the daughter product produced at the edges. This results in a difference in the time of grain core vs. rim closure. In the context of the slow cooling model the timing of entry and exit into the PRZ is recorded by the core and rims of a grain, respectively. If the sample cooled slowly enough, the resulting difference in time between core and rim closure may be significant, with longer durations in the PRZ yielding larger differences. To illustrate the relationship between a grain's internal Pb diffusion profile and whole grain U-Pb date, figure 3 shows a concordia diagram with the U-Pb ratios from along a grain's diffusion profile and the whole grain measurement that results from this internal profile. The internal U-Pb dates across the radius of this 200 micron grain (lower inset) were produced by a model run for slow cooling at a rate of 0.1 °C/Ma (upper inset). Plotting the internal profile in 2 micron increments (circles) on a concordia reveals a curvilinear array spanning between the apparent time of core and rim closure. A whole-grain analysis (star) reflects mixing of these internal dates and their corresponding $^{238}U/^{235}U$ values, yielding a discordant analysis.

These profile U-Pb dates (dots) plotted in U-Pb concordia space however, are not concordant, because each U-Pb decay scheme has a unique PRZ as a result of different production rates for ^{206}Pb and ^{207}Pb. At high temperatures the diffusion of lead is the dominant process. As the rock cools and diffusion

decreases, diffusion will come into balance with the high production rate ^{235}U-^{207}Pb system prior to the ^{238}U-^{206}Pb system (fig 3 upper inset). At the bottom of the partial retention zone, the production of ^{207}Pb will exceed the lower diffusivity that accompanies decreased temperatures, leading to the complete closure of the ^{235}U-^{207}Pb system prior to the ^{238}U-^{206}Pb system. This off-set in each U-Pb system's partial retention zone leads to a small excess of ^{207}Pb within slowly-cooled minerals as a direct result of the ^{235}U-^{207}Pb earlier system closure. We can see this effect of relative system closure by comparing the U-Pb system's internal age profiles (fig 3 lower inset) as well as the location of the internal U-Pb profile dates plotted on concordia.

The length scale dependency of diffusion also predicts that the resulting Pb diffusion profile and the temperatures of Pb retention will vary as a function of grain size, for any one time-temperature path. Because of this dependency, each individual grain size will have a distinct Pb diffusion profile, partial retention zone and whole-grain parent daughter ratio (i.e. location on concordia plot). Figure 4, serves to illustrate this relationship between these parameters. Lead diffusion profiles (Fig 4a) are shown for grains with radii of 25, 50, 100 and 200 micrometers. Length scale dependency causes larger diffusion domains to retain Pb at higher temperatures than smaller grains. As stated above these apparent U-Pb dates across the radius of the crystal provide us with the approximate time-span of partial lead retention. Figure 4b shows how the timing of this partial lead retention can be superimposed on a slow cooling time-temperature path (0.1 °C/Ma) for each grain size. The length-scale dependency of Pb, leads directly to a unique and separate PRZ for every grain size. As such, large and small grains can be used to resolve different parts of the time-temperature history. As an individual grain cools through its partial retention zone, the whole-grain age evolution through time of this grain can be tracked and plotted in U-Pb concordia space. The bulk grain age-evolution of 25, 50, 100 and 200 micron radius grains are plotted in figure 4c in 50 Ma increments. Each grain is concordant at the top of its PRZ when it first begins to retain Pb produced by a singular or narrow composition of $^{238}U/^{235}U$. As each grain cools through its' PRZ it retains Pb of different isotopic compositions as a result of the time-variant parent isotopic compositions ($^{238}U/^{235}U$). A whole-grain analysis of a grain with this internal diffusion profile will result in a mixture of these different Pb compositions that will become increasingly discordant as the grain incorporates a higher variability of $^{207}Pb/^{206}Pb$ (fig 4c). U-Pb whole grain dates for this same range of grain sizes and cooling paths is shown in figure 4d. The discordant array of data has an asymptotic topology that occurs as a result of each grain having its own unique PRZ and acquiring different amounts of variable isotopic compositions of Pb. Below we will see how these asymptotic trajectories in slow-cooling systems are highly sensitive to duration and thus cooling rate through the PRZ and can be used as a tool to determine time-temperature histories.

2.3.3 Slow Cooling: Resolving unique cooling rates

Cooling rate estimates are derived from the relationship between cooling rate and duration in the PRZ; the slower the cooling rate through the PRZ the longer the duration. Forward modeled U-Pb data with variable linear cooling paths are plotted in figure 5. Results of calculations using titanite (Cherniak, 1993), rutile (Cherniak, 2000) and apatite (Cherniak et al., 1991) diffusion kinetics are plotted in figures 5 a, b and c respectively. For each set of kinetics, cooling rates between 10 and 0.075 °C/Ma are explored. For cooling rates of 10 °C/Ma or faster, data plots near the model start time (3000 Ma). This relatively rapid cooling rate through the PRZ causes little to no difference between large and small grains. For cooling rates slower than 10 °C/Ma the effect of grain size causes a dispersion of data along concordia, with smaller grains yielding younger dates. Cooling rates slower than ~0.25 °C/Ma are not only dispersed according to grain sizes but become discordant and highly asymptotic to concordia. A general trend of slower cooling rates and thus longer time spent within the PRZ, is shown to yield extended arrays of data. Calculated data sets for multiple minerals with different diffusion kinetics are shown to demonstrate the relative independence between diffusion kinetics and data topology. Though each mineral retains Pb at a different temperature range (figure 5 insets), the data topologies for all three minerals at one cooling rate are similar. Trends between data topology and cooling rate will not only aid in deciphering cooling rates, but also help us resolve time-temperature paths even for minerals such as rutile where the temperature of Pb-closure is still debated.

2.3.4 Episodic Pb-loss and reheating t-T paths

Episodic Pb-loss or reheating can induce discordant U-Pb data similar to what is observed in accessory minerals from lower crustal xenoliths. In this end member thermal history, a rock has experienced rapid cooling during some initial event followed by open to partially open system behavior during a subsequent reheating event. As shown in figure 1a, the upper intercept records the initial time of system closure, while the lower intercept records the time of a secondary reheating event.

As in the case of slow cooling, each whole grain analysis is discordant a result of mixing an internal Pb diffusion profile of different U-Pb ratios. Figure 3b shows a plot of the calculated U-Pb dates along the radius of a 200 um grain on a concordia diagram (dots). The model whole grain date that results from this profile is also plotted (star) and unlike the case of slow cooling, lies *on* the mixing line between the initial rapid cooling (t_1) and subsequent reheating event (t_2). Prior to the reheating event, this grain had a uniform profile across the radius. The heating event results in a continuous gradient of dates along the radius of the grain that lie between the initial and secondary event.

The finite difference diffusion model allows us to explore the effects of different heating magnitudes and durations. Figure 1 shows the results of forward modeled titanite U-Pb dates for reheating

of grains of varying size. A reheating event at 1000 Ma is modeled as a dike or half-space intrusion of variable half-widths and an initial temperature of 1200 °C. All parameters, including start time and temperature, distance from the intrusion to the sample, grain sizes and initial cooling rate are held constant. Only the size of the intrusion is varied between model runs. Comparison of reheating data sets to the linear cooling reveal that heating events such as the 100m half-width dike cause sufficient lead loss to completely change the data topology. Much like the internal profile for a reheating path shown in figure 3b, the variable grain size data define a linear array between the initial start of the system and the time of reheating (fig 1b). Small deviations from the linear array are due to the conductive cooling of the half-space after reheating. Larger intrusions on the order of 1km, yield extremely discordant data arrays that nearly span the distance between primary and secondary events. A large event will induce almost complete Pb loss, with modeled data clustered at a lower intercept. For a given mineral, there is a trade-off between duration and temperature of heating events such that small intrusions of high temperature can induce the same Pb loss as larger intrusions at lower temperatures. Analysis of multiple thermochronometers can solve this ambiguity and deliver a unique cooling path (Schoene and Bowring 2007).

2.3.5 Multiple sample approach

In addition to using the topology of individual data sets to determine cooling path and rate, we can employ a multiple sample approach where data from multiple xenoliths, each of a different depth, contribute to a unique thermal history for the entire lithospheric column. This method assumes that the thermal history recorded by a suite of xenoliths reflects that of the lithosphere. Let us consider the two end-member t-T paths of reheating and slow cooling within a section of lithosphere where three xenoliths, each from a different depth are dated.

Slow cooling t-T paths for samples of variable depth can be modeled by allowing a column of lithosphere at a specified initial temperature, thickness and internal heat production, to cool by conduction. The purpose of this thermal model is to predict how variable depths influence the time temperature path and the resulting U-Pb thermochronometric data. Time-temperature paths for 'samples' at 20, 30 and 40 km depths within the lithosphere have the same shape, cool at comparable rates, but at different times (fig 6a). The initial cooling along an exponential t-T path is controlled by sample depth, with the shallowest samples cooling fastest and the deep sample the slowest. Once a near steady thermal state is reached, however, samples cool at similar rates independent of residence depth (fig. 6a inset). Like modeled data from previous slow cooling model runs, modeled U-Pb data arrays are highly discordant and become asymptotic to concordia. Because the time of entry and exit into the PRZ is different for each depth, both the lower and upper intercepts of these data arrays are *resolvable* from one another.

A similar multiple sample analog can be set up to examine the effects of reheating on a column of lithosphere where 3 xenolith samples, each at a different depth, are heated during a large-scale regional thermal event. The duration and temperature of reheating events required to induce a similar magnitude of discordance as those observed in the data are considerable (>50% fractional loss Pb); requiring holding times on the order of millions of years for reheating events below 1000 °C and durations in the hundreds to thousands of years at mantle temperatures (Schmitz and Bowring, 2003). Any significant thermal event such as this will likely be recorded by each sample within the lithosphere with the effects of the reheating event varying as function of the sample distance from the heat source. To simulate this setting, a half-space model was used to heat the base of the lithosphere, with samples positioned at 20, 30 and 40 km from the heat source margin (fig. 6b inset). Because each sample is from a different distance from the source of heat, each will experience a different magnitude of reheating, simulating the effects of variable xenolith residence depth. The U-Pb thermochronologic data that results from t-T paths for each sample are plotted on concordia diagram in figure 6b. Unlike the slow cooling end member, the discordant arrays of data *share a common* lower intercept that is coincident in time with the reheating event.

2.3.6 Testing the effects of magmatic exhumation

In addition to understanding the thermal history of lower crustal samples, we must quantify the thermal affects of volcanic exhumation on the U-Pb systematics in accessory phases. Petrologic and experimental studies of xenolith bearing magmas (Canil and Fedortchouk, 1999; Edgar et al., 1988; Eggler and Wendlandt, 1979; Esperanca and Holloway, 1987) along with dynamical force balancing (Morin and Corriveau, 1996; Sparks et al., 2006; Spera, 1984) allow us to estimate the temperatures and holding times experienced by a lower crustal sample during exhumation. These conditions can then be used to calculate the minimum temperatures and holding times required to perturb U-Pb systematics within accessory phases.

Reliable estimates of xenolith residence time and host magma temperature are key to understanding the effects of volcanic exhumation on U-Pb systematics. Magma ascent rates for alkalic, mantle-derived magmas can in general be considered a rapid process. The occasional presence of diamonds, abundant xenoliths, some as large as 100 cm in diameter, imply that eruption rates are fast enough to transport the xenolith load from lower crustal and upper mantle depths. Typical ascent rates for alkaline magmas are estimated to be on the order of 10^1-10^3 cm/s or 1-5 day durations from upper mantle to lower crustal depths (Rutherford, 2008). Kimberlite and minette eruption rates have been further refined to rates on the order of hours to days by both dynamic calculations and experimental studies (Canil and Fedortchouk, 1999; Morin and Corriveau, 1996; Rutherford, 2008). An upper bound of magma temperatures can be provided from estimates of magma liquidus temperatures, which for

kimberlite and minette magmas has been estimated between 1050-1200 °C (Edgar et al., 1988; Eggler and Wendlandt, 1979; Esperanca and Holloway, 1987). The actual magma transport temperatures are likely lower than the liquidus temperatures as a result of heat loss to country rock/xenoliths and volatile degassing (Sparks et al., 2006).

The extreme upper boundary conditions of 5 days and 1200 °C can be used to estimate the maximum effects of volcanic transport on the topology of U-Pb data. This calculation has typically been solved for using the fractional loss equations from Crank (1956). This calculation provides us only with a minimum estimate to the conditions required to induce Pb-loss, as the solution assumes a homogenous initial distribution of diffusant within the crystal prior to perturbation. Accessory minerals that have experienced slow cooling or reheating, however, have pre-existing rounded diffusion profiles that will respond more slowly to diffusive loss during thermal perturbation. In reality the transporting magma would have to be hotter and/or heat longer to induce the same amount of fractional loss as with a homogenous distribution of Pb. The finite different model presented above can be used to simulate the conditions of magmatic heating on a rounded diffusion profile demonstrating that the fractional loss of Pb is as much as 10% less with a rounded initial profile when compared to a homogenous one. The finite difference calculation suggests that short-lived high temperature heating events of this magnitude do induce some Pb-loss even on grains with rounded initial profiles. Figure 7 shows the predicted effect of magmatic heating on U-Pb thermochronologic data. The 5 day maximum of holding time at the temperature of 1200 °C is shown to have a slight effect on the topology of U-Pb data, shifting all data points to lower U/Pb values. The loss of Pb, however, has little effect on the topology of U-Pb data and the final interpretation of a t-T path. This observation coupled with the likelihood that the eruptions of the xenolith bearing lavas are likely faster and cooler than the maximum limit modeled here, suggest that the effect of Pb loss from magmatic heating can largely be ignored. Only titanite and apatite kinetics allow loss of Pb, there is no appreciable Pb loss (<0.25%) using rutile diffusion kinetics. The accuracy of this finite difference calculation can be tested using a homogenous initial concentration of Pb prior to the reheating event and comparing the results to the fractional loss equations calculated with the same initial conditions (fig. 7 inset).

2.4 Rutile diffusion kinetics

Calculating Dodson closure temperatures from experimentally determined diffusion kinetics for Pb in accessory phases provides a means to compare the relative closure between different phases. The Dodson closure temperatures (T_C) calculated using kinetic values from Cherniak and Watson (2001), Cherniak (1993, 2000) and Cherniak et al. (1991) yield a relative order of Pb closure: Zircon (T_C >1000 °C), Rutile (T_C ~600-700 °C), Titanite (T_C ~600-650 °C) and Apatite (T_C ~450-500 °C) (fig. 8). Empirical

estimates for the temperatures of Pb closure yield a relative order that contrasts with experimentally determined values: zircon and Monazite (T_C >1000 °C) Titanite (T_C ~600-650 °C), Apatite (T_C ~500-550 °C), Rutile (T_C 450±50 °C) (Mezger et al., 1989; Schmitz and Bowring, 2003b). The rutile Pb closure temperature estimates from over ten U-Pb thermochronologic studies have been compiled and plotted in figure 8 (black circles). Estimates of rutile closure, grain size and cooling rate are cited directly from the reference when available. When closure estimates were unspecified, comparison between available titanite and apatite U-Pb and amphibole, phlogopite, muscovite $^{40}Ar/^{39}Ar$ data were used to bracket a temperature. In all but one study, rutile U-Pb dates are younger than titanite U-Pb and amphibole $^{40}Ar/^{39}Ar$ dates. The exception to this is an overlapping rutile U-Pb and amphibole $^{40}Ar/^{39}Ar$ dates from a moderately slowly cooled terrane (DT/dt= 1.5 °C/) (Mezger et al., 1989). In four studies, rutile U-Pb dates are younger or overlap with apatite U-Pb dates (Corfu and Easton, 2001; Corfu and Stone, 1998; Flowers et al., 2006; Schmitz and Bowring, 2003b). In several additional studies, rutile Pb closure is constrained between Titanite U-Pb/Amphibole $^{40}Ar/^{39}Ar$ and the lower temperature muscovite and biotite $^{40}Ar/^{39}Ar$ chronometers, (Anderson et al., 2001; Flowers et al., 2006; Mezger et al., 1989; Miller et al., 1996; Moller et al., 2000). Two conclusions can be drawn from this data compilation (fig 8): 1) Empirical estimates of rutile closure are significantly lower than predicted by diffusion kinetics, 2) Rutile has a Pb closure temperature between 400 and 500 °C.

2.5 Case Study

2.5.1 Geologic overview

Eocene minettes and kimberlites (~50 Ma) have exhumed a large population of lower crustal xenoliths just east of the Cordilleran deformation front in central Montana. Beneath the Phanerozoic sedimentary cover, the Archean Medicine Hat Block (MHB) to the north and the Wyoming Province (WP) to the south are separated by the largely unexposed Great Falls Tectonic Zone (GFTZ) (Davis and Ross, 1999; Gorman et al., 2002; Mueller et al., 2005; Mueller et al., 2002). To demonstrate the numerical and laboratory techniques described here, a case study for lower crustal xenoliths collected from the Sweetgrass Hills minette within the MHB are presented. U-Pb zircon data from basement rocks sampled by drilling reveal crystallization ages that range from 2.6-3.2 Ga, with the majority of samples yielding ages of ~2.7 Ga (Villeneuve et al., 1993). The Deep Probe seismic refraction study conducted as part of Lithoprobe, produced a high-resolution model for crust beneath the Northern Rockies (Gorman, et al., 2002). Velocity models indicate a thick (10-15 km) high velocity layer beneath the region at depths between 40 and 55km. Previous zircon U-Pb analyses from lower crustal xenoliths exhumed from the MHB yield a range of dates between 2.7 and 1.7 Ga (Davis et al., 1995). While tonalitic middle to lower crustal xenoliths from the Medicine Hat Block indicate Archean zircon growth, all lower crustal xenoliths

analyzed by these workers (four mafic and one felsic sample) yielded only ~1.8-1.7 Ga zircon dates. This led to an interpretation that the high-velocity layer is a Paleoprotoerzoic magmatic under-plate associated with the formation of the GFTZ (Gorman, et al. 2002).

2.6 Methods

2.6.1 Sample description and petrology

Three xenoliths from the Sweet Grass Hills minettes were selected for analysis. Two of the samples (05SG02 and 05SG05) have similar primary metamorphic mineral assemblages of Grt + Pl + Kfs + Bt (minor) ± Sil + Qz + Rt (Whitney and Evans, 2010). The third sample contains the mafic assemblage Grt + Cpx + Pl + Rt + Ilm. All three samples are well-preserved and exhibit granoblastic textures. Sample 05SG05 contains mm-scale gneissic layering defined primarily by garnet, feldspar, and quartz. In all samples, rutile is relatively abundant (~0.3-0.6 volume % - see appendix for details), occurs in the matrix and as inclusions within garnet and other major phases, and is interpreted as part of the peak metamorphic assemblage. This is an important constraint because it establishes initial rutile growth prior to or during development of peak temperatures, which are well above the temperatures of rutile Pb retention (Fig 8). Thus, the mineral can be utilized as a reliable thermochronometer. Minor ilmenite overgrowths on some rutile grains represent a late phase that probably developed during exhumation.

Thermobarometric estimates of peak metamorphic conditions were determined via several methods. First, initially determinations used the program TWQ 2.34 (Berman, 1991, 2007). Isochemical phase diagrams were also calculated with the program Perple_X (Connolly and Petrini, 2002) using the Na_2O-CaO-K_2O-FeO-MgO-Al_2O_3-SiO_2-H_2O-TiO_2 chemical system. Temperatures were also estimated based on Zr-in-rutile thermometry (Ferry and Watson, 2007; Watson et al., 2006). The best estimates of peak metamorphic conditions for samples 05SG02, 05SG05 and 05SG20 are 0.8 GPa/900 °C, 1.1 GPa/900 °C and 1.3GPa/890 °C, respectively. These data allow us to construct a relative stratigraphy between the MHB samples; from shallow to deep, 05SG02, 05SG05 and 05SG20. Thermobarometry data is included in the inset of figure 9. Additional sample description and details of thermobarometric calculations are included in the appendix.

2.6.2 U-Pb Laboratory Methods

Accessory phases used by this study were extracted from collected xenoliths following standard rock crushing and mineral separation procedures. Crushed rocks were then hand washed, dried and separated using standard magnetic and heavy mineral separation techniques were used to isolate heavy minerals such as apatite, titanite, rutile and zircon. Prior to dissolution and analysis, all grains were

photographed and measured. In the case study presented here, rutile was dated by U-Pb methods following procedures outlined by Schmitz and Bowring (2003) and Schoene and Bowring (2007). A mixed ^{205}Pb-^{233}U-^{235}U tracer solution was used for all ID-TIMS analyses. Samples were dissolved using standard Parr vessel HF/HCl treatments. Separates of U and Pb are purified separately using standard HBr and HCl column chemistry. Typical Pb blanks ranged between 0.5 and 1.2 pg. All U and Pb analyses were run on the Sector 54 Thermal Ionization Mass Spectrometer (TIMS) at MIT.

For sample presented here, at least ten rutile grains of varying size were dated by the above methods. The typical grain sizes (shortest radius) in lower crustal samples range between 10 and 250 microns. Grains without inclusions that had euhedral habit and no cracks produced reproducible grain-size age relationships. In preliminary study, poor quality grains, in particular large non-gem quality black rutiles often displayed multi-domain behavior, yielding younger U-Pb dates than previous analyses from a much smaller grain. To empirically demonstrate the presence of diffusion profiles, the edges of grains were isolated for U-Pb analysis. Whole rutile grains from sample 05SG05 were mounted in epoxy resin with the *a*/*b* axis of grains exposed at the polishing surface. Grains were then polished to remove over 95% of material. Isolated rims were dated using the procedures described above. Rutile grains from sample 05SG02 were mechanically abraded in attempt to enhance the older recorded cooling history within the core of the grain. Both grain cores and rims were excluded from comparison to forward difference models, which calculate data for whole grains.

Zircon grains from lower crustal rocks often have complicated growth histories, with individual grains consisting of an older core surrounded by as many as 1-3 periods of zircon growth. Procedures for dating complex zircons include imaging grains by Cathode Luminescence (CL) followed by micro-sampling each distinct zircon growth history for analysis using Chemical Abrasion U-Pb Thermal Ionization Mass Spectrometry (CA-TIMS) (Mattinson, 2005).

2.7 Results

2.7.1 U-Pb data

Zircons were recovered only from samples 05SG02 and 05SG05, the middle/lower crustal felsic granulites. and analytical results are tabulated in table 1. Grains from sample 05SG05 were homogenous and yielded dates of ~1.8 Ga. Distinct cores of grains from 05SG02 were as old as 2.7Ga, with rims plotting discordantly between ~2.7 and 2.0 Ga. Whole grain analyses from 05SG02 were discordant between 2.7 and 2.0 Ga. There were no zircons recovered from sample 05SG20.

Single grain rutile analyses of variable grain sizes (Fig. 9) define discordant data arrays for all three samples. The most shallow sample from the MHB, 05SG02, yields ^{238}U-^{206}Pb dates that range between

~1000 and 1400 Ma, sample 05SG05 a range between ~600 and 1100 Ma and the deepest sample 05SG20 a range between ~200 and 400 Ma. Each array of data define a curvilinear trajectory that becomes asymptotic to concordia. The data as a whole, roughly define a single trajectory, with the oldest analyses from sample 05SG20 overlapping in concordia space with a young analyses from 05SG05. The same phenomena occur between several old analyses from 05SG05 and younger grains from 05SG02.

Mechanically isolated rutile rims from sample 05SG05 yield overlapping ^{238}U-^{206}Pb dates within error of the minette host rock eruption age and demonstrate empirically that volume diffusion is operating in these grains. Isolated grain cores from sample 05SG02 yield U-Pb dates far older than whole grain, again empirically demonstrating the presence of diffusion profiles. Euhedral, gem quality rutile grains in samples 05SG02 and 05SG05 often contained no common lead, with analyses yielding laboratory blank levels. High common Pb rutile grains typically have black ilmenite rims and ilmenite intergrowth within the interior of grains. Sample 05SG05 had no ilmenite intergrowths and demonstrated a near perfect age vs. grain size relationship, with the smallest grains yielding the youngest dates and the largest yielding the oldest. Sample 05SG02 behaved similarly at small grain sizes, between 20 and 50 microns, however this relationship breaks down with larger poor quality grains that contained ilmenite intergrowths. Rutile U-Pb results are tabulated in table 2.

2.7.2 Modeling U-Pb data

Here we evaluate the potential time-temperature paths that can explain the U-Pb data presented above. Each sample is considered individually and fit with modeled data from both reheating and slow-cooling T-t paths. Modeled grain sizes for each sample use the minimum and maximum range of sizes recorded from dated grains using diffusion kinetics from Cherniak (2000). Zircon U-Pb analyses and geothermometry constrain the model start time/temperature to 1800 Ma/900 °C for these samples.Model calculations for reheating paths that attempt to fit rutile data from MHB are presented in figure 10a. For this end-member t-T path the shallowest sample, 05SG02, would have had to cool quickly through the Pb PRZ at 1800 Ma and been reheated at 800 Ma. Deeper samples 05SG05 and 05SG20 can be fit by similar paths with each quenching and reheating events occurring at different and younger times. As in the modeled data presented in figure 1a, the topology of the modeled data is a straight line between the timing of the initial cooling and the subsequent reheating event. Unlike the singular lower intercept produced during the reheating of multiple samples of variable depth test presented in figure 6b, these data could only be explained by multiple reheating events, each with is own resolvable lower intercept. This model has an additional requirement that each individual thermal event remain thermally isolated from the samples of different depths.

Forward calculated U-Pb data from slow cooling t-T paths can also be fit to each sample from

Sweetgrass (fig 10 b-d). To make systematic modeling easier, exponential cooling paths are approximated as segmented linear cooling paths.. Several cooling rates through the rutile Pb PRZ are then tested to bracket the array of measured data. Each sample from Sweetgrass cools through the Pb PRZ at rates lower than 0.25 °C/Ma with the shallowest sample cooling first and the deepest sample cooling last. The modeled data for each sample consists of a discordant array of data with an upper and lower intercept that is resolvable from the other samples. The topology of the modeled data is curvilinear and becomes asymptotic as it approaches concordia.

2.8 Discussion

Each rutile U-Pb dataset can be approximated with modeled data produced from reheating and slow cooling time-temperature paths (fig 10) and suggests the interpretation of data would be aided by a more general analysis of data trends. Though reheating t-T paths can roughly fit the data, this model requires discrete quenching and heating events throughout the history of the lithosphere (fig 10a inset). Zircon U-Pb data from these xenoliths as well as previous U-Pb zircon data from the region record only one significant thermotectonic event: the formation of the GFTZ at ~1.8 Ga (Table 1), (Bolhar, et al. 2007; Davis and Ross 1999; Gorman et al. 2002). There are no geochronologic data within these xenoliths or from regional surface exposures that record high temperature events coincident in time with the lower intercepts from samples 05SG02 and 05SG05 (~800 and 500 Ma respectively). Furthermore, the reheating model would require that each individual event is large enough to cause significant loss of Pb within one sample yet remain thermally insulated from the samples above and below. This is inconsistent with the expectations for a multi-sample approach (fig 6b), where reheating events resulted in samples from different depths sharing a common lower intercept as a result of reheating.

We can also evaluate the fit of the modeled slow cooling t-T paths to the data. Each sample U-Pb data set defines a curvilinear array that is asymptotic to concordia, consistent with the expected topology of data for slow cooling samples. Each array of data can be well-bracketed with model data with the same curvilinear trajectory and asymptotic curvature (fig 10 b-d). When we consider the 3 data sets as a whole the most important trend is the correlation between U-Pb dates for each xenolith and it's estimated residence depth. The simplest way to explain this trend is that these samples all record the progressive relaxation of a post-orogenic geothermal gradient. At ~1.8 Ga during the orogenic event, this geothermal gradient was sufficiently high to prevent lead retention in rutile from all depths. As the lithosphere cooled, the shallowest sample first entered the rutile PRZ, the timing of which is marked by the sample's upper intercept. The upper intercept of the shallowest sample (~1800 Ma) is coincident with $^{40}Ar/^{39}Ar$ biotite and amphibole dates from nearby surface exposures (Holm and Schneider, 2002). This is interpreted to indicate that temperatures within the MHB at ~25 km depth were <500 °C shortly after the

collision event. The next deepest sample, 05SG05 cooled to the top of its PRZ by ~1.5 Ga. Finally the deepest sample 05SG20 began to retain Pb by ~1.0 Ga. In the slow cooling model, the lower intercepts of each data set records the samples' exit from the rutile Pb PRZ. The coincidence of the lower intercept of 05SG20 with the age of the kimberlite is significant, as it marks the exhumation of the xenolith from within the rutile PRZ onto the Earth's surface where it was quenched. This also indicates that the crust at this depth was 450±50 °C at ~50 Ma. The trend of overlapping data previously modeled in figures (6a) is also observed within the rutile data from the MHB, suggesting that the slow cooling recorded by each sample occurred at a comparable rate. The slow-cooling model does not require temporally discrete quenching or reheating events and the trends within the data can be explained by a simple model for lithospheric thermal evolution. In the following section we will try to define an upper limit to the cooling rate for these samples by exploring the relationship between data topology and diffusion kinetics.

2.8.1 Data topology and the effects of diffusion kinetics

In a slowly cooled system, the degree of discordance in the U-Pb system is controlled by the cooling rate through PRZ. The extent of the PRZ in time-temperature space, based on numerical modeling (fig. 5), is fairly insensitive to the diffusion kinetics. Further exploration of the relationship between PRZ residence time and diffusion kinetics can be made using the Dodson solution for closure temperature (Dodson, 1973). This analytical solution provides a rapid way to evaluate how variation in diffusion kinetics affects the duration of partial system behavior; the later of which is roughly approximated by the difference in time (Δt) between the largest and smallest grain sizes for a particular cooling rate (fig. 11). At the slow cooling rates we are examining, the absolute values of Δt predicted by the Dodson solution are inaccurate, as the solution does not accurately account for exponential Pb production by radiogenic decay. However, for our purpose of examining the *trends* between variable diffusion kinetics and the extent of partial system behavior, the Dodson solution is suitable. At cooling rates of 1.0 °C/My and faster, the size of the PRZ is nearly completely insensitive to diffusion kinetics, yielding comparable Δt's for all combinations of kinetic values (fig.11). At cooling rates slower than 1.0 °C/My, diffusion kinetics have an increased though second order effect on the size of the PRZ. For example, at a rate of 0.25 °C/My, the entire range of Pb activation energies and diffusion coefficients yields a ~50% maximum range of Δt's , while decreasing the cooling rate from 0.25 to 0.1 °C/My would change the Δt over 200%. At cooling rates as low as 0. 1 °C/My, the range of the PRZ becomes highly sensitive to diffusion kinetics, thus decreasing our ability to conclude on a cooling rate a this range. At cooling rates between 1-0.25 °C/My relative independence between diffusion kinetics and the size of the PRZ suggests that the topology of rutile U-Pb data alone can be used to place an upper limit to the cooling rate through the minerals' PRZ.

Though one cannot accurately model the exact temperatures of Pb retention in rutile without accurate diffusion kinetics, U-Pb data does confirm that rutile is obeying volume diffusion behavior based on the grain size dependencies in measured U-Pb dates, in particular the high quality grains from sample 05SG05 and 05SG02 (fig 10). Combining the empirical constraints on rutile Pb closure (fig. 8) and a demonstration of cooling rate dependent data topology that is relatively insensitive to diffusion kinetics (figs. 5 and 11) allows for the conclusion that the cooling rate for samples from the Sweetgrass hills, through the rutile thermal window (450±50 °C) is on the order of 0.25 °C/My or less.

2.8.2 Thermal state recorded by lower crustal thermochronometers

We can evaluate the thermal/tectonic state and mechanism of cooling within the lithosphere through a comparison of both the absolute temperatures recorded by the lower crustal thermochronometers and those predicted by physical models for heat transfer in the lithosphere (Ehlers et al., 2005). One of the most broadly applicable lithosphere thermal models is a stratified 1-D calculation, first described by (Pollack and Chapman, 1977), that extrapolates the measured surface heat flux to the rest of the lithosphere while stripping out the internal heat contribution from the crust, lower crust and lithospheric mantle. This model allows us to test the sensitivity of lower crustal temperatures to any model parameter and explore a possible range of lower crustal temperatures. The assumed surface heat flux in this calculation has the most significant effect on lower crustal temperatures, with temperatures at 40 km depth ranging between 380 °C on a cratonic geotherm (40mW/m^2) to over 800 °C at a high geothermal gradient (80mW/m^2) (Chapman, 1986). Other influential parameters include the distribution and concentration of heat producing elements (HPE) within the crust (Rudnick et al., 2003; Rudnick et al., 1998), thermal conductivity and Moho depth. Realistic variations in each of these parameters can cumulatively effect the temperature at 40 km depth by over 10%, yielding a range of lower crustal temperatures between 380 and 450 °C for a cratonic geotherm (40mW/m^2)(Chapman, 1986). These temperatures predicted for the low cratonic geothermal gradient are well within the temperatures of rutile Pb retention.

2.9 Conclusions

We have demonstrated how U-Pb thermochronology can be used to resolve unique time-temperature paths for lower crustal rocks exhumed by volcanic eruptions. Numerical solutions to the diffusion equation provide us with the means to exploring the U-Pb thermochronologic system's dependencies on: (1) grain size, (2) decay rate (^{238}U vs. ^{235}U), (3) cooling rate through the partial retention zone (PRZ) and (4) sensitivity to diffusion kinetics.

(1) The length scale dependency of Pb diffusion causes grains of variable size to each have its own unique zone of Pb retention in time-temperature space. This results in grains of one size to retain a different Pb isotopic composition (produced by the decay of a different composition of parent U) than a grain of any other size.

(2) The dramatically different decay rates for ^{238}U and ^{235}U are manifested in two ways. First, because the PRZ of any system is dependent upon production rate, the ^{235}U-^{207}Pb and ^{238}U-^{206}Pb systems each have their own PRZ. The higher production rate of ^{207}Pb leads to a relative excess in retained ^{207}Pb. Second, the difference in ^{238}U and ^{235}U decay constants yields time sensitive information on Pb diffusion that can be utilized for resolving the difference between reheating and slow-cooling events. Reheating time-temperature paths lie along a straight line between the time of initial quenching and the subsequent thermal event. Slow cooling t-T paths yield an asymptotic topology of data for multiple analyses of variable grain size.

(3) The topology of data produced by slow cooling t-T paths is strongly dependent upon cooling rate through the PRZ. Longer durations yield longer more discordant arrays of data providing a tool for estimating the cooling rate through the PRZ.

(4) The topology of this variable grain size data is generally insensitive to kinetics in comparison to cooling rate, allowing users to estimate cooling rate for minerals with poorly constrained diffusion kinetics.

In the Montana study area, rutile U-Pb data from three xenoliths derived from different depths from a single volcanic epicenter are best interpreted by slow cooling t-T paths where the shallowest sample cooled first and the deepest last. Combining the topological dependence of U-Pb data on cooling path with the multiple sample of variable depth approach supports the conclusion that lower crustal thermochronometers record a slow thermal relaxation since the Paleoproterozoic. Comparing the rates predicted by these thermochronologic results with the rates predicted for physical models of heat transfer within the earth will allow future studies to evaluate the mechanisms for cooling and heat transfer within the lithosphere.

Acknowledgments: Primary funding for this project was provided through EarthScope grant EAR-0746205. The authors would like to thank D. Canil and F. Corfu for their constructive reviews and Timothy Grove for his editorial handling. Discussions throughout this study with both Doug Walker and Noah McLean were insightful and greatly appreciated.

2.10 Figure Captions

Fig. 1 Comparison of data topologies on U-Pb concordia diagram for a) Episodic/reheating and b) continuous or slow cooling time temperature paths. Forward calculated reheating time-temperature paths are plotted as symbols along with the graphical solution in black (line) from Wetherill, (1956) (a). Discordant arrays of data are produced by rapidly cooling the sample at some initial time (t_1) followed by a secondary reheating event at t_2. The reheating event is modeled as a half-space model. Constant model parameters for all tested t-T paths include: grain sizes, start temperature and time, distance of sample from dike, diffusion kinetics, intrusion temperature and intrusion time. Only the size of the intrusion is varied. (b) A comparison between analytical (crosses) and numerical solution (circles) for continuous diffusion is used to test the accuracy of the finite difference solution

Fig. 2 Forward modeling of time temperature paths for reheating (squares) and slow cooling (circles) reveal the potentially indistinguishable data sets for both a) grain size vs. age relationships or b) internal diffusion profiles; two data types often produced by single isotopic thermochronometric systems to elucidate t-T paths. Plotting U-Pb ratios for both systems on Concordia diagram (c) for the same reheating and slow cooling time temperature paths reveals data topologies that are distinguishable from one another. Diffusion occurring continuously during a slow cooling t-T path yields an asymptotic topology (circles) that is resolvable from the straight-line topology produced from the reheating t-T path (squares)

Fig. 3 Comparison of internal U-Pb profiles (dots) and whole-grain U-Pb dates (star) plotted on concordia diagram for a) reheating and b) slow cooling t-T paths. Slow cooling t-T paths (a) produce discordant whole-grain points as a result of mixing Pb produced from different isotopic compositions of U. Additional processes inducing disequilibrium between the different decay schemes are the offset between the ^{238}U-^{206}Pb and ^{235}U-^{207}Pb PRZ's (upper inset). The different decay rates for each daughter product leads to different times in which daughter production comes to balance with daughter diffusion. Reheating t-T paths (b) induce internal Pb diffusion profiles where the core records the initial time of cooling (t_1) and the grain rim, the subsequent reheating event (t_2)

Fig. 4 For a single slow cooling path, variable grain sizes yield different ranges of internal U-Pb dates (a) with large grains retaining Pb at earlier times and higher temperatures. Subplot (b) plots the PRZ for each grain size on the tested time-temperature path. Each grain is recording a discrete region of the time temperature path. This results in a unique set of: internal U-Pb dates (a), and a different U-Pb whole grain date. Subplot (c) tracks several grains in 50 Ma increments. Upon entry into the PRZ every grain is concordant, meaning it contains Pb produced by a uniform $^{238}U/^{235}U$. Each grain becomes more discordant through time, as the whole grain begins to retain more Pb produced by the decay of different $^{238}U/^{235}U$. Length scale dependency of diffusion leads to discrete ranges of Pb retention for each grain size which in turn leads to the asymptotic topology (d)

Fig. 5 Series of concordia plots showing the results of slow cooling time-temperature paths at a variable cooling rate. Colors of data correlate to the colors of cooling rates shown in the inset time-temperature path. Slower cooling rates yield longer durations in the PRZ, in turn resulting in longer discordant data arrays. Start time and temperature, grain sizes are kept constant. Only the cooling rate and diffusion kinetics are variable; (a) titanite, (b) rutile, (c) apatite. Modeled results using multiple diffusion kinetics are plotted to demonstrate the potential for different U-Pb thermochronometers as well the relative independence between diffusion kinetics and data topology

Fig. 6 Forward modeling U-Pb data for multiple xenolith samples of different depths within the lithosphere produced by thermal models for lithosphere a) slow cooling and b) reheating. Multiple sample analyses of a Slow cooling (b) lithosphere yields curvilinear discordant arrays of U-Pb data with resolvable and unique upper and lower intercepts. Reheated lithosphere (a) produce overlapping straight lines of discordant U-Pb data with a common irresolvable lower intercept. The intercepts of these lines are coincident in with the timing of initial cooling and the reheating event or with cooling shortly after

Fig. 7 Concordia plot showing the effects of magmatic exhumation on U-Pb data. Finite difference model tests the effects of short-lived heating events on thermchronometers with rounded initial profiles. Rounded diffusion profiles lessen the diffusant loss during a secondary reheating event. Independent constraints on magma temperature and eruption rate can only place maximum heating conditions at 1200 °C and 5 days, though lower temperatures and shorter holding times are more likely. Decreasing the magma holding temperature to 1000 °C yields Pb loss below 1%. Titanite and apatite kinetics are used, rutile kinetics predict negligible loss at these conditions. Figure inset show an accuracy test of this calculation using the same initial conditions in the numerical solution (blocks and circles) as those used by the analytical solution (solid lines)

Fig. 8 Three-dimensional plot showing the variation of Dodson closure temperature as a function of both cooling rate (°C/ My) and grain radius (μm). Three-dimensional planes are calculated using Dodson equations and experimentally measured diffusion kinetics. Circles mark the estimated closure for rutile based on empirical studies, see text for references. Diffusion kinetics for $^{40}Ar/^{39}Ar$ chronometers are from Harrison (1982), Giletti (1974), and Hames and Bowring (1994)

Fig. 9 Rutile U-Pb data plotted on a single Concordia diagram. Samples 05SG02(green), 05SG05(blue), and 05SG20 (red). Figure inset shows P-T diagram of thermobarometry, where the shaded regions represent calculated stability fields for the peak assemblages from phase assemblage diagrams. Solid red lines for 05SG20 show intersection of Grt-Cpx-Pl-Qz equilibria calculated with TWQ. Dashed lines are Zr-in-rutile thermometer results. See appendix for more detailed description

Fig. 10 Concordia plots showing a comparison between measured U-Pb data from lower crustal samples from the Sweetgrass volcanics (MHB) and forward calculated data assuming (a) reheating paths and (b-d) slow cooling paths

Fig. 11 Dodson equation calculated difference in time between small and large diffusion domains (Δt) over a range of diffusion coefficients, activation energies (E_a) and cooling rates (DTdt). Boxes are placed at the intersection of E_a and D_0 for each phase, marking the Δt at a particular cooling rate for that phase. The Dodson analytical solution provides a rapid way to test how sensitive the size of the Pb partial retention zone is to diffusion kinetics

2.11 References

Anderson, S.D., Jamieson, R.A., Reynolds, P.H., Dunning, G.R., 2001. Devonian Extension in Northwestern Newfoundland: 40Ar/39Ar and U-Pb Data from the Ming‚Äôs Bight Area, Baie

Verte Peninsula. The Journal of Geology 109, 191-211.
Baldwin, J., Bowring, S.A., Williams, M.L., Williams, I.S., 2004. Eclogites of the Snowbird tectonic zone: petrological and U-Pb geochronological evidence for Paleoproterozoic high-pressure metamorphism in the western Canadian Shield. Contributions to Mineralogy and Petrology 147, 528-548.
Berman, R.G., 1991. Thermobarometry using multi-equilibrium calculations; a new technique, with petrological applications; Quantitative methods in petrology; an issue in honor of Hugh J. Greenwood. The Canadian Mineralogist 29, 833-855.
Berman, R.G., 2007. winTWQ (version 2.3): a software package for performing internally consistent thermobarometric calculations, Geological Survey of Canada Open File report 5462, p. 41.
Canil, D., Fedortchouk, Y., 1999. Garnet dissolution and the emplacement of kimberlites. Earth and Planetary Science Letters 167, 227-237.
Chapman, D.S., 1986. Thermal gradients in the continental crust. Geological Society, London, Special Publications 24, 63-70.
Cherniak, D.J., 1993. Lead diffusion in titanite and preliminary results on the effects of radiation damage on Pb transport. Chemical Geology 110, 177-194.
Cherniak, D.J., 2000. Pb diffusion in rutile. Contributions to Mineralogy and Petrology 139, 198-207.
Cherniak, D.J., Lanford, W.A., Ryerson, F.J., 1991. Lead diffusion in apatite and zircon using ion implantation and Rutherford Backscattering techniques. Geochimica et Cosmochimica Acta 55, 1663-1673.
Cherniak, D.J., Watston, E.B., 2001. Pb diffusion in zircon. Chemical Geology 172, 5-24.
Connolly, J.A.D., Petrini, K., 2002, 2002. An automated strategy for calculation of phase diagram sections and retrieval of rock properties as a function of physical conditions. Journal of Metamorphic Geology 20, 267-708.
Corfu, F., Easton, R.M., 2001. U-Pb evidence for polymetamorphic history of Huronian rocks within the Grenville front tectonic zone east of Sudbury, Ontario, Canada. Chemical Geology 172, 149-171.
Corfu, F., Stone, D., 1998. The significance of titanite and apatite U-Pb ages: constraints for the post-magmatic thermal-hydrothermal evolution of a batholithic complex, Berens River area, northwestern Superior Province, Canada. Geochimica et Cosmochimica Acta 62, 2979-2995.
Crank, J., 1956. Mathematics of diffusion. Clarendon Press, Oxford.
Davis, W., J., Berman, R., Kjarsgaard, B., 1995. U-Pb Geochronology and Isotopic Studies of Crustal Xenoliths from the Archean Medicine Hat Block, Northern Montana and Southern Alberta: Paleoproterozoic Reworking of Archean Lower Crust., in: Ross, G.M. (Ed.), Alberta Basement Transects: Lithoprobe Report #47, pp. 329-334.
Davis, W.J., Canil, D., MacKenzie, J.M., Carbno, G.B., 2003. Petrology and U-Pb geochronology of lower crustal xenoliths and the development of a craton, Slave Province, Canada. Lithos 71, 541-573.
Davis, W.J., Ross, G.M., 1999. Proterozoic underplating of the Archean Wyoming Craton and Medicine Hatt Block during Assembly of Western Laurentia. Ninth Annual V.M. Goldschmidt Conference.
Dodson, M.H., 1973. Closure temperature in cooling geochronological and petrological systems. Contributions to Mineralogy and Petrology 40, 259-274.

Edgar, A.D., Arima, M., Baldwin, D.K., Bell, D.R., Shee, S.R., Skinner, E.M.W., Walker, E.C., 1988. High-pressure-high-temperature melting experiments on a SiO 2 -poor aphanitic kimberlite from the Wesselton Mine, Kimberley, South Africa. American Mineralogist 73, 524-533.
Eggler, D.H., Wendlandt, E., 1979. Experimental studies on the relationship between kimberlite magmas and partial melting of peridotite, in: Boyd, F.R., Meyer, H.O.A. (Eds.), Kimberlites, Diatremes, and Diamonds: Their Geology, Petrology, and Geochemistry. American Geophysical Union, Washington, D.C., pp. 330-338.
Ehlers, T.A., Chaudhri, T., Kumar, S., Fuller, C.W., Willett, S.D., Ketcham, R., Brandon, M.T., Belton, D., Kohn, B., Gleadow, A.J., Dunai, T., Fu, F., 2005. Computational tools for low-temperature thermochronometer interpretation. Reviews in Mineralogy and Geochemistry 58, 589-622.
Esperanca, S., Holloway, J.R., 1987. On the origin of some mica-lamprophyres: experimental evidence from a mafic minette. Contributions to Mineralogy and Petrology 95, 207-216.
Ferry, J., Watson, E., 2007. New thermodynamic models and revised calibrations for the Ti-in-zircon and Zr-in-rutile thermometers. Contributions to Mineralogy and Petrology 154, 429-437.
Flowers, R.M., Mahan, K.H., Bowring, S.A., Williams, M.L., Pringle, M.S., Hodges, K.V., 2006. Multistage exhumation and juxtaposition of lower continental crust in the western Canadian Shield: Linking high-resolution U-Pb and 40Ar/39Ar thermochronometry with pressure-temperature-deformation paths. Tectonics 25, TC4003.
Gorman, A., R., Clowes, R., M., Ellis, R., , M., Henstock, T., J., Spence, G., D., Keller, R., G, Levander, A., Snelson, C., M., Burianyk, M., Kanasewich, E., R., Asudeh, I., Hajnal, Z., Miller, K., C., 2002. Deep Probe: imaging the roots of western North America. Canadian Journal of Earth Sciences 39, 375.
Heizler, M., 2002. Slow-cooling or reheating: can SW USA thermochronological data be reconciled?, Geological Society of America, Denver.
Hodges, K.V., Bowring, S.A., 1995. 40Ar/39Ar thermochronology of isotopically zoned micas: Insights from the southwestern USA proterozoic orogen. Geochimica et Cosmochimica Acta 59, 3205-3220.
Holm, D., Schneider, D., 2002. 40Ar/39Ar evidence for ca. 1800 Ma tectonothermal activity along the Great Falls tectonic zone, central Montana. Canadian Journal of Earth Sciences 39, 1719.
Jordan, T., H., 1988. Structure and Formation of the Cotinental Tectosphere. Journal of Petrology Special Lithosphere issue, 11-37.
Kooijman, E., Mezger, K., Berndt, J., Constraints on the U-Pb systematics of metamorphic rutile from in situ LA-ICP-MS analysis. Earth and Planetary Science Letters In Press, Corrected Proof.
Mattinson, J.M., 2005. Zircon U-Pb chemical abrastion ("CA-TIMS") method: combined annealing and multi-step partial dissolution analysis for improved precision and accuracy of zircon ages. Chemical Geology 220, 47-66.
Mezger, K., Hanson, G.N., Bohlen, S.R., 1989. High-precision U-Pb ages of metamorphic rutile: application to the cooling history of high-grade terranes. Earth and Planetary Science Letters 96, 106-118.
Miller, B.V., Dunning, G.R., Barr, S.M., Raeside, R.P., Jamieson, R.A., Reynolds, P.H., 1996. Magmatism and metamorphism in a Grenvillian fragment: U-Pb and 40Ar/39Ar ages from the Blair River Complex, northern Cape Breton Island, Nova Scotia, Canada. Geological Society of America Bulletin 108, 127-140.

Moller, A., Mezger, K., Schenk, V., 2000. U-Pb dating of metamorphic minerals: Pan-African metamorphism and prolonged slow cooling of high pressure granulites in Tanzania, East Africa. Precambrian research 104, 123-146.
Morin, D., Corriveau, L., 1996. Fragmentation processes and xenolith transport in a Proterozoic minette dyke, Grenville Province, Québec. Contributions to Mineralogy and Petrology 125, 319-331.
Mueller, P., A., Burger, H.R., Wooden, J., L., Brady, J., B., Cheney, J., T., Harms, T., A., Heatherington, A., L., Mogk, D., W., 2005. Paleoproterozoic metamorphism in the Northern Wyoming Province: Implications for the Assembly of Laurentia. The Journal of Geology 113, 169-179.
Mueller, P., A., Heatherington, A., L., Kelly, D., M., Wooden, J., L., Mogk, D., W., 2002. Paleoproterozoic crust within the Great Falls tectonic zone: Implications for the assembly of southern Laurentia. Geology 30, 127-130.
Pollack, H.N., Chapman, D.S., 1977. On the regional variation of heat flow, geotherms, and lithospheric thickness. Tectonophysics 38, 279-296.
Rudnick, R.L., Gao, S., Heinrich, D.H., Karl, K.T., 2003. Composition of the Continental Crust, Treatise on Geochemistry. Pergamon, Oxford, pp. 1-64.
Rudnick, R.L., McDonough, W.F., O'Connell, R.J., 1998. Thermal structure, thickness and composition of continental lithosphere. Chemical Geology 145, 395-411.
Rutherford, M., J., 2008. Magma Ascent Rates, in: Putirka, K., D., Tepley, F.J. (Eds.), Minerals, Inclusions and Volcanic Processes. Mineralogical Society of America, pp. 241-271.
Schmitz, M.D., Bowring, S., 2003a. Ultrahigh-temperature metamorphism in the lower crust during Neoarchean Ventersdorp rifting and magmatism, Kaapvaal Craton, southern Africa. Geological Society of America Bulletin 115, 533-548.
Schmitz, M.D., Bowring, S., A., 2003b. Constraints on the thermal evolution of continental lithosphere from U-Pb accessory mineral thermochronometry of lower crustal xenoliths, southern Africa. Contributions to Mineralogy and Petrology 144, 592-618.
Schoene, B., Bowring, S.A., 2007. Determining accurate temperature-time paths from U-Pb thermochronology: An example from the Kaapvaal craton, southern Africa. Geochimica et Cosmochimica Acta 70, 165-185.
Sparks, R.S.J., Baker, L., Brown, R.J., Field, M., Schumacher, J., Stripp, G., Walters, A., 2006. Dynamical constraints on kimberlite volcanism. Journal of volcanology and geothermal research 155, 18-48.
Spera, F.J., 1984. Carbon dioxide in petrogenesis III: role of volatiles in the ascent of alkaline magma with special reference to xenolith-bearing mafic lavas. Contributions to Mineralogy and Petrology 88, 217-232.
Tilton, G.R., 1960. Volume Diffusion as a Mechanism for Discordant Lead Ages. Journal of Geophysical Research 65, 2963-2945.
Villeneuve, M.E., Ross, G.M., Theriault, R.J., Miles, W., Parrish, R.R., Broome, J., 1993. Tectonic Subdivision and U-Pb Geochronology of the Crystalline Basement of the Alberta Basin, Western Canada. Geological Survey of Canada Bulletin 447.
Watson, E., Wark, D., Thomas, J., 2006. Crystallization thermometers for zircon and rutile. Contributions to Mineralogy and Petrology 151, 413-433.
Wetherill, G., 1956. Discordan Uranium-Lead ages, I. Transactions, American Geophysical Union 37, 320-326.

Whitney, D.L., Evans, B.W., 2010. Abbreviations for names of rock-forming minerals. American Mineralogist 5, 185-187.

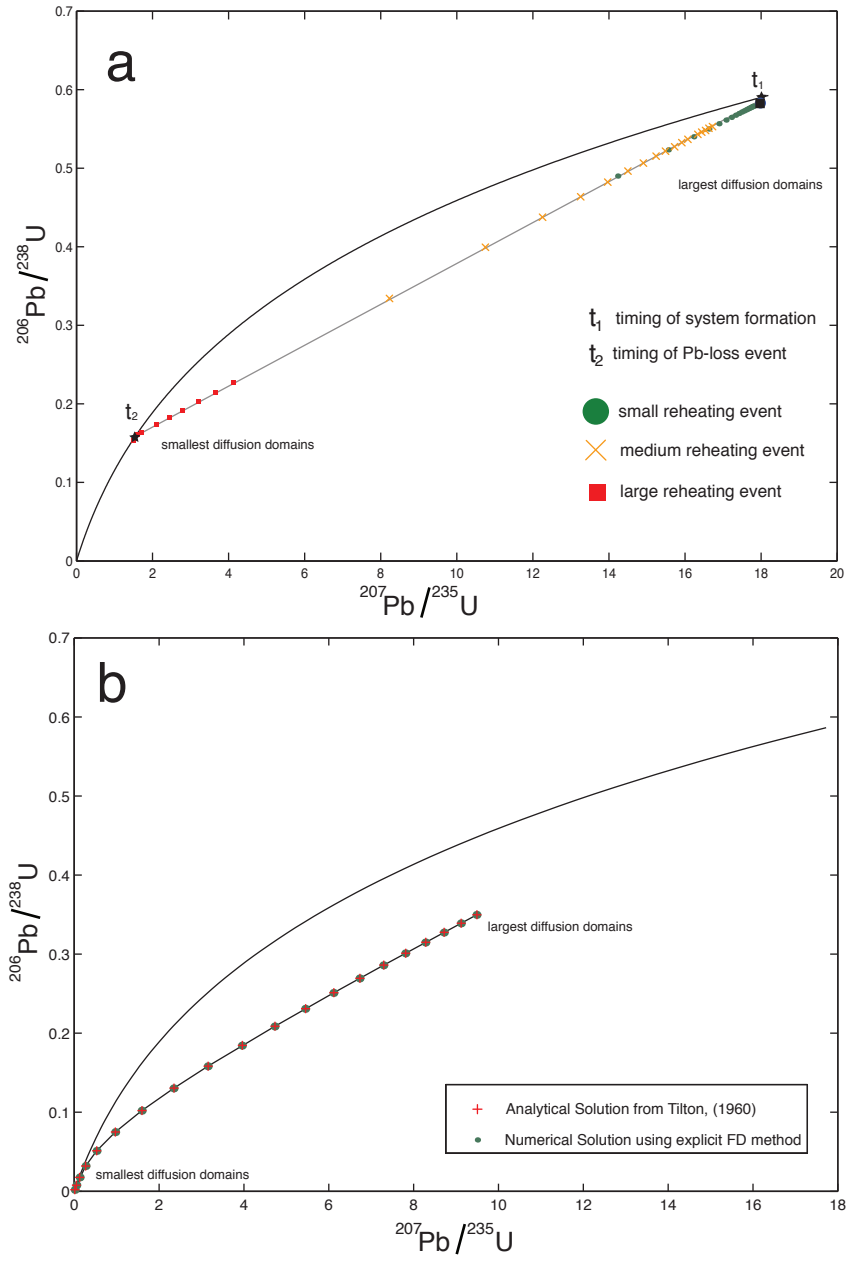
a
t_1
t_2
largest diffusion domains
smallest diffusion domains
t_1 timing of system formation
t_2 timing of Pb-loss event
small reheating event
medium reheating event
large reheating event
$^{206}Pb/^{238}U$
$^{207}Pb/^{235}U$
b
largest diffusion domains
smallest diffusion domains
Analytical Solution from Tilton, (1960)
Numerical Solution using explicit FD method
$^{206}Pb/^{238}U$
$^{207}Pb/^{235}U$

Figure 2.1

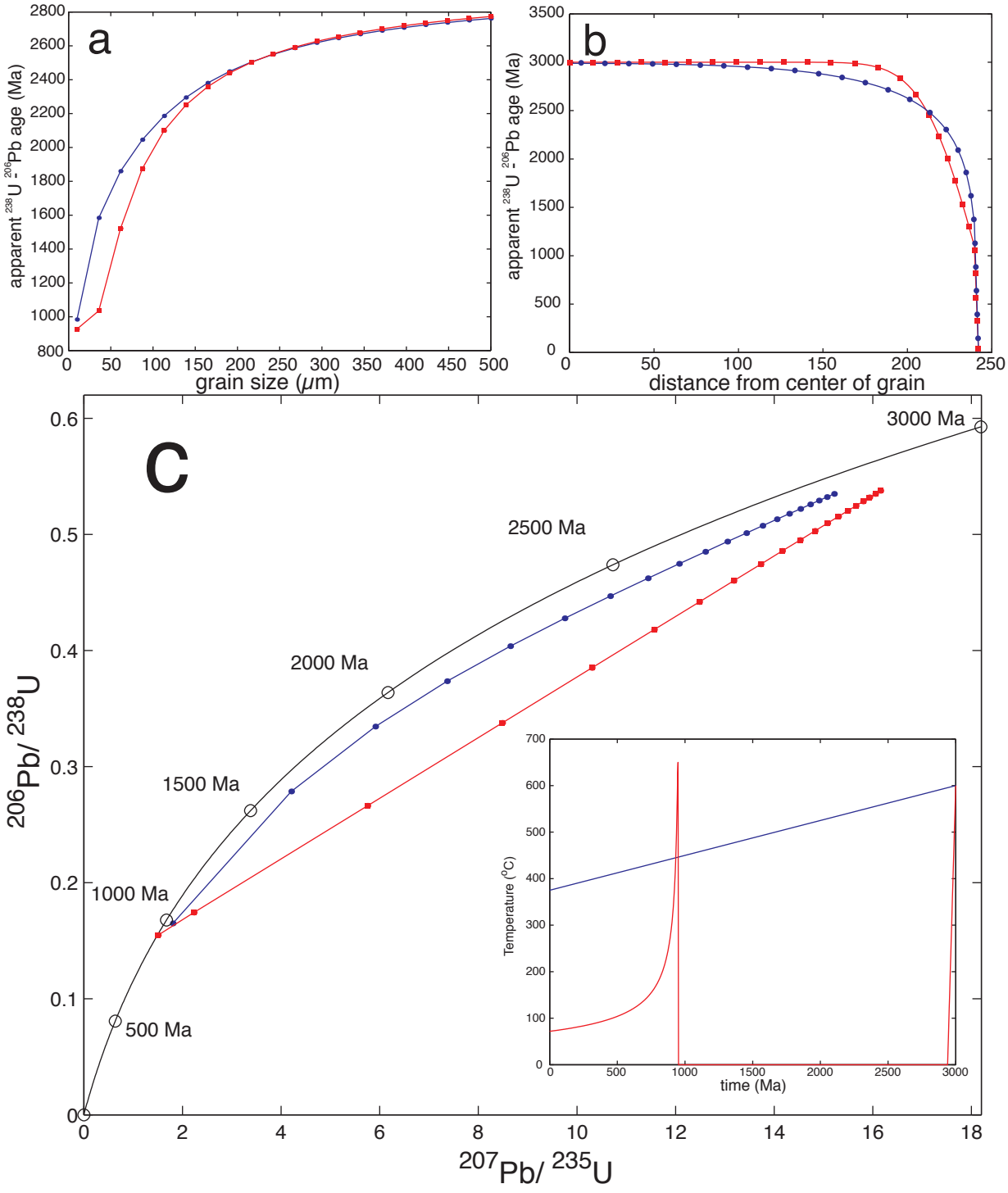
a
apparent ^{238}U - ^{206}Pb age (Ma)
grain size (μm)
b
apparent ^{238}U - ^{206}Pb age (Ma)
distance from center of grain
c
3000 Ma
2500 Ma
2000 Ma
1500 Ma
1000 Ma
500 Ma
^{206}Pb/ ^{238}U
^{207}Pb/ ^{235}U
Temperature (^{o}C)
time (Ma)

Figure 2.2

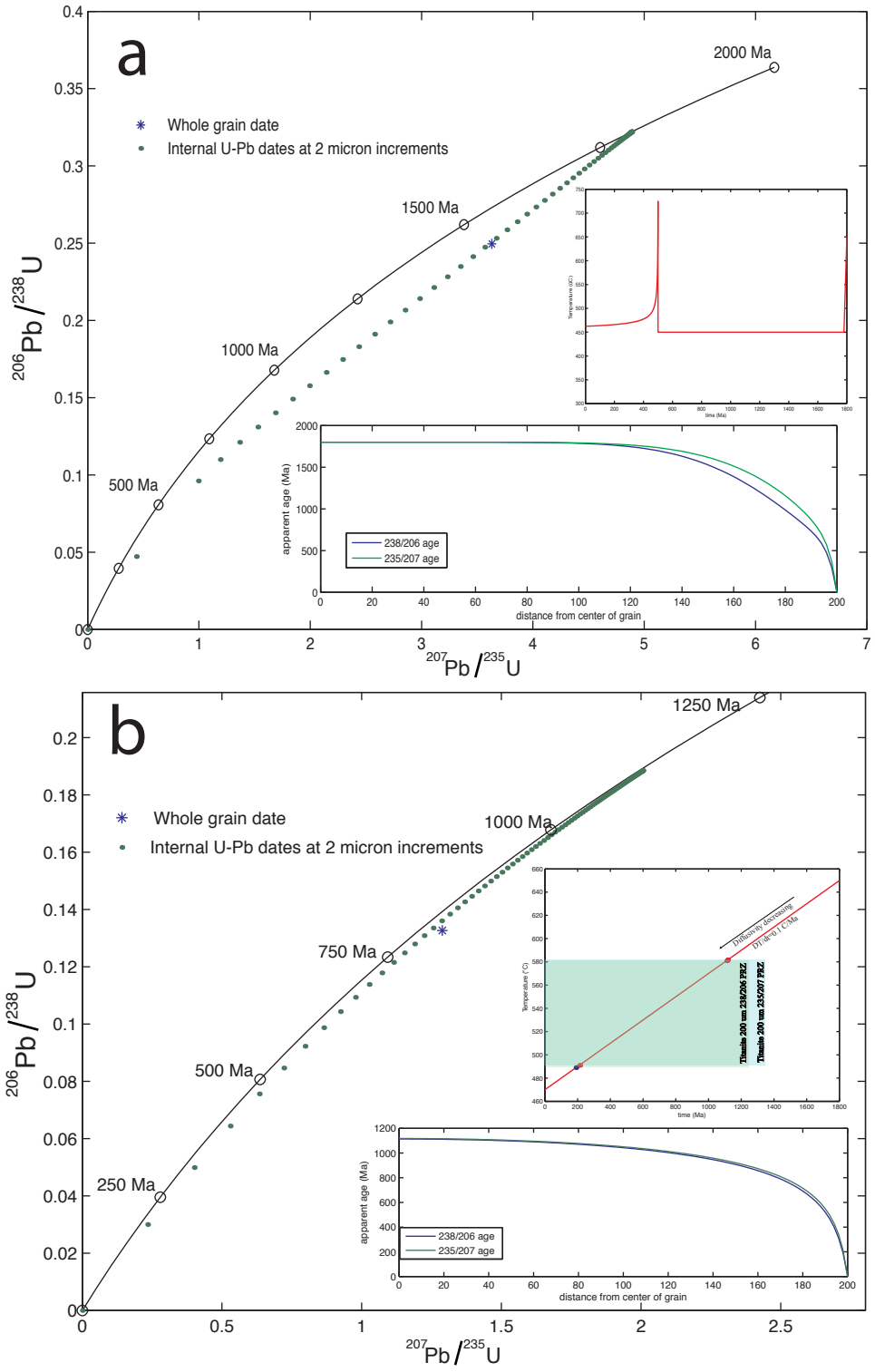
a
Whole grain date
Internal U-Pb dates at 2 micron increments
2000 Ma
1500 Ma
1000 Ma
500 Ma
apparent age (Ma)
238/206 age
235/207 age
distance from center of grain
206Pb/238U
207Pb/235U
b
Whole grain date
Internal U-Pb dates at 2 micron increments
1250 Ma
1000 Ma
750 Ma
500 Ma
250 Ma
Diffusivity Anisotropy
DTa=a/1 C/Ma
apparent age (Ma)
238/206 age
235/207 age
distance from center of grain
206Pb/238U
207Pb/235U

Figure 2.3

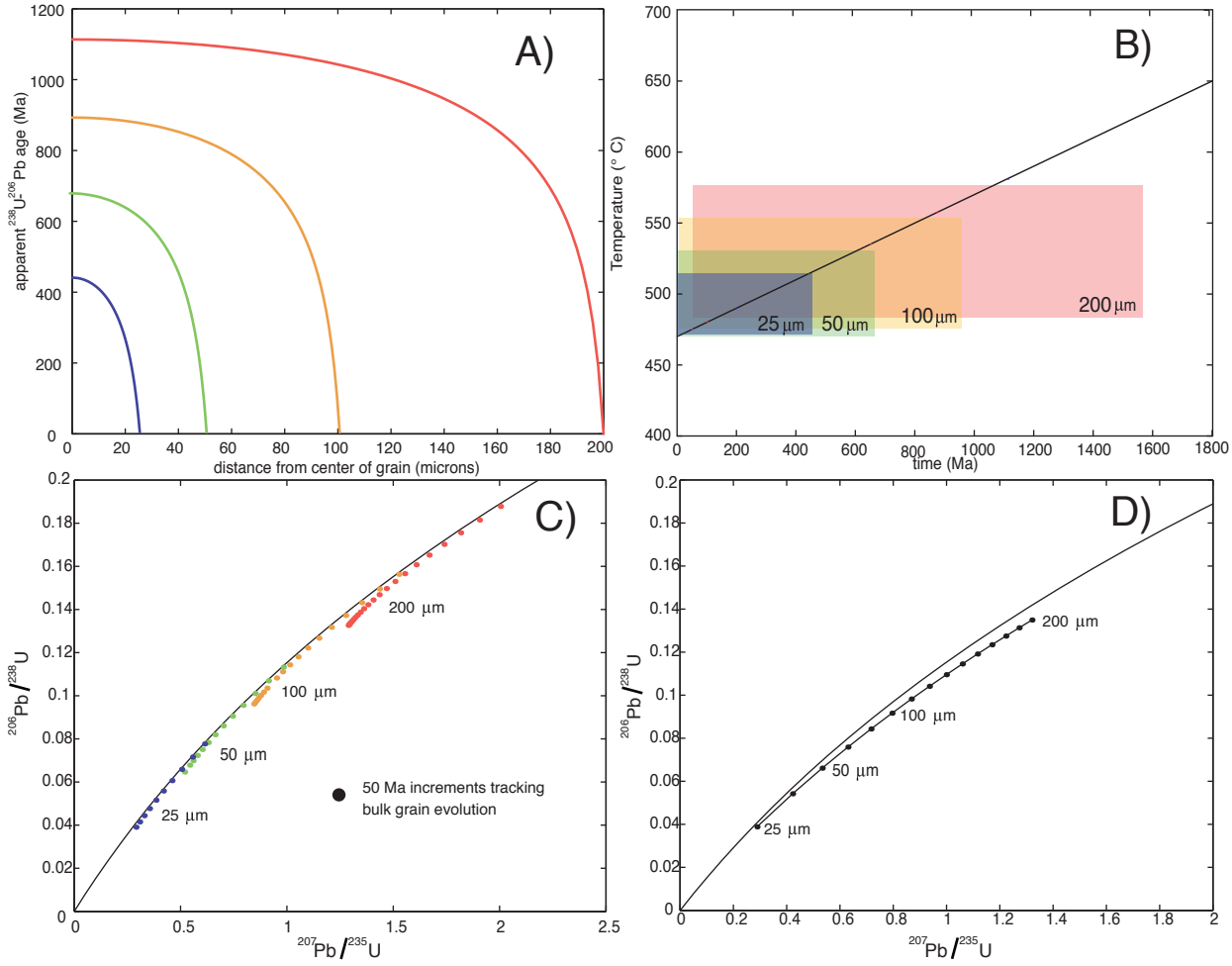
A)
apparent ^{238}U-^{206}Pb age (Ma)
distance from center of grain (microns)
B)
Temperature (° C)
time (Ma)
25 µm
50 µm
100 µm
200 µm
C)
$^{206}Pb/^{238}U$
$^{207}Pb/^{235}U$
25 µm
50 µm
100 µm
200 µm
50 Ma increments tracking bulk grain evolution
D)
$^{206}Pb/^{238}U$
$^{207}Pb/^{235}U$
25 µm
50 µm
100 µm
200 µm

Figure 2.4

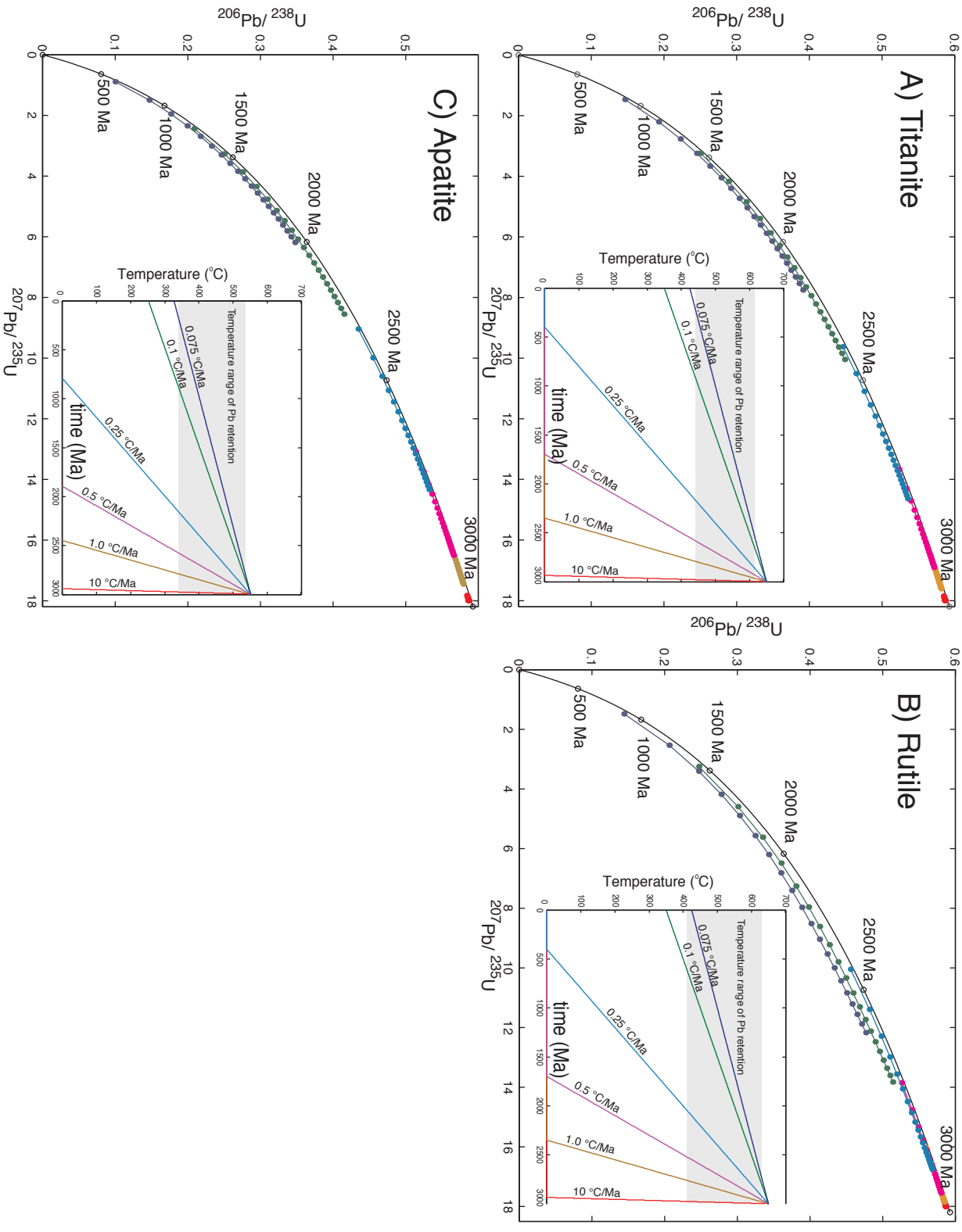
A) Titanite
B) Rutile
C) Apatite
$^{206}Pb/^{238}U$
$^{207}Pb/^{235}U$
500 Ma
1000 Ma
1500 Ma
2000 Ma
2500 Ma
3000 Ma
Temperature (°C)
Temperature range of Pb retention
0.075 °C/Ma
0.1 °C/Ma
0.25 °C/Ma
0.5 °C/Ma
1.0 °C/Ma
10 °C/Ma
time (Ma)

Figure 2.5

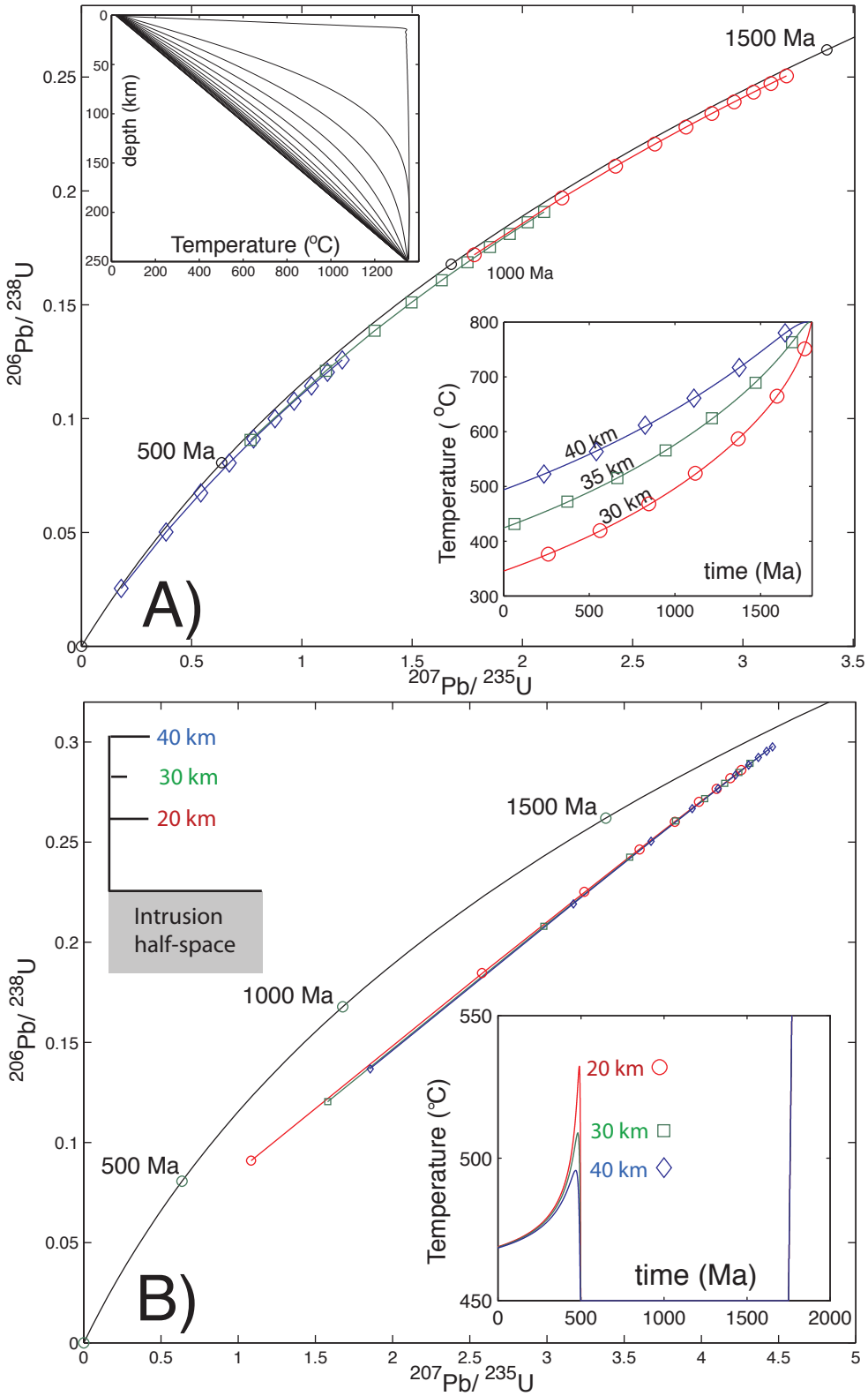
A)
1500 Ma
1000 Ma
500 Ma
depth (km)
Temperature (ºC)
Temperature (ºC)
40 km
35 km
30 km
time (Ma)
206Pb/ 238U
207Pb/ 235U
B)
40 km
30 km
20 km
Intrusion
half-space
1500 Ma
1000 Ma
500 Ma
Temperature (ºC)
20 km
30 km
40 km
time (Ma)
206Pb/ 238U
207Pb/ 235U

Figure 2.6

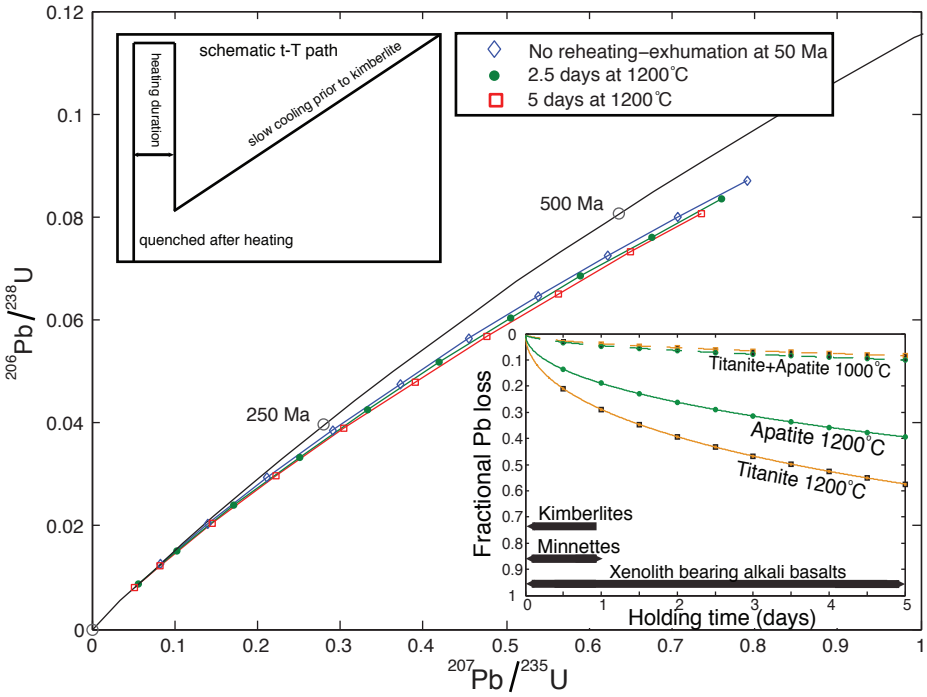
schematic t-T path
heating duration
slow cooling prior to kimberlite
quenched after heating
No reheating–exhumation at 50 Ma
2.5 days at 1200°C
5 days at 1200°C
500 Ma
250 Ma
Fractional Pb loss
Titanite+Apatite 1000°C
Apatite 1200°C
Titanite 1200°C
Kimberlites
Minnettes
Xenolith bearing alkali basalts
Holding time (days)
206Pb/238U
207Pb/235U

Figure 2.7

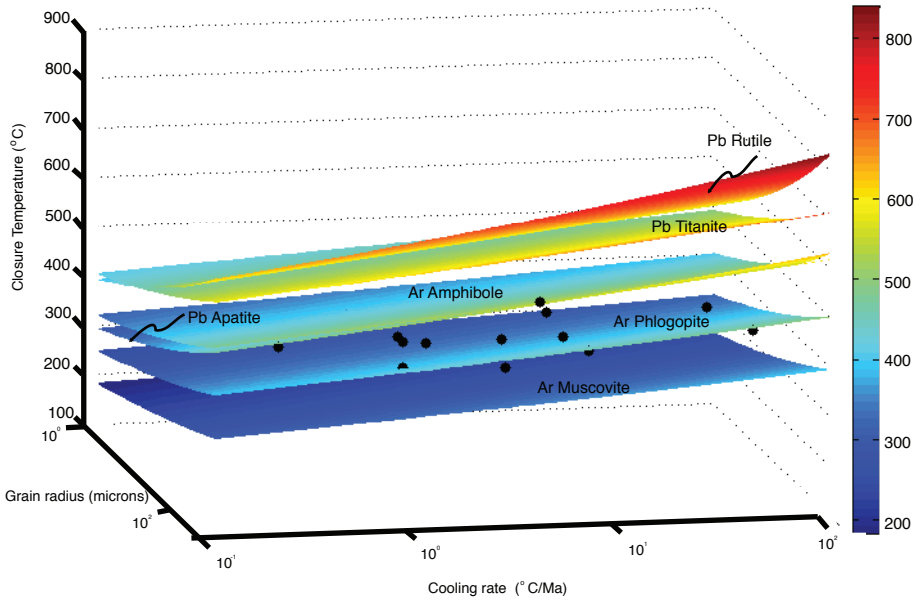
Closure Temperature (°C)
900
800
700
600
500
400
300
200
100
Pb Rutile
Pb Titanite
Ar Amphibole
Pb Apatite
Ar Phlogopite
Ar Muscovite
Grain radius (microns)
10^0
10^2
10^1
10^0
10^1
10^2
Cooling rate (°C/Ma)
800
700
600
500
400
300
200

Figure 2.8

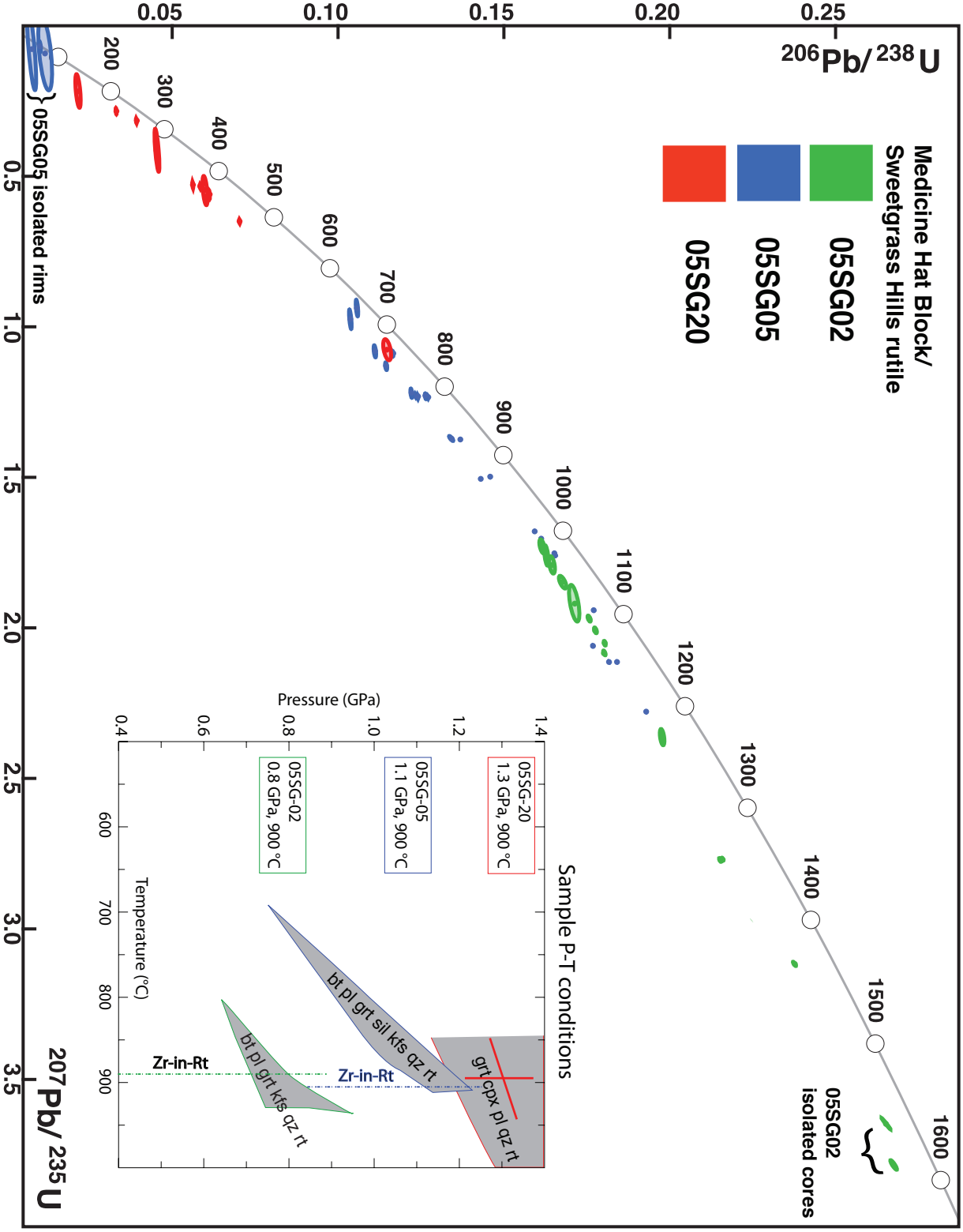
Medicine Hat Block/
Sweetgrass Hills rutile
05SG02
05SG05
05SG20
05SG02
isolated cores
05SG05 isolated rims
206Pb/238U
207Pb/235U
Sample P-T conditions
Pressure (GPa)
Temperature (°C)
05SG-20
1.3 GPa, 900 °C
05SG-05
1.1 GPa, 900 °C
05SG-02
0.8 GPa, 900 °C
grt cpx pl qz rt
bt pl grt sil kfs qz rt
bt pl grt kfs qz rt
Zr-in-Rt
Zr-in-Rt

Figure 2.9

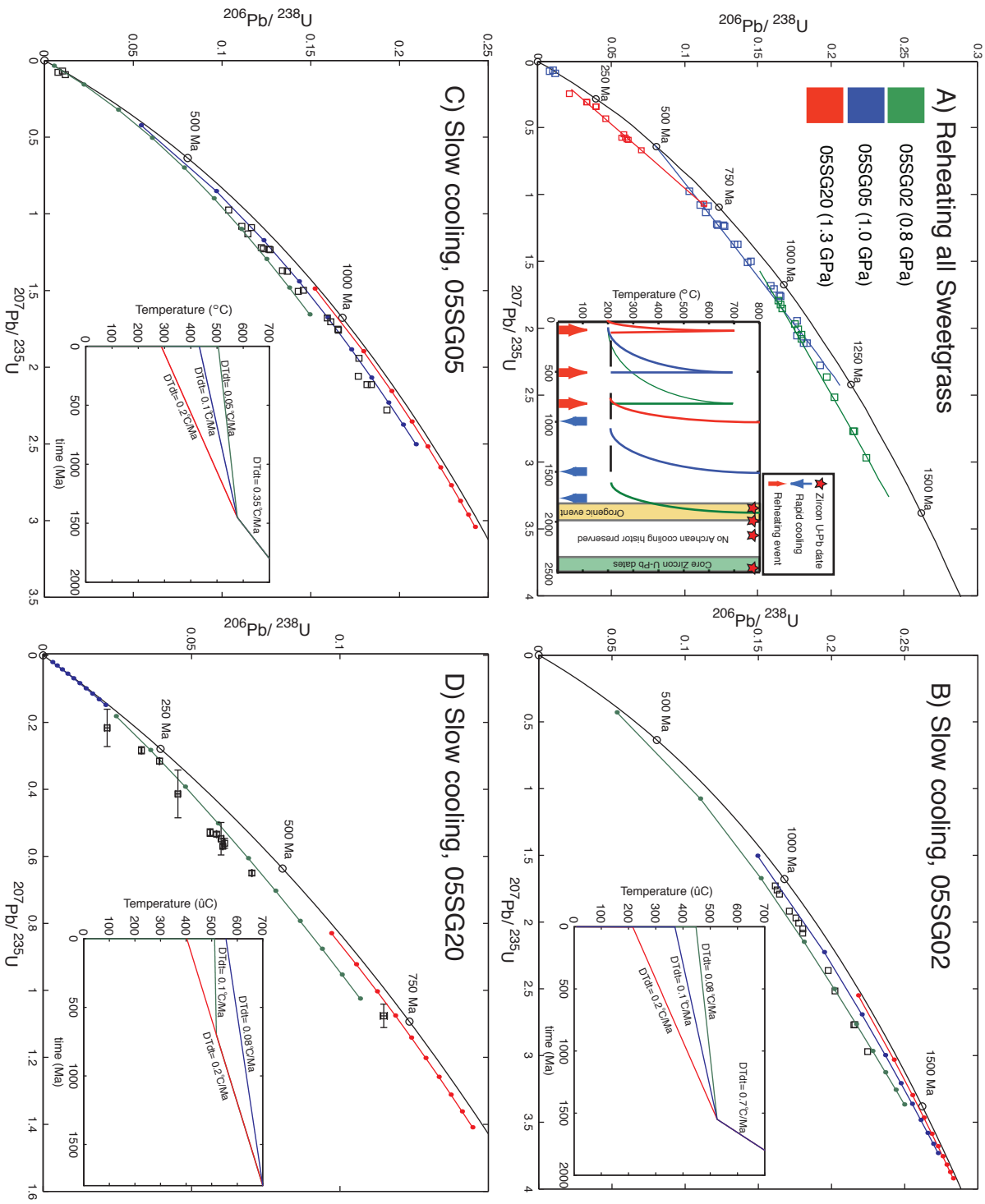
A) Reheating all Sweetgrass
05SG02 (0.8 GPa)
05SG05 (1.0 GPa)
05SG20 (1.3 GPa)
Zircon U-Pb date
Rapid cooling
Reheating event
Core Zircon U-Pb dates
No Archean cooling histor preserved
Orogenic event
Temperature (°C)
B) Slow cooling, 05SG02
C) Slow cooling, 05SG05
D) Slow cooling, 05SG20
DTdt= 0.7°C/Ma
DTdt= 0.2°C/Ma
DTdt= 0.1°C/Ma
DTdt= 0.08°C/Ma
DTdt= 0.05°C/Ma
DTdt= 0.35°C/Ma
time (Ma)
Temperature (ûC)
206Pb/ 238U
207Pb/ 235U

Figure 2.10

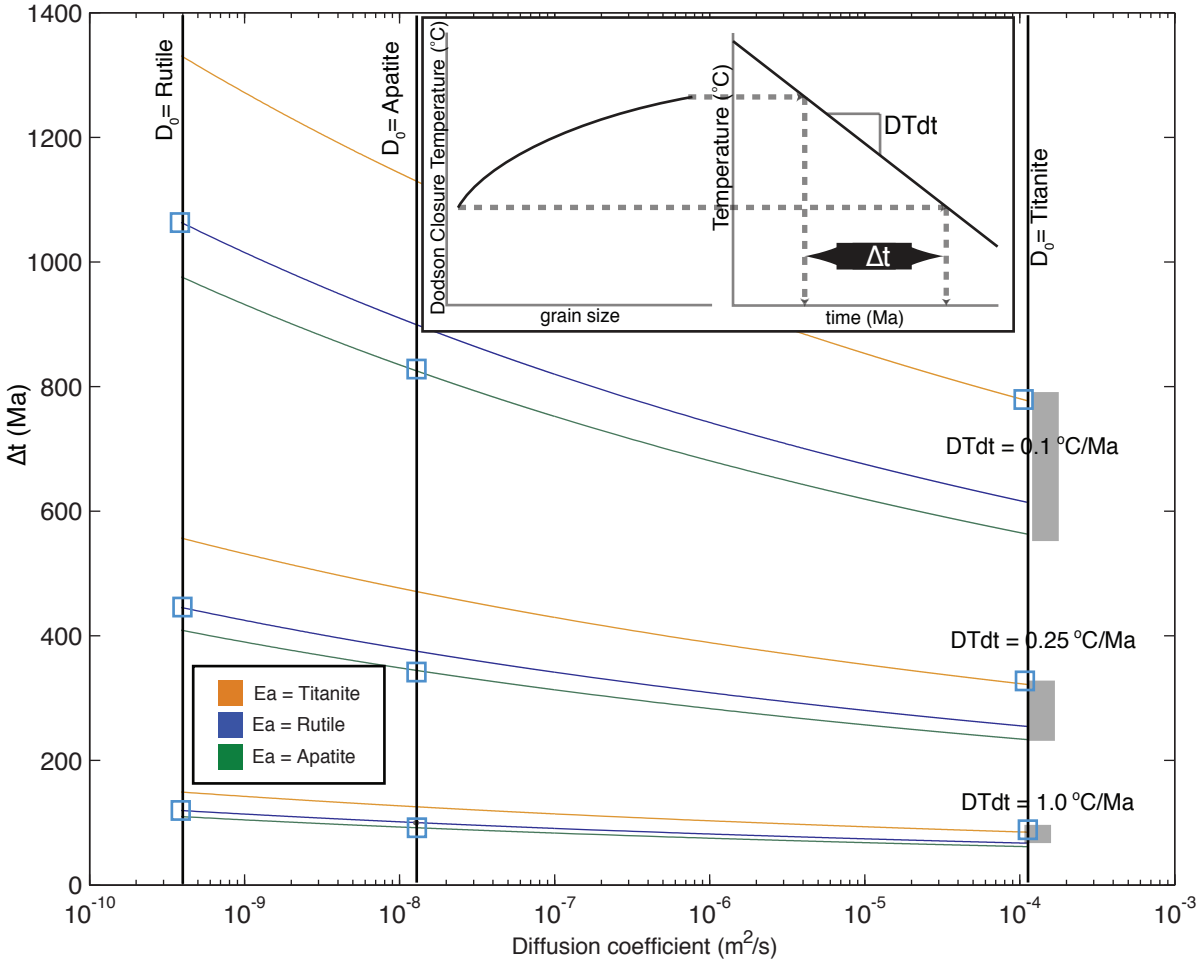
1400
1200
1000
800
600
400
200
0
Δt (Ma)
10^{-10}
10^{-9}
10^{-8}
10^{-7}
10^{-6}
10^{-5}
10^{-4}
10^{-3}
Diffusion coefficient (m^2/s)
D_0= Rutile
D_0= Apatite
D_0= Titanite
DTdt = 0.1 °C/Ma
DTdt = 0.25 °C/Ma
DTdt = 1.0 °C/Ma
Ea = Titanite
Ea = Rutile
Ea = Apatite
Dodson Closure Temperature (°C)
grain size
Temperature (°C)
time (Ma)
DTdt
Δt

Figure 2.11

Table 2.1 Zircon U-Pb data

Fractions	206Pb/ 238U	±2σ %	207Pb/ 235U	±2σ %	207Pb/ 206Pb	±2σ %	Age (Ma) 206 Pb 238 U	Age (Ma) 207 Pb 235 U	Age (Ma) 207 Pb 206 Pb	corr. coef.	Pbc (pg)	Pb*/ Pbc
05SG02:zircon												
z1.1	0.50552	0.090	13.090	0.11	0.18781	0.058	2637	2686	2723	0.839	4.92	72
z2	0.52118	0.070	13.783	0.090	0.19180	0.055	2704	2735	2758	0.788	1.35	155
z3	0.50969	0.074	13.232	0.090	0.188292	0.051	2655	2696	2727	0.823	1.95	415
z4	0.36990	0.17	6.711	0.20	0.13158	0.093	2029	2074	2119	0.881	0.80	66
z5	0.42974	0.062	9.2243	0.081	0.155680	0.052	2305	2361	2409	0.763	0.75	121
z6	0.43072	0.14	9.375	0.18	0.15786	0.10	2309	2375	2433	0.810	1.22	87
z7	0.4779	0.54	12.043	0.57	0.18278	0.17	2518	2608	2678	0.952	1.85	26
z9	0.50179	0.058	13.026	0.084	0.18827	0.060	2621	2682	2727	0.699	0.74	250
SG05:zircon												
z3	0.32382	0.096	4.973	0.26	0.11138	0.22	1808	1815	1822	0.601	0.84	1013
z2	0.32419	0.063	4.9556	0.10	0.110865	0.056	1810	1812	1814	0.854	1.12	247
z4	0.32596	0.16	5.051	0.70	0.11238	0.61	1819	1828	1838	0.660	39.25	7

a Isotopic dates calculated using the decay constants λ238 = 1.55125E-10 and λ235 = 9.8485E-10 (Jaffey et al. 1971).

Table 2.2 Rutile U-Pb data

Fractions	grain descr.	grain size (μm) w	l	Concentration (ppm) U	Pb*	206 Pb / 238 U	% err	207 Pb / 235 U	% err	Age (Ma) 206 Pb / 238 U	207 Pb / 235 U	207 Pb / 206 Pb	corr. coef.	common Pb (pg)	est. Pb Blank (pg)	Pb*/Pbc
05SG02 rutile																
r09-1	1	25	150	38.1	5.5	0.1645	0.5390	1.7908	1.6059	981.6	1042.1	1171.4	0.46	1.84	0.60	1.00
r09-2	1	30	185	71.1	11.6	0.1757	0.2731	1.9692	0.5024	1043.2	1105.0	1228.8	0.63	0.80	0.80	8.11
r09-3	1	50	140	40.7	6.7	0.1776	0.2447	2.0082	0.4707	1053.7	1118.3	1246.1	0.58	0.53	0.52	15.33
r09-4	1	50	150	110.7	20.1	0.1977	0.3483	2.3629	1.1357	1162.9	1231.5	1353.6	0.46	7.66	0.60	3.52
r09-5	1	60	170	63.0	10.6	0.1804	0.1704	2.0510	0.3748	1069.1	1132.6	1256.4	0.50	0.79	0.78	26.91
r09-6	1	25	130	103.6	16.3	0.1712	0.9136	1.9182	3.1668	1018.6	1087.5	1228.0	0.59	2.13	2.00	2.09
r09-7	1	25	140	65.9	9.9	0.1628	0.3866	1.7596	1.9052	972.4	1030.7	1156.5	0.54	0.77	0.77	3.85
r09-9	1	18	140	244.7	36.4	0.1615	0.5047	1.7293	1.3400	965.4	1019.5	1137.6	0.54	0.96	0.96	5.75
r09-12	1	60	95	39.5	6.1	0.1677	0.6696	1.8483	1.1352	999.4	1062.8	1195.4	0.67	0.90	0.89	7.55
r1	2	220	500	49.7	11.2	0.2376	0.1936	3.1162	0.2253	1374.0	1436.7	1530.9	0.86	5.71	1.30	157.78
r3	2	100	400	107.2	21.6	0.2152	0.1510	2.7709	0.2258	1256.5	1347.7	1495.6	0.68	6.62	1.50	32.79
r5	2	100	225	13.8	2.3	0.1803	0.2030	2.0832	0.3792	1068.6	1143.3	1287.9	0.67	3.29	1.50	7.09
r6	2	75	245	78.1	15.8	0.2159	0.1077	2.7684	0.1804	1260.4	1347.1	1487.5	0.64	2.30	1.50	31.71
r10	A,2	-	-	-	-	0.2652	0.5077	3.6469	0.5147	1516.4	1559.8	1619.1	0.99	7.44	1.30	515.48
r13	A,4	-	-	-	-	0.2675	0.3707	3.7841	0.4183	1528.3	1589.4	1671.3	0.89	9.10	1.30	398.33
5SG05 rutile																
r1	3	223	359	104.3	17.8	0.1817	0.0923	2.1132	0.1081	1076.1	1153.1	1300.9	0.86	10.92	1.00	86.32
r3	3	266	426	81.5	14.4	0.1841	0.0629	2.1130	0.0844	1089.3	1153.1	1275.0	0.75	29.79	1.00	34.09
r4	3	258	270	63.5	11.5	0.1929	0.0502	2.2793	0.0722	1137.0	1205.9	1331.5	0.70	4.27	1.00	110.23
r5	3	223	266	173.0	28.9	0.1768	0.0553	2.0586	0.0784	1049.4	1135.1	1303.0	0.71	15.22	1.00	66.80
r6	3	161	265	46.3	7.7	0.1771	0.0671	1.9414	0.0960	1051.2	1095.5	1184.7	0.72	4.94	1.00	65.86
r7	3	123	300	120.4	16.0	0.1430	0.0581	1.5056	0.0952	861.4	932.6	1105.0	0.62	2.06	1.00	130.77
r9	2	80	160	107.4	14.5	0.1458	0.0517	1.4983	0.1222	877.5	929.7	1055.6	0.52	0.83	0.83	75.54
r11	1	40	150	46.8	5.0	0.1165	0.1440	1.0891	0.8610	710.5	748.1	862.2	0.53	0.51	0.51	9.30
r12	1	50	100	77.9	8.9	0.1233	0.0699	1.2279	0.4242	749.4	813.4	992.8	0.56	0.79	0.79	17.74
r13	2	50	170	25.2	2.9	0.1271	0.0797	1.2341	0.4456	771.1	816.2	941.1	0.50	0.70	0.70	18.66
r14	2	80	210	123.5	15.6	0.1368	0.0475	1.3747	0.0985	826.4	878.2	1011.2	0.54	0.49	0.49	126.42
r15	2	70	150	1237.1	184.5	0.1612	0.0447	1.7037	0.0783	963.5	1009.9	1112.0	0.61	0.55	0.55	166.75

Table 2.2 (cont.)

Fractions	grain descr.	grain size (µm) w	l	Concentration (ppm) U	Pb*	206 Pb / 238 U	% err	207 Pb / 235 U	% err	Age (Ma) 206 Pb / 238 U	207 Pb / 235 U	207 Pb / 206 Pb	corr. coef.	common Pb (pg)	est. Pb Blank (pg)	Pb*/Pbc
05SG05 rutile																
r18	2	40	120	65.8	7.0	0.1145	0.2704	1.1308	1.1256	699.0	768.1	974.7	0.45	0.59	0.59	8.63
r19	2	45	200	81.9	9.5	0.1264	0.1779	1.2307	0.7753	767.2	814.7	946.6	0.48	0.61	0.61	11.70
r20	2	50	135	80.8	10.0	0.1341	0.4779	1.3709	0.5984	811.1	876.5	1045.7	0.83	0.54	0.54	24.39
r24	1	20	130	80.0	16.6	0.1057	0.3461	0.9376	2.9328	647.5	671.6	753.5	0.59	1.10	1.09	3.34
r25	1	25	200	60.0	5.7	0.1037	0.3745	0.9749	3.3111	636.2	691.0	873.7	0.67	0.83	0.83	2.41
r27	1	40	120	65.4	7.3	0.1221	0.2332	1.2205	1.2537	742.7	810.0	999.8	0.52	1.82	1.00	3.33
r28	1	35	120	69.0	7.0	0.1111	0.3320	1.0814	1.8469	679.3	744.3	945.2	0.52	1.14	1.00	3.86
r29	2	45	155	71.8	8.2	0.1240	0.1025	1.2324	0.6430	753.3	815.4	988.9	0.57	0.91	0.91	11.72
r21	A,3	-	-	-	-	0.1653	0.0623	1.7521	0.0971	986.3	1027.9	1117.6	0.66	0.50	0.49	183.36
r22	A,3	-	-	-	-	0.1655	0.0919	1.7587	0.1146	987.4	1030.4	1122.7	0.81	11.15	1.00	47.68
r23	A,3	-	-	-	-	0.1593	0.0530	1.6788	0.0772	953.0	1000.5	1106.2	0.70	2.23	1.00	143.95
Redg1	E,1	-	-	-	-	0.0076	18.2119	0.0774	176.0267	48.9	75.7	1032.0	0.75	0.66	0.66	0.05
Redg2	E,1	-	-	-	-	0.0117	17.7851	0.0927	131.3821	75.2	90.0	504.1	0.52	1.28	1.00	0.07
Redg4	E,1	-	-	-	-	0.0101	3.1316	0.0692	26.0069	64.7	67.9	184.3	0.53	0.93	0.90	0.41
05SG20 rutile																
r1	2	165	200	3.17	0.17	0.0612	0.2512	0.5608	2.6081	382.7	452.1	822.4	0.64	3.32	0.70	1.64
r2	2	240	265	9.42	0.60	0.0703	0.1623	0.6499	1.1133	438.0	508.4	839.3	0.53	3.64	0.70	3.36
r3	2	150	270	4.30	0.23	0.0584	0.1545	0.5339	1.2243	365.9	434.4	815.7	0.53	3.13	0.70	2.24
r5	2	200	300	1.77	0.10	0.0605	0.1761	0.5699	1.0208	378.7	457.9	878.3	0.49	2.51	0.70	2.78
r6	2	160	230	2.07	0.07	0.0392	0.3034	0.3157	2.7291	247.9	278.6	545.5	0.56	2.05	0.70	1.79
r7	2	150	300	2.49	0.07	0.0331	0.4135	0.2836	3.7378	209.9	253.5	679.2	0.59	2.51	0.70	0.92
r8	2	150	300	4.46	0.22	0.0562	0.2179	0.5291	2.1264	352.6	431.2	876.0	0.67	5.64	0.70	1.26
r11	2	150	220	0.65	0.03	0.1148	1.0451	1.0762	3.2525	700.3	741.8	869.0	0.48	3.57	0.70	1.14
r12	3	150	170	-	-	0.0599	1.2739	0.5474	8.8433	375.3	443.3	813.5	0.53	1.23	0.70	0.60
r14	3	150	150	-	-	0.0216	3.7176	0.2166	25.7215	137.5	199.1	1010.6	0.56	1.40	0.70	0.18
r15	3	75	150	-	-	0.0454	1.6125	0.4136	17.2343	286.3	351.4	808.1	0.72	2.38	0.70	0.31

grain morphology: A = abraded, E=isolated grain rim, 1 = euhedural, red, translucent
2 = euhedral to subhedral, red to black, portions translucent, 3 = subhedral to anhedral, black

Chapter 3: An exhumation history of continents over billion year time-scales

Blackburn, T,J., Bowring, S.A., Perron, T., Mahan K., Dudas F., Barnhart, K. (2012) An exhumation history of continents over billion year time-scales, *Science*, v. 335, p 73-76.

3.1 Introduction: The continental lithosphere contains the oldest and most stable structures on Earth, where fragments of ancient material have withstood destruction by tectonic and surface processes operating over billions of years. Though present-day erosion of in these remnants is slow, a record of how they have uplifted, eroded and cooled over Earth's history can provide insight into the physical properties of the continents and forces operating to exhume them over geologic time. We constructed a continuous record of ancient lithosphere cooling using U-Pb thermochronology on volcanically exhumed lower crustal fragments. Combining these measurements with thermal and Pb-diffusion models constrains the range of possible erosion histories. Measured U-Pb data are consistent with extremely low erosion rates persisting over time scales approaching the age of the continents themselves.

The preservation of ancient fragments of Archean continental crust, or "cratons," over geologic time is intimately linked with the presence of a low-density mantle root that buoyantly supports and protects the overlying continent (Jordan, 1988). The long-term stability of these roots implies an apparent "isopycnic" balance between the negative thermal buoyancy from contraction during cooling and the positive chemical buoyancy from the depletion of the root's denser basaltic component during craton formation (Forte and Claire Perry, 2000; Jordan, 1988). Despite this stability, cratons must survive exposure to surface processes working to erode on

durations lasting billions years, a process that results in continued rock exhumation towards the Earth's surface. Though present-day erosion within these stable regions is low, the assembly of continental masses through mountain building processes (Hoffman, 1988) requires these terranes experienced periods of rapid erosion following the construction of topographically high mountain belts. An erosional history recording the duration of this early rapid erosional phase and the timing and rate of transition to the slow erosion observed today will provide a test to this isopycnic hypothesis, allowing us to understand more about the composition and density of the lithosphere, its relationship with the underlying mantle, and the thermal, buoyant and mechanical forces operating to exhume or bury the continents over the geologic history of the Earth.

Because the exhumation or burial of the Earth's surface has a direct effect on the rate of heat loss within the lithosphere, a continuous record of lithosphere exhumation can be reconstructed through the use of a temperature-sensitive radiometric dating technique known as thermochronology. The combination of thermochronologic data with thermal models for heat transfer in the lithosphere can be used to measure the processes operating to cool or heat the lithosphere in the geologic past (Ehlers and Farley, 2003). Thermochronologic studies have typically employed geochronologic systems sensitive to cooling at temperatures <110 °C. These techniques are most useful for measuring cooling due to deformation in the upper crust and erosion of topography (Braun, 2002). A thermochronologic system sensitive to cooling at higher temperatures and greater depths is insensitive to the "noise" associated with near-surface cooling and therefore provides a measure of the background rate of erosion or burial associated with the vertical motions of a craton. The U-Pb thermochronologic system is sensitive to cooling at temperatures of ~400-650 °C, corresponding to lower crustal depths in cratonic regions of ~20-50 km (Schmitz and Bowring, 2003). Here we utilize this technique to reconstruct an ancient and long-lived thermal history of volcanically exhumed lower crustal fragments, samples that resided at depth for billions of years before recent volcanism transported them to the surface as "xenoliths". A high fidelity reconstruction of time-temperature paths for these samples is produced using the U-Pb system's dual decay scheme, where parent isotopes ^{238}U and ^{235}U decay at different rates to daughter isotopes ^{206}Pb and ^{207}Pb, respectively. Coupling this dual isotopic system with diffusion's length scale dependency, which causes different crystal sizes to retain Pb over different absolute time scales, results in a set of parent and daughter isotopic compositions for a range of crystal sizes that is unique to the time-temperature history of the sample

(Blackburn et al., 2011). Measured and modeled U-Pb results presented here explore a range of crystal grain sizes to exploit these advantages .

The thermal processes operating to cool or heat the deep lithosphere include conductive heat loss, heat input from the underlying mantle, heat production from the decay of heat producing elements (HPE), and cooling or insulation due to surface erosion or burial, respectively. The combined effects of these processes on the U and Pb isotopic evolution of a set of rutile crystals can be described with a simple thermal model . The modeled lithosphere thermal history begins with a steep geothermal gradient, consistent with formation or reheating during mountain building events, that is followed by cooling due to heat loss at the lithosphere surface (Fig. 1A). The time-temperature histories for crustal depths from the thermal model (Fig. 1B) are then used as the input to a model of Pb production and diffusion . Modeled U-Pb thermochronologic data correlate directly with sample depth (Fig. 1C). Shallow samples cool quickly through the 400-600 °C rutile thermal window, yielding U-Pb dates that are consistent with the model start time, while the deepest samples never cool below the Pb closure for rutile, accumulate no radiogenic Pb and yield U-Pb dates of 0 Ma (Fig. 2C). The faster cooling, shallow samples yield dates that plot on the concordia curve, indicating agreement between the ^{238}U-^{206}Pb and ^{235}U-^{207}Pb systems and closed system behavior. Samples at intermediate depths accumulate different amounts of radiogenic Pb, depending on depth, forming a curvilinear 'discordant' array off concordia that indicates partially open system behavior. Mineral grains that spend a long time in the Pb-Partial Retention Zone (PRZ), a temperature range where the diffusion and production of radiogenic daughter are at or near a balance, result in the partial retention of Pb with a range of isotopic compositions (^{207}Pb/^{206}Pb). A whole-crystal analysis yields an integrated measure of the internal Pb-diffusion profile, resulting in the apparent difference between the measured ^{235}U-^{207}Pb and ^{238}U-^{206}Pb dates (hereafter referred to as Δ U-Pb). Slower cooling, and thus longer durations in the PRZ, results in a Pb diffusion profile containing a wider range of ^{207}Pb/^{206}Pb compositions, and thus a greater Δ U-Pb age difference (Fig. 1D) (Blackburn et al., 2011). Because the vertical advection of lower crustal rocks towards the Earth's surface increases the rate of cooling at depth, there is a strong correlation between the maximum Δ U-Pb value and net exhumation, where higher net exhumation rates yield lower Δ U-Pb values (Fig. 1D). The U-Pb system's sensitivity to cooling rate and, in this thermal setting, to exhumation rate, is the key factor that allows constraints to be placed on the long-term evolution of continental surfaces.

Along the southwestern edge of the North American Craton within Montana, USA, the Archean Medicine Hat Block (MHB) and Wyoming Province (WP) collided at ~1800 Ma to form the Great Falls Tectonic Zone (GFTZ), a Proterozoic suture between the two terranes (Mueller et al., 2002) (Fig. 2B inset). Lower crustal xenoliths used in this study were collected from four ~50 Ma volcanic epicenters within each terrane. The volcanic entrainment of samples at 50 Ma is so rapid that U/Pb loss due to volcanic reheating is insignificant (Blackburn et al., 2011). Lower crustal U-Pb thermochronologic data yield the "humped" topology of ΔU-Pb data predicted by the thermal model (Fig 1D), supporting the use of this model to infer lithosphere exhumation rate (Fig. 2). The onset of cooling in both regions is recorded by the higher temperature titanite U-Pb thermochronometer. Within the Archean regions this occurs at ~2000 Ma, indicating the diffusive loss of a Archean cooling record during the younger reheating event (Fig. 2A). Within the Proterozoic GFTZ, the onset of cooling in the region does not occur until ~300 My after the formation of the inferred mountain belt, a delay in cooling that is consistent with rapid erosion rates between 1800 and 1500 Ma (Fig. 2B)). The subsequent long-term cooling history in each terrane is recorded by the lower temperature rutile thermochronometer, where analyses from xenoliths of different depths provide a continuous and overlapping cooling record lasting more than ~1500 My (Fig. 2). Thermobarometrically determined xenolith depths (Barnhart, 2010; Blackburn et al., 2011) correlate with the timing of cooling, with the shallowest samples cooling first and deeper samples cooling at progressively younger times (Fig. 2). Assuming an intermediate lithosphere thickness of 225 km (Burdick et al., 2008; Hearn, 2004; Yuan and Romanowicz) and the recommended HPE concentrations from compiled datasets (Rudnick et al., 2003; Rudnick et al., 1998), forward modeled rutile data for a range of exhumation rates from -2.5 to 2.5 m/My (where a negative exhumation rate corresponds to burial) bracket the measured data (Fig. 2). Secular variations in exhumation rate control the symmetry of the ΔU-Pb vs. time curves. For example, decreasing the exhumation rate over time skews the curve left, yielding modeled data that are also consistent with the measured results, yet their average exhumation rates are bracketed by those assuming constant exhumation (Fig. 2A).

Though the long-term exhumation rates reported here (-2.5-2.5 m/My) are in good agreement with shorter duration observations of some of the slowest-eroding surfaces on Earth (Portenga and Bierman, 2011), they are far slower than what is observed for the majority of continental surfaces (50-500 m/My) (Portenga and Bierman, 2011). This disparity can be

attributed to the difference in the time scales of observation and secular variations in exhumation. The exhumation rates presented here are long-term integrated estimates, and do not preclude the occurrence of brief periods of faster exhumation associated with tectonic (Portenga and Bierman, 2011) or climatic forces (Reiners et al., 2003) operating over intervals much shorter than the observational time-scale for this technique. Once a continental mass is laterally isolated from active plate boundaries and vertically supported by a thickened mantle root, the long-term uplift of a mountain belt is more likely dominated by the relative densities of the lithosphere and mantle (isostasy) (Fischer, 2002) with a potentially transient and smaller contribution to uplift or burial imposed by density and thermal anomalies in the underlying convecting mantle (dynamic topography)(Braun, 2010).

The U-Pb system's sensitivity to the magnitude and time variability of exhumation rate can be used to set limits on the timing and duration of events that exhumed or buried the surfaces of continents in the deep geologic past. First, we can gauge the duration of rapid erosional unroofing following mountain building from the difference between collision age and onset of cooling. Within the GFTZ (Fig. 2B), the 300 My difference between the onset of cooling and the mountain building event establishes an upper limit at which isostatically driven uplift can persist at the rates observed in young and topographically high mountain belts (50-100 m/My)(Fischer, 2002). Second, we can rule out erosional histories that include periods of exhumation or burial faster than a given rate or longer than a given time interval (with a trade-off between duration and rate). For example, we can dismiss histories for the GFTZ with exhumation or burial lasting longer than 50 My at rates that exceed ± 50 m/My. More subtle transient deformation mechanisms such as dynamic topography, with a characteristic amplitude less than 1 km over a distance of 1000 km or more, will be undetected on the short time scales (tens to hundreds of My) and modest exhumation/burial rates (10 to 100 m/Ma) at which this process operates (Braun, 2010). Despite the possibility of brief erosional or burial events of moderate magnitude, the data presented here require an overall cratonic history dominated by vertical motion rates near zero. This indicates that the isostatic balance observed in the present-day continents has been largely maintained over geologic time, extending back at least to the onset of cooling within each terrane. Since this stability was first meet, the craton has experienced a balance between erosion and burial, with a corollary balance between the lithosphere's internal buoyancy forces (1, 2) and near zero isostatic uplift, further indicating a minimal change in the relative densities

of the lithosphere and mantle over intervals lasting billions of years.

3.2 Figure Captions

Figure 1. Thermal history for the lithosphere (A) used to produce time-temperature paths (B) for samples at middle to lower crustal depths. (C) Time-temperature paths are used to calculate modeled U-Pb thermochronologic data for each sample depth (colors) and over a range of grain sizes. The "concordia" curve represents the daughter to parent ratios of ^{235}U-^{207}Pb and ^{238}U-^{206}Pb for a U-Pb system that remains closed throughout Earth history. The shallowest samples cool quickly through the Pb Partial Retention Zone (PRZ), yielding old ^{238}U-^{206}Pb dates that plot on concordia (C) or yield Δ U-Pb values close to zero (D). The deepest samples reside at temperatures that are too hot for Pb retention in rutile, and thus yield young to 0 Ma dates. The middle to lower crust spends a long time in the Pb-PRZ, resulting in discordance (C) and a large apparent offset between the two U-Pb systems (D). The magnitude of Δ U-Pb values (D) is correlated with lithosphere exhumation rate.

Figure 2. Plot of Δ U-Pb vs. time for measured and modeled lower crustal xenolith data from a NW-SE transect through Montana: (A) Archean Medicine Hat Block (MHB) and Wyoming Province (WP), (B) Proterozoic Great Falls Tectonic Zone (GFTZ). Figure inset provides sample number and geobarometrically determined depth. Faster-cooling, shallow samples yield older dates with a trend of increasing Δ U-Pb in time, while deeper samples decrease with time, consistent with the results predicted by the thermal model (Fig. 1D). Uncertainties on individual analyses are shown at the 2σ level and are dominated by the uncertainty of the ^{235}U-^{207}Pb date. Dashed, dotted and solid lines mark the forward-modeled U-Pb results with exhumation rates of -2.5 to 2.5 m/My. A dashed-dot line in (A) marks the data produced by an erosional history that decreased in time. Figure inset: simplified geologic terrane map of Montana, USA. Stars mark the xenolith sample location within each geologic terrane.

3.3 References:

Barnhart, K., 2010. Deep crustal xenoliths from the Great Falls Tectonic Zone, Montana: Investigating the timing and mechanisms of high-velocity lower crust formation, Department of Geological Sciences. University of Colorado Boulder, Boulder, p. 68.

Blackburn, T., Bowring, S., Schoene, B., Mahan, K., Dudas, F., 2011. U-Pb thermochronology: creating a temporal record of lithosphere thermal evolution. Contributions to Mineralogy and Petrology 162, 479-500.

Braun, J., 2002. Quantifying the effect of recent relief changes on age-elevation relationships. Earth and Planetary Science Letters 200, 331-343.

Braun, J., 2010. The many surface expressions of mantle dynamics. Nature Geosci 3, 825-833.

Burdick, S., Li, C., Martynov, V., Cox, T., Eakins, J., Mulder, T., Astiz, L., Vernon, F.L., Pavlis, G.L., van der Hilst, R.D., 2008. Upper Mantle Heterogeneity beneath North America from Travel Time Tomography with Global and USArray Transportable Array Data. Seismological Research Letters 79, 384-392.

Ehlers, T.A., Farley, K.A., 2003. Apatite (U–Th)/He thermochronometry: methods and applications to problems in tectonic and surface processes. Earth and Planetary Science Letters 206, 1-14.
Fischer, K.M., 2002. Waning buoyancy in the crustal roots of old mountains. Nature 417, 933-936.
Forte, A.M., Claire Perry, H.K., 2000. Geodynamic Evidence for a Chemically Depleted Continental Tectosphere. Science 290, 1940-1944.
Hearn, C., B., 2004. The Homestead kimberlite, central Montana, USA: mineralogy, xenocrysts, and upper-mantle xenoliths. Lithos 77, 473-491.
Hoffman, P.F., 1988. United Plates of America, The Birth of a Craton: Early Proterozoic Assembly and Growth of Laurentia. Annual Review of Earth and Planetary Sciences 16, 543-603.
Jordan, T.H., 1988. Structure and Formation of the Continental Tectosphere. Journal of Petrology Special_Volume, 11-37.
Mueller, P., A., Heatherington, A., L., Kelly, D., M., Wooden, J., L., Mogk, D., W., 2002. Paleoproterozoic crust within the Great Falls tectonic zone: Implications for the assembly of southern Laurentia. Geology 30, 127-130.
Portenga, E.W., Bierman, P.R., 2011. Understanding Earth's eroding surface with 10Be. GSA Today 21, 4-10.
Reiners, P.W., Ehlers, T.A., Mitchell, S.G., Montgomery, D.R., 2003. Coupled spatial variations in precipitation and long-term erosion rates across the Washington Cascades. Nature 426, 645-647.
Rudnick, R.L., Gao, S., Heinrich, D.H., Karl, K.T., 2003. Composition of the Continental Crust, Treatise on Geochemistry. Pergamon, Oxford, pp. 1-64.
Rudnick, R.L., McDonough, W.F., O'Connell, R.J., 1998. Thermal structure, thickness and composition of continental lithosphere. Chemical Geology 145, 395-411.
Schmitz, M.D., Bowring, S.A., 2003. Constraints on the thermal evolution of continental lithosphere from U-Pb accessory mineral thermochronometry of lower crustal xenoliths, southern Africa. Contributions to Mineralogy and Petrology 144, 592-618.
Yuan, H., Romanowicz, B., Lithospheric layering in the North American craton. Nature 466, 1063-1068.

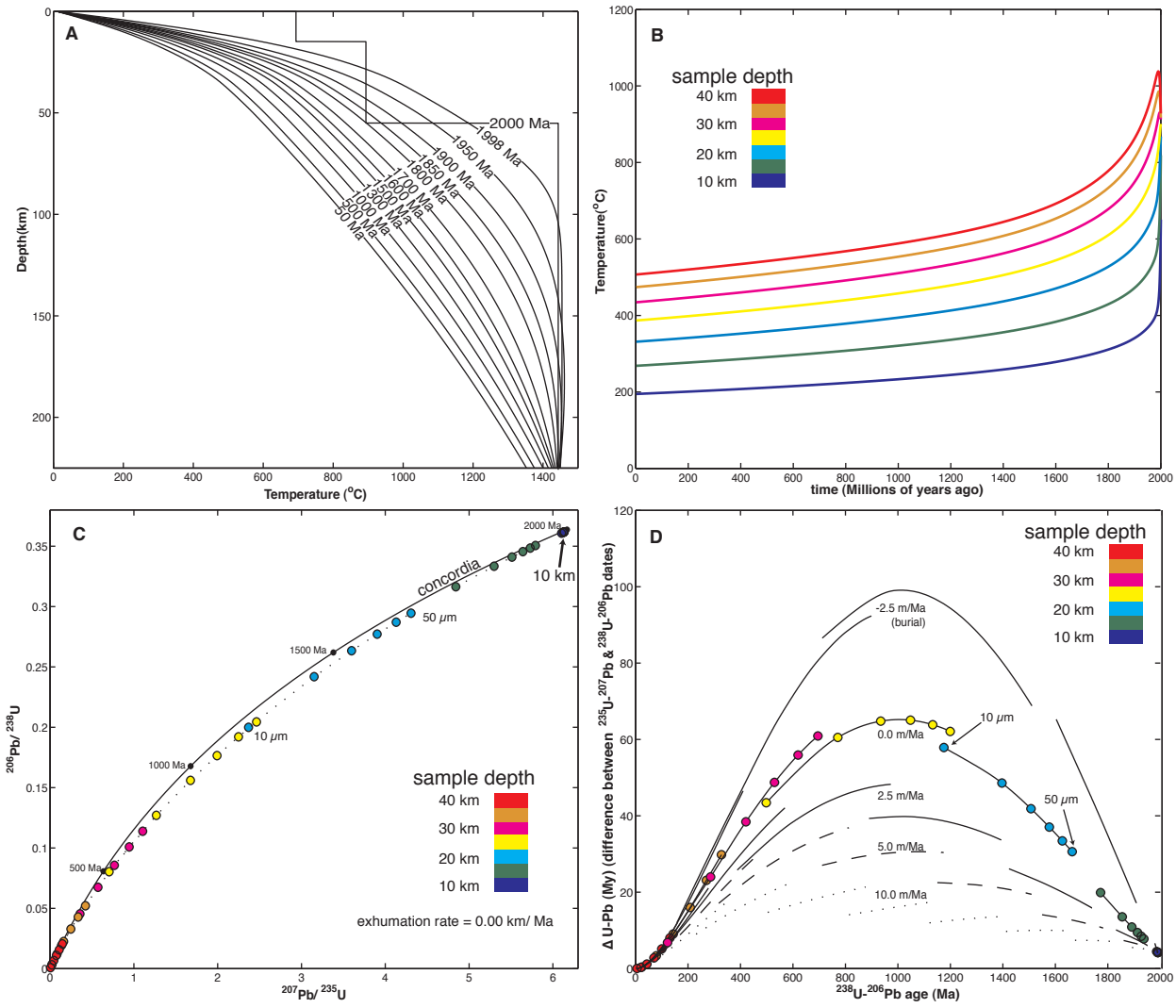
A
Depth(km)
Temperature (°C)
2000 Ma
1998 Ma
1950 Ma
1900 Ma
1850 Ma
1800 Ma
1700 Ma
1600 Ma
1500 Ma
1400 Ma
1300 Ma
1200 Ma
1100 Ma
1000 Ma
900 Ma
800 Ma
700 Ma
600 Ma
500 Ma
B
sample depth
40 km
30 km
20 km
10 km
Temperature(°C)
time (Millions of years ago)
C
concordia
2000 Ma
10 km
50 μm
1500 Ma
10 μm
1000 Ma
500 Ma
sample depth
40 km
30 km
20 km
10 km
exhumation rate = 0.00 km/ Ma
206Pb/ 238U
207Pb/ 235U
D
sample depth
40 km
30 km
20 km
10 km
-2.5 m/Ma
(burial)
10 μm
0.0 m/Ma
50 μm
2.5 m/Ma
5.0 m/Ma
10.0 m/Ma
Δ U-Pb (My) (difference between 235U-207Pb & 238U-206Pb dates)
238U-206Pb age (Ma)

Figure 3.1

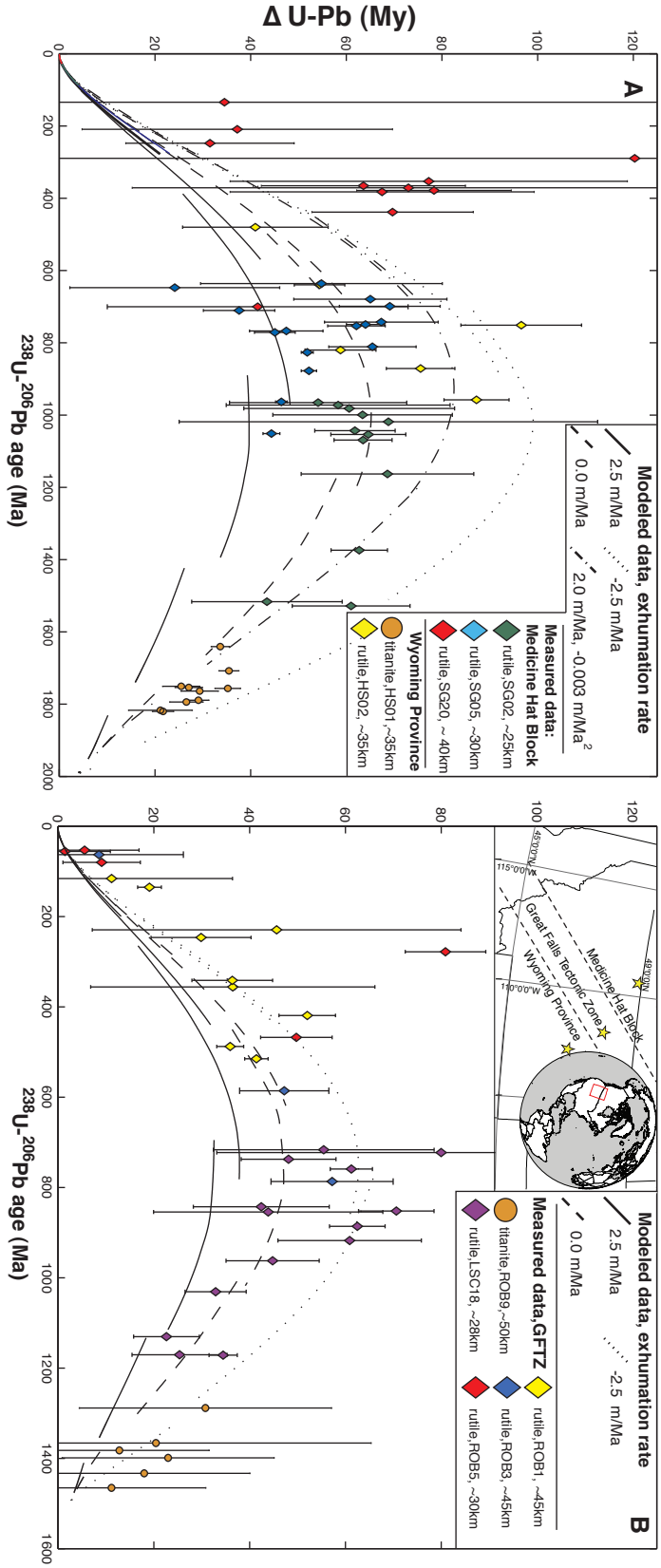
Δ U-Pb (My)
A
Modeled data, exhumation rate
2.5 m/Ma
-2.5 m/Ma
0.0 m/Ma
2.0 m/Ma, -0.003 m/Ma²
Measured data:
Medicine Hat Block
rutile,SG02, ~25km
rutile,SG05, ~30km
rutile,SG20, ~ 40km
Wyoming Province
titanite,HS01,~35km
rutile,HS02, ~35km
238U-206Pb age (Ma)
B
Modeled data, exhumation rate
2.5 m/Ma
-2.5 m/Ma
0.0 m/Ma
Measured data,GFTZ
titanite,ROB9,~50km
rutile,ROB1, ~45km
rutile,ROB3, ~45km
rutile,LSC18, ~28km
rutile,ROB5, ~30km
Great Falls Tectonic Zone
Wyoming Province
Medicine Hat Block
49°0'0"N
115°0'0"W
110°0'0"W
238U-206Pb age (Ma)

Figure 3.2

Chapter 4: Zirconium in rutile speedometry: constraining lower crustal cooling rates and residence temperatures

Blackburn, T., Bowring, S.A., Schoene B., Mahan K., (2012) Zirconium in rutile speedometry: constraining lower crustal cooling rates and residence temperatures., *Earth and Planetary Science Letters*, v. 317-318, p 231-240.

Abstract: The incorporation of zirconium into the mineral rutile (TiO_2) has been both empirically and experimentally calibrated as a measure of rutile crystallization temperatures (Watson et al., 2006). This temperature sensitive system has been employed as a geothermometer with applications to a number of different geologic settings and rock types. Experimentally measured kinetics for Zr diffusion in rutile (Cherniak et al., 2007) indicate that Zr can be lost to temperature dependent diffusion, warranting further investigation of the geologic significance of calculated temperatures. Coupling diffusion kinetics with numerical solutions to the diffusion equation provides a means to forward model the time and temperature dependency of the system. Modeled results indicate a strong dependency of Zr concentration in rutile on both: 1) initial cooling rate following high-temperature metamorphism/crystallization and 2) temperature and duration of long-term geologic residence. Zr concentrations measured in rutile from lower crustal xenoliths that resided at 25-45 km depths for ~2000 My, reveal Zr concentrations in the approximate grain center that are consistent with temperatures measured by independent thermometers. Forward models for Zr diffusion show that preserving a Zr record of these initial temperatures in the center of a rutile crystal with a 50 μm radius requires rapid cooling (>300 °C/Ma) from magmatic/metamorphic temperatures followed by a long-term residence (2000 My) at temperatures <550°C. This provides a new way to determine cooling rates between 900-500 °C and for constraining the temperature of the deep crust. Modeled temperature-time paths using combined rutile Zr and U-Pb geochronological data permit evaluation/refinement of published diffusion kinetics. Properly quantified, this system can be utilized as a high temperature geo-speedometer: a powerful tool for evaluating heat transfer rates at these very high and often unconstrained temperatures.

4.1 Introduction:

Creating a comprehensive model for any solid Earth system, whether a study in rock rheology, mantle dynamics or planetary formation, often requires a measure of a system's initial

temperature. Geothermometry, as broadly defined, permits estimation of equilibrium temperatures for systems using empirical or experimental calibrations of a measured state of mineral phase equilibrium. Utilizing a temperature sensitive equilibrium of silica, zirconium and titanium in the minerals quartz, zircon and rutile, the Zr-in-rutile thermometer (ZRT) has recently been developed to constrain the crystallization temperatures of a variety of rocks. The original calibration of the system utilized temperature constraints from independent thermometers, correlated with Zr concentration in rutile (Zack et al., 2004). The ZRT was verified and refined by several experimental studies (Ferry and Watson, 2007; Tomkins et al., 2007; Watson et al., 2006) resulting in a well-defined relationship between rutile Zr concentration and equilibrium temperature and pressure. This novel accessory mineral thermometer has been applied to a wide variety of rock types and extreme geologic environments, from ultra-high-temperature (UHT) granulites (Baldwin and Brown, 2008) to ultra-high pressure eclogites and blueschists (Spear et al., 2006; Zack and Luvizottow, 2006). The mobility of Zr in rutile by solid state diffusion was investigated by Cherniak et al. (2007) in order to evaluate the potential for diffusive loss of Zr from rutile. This previous experimental study indicates that Zr in rutile obeys thermally activated volume diffusion with an activation energy (E_a) and prefactor (D_0) of 170±30 kJ/mol and 9.8e-15 m^2/s, respectively (Cherniak et al., 2007). An important implication derived from this study is that high temperature rocks (800-1000 ºC), including the previously studied granulites and high temperature eclogites, will only retain the Zr concentration associated with UHT/HT conditions if cooling rates following these high temperatures are extremely rapid (>10^4 ºC/M; (Cherniak et al., 2007). Therefore, the preservation of high-temperature systems recorded by the ZRT implies that the extremely rapid cooling required to preserve these concentrations is perhaps inherently linked with UHT/HT conditions.

The purpose of this paper is to systematically explore the temperature and time dependence of Zr concentrations in rutile by applying the experimentally determined diffusion kinetics (Cherniak et al., 2007) and numerical solutions to the diffusion equation to understanding intracrystal Zr concentration measurements in rutile. We show that the Zr-in-rutile system for lower crustal rocks may or may not yield a temperature of crystallization, but can record: 1) the cooling rate through a thermal window of approximately 1000-500 ºC (Fig. 1a) and 2) a maximum estimate for the long-term residence temperature experienced by the sample.

Quantifying the degree of Zr diffusion in rutile from lower crustal samples can constrain thermal histories not recorded by other thermochronometric techniques. Previously employed temperature sensitive systems such as the U-Pb and $^{40}Ar/^{39}Ar$ thermochronometers have an initial state with a concentration gradient of zero that increases only with the in-situ production of daughter isotope(s) and decreasing temperatures (Fig. 1b). The Zr-in-rutile system, however, begins with an extremely steep gradient making it highly susceptible to diffusive loss during initial cooling from magmatic/metamorphic temperatures, and thereby provides a measure of cooling rates between 700-1000 ºC; a temperature range that other thermochronometers remain insensitive to. Determining the amount of Zr lost by diffusion can provide new insight into the Earth's thermal history and allow users to quantify the rates of heat transfer in underexplored regions of the lower crust and upper mantle.

4.1.1 Geologic applications: High temperature cooling rates and long-term residence temperatures

There has been a great deal of interest in understanding the geologic setting of rocks recording high-temperature (HT) and ultra-high temperature (UHT) metamorphism (Baldwin and Brown, 2008; Harley, 1998). Understanding the time-scales and conditions for UHT petrogenesis and the subsequent exhumation of these samples holds important information on the conditions and composition of the deep crust and the plate tectonic processes operating to exhume them (Hacker et al., 2005). Despite the focus on these unusual rocks, the time-scales and processes leading to their subsequent exhumation to the Earth's surface remain unclear (Baldwin et al., 2004; O'Brien and Rötzler, 2003). This may be due to an incomplete determination of their P-t-T history, in particular at a gap between the UHT and HT conditions (>800 °C) recorded by geothermometers and the low to moderate temperatures (400-600 °C) recorded by thermochronologic systems (U-Pb, $^{40}Ar/^{39}Ar$). The Zr-in-rutile system has potential as a geospeedometer capable of describing the cooling rates of rocks through this previously unconstrained thermal window (700-1000 °C), thus providing insight into physical models for heat transfer in the Earth.

Similarly enigmatic are the long-term residence temperatures that lower to middle crustal rocks experience after the initial cooling from magmatic/metamorphic conditions. There remains a 200-300 °C discrepancy in lower crustal temperature estimates inferred from different sources

of data used for measuring the lithosphere's geothermal gradient. Geothermal gradients produced by mantle xenolith P-T arrays when extrapolated upwards yield lower crustal temperatures of 600 °C or more (McKenzie et al., 2005). Meanwhile, thermal models utilizing surface heat flux measurements, often yield lower crustal temperatures of 500 °C or less (Jaupart and Mareschal, 1999; Pollack and Chapman, 1977). Similar temperatures are implied by U-Pb thermochronologic data from lower crustal xenoliths that record slow cooling over a billion years or more at lower crustal temperatures between 400-600 °C (Blackburn et al., 2011; Schmitz and Bowring, 2003). By measuring Zr concentrations in rutile from a suite of lower crustal xenoliths over a range of depths, one can place maximum estimates on the long-term residence temperatures for these samples. The Zr-in-rutile system's sensitivity to holding temperature over geologic time can be employed to place limits on the temperatures experienced at middle to lower crustal depths and resolve the discrepancy between mantle xenolith and surface heat flux/model geothermal gradients. This information will help to inform a new and independent measure of lithosphere temperature conditions as recorded at lower to mid-crustal depths.

4.2 Methods

To quantify a sample's thermal history over the 1000 -500 ºC temperature range in which the Zr-in-rutile system is sensitive, one must either: 1) characterize the diffusion profile of Zr within a single grain or 2) measure the Zr concentrations in grains of variable size. Accurate measurement of a diffusion profile using intracrystal measurement techniques is often complicated by variations in grain orientation, and level of sectioning into the grain. Because of these variations, any intracrystal Zr measurement from a rutile crystal with a 3-D Zr diffusion profile will lack sufficient spatial control with which to infer any meaningful information about the diffusion profile and thus the time-temperature history of the sample. In short, a singular "spot" analysis represents a spatially uncontrolled sub-sampling of a diffusion profile and by itself has limited significance. Previous ZRT studies have commonly used an ion microprobe (SIMS) or electron microprobe (EMP) techniques for Zr analyses. Because the majority of published ZRT data were acquired using these techniques, the numerical modeling results presented here will focus on extracting information from these in-situ data.

A criterion for evaluating Zr diffusion from intracrystal measurements must be developed in order to place meaningful limits on a sample's thermal history. The essential constraint

employed here is the presence or absence of "center retention" – a term previously used by Cherniak et al. (2007) to describe whether equilibrium Zr concentrations within the core of the grain have been preserved after particular t-T history (Fig. 1). Numerical modeling presented here will focus on extracting information pertaining to a sample's time-temperature history based on the retention or loss of equilibrium conditions within the grain center. Importantly, the center retention criterion can be evaluated using SIMS or EMP techniques. An independent measure of the system's initial temperature is required for comparison, with the further assumption that both thermometers are recording the same maximum temperatures.

4.2.1 Zr laboratory methods

In this study, Zr concentrations were determined using a Cameca IMS 1280 ion microprobe at the Northeast National Ion Microprobe Facility at Woods Hole Oceanographic Institution. A beam of negatively charged oxygen ions ($^{16}O^-$) with a current ranging from 750 pA to 1.1 nA was focused to a spot of approximately 10 – 15 mm. Secondary ion intensities of $^{46}Ti^+$ and $^{90}Zr^+$ were measured by jumping magnetic field from ^{46}Ti to ^{90}Zr cyclically 10 times for each analysis with a mass resolving power of 5500. Natural and synthetic rutiles standards with Zr concentrations ranging from 4.45 ppm to 769 ppm (Zack et al., 2004) were used to determine a relationship between Zr contents and $^{90}Zr/^{46}Ti$ intensity ratios (a calibration line). The calibration line is expressed as: Zr (ppm) = 7.22E5 * ($^{90}Zr/^{46}Ti$) with an error (2s) for the slope of ±2.5%, and the session-to-session reproducibility of the slope is within ±5%. For the range of concentrations encountered here (>2500 ppm), the largest uncertainties are derived from the calibration line slope error described above, since errors for $^{90}Zr/^{46}Ti$ measurements are much less than 1% (2s). Zr measurements were collected from rutile samples mounted length-wise, ground down/sectioned so that the approximate grain center was exposed and polished. Spot analyses were made from both the grain centers and grain tips.

4.2.2 Modeling Zr diffusion in rutile

Modeled intracrystal Zr diffusion profiles for rutile are produced using numerical forward models and are used to evaluate the temperature and time dependence of Zr retention/diffusion within rutile. Numerical solutions to the diffusion equation using experimentally determined kinetics have previously been employed to develop accurate and stable solutions to model

diffusion in other temperature dependent systems (Blackburn et al., 2011; Schoene and Bowring, 2007). The finite difference model employed here utilizes a Crank-Nicholson solution to the spherical form of the diffusion equation and results in an intracrystal Zr concentration profile for any pre-assumed time temperature path. The spherical form of the diffusion equation provides a suitable replacement for cylindrical grains with equivalent surface to volume ratios (Meesters and Dunai, 2002). Unlike analytical solutions to the diffusion equation, numerical models are not restricted to a constant diffusivity and allow testing of time-temperature paths in any form. The initial Zr concentration within a modeled rutile crystal are homogeneously distributed and set to a value that corresponds to the initial temperature for the model run using the algorithm from Ferry and Watson (2007) (Fig. 1a). Employing this model for measuring rock cooling rates and residence temperatures is based on two assumptions: 1) equilibrium is attained continuously at grain edges at all temperatures and (2) the system is continuously saturated with Zr at all times. These assumptions make it possible to convert all Zr concentrations to temperatures with the experimental calibrations for Zr and temperature. Further, the homogenous initial condition assumes that any variations in the initial Zr concentration as a result of changes in temperature or Zr activity during rutile crystallization are negligible. Equilibrium conditions at the grain edge are modeled using a boundary condition that changes with temperature and time, reflecting the equilibrium Zr concentration within the surrounding host rock (Fig. 1a) (also using the algorithm from Ferry and Watson (2007)). Exponential cooling paths, typical for rocks in the lithosphere, result in a significant early decrease in temperature and are thus accompanied by an early decrease in Zr at the grain edge. The resulting large concentration gradient between the high Zr concentrations within rutile and low concentrations in the host rock leads to the possible diffusive loss of Zr (Fig. 1a). The purpose of this model is to constrain: 1) the minimum initial cooling rates required to preserve Zr concentrations consistent with metamorphic/igneous temperatures and 2) place a maximum estimate on the long-term residence temperatures required to preserve Zr over geologic time scales.

4.2.2.1 Cooling rate sensitivity

The retention of Zr concentrations consistent with equilibrium conditions within a rutile grain is highly sensitive to the sample's cooling rate, allowing the system to be employed as a geospeedometer. Forward modeled results indicate that quickly cooled grains retain Zr

concentrations consistent with initial temperatures, while slow cooling allows for the diffusive loss of Zr from the rutile crystal, resulting in a rounded Zr profile and (potentially) sufficient loss of Zr so that center retention criteria are no longer meet. Figure 1a shows the internal diffusion profiles for a range of cooling rates (10^1 – 10^5 °C/Ma, for an initial temperature of 900 °C). With decreasing cooling rate the difference between the initial core concentration and the measured core concentration (Δcore) will consistently increase (Fig. 2). If the measured core concentration is equal to the initial core concentration, then center retention criteria are met. To utilize the relationship between initial and measured core concentration as a geospeedometer one must have an independent measure of the systems initial temperature. Though the difference between core and rim concentrations of a single grain is indicative of a diffusion profile (Δcore-rim), the relationship between cooling rate and this value is also dependent upon core concentration value (Fig. 2). For a 50 μm radius grain within an initial temperature of 900 °C, cooling rates as low as 500 °C/Ma can meet center retention, assuming the highest experimentally determined activation energy (200 kJ/mol) within the reported uncertainty (170±30 kJ/mol, Cherniak et al., 2007). Cooling rates of at least 10^4 °C/Ma and 10^6 °C/Ma are required to meet center retention of 170 kJ/mol and 140 kJ/mol Ea, respectively; rates that exceed expectations for cooling in the dry and conductive lower crust. Increased temperatures are accompanied by an increase in Zr diffusivity, requiring even faster cooling to preserve UHT conditions. For example, with an initial temperature of 1000 °C, cooling rates of more than 2500 °C/Ma are required to maintain center retention. At lower initial temperatures of 800 °C, cooling rates of at least 100 °C/Ma will meet center retention for a crystal with a 50 μm radius. Similarly, decreasing the grain radius to 20 μm will require increased cooling rates (>1500 °C/Ma) to meet center retention for an initial temperature of 900 °C.

4.2.2.2 Constraining maximum residence temperatures

Following initially rapid cooling, the future preservation of Zr in the system is then dependent upon the long-term residence temperature of the system. Forward models assuming initially rapid cooling followed by isothermal holding can be used to explore the relationship between long-term residence temperature and the concentration of Zr within the center of a rutile crystal. The resulting center retention partial retention zone (CR-PRZ) shown in figure 3, describes the Zr concentration within the center of crystals with radii between 10 and 50 μm as a

function of increasing temperature or depth through the lithosphere. Plotted along with the CR-PRZ are the experimental (Ferry and Watson, 2007; Tomkins et al., 2007; Watson et al., 2006) and empirical calibrations of Zr (Zack et al., 2004) for comparison.

Grains retaining Zr concentrations consistent with initial high temperature equilibrium extend to isothermal holding temperatures of 450-550 °C, where the range in temperature correlates to grain sizes of 10 and 50 μm. At these low holding temperatures, diffusion is slow enough to prevent the diffusive loss of Zr, yielding a reliable record of initial temperature conditions. At temperatures greater than 600 °C, diffusion is sufficient to permit the loss of Zr associated with initial temperatures and instead yield Zr concentrations consistent with the isothermal holding temperatures (Fig. 2). This indicates that rutile residing above 600 °C will yield Zr concentrations that correlate to the sample's temperature at the time of exhumation towards the surface. The ~450-600 °C temperature window between these two regimes marks the CR-PRZ for the system, a region where grains experience partial loss of Zr derived from initial high temperature equilibrium, yet still yield Zr concentrations hundred's to thousand's of ppm higher than the Zr concentrations predicted by the experimental and empirical calibrations for these temperatures (Fig. 3). The convergence between the CR-PRZ at temperatures > 600 °C and the experimental calibrations are the direct result of our model's use of a changing boundary condition where the Zr concentration at the grain edge correspond to the system temperature. If the model employed a zero concentration boundary condition for the grain edge, the CR-PRZ would be near identical at temperatures above 600 °C, yet would decrease to zero concentrations with increasing temperature.

Preservation of high Zr concentrations associated with metamorphsim/igneous events can be used to infer a residence at temperatures less than ~550 °C (for durations of 2000 My); a value that is insensitive to initial Zr concentration (i.e. equilibrium temperature) (Fig. 3). This 550 °C estimate serves as a maximum value, as it uses the maximum activation energy permitted by the reported uncertainty (200 kJ/mol) (Cherniak et al., 2007). Lack of center retention may be the result of either cooling at rates $<10^3$ °C/Ma through 700-1000 °C or holding at temperatures > 550 °C. The presence of center retention permits the conclusion that both requirements of a minimum initial cooling rate of 10^3 °C/Ma and long-term residence below ~550 °C were met. Variations from these simple cooling paths, such as short reheating events, can potentially go unrecorded. For example, samples experiencing long-term residence at 450 °C, could still retain

center retention while being reheated to 600 °C for 100 My or to 800 °C for < 2 My. Higher temperatures or longer durations of reheating will result in the loss of center retention. Predictably, the system becomes more sensitive to reheating events at higher residence temperatures, i.e. durations of reheating are even shorter if long-term residence is 550 °C. The system's sensitivity to reheating events allows users to conclude that if center retention is observed, than the majority of the sample's time-temperature history is consistent with rapid initial cooling (>10^3 °C/Ma) followed by residence below 550 °C. By assuming a geothermal gradient for the region, a temperature can be assigned to each xenolith depth, permitting measured Zr data to be compared to the modeled CR-PRZ (Fig. 3). Varying the assumed geothermal gradient will cause the CR-PRZ to move either closer (hotter geotherm) or further (colder geotherm) from the Earth's surface.

4.2.2.3 Detecting volume diffusion with intracrystal analyses

This study's use of center retention criterion to place constraints on the time-temperature history of the sample provides a means to evaluate histories without the requirement of producing a direct measure of a crystal's internal diffusion profile. Despite this, it is worthwhile exploring how volume diffusion may manifest itself within a dataset produced by intracrystal measurement techniques. Figure 4 presents a schematic illustration of the data that could result from an internal transect of Zr "spot" analyses oriented parallel to the *c*-axis of a grain. We consider cases of both isotropic (Fig. 4a) or anisotropic (Fig. 4b and c) diffusion operating. Experimental diffusion data for Zr in rutile were measured for diffusion parallel to the *c*-axis (Cherniak et al., 2007).

In cases of isotropic (Fig 4a) or anisotropic diffusion where diffusion is faster in the *a*/*b* direction than *c* (Fig 3b), the variation in Zr concentration revealed by intracrystal analyses would depend on the depth of sectioning into the grain (Fig. 3d). Any observed variation in concentration from core to rim would yield an *apparent* profile dependent on the level of sectioning into the grain (Fig. 4a). Information pertaining to the time-temperature history of the sample, may be constructed through a series of measurements through the grain parallel to the *a* or *b* axis. If, however, Zr diffusion were anisotropic with the dominant direction of diffusion parallel with the *c*-axis, grains mounted parallel to the *c*-axis (length-wise) would allow the

diffusion profile to be mapped by several spot analyses from core to rim (Fig. 4c). Any measured variation with Zr concentration would reflect the actual diffusion profile.

In the case of isotropic or *a*/*b* dominant diffusion, if the centers of several grains of approximately the same grain size were analyzed, with each grain (unavoidably) sectioned to a different depth, we can anticipate a range of Zr concentrations that reflect the true variation of values along some portion of the true diffusion profile (Fig 4d). For example, in a quickly cooled sample, the Zr-in-rutile system would record a uniform concentration among grains, independent of the level of polishing. Slow cooling or high temperatures over long time-scales however, will yield significant variations in Zr concentration from grain to grain. This model predicts an increase in the variability in Zr from the centers of grains with increasing depth into the crust (xenolith depth). These data would only be symptomatic of diffusion and because the data is not spatially controlled one cannot reconstruct a diffusion profile. An enhanced measure of Zr diffusion could be provided by whole grain Zr concentration measurements over a range of rutile grain sizes, where internal diffusion profiles are inferred based on variations in Zr with grain size.

4.3 Geologic Setting: Pressure-Temperature-time constraints

Zr concentration in rutile grains were measured from middle to lower crustal xenolith samples, derived from the Archean Medicine Hat Block (MHB) and adjoining Great Falls Tectonic Zone (GFTZ), both located within Montana, USA (Fig. 5c inset). Previous published data for samples SG02 and SG05 from the MHB include, major element/phase thermobarometery and pseudosection analysis, U-Pb rutile thermochronology and U-Pb zircon geochronology (Blackburn et al., 2011). Rutile and zircon data for sample ROB1 from the GFTZ are included in the appendix. Pressure estimates are 0.8 for SG02, 1.0 GPa for SG05 and 1.3 GPa for ROB1. Temperature estimates from pseudosection construction lie between 800-950 °C for SG02 and 700-900 °C for SG05. Garnet-biotite thermometry for these samples yield temperatures on the lower end of this range at ~700 °C. Garnet-Biotite and garnet-clinopyroxene-thermometry yield temperature estimates of 800 and 750 °C respectively for ROB1 (Barnhart, 2011). Zircon U-Pb data record Archean protolith formation for the shallowest sample SG02, with zircon overgrowths at ~1800 Ma from what is interpreted to be the timing of the amalgamation of the MHB craton onto North America (Mueller et al., 2002). Zircon from

SG05 and ROB1 record crystallization between ~1680 and 1800 Ma (ROB 1 see DR Table 3). Rutile U-Pb thermochronometry from each of these samples record a post-Archean cooling history (Blackburn et al., 2011). Paleoproterozoic zircon U-Pb dates and a post-Archean cooling history both suggest that measured Zr concentrations and ZRT temperatures from these samples were derived during this younger orogenic event.

Following the Proterozoic orogenic event rutile U-Pb thermochronometric data record extremely slow cooling through the ~400-600 °C rutile Pb PRZ. The shallowest sample SG02 yields U-Pb rutile dates over a range of ~1400 to 1000 Ma, where the largest rutile crystal yields the oldest date and the smallest crystal the youngest –consistent with volume diffusion. The next deepest sample SG05 yields dates between 1100 and 650 Ma, also correlating with grain size. The deepest, 45 km sample from the nearby GFTZ records cooling between ~550 and 50 Ma. The significant span of dates within each sample combined with a trend of younging downward with sample depth are interpreted to indicate prolonged lower crustal residence and slow relaxation of a conductive geotherm (Blackburn et al., 2011).

4.4 Results

Zirconium concentration measurements for the xenolith samples ranged between ~2800-3500 for the shallowest sample SG02, ~3800-5000 ppm for the deeper xenolith SG05 and between ~165 and 1600 ppm for the deepest sample ROB1 (core Zr concentrations plotted Fig. 3 and 5). Multiple spot analyses within single grains were measured yet systematic variations in Zr concentration were only detected within sample ROB1, where spot measurements close to the grain tip decrease by as much as 120 ppm (0-50%) when compared to the core measurement. Shallower xenolith samples SG02 and SG05 were homogenous on the ~100-200 ppm level, with these small-scale variations (2-3%) both increasing and decreasing towards the grain edge. A full report of measured Zr data is included in table A.1. The measured concentrations yield temperatures of ~870-900 °C for SG02, ~900-940 °C for SG05 and ~600-800 °C for ROB1 using the Ferry and Watson (2007) thermometer. Center retention is met for all three samples with at least one analysis from each sample reaching concentrations consistent with or exceeding independent temperature estimates (Fig. 5a). For the ~40-50 μm grains (radius) in sample ROB1 this implies initial cooling rates of at least 300 °C/Ma, followed by long-term residence at temperatures less than ~550 °C. The smaller range of grain sizes (~20-30 μm radius) from SG02

and SG05 require lower long term holding temperatures of ~ 500-520 °C and faster cooling rates on the order of 2000 °C/Ma.

Deviations from this center retention value were observed in each sample. In the shallow sample SG02, deviations of up to 20-26 % are observed for a range of ~10-25 μm (radius) grains, up to 30- 60% difference over a range of 10-50 μm grains in the 35km sample SG05 and up to 130-160 % for 30-45 μm grains from the 45km deep sample ROB1 (Fig. 5c). The trend of increasing percent variation with xenolith residence depth suggests an increase in the diffusive loss of Zr with sample depth (Fig. 5c).

4.5 Discussion

4.5.1 Evaluating rapid cooling rates

A limit on the body size of intrusive bodies for the lower crustal samples studied here can be placed by examining the rates of cooling predicted for 2 end-members of cooling within the lithosphere: 1) conduction only and 2) magmatic cooling. The well-insulated and dry lower crust should thus represent a near end-member of slower cooling that can be approximated by a purely conductive thermal model where the time-scale of cooling (*t)* is proportional to the size of the intrusive body and the temperature of the surrounding country rock ($t \sim pluton\ radius^2$)(Spera, 1980). We can refine this calculation using a model for the temperature dependent thermal diffusivity from Whittington (2009) and a analytical half-space solution from Carslaw and Jager (1959). For a minimum country rock temperature of 400 °C, the largest intrusive body radius that yield cooling rates consistent with the requirement of the Zr data presented here ($>10^3$ °C/Ma) is ~5 km.

Within a magma chamber there are several additional processes operating to both cool and heat the system. Cooling processes include conduction, both at the intrusion wall as well as within the magma, convection both within the magma and externally by hydrothermal circulation. The efficiency of this cooling is highly variable and dependent upon such variables as magma composition and viscosity, magma water content, and the depth of intrusion (Spera, 1980). These processes potentially culminate in cooling timescales (*t*) far shorter than from just heat conduction alone ($t \sim pluton\ radius^{1.3}$), permitting the intrusion body sizes slightly larger than 5 km (Spera, 1980).

In the case of xenoliths from Montana, the presence of 1800 Ma zircon growth and the lack of any Archean cooling signature recorded by the rutile U-Pb system suggest the partial remelting and massive reheating of an Archean protolith occurred during amalgamation of the MHB terrane onto the North American craton. Cooling following this event could only occur at rates up to 10^3 °C/Ma if rocks were juxtaposed onto colder material. The fact that center retention is met by samples from the lower crust at all depths between ~25-45 km indicate that only small and localized regions of the lower crust, likely smaller than 5km in radius, are heated during magmatism and/or metamorphism and then cooled rapidly due to low temperatures in the surrounding country rock.

4.5.2 Differences in t-T path sensitivity between the Zr and Pb systems in rutile

The U-Pb and Zr rutile systems deliver information used to constrain a different portion of sample's cooling history. The rutile U-Pb system is highly sensitive to a sample's low to moderate temperature cooling history (400-600 °C). Though long-term temperatures also control the Zr-in-rutile system, this system is highly sensitive to the initial cooling rate from magmatic or metamorphic temperatures; a temperature range the U-Pb system cannot constrain. The cause for difference in the temperature range at which each system is sensitive to lies in the relative difference between internal concentration gradients of each diffusant at the time of system formation. The Zr-in-rutile system begins with a high initial concentration that correlates to equilibrium temperatures. As a rock cools and the concentration at the grain boundary decreases, a large concentration gradient develops between the high Zr concentrations within the grain and the lower concentrations in the surrounding matrix or host rock (Fig. 1a). The system's sensitivity to cooling rate from high temperatures is the direct result of this large concentration gradient; without rapid initial cooling, Zr concentrations that correlate to maximum temperatures would be lost by diffusion. The rutile Pb system however, has zero radiogenic lead at the time of system formation. Only with decreased temperature/diffusion can Pb produced by decay of U begin to accumulate and build a Pb diffusion profile. Figure 1 plots the internal concentration profiles of Pb and Zr within a rutile grain for the same time-temperature path (Fig. 1 inset). Zr concentration decreases dramatically along the rutile grain rim in a time frame (<1 My) where no Pb retention has occurred. The two systems complement one another to provide complete (>900-400 °C) constraints on a sample's time-temperature history.

4.5.3 Combining U-Pb and Zr rutile systems and refining Pb/Zr diffusion kinetics

A time-temperature path for the lower crustal xenoliths from Montana can be determined by finding the thermal histories that fit observed data from both the Zr and U-Pb systems. The Zr system sets a limit to the *maximum* temperature for the lower crust; samples residing at temperatures higher than this maximum will result in a loss of Zr center retention. The U-Pb system, however, provides a *minimum* temperature limit to this long-term residence: measured U-Pb data require slow cooling through the rutile Pb PRZ, faster cooling rates will result in model dates that are too old and lack the observed discordance and ~500 Ma spread dates in grain size vs. age (Fig. 6). By testing a series of t-T paths with initially rapid cooling followed by slow cooling through a range of residence temperatures, we can find which paths yield forward modeled data that agree with both U-Pb and Zr rutile data. Finding a time-temperature path that fits each system provides an independent test for the diffusion kinetics for Pb in rutile, the accuracy of which has been debated due to the differences between apparent field closure (400-500 °C) (Mezger et al., 1989) and Dodson closure temperatures calculated using the measured Pb in rutile kinetics (T_C=485-630 °C, DTdt = 0.1-100 °C/Ma) (Cherniak, 2000; Dodson, 1973).

The temperature range at which Pb retention in rutile occurs is highly sensitive to the diffusion kinetics of the system. The diffusion kinetics, however, have little affect on the interpreted cooling rate, as this value is interpreted from the topology of U-Pb data utilizing the U-Pb system's dual decay scheme (Blackburn et al., 2011). A lower E_a for Pb would permit cooling at a lower temperature and not affect the conclusion of ~0.05-0.1 °C/Ma cooling rates (Fig. 6). Zr activation energy is at their maximum for this analysis, suggesting a lower activation energy for Pb diffusion is the only variable remaining to be explored. The nominal published kinetics for Pb diffusion in rutile measured in a synthetic sample are: E_a 250±12 kJ/mol and (D_0) of and 3.9e-10 m^2/s (Cherniak, 2000). Additional experiments for Pb diffusion in rutile by Cherniak (2000) used natural rutile samples with experimental data reported for both parallel to *c*-axis and normal to *c*-axis diffusion. Our regression of diffusion kinetics from this data yields an E_a = 260 ± 30 kJ/mol and D_0 = 6.9e-10m^2/s for parallel to *c*-axis diffusion and E_a =220 ± 22 kJ/mol and D_0 =2.08e-11m^2/s for normal to *c*-axis diffusion (Fig. 6b inset).

Measured rutile U-Pb data from each xenolith and the forward modeled U-Pb data following Blackburn et al. (2011) are plotted on a concordia diagram in figure 6a. The measured

U-Pb data are bracketed by modeled data with cooling paths that are initially rapid (2000 °C/Ma) until a specified inflection temperature (T_{infl}), followed by slow cooling at a rate between 0.05-0.1 °C/Ma (Fig. 6). Using the nominal diffusion kinetics for Pb, the inflection temperatures that yields a good fit with the data are is consistently too high to permit the retention of Zr (Fig. 6d). To satisfy both systems, the kinetics for Pb diffusion in natural rutile (220 ± 22 kJ/mol, 2.08e-11 m^2/s) with a activation energy of at least 220 kJ/mol (Fig. 6b inset) are required. This value lies outside the uncertainty of activation energies reported for the synthetic rutile (Fig. 6a inset).

It is important to note that this analysis assumes a maximum Zr E_a of 200 kJ/mol and values for Pb would change if a lower Zr value were used. Lower E_a values for Zr diffusion, however, were shown previously to require cooling rates to meet center retention far above those anticipated in the conductively cooling lithosphere. Because of this we support a value of 200 kJ/mol, 9.8e-15 m^2/s for Zr and 220 kJ/mol, 2.08e-11m^2/s for Pb diffusion in rutile as the most internally self-consistent values. This corresponds to a Dodson T_C for Pb in rutile of 420-570 °C (*DTdt* = 0.1-1 °C/Ma, a = 10-100 μm); values that are consistent with field studies (Anderson et al., 2001; Corfu and Easton, 2001; Corfu and Stone, 1998; Flowers et al., 2006; Mezger et al., 1989; Miller et al., 1996; Moller et al., 2000; Schmitz and Bowring, 2003). These kinetics are used to conclude a lower crustal history where maximum residence temperatures of 500 °C at depths up to 35 km and 550 °C at a depth of 45 km are met within <0.5 Ma following orogenesis at ~1800 Ma. The initial rapid cooling is followed by prolonged slow cooling at rates between 0.05-0.1 °C/Ma, where the shallowest xenoliths cool first and the deepest last.

4.6 Conclusions

The use of temperature sensitive chemical reactions provides the fundamental basis for which geothermometry can yield reliable temperature estimates for a particular system within the Earth. The preservation of this state of chemical equilibrium, and thus the temperatures derived from any measurement, are susceptible to alteration through many processes, including diffusion. Experimental measurements of Zr in rutile indicate that Zr obeys temperature dependent volume diffusion (Cherniak et al., 2007). Forward modeled calculations presented here indicate a strong dependency of the preserved Zr concentration on the rate at which the sample cools. Characterizing the internal diffusion profile or the correlation between grain size and Zr concentration allows the system to be exploited as a geo-speedometer, used to estimate the

sample cooling rate through a temperature range of ~500-1000 °C. Measurements of Zr in rutile have nearly always been conducted using intracrystal measurement techniques. The preservation of Zr concentrations that correlate to the equilibrium temperatures within the center of a rutile grain or center retention provides a means to constrain some aspects of a sample's time-temperature history. This method requires independent measure of the system's initial temperature for comparison. Preservation of center retention within a grain is sensitive to both initial cooling rate of a system and long term holding temperature. This allows users to fill the once unconstrained gap between high magmatic and metamorphic temperatures and the temperatures recorded by moderate temperature thermochronometers. The Zr-in-rutile system's sensitivity to long-term residence temperature allows an independent maximum constraint to be placed on temperatures within the lower crust and a means to independently evaluate the accuracy of diffusion kinetics for Pb. We conclude here that the maximum activation energy for Zr diffusion within the reported uncertainty of 200 kJ/mol and that the experimentally determined values for Pb diffusion in natural rutile perpendicular to the *c*-axis (220 kJ/mol, D_0 of 2.08e-11 m^2/s) are the most self-consistent values. In the presented case study of xenoliths from Montana, integrating ZRT data with independent temperature and pressure constraints allows a maximum estimate of 500-550 °C to be placed on temperatures within the lower crust providing a new data point for accurately constructing geothermal gradients for the lithosphere.

4.7 Figure Captions

Fig. 1. Zr and Pb evolution in a single rutile grain. (a) Internal concentration profiles of Zr and (b) Pb for a 50 μm radius rutile grain that experienced the time-temperature path shown in figure inset. The initially high concentration profile for Zr causes the system to be highly susceptible to diffusive loss during the initial cooling following high temperatures associated with metamorphism/magmatism. Note that the boundary at the grain edge changes from high concentrations equivalent to equilibrium temperatures, to concentrations < 200 ppm that correlate to lower crustal temperatures < 600 °C. This change in boundary condition during cooling permits the diffusive loss of Zr. The Pb system, however, begins with zero retained radiogenic Pb, and does not build a diffusion profile until sufficient time and decreased diffusivity permits the retention of radiogenic Pb. The Pb system is thus more sensitive to low-temperature (400-600 °C) diffusive loss. Together the Zr and Pb systems can constrain the time-temperature path of a single sample from over 1000 °C to less than 400 °C.

Fig. 2. Effect of initial cooling rate on internal Zr concentration diffusion profiles. Results of forward modeled calculations for internal diffusion profiles with variable cooling rate. (A) A minimum cooling rate of ~300 °C/Ma) is required to maintain center retention (E_a = 200 kJ/mol, 50 μm radius). Modeled boundary condition assumes minimum temperature of 600 °C, correlating to 170 ppm Zr. The difference between initial core concentration and measured core concentration (Δ core) will consistently increase with decreasing cooling rate (B,C). The difference between the core and rim concentration (Δ core-rim), though symptomatic of diffusion, does not yield a consistent relationship with cooling rate and is a less useful parameter for quantifying a thermal history.

Fig. 3. Center retention Partial retention zone (CR-PRZ). Modeled Zr concentrations for the center of a rutile grain plotted as a function of isothermal holding temperature. Model runs assume an initially rapid cooling rate (>10^3 °C/Ma) followed by isothermal holding at variable temperatures for a duration of 2000 My. All runs use a maximum E_a of 200 kJ/mol. Center retention is maintained at isothermal holding temperatures less than 450-550 °C (depending on grain size). At temperatures > 600 °C diffusion is sufficient to permit loss of Zr associated with initial high temperatures, yielding Zr concentrations that record long-term residence temperatures. The CR-PRZ lies between these two regimes (450-600 °C), where rutile grains retain a portion of Zr derived from initial high temperature equilibrium, yet still yield concentrations far higher than what is predicted by experimental Zr calibrations for these temperatures (< 170 ppm). Zr measurements from grain centers for Montana xenoliths are plotted as a function of depth (assuming a geothermal gradient of 50 mW/m2). Center retention in each sample suggests each sample cooled quickly from initial temperatures (>10^3 °C/Ma) and resided at temperatures less than ~550 °C for the duration their history.

Figure 4. Cartoon illustrating the how volume diffusion manifest itself in intracrystal analyses. The lack of spatial control within a 3-D diffusion profile ensures that intracrystal analyses cannot directly constrain a Zr diffusion profile. Potential data that would result from (a) isotropic diffusion (b) *a*-*b* axis dominated diffusion and (c) *c*-axis dominated diffusion. If diffusion is isotropic or is faster along the *a*/*b* axis, the depth of sectioning into grains will affect the data produced from intracrystal analyses.

Fig. 5. Zirconium in rutile data for grain centers from Montana xenoliths. Each sample meets center retention, i.e. one or more core analyses match the independent constraints on sample temperature. (a) Over a narrow range of grain sizes, that differs for each sample, the concentration from a grain center can vary from the maximum values that correlate to (or exceed) the independent T estimate by 100-1000's ppm or (b) 1-160 % . (c) The correlation with this % difference and depth is interpreted to reflect an increase in diffusive loss of Zr with depth.

Fig. 6. Refining Zr and Pb rutile diffusion kinetics. The coupled Zr and Pb in rutiles systems requires that an acceptable time-temperature path to remain consistent with both systems. (a-c) Measured U-Pb data from Montana xenoliths can be bracketed by forward modeled U-Pb produced following (2011) by a t-T path with initially rapid cooling from high temperatures followed by slow cooling at rates of ~0.05-0.1 °C/Ma after a inflection temperature is meet. Note that forward modeled U-Pb data for a common cooling rate overlap despite different diffusion kinetics. Cooling rate dominates the position on concordia of modeled data, only the

temperatures at which Pb retention occurs change with each set of kinetics. To maintain Zr concentrations in the center of a 20-50 μm grain for each sample, requires long-term residence temperatures < 500-550 °C depending on the grain size (d). Using the nominal Pb diffusion kinetics for synthetic rutile experiments from Cherniak (2000) yields thermal histories with significant periods of time at temperatures above 500-550 ºC that permit diffusive loss of Zr at the grain center (d). Time-temperature paths using kinetics for Pb published for natural rutile perpendicular to the *c*-axis yields forward modeled data that match the U-Pb data and whose t-T paths permit center retention of Zr.

4.8 References

Anderson, S.D., Jamieson, R.A., Reynolds, P.H., Dunning, G.R., 2001. Devonian Extension in Northwestern Newfoundland: 40Ar/39Ar and U,ÄêPb Data from the Ming,Äôs Bight Area, Baie Verte Peninsula. The Journal of Geology 109, 191-211.
Baldwin, J., Bowring, S.A., Williams, M.L., Williams, I.S., 2004. Eclogites of the Snowbird tectonic zone: petrological and U-Pb geochronological evidence for Paleoproterozoic high-pressure metamorphism in the western Canadian Shield. Contributions to Mineralogy and Petrology 147, 528-548.
Baldwin, J.A., Brown, M., 2008. Age and duration of ultrahigh-temperature metamorphism in the Anápolis–Itauçu Complex, Southern Brasília Belt, central Brazil – constraints from U–Pb geochronology, mineral rare earth element chemistry and trace-element thermometry. Journal of Metamorphic Geology 26, 213-233.
Barnhart, K., 2011. Deep crustal xenoliths from the Great Falls Tectonic Zone, Montana: Investigating the timing and mechanisms of high-velocity lower crust formation, Department of Geological Sciences. University of Colorado Boulder, Boulder, p. 68.
Blackburn, T., Bowring, S., Schoene, B., Mahan, K., Dudas, F., 2011. U-Pb thermochronology: creating a temporal record of lithosphere thermal evolution. Contributions to Mineralogy and Petrology 162, 479-500.
Carslaw, H.S., Jaeger, J.C., 1959. Conduction of heat in solids. Clarendon Press, Oxford.
Cherniak, D.J., 2000. Pb diffusion in rutile. Contributions to Mineralogy and Petrology 139, 198-207.
Cherniak, D.J., Manchester, J.E., Watson, E., 2007. Zr and Hf diffusion in rutile. Earth and Planetary Science Letters 261, 267-279.
Corfu, F., Easton, R.M., 2001. U-Pb evidence for polymetamorphic history of Huronian rocks within the Grenville front tectonic zone east of Sudbury, Ontario, Canada. Chemical Geology 172, 149-171.
Corfu, F., Stone, D., 1998. The significance of titanite and apatite U-Pb ages: constraints for the post-magmatic thermal-hydrothermal evolution of a batholithic complex, Berens River area, northwestern Superior Province, Canada. Geochimica et Cosmochimica Acta 62, 2979-2995.
Dodson, M.H., 1973. Closure temperature in cooling geochronological and petrological systems. Contributions to Mineralogy and Petrology 40, 259-274.
Ferry, J., Watson, E., 2007. New thermodynamic models and revised calibrations for the Ti-in-zircon and Zr-in-rutile thermometers. Contributions to Mineralogy and Petrology 154, 429-437.
Flowers, R.M., Mahan, K.H., Bowring, S.A., Williams, M.L., Pringle, M.S., Hodges, K.V., 2006. Multistage exhumation and juxtaposition of lower continental crust in the western

Canadian Shield: Linking high-resolution U-Pb and 40Ar/39Ar thermochronometry with pressure-temperature-deformation paths. Tectonics 25, TC4003.
Hacker, B., Luffi, P., Lutkov, V., Minaev, V., Ratschbacher, L., Plank, T., Ducea, M., Pati√ëO-Douce, A., McWilliams, M., Metcalf, J.I.M., 2005. Near-Ultrahigh Pressure Processing of Continental Crust: Miocene Crustal Xenoliths from the Pamir. Journal of Petrology 46, 1661-1687.
Harley, S.L., 1998. On the occurrence and characterization of ultrahigh-temperature crustal metamorphism. Geological Society, London, Special Publications 138, 81-107.
Jaupart, C., Mareschal, J.C., 1999. The thermal structure and thickness of continental roots. Lithos 48, 93-114.
McKenzie, D., Jackson, J., Priestley, K., 2005. Thermal structure of oceanic and continental lithosphere. Earth and Planetary Science Letters 233, 337-349.
Meesters, A.G.C.A., Dunai, T., J., 2002. Solving the production-diffusion equation for finite diffusion domains of various shapes Part l. Implications for low-temperature (U-Th)/He thermochronology. Chemical Geology 186, 333-344.
Mezger, K., Hanson, G.N., Bohlen, S.R., 1989. High-precision U-Pb ages of metamorphic rutile: application to the cooling history of high-grade terranes. Earth and Planetary Science Letters 96, 106-118.
Miller, B.V., Dunning, G.R., Barr, S.M., Raeside, R.P., Jamieson, R.A., Reynolds, P.H., 1996. Magmatism and metamorphism in a Grenvillian fragment: U-Pb and 40Ar/39Ar ages from the Blair River Complex, northern Cape Breton Island, Nova Scotia, Canada. Geological Society of America Bulletin 108, 127-140.
Moller, A., Mezger, K., Schenk, V., 2000. U-Pb dating of metamorphic minerals: Pan-African metamorphism and prolonged slow cooling of high pressure granulites in Tanzania, East Africa. Precambrian research 104, 123-146.
Mueller, P., A., Heatherington, A., L., Kelly, D., M., Wooden, J., L., Mogk, D., W., 2002. Paleoproterozoic crust within the Great Falls tectonic zone: Implications for the assembly of southern Laurentia. Geology 30, 127-130.
O'Brien, P.J., Rötzler, J., 2003. High-pressure granulites: formation, recovery of peak conditions and implications for tectonics. Journal of Metamorphic Geology 21, 3-20.
Pollack, H.N., Chapman, D.S., 1977. On the regional variation of heat flow, geotherms, and lithospheric thickness. Tectonophysics 38, 279-296.
Schmitz, M.D., Bowring, S.A., 2003. Constraints on the thermal evolution of continental lithosphere from U-Pb accessory mineral thermochronometry of lower crustal xenoliths, southern Africa. Contributions to Mineralogy and Petrology 144, 592-618.
Schoene, B., Bowring, S.A., 2007. Determining accurate temperature-time paths from U-Pb thermochronology: An example from the Kaapvaal craton, southern Africa. Geochimica et Cosmochimica Acta 70, 165-185.
Spear, F., Wark, D., Cheney, J., Schumacher, J., Watson, E., 2006. Zr-in-rutile thermometry in blueschists from Sifnos, Greece. Contributions to Mineralogy and Petrology 152, 375-385.
Spera, F., 1980. Thermal Evolution of Plutons: A Parameterized Approach. Science 207, 299-301.
Tomkins, H.S., Powell, R., Ellis, D.J., 2007. The pressure dependence of the zirconium-in-rutile thermometer. Journal of Metamorphic Geology 25, 703-713.
Watson, E., Wark, D., Thomas, J., 2006. Crystallization thermometers for zircon and rutile. Contributions to Mineralogy and Petrology 151, 413-433.

Whittington, A.G., Hofmeister, A.M., Nabelek, P.I., 2009. Temperature-dependent thermal diffusivity of the Earth/'s crust and implications for magmatism. Nature 458, 319-321.
Zack, T., Luvizottow, G.L., 2006. Application of rutile thermometry to eclogites. Mineralogy and Petrology 88, 69-85.
Zack, T., Moraes, R., Kronz, A., 2004. Temperature dependence of Zr in rutile: empirical calibration of a rutile thermometer. Contributions to Mineralogy and Petrology 148, 471-488.

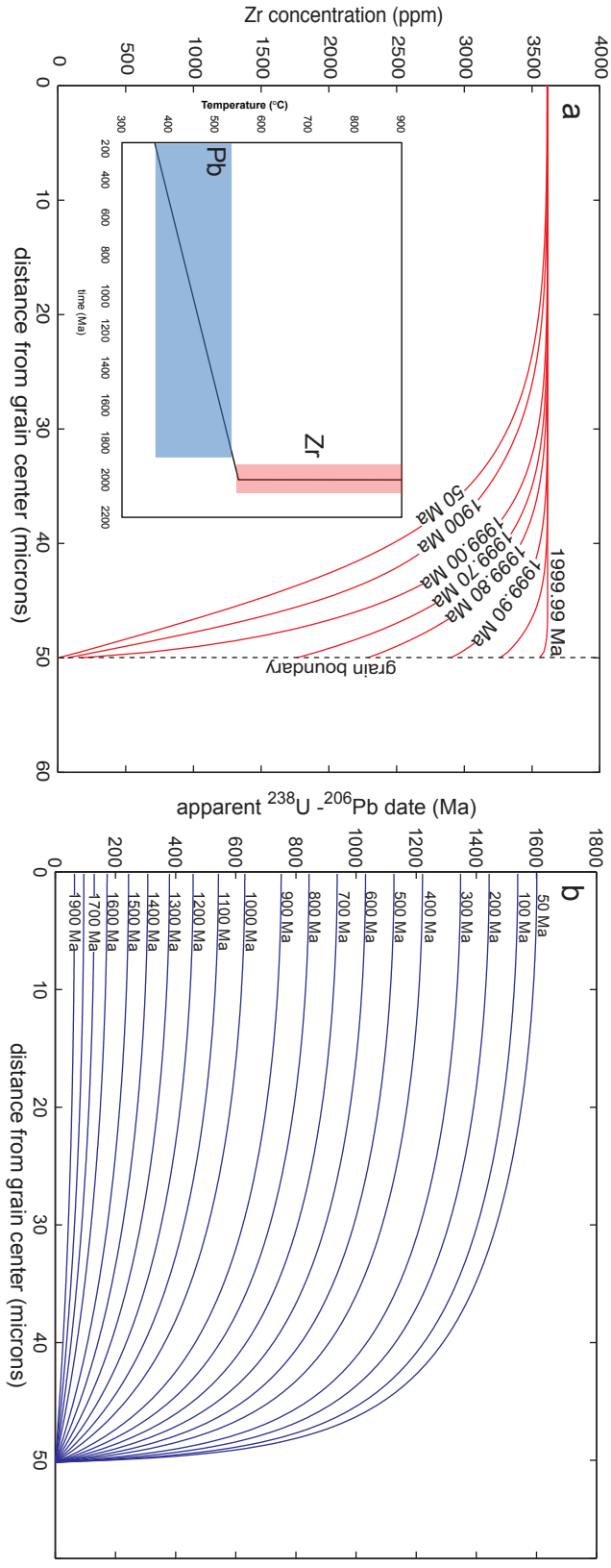
a
Zr concentration (ppm)
distance from grain center (microns)
grain boundary
1999.99 Ma
1999.90 Ma
1999.80 Ma
1999.70 Ma
1999.00 Ma
1900 Ma
50 Ma
Temperature (°C)
time (Ma)
Pb
Zr
b
apparent 238U -206Pb date (Ma)
distance from grain center (microns)
50 Ma
100 Ma
200 Ma
300 Ma
400 Ma
500 Ma
600 Ma
700 Ma
800 Ma
900 Ma
1000 Ma
1100 Ma
1200 Ma
1300 Ma
1400 Ma
1500 Ma
1600 Ma
1700 Ma
1900 Ma

Figure 4.1

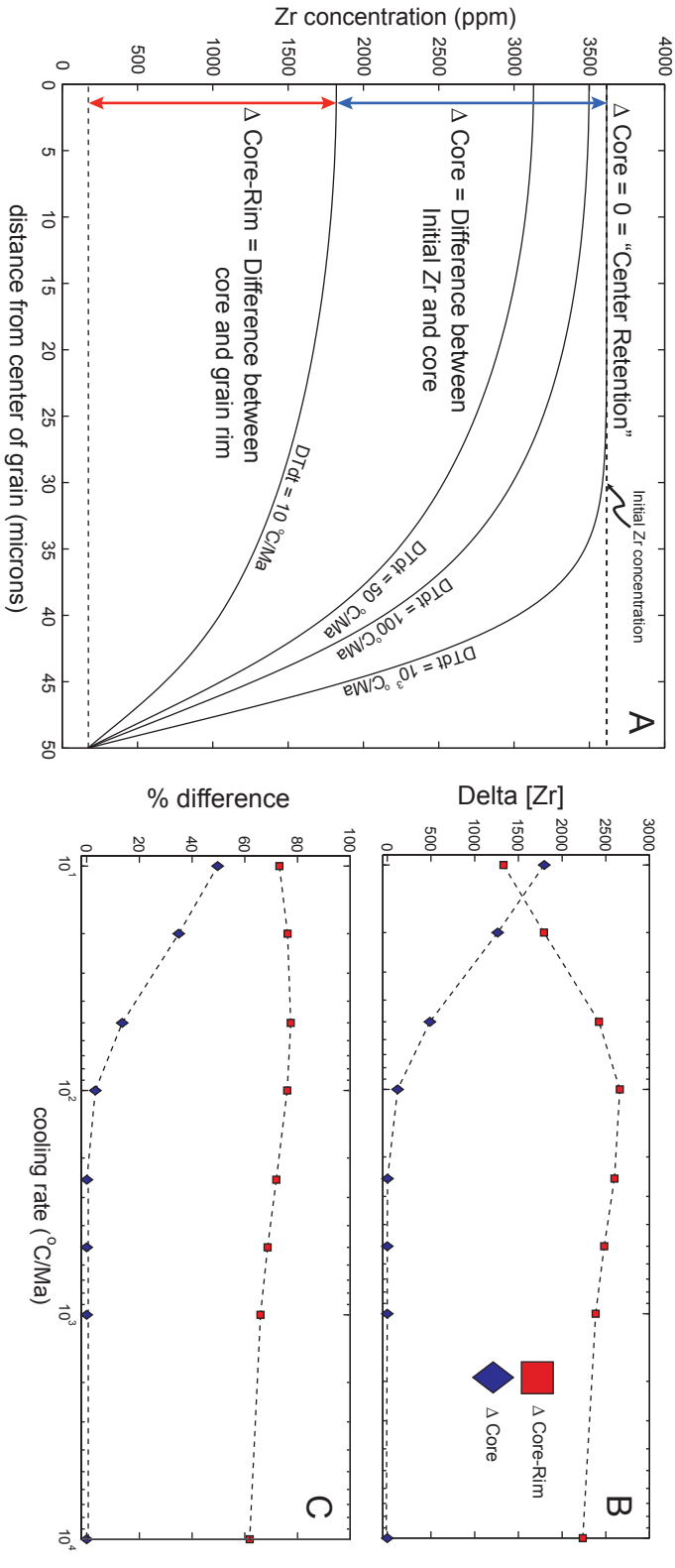
Zr concentration (ppm)
distance from center of grain (microns)
Δ Core = 0 = "Center Retention"
Initial Zr concentration
Δ Core = Difference between Initial Zr and core
Δ Core-Rim = Difference between core and grain rim
DTdt = 10 °C/Ma
DTdt = 50 °C/Ma
DTdt = 100 °C/Ma
DTdt = 10³ °C/Ma
A
Delta [Zr]
Δ Core
Δ Core-Rim
B
% difference
cooling rate (°C/Ma)
C

Figure 4.2

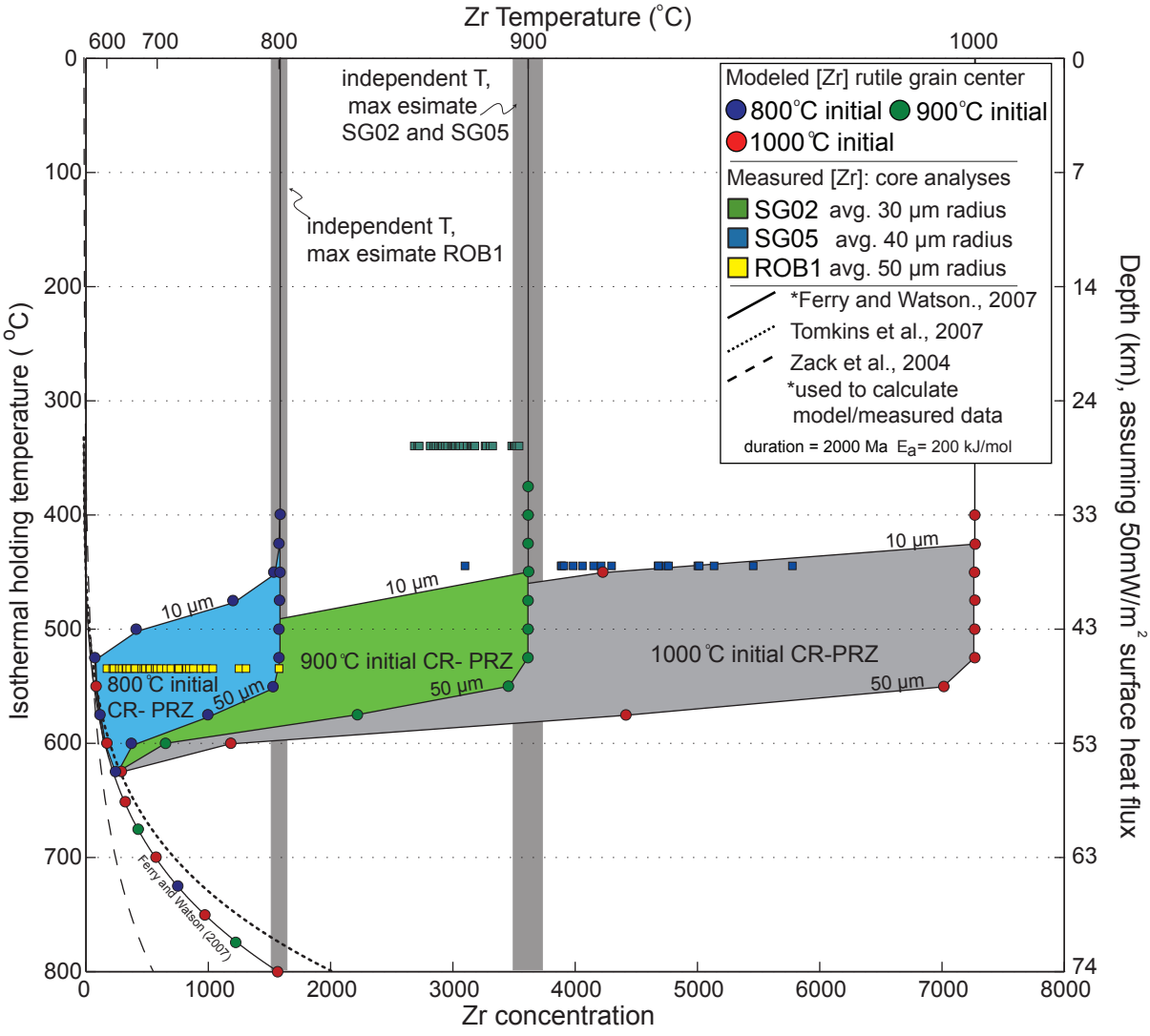
Zr Temperature (°C)
600
700
800
900
1000
independent T,
max esimate
SG02 and SG05
independent T,
max esimate ROB1
Modeled [Zr] rutile grain center
800°C initial
900°C initial
1000°C initial
Measured [Zr]: core analyses
SG02 avg. 30 µm radius
SG05 avg. 40 µm radius
ROB1 avg. 50 µm radius
*Ferry and Watson., 2007
Tomkins et al., 2007
Zack et al., 2004
*used to calculate
model/measured data
duration = 2000 Ma Ea= 200 kJ/mol
10 µm
10 µm
10 µm
800 °C initial
CR- PRZ
50 µm
900 °C initial CR- PRZ
50 µm
1000 °C initial CR-PRZ
50 µm
Ferry and Watson (2007)
Isothermal holding temperature (°C)
Depth (km), assuming 50mW/m2 surface heat flux
Zr concentration
0
100
200
300
400
500
600
700
800
0
1000
2000
3000
4000
5000
6000
7000
8000
7
14
24
33
43
53
63
74

Figure 4.3

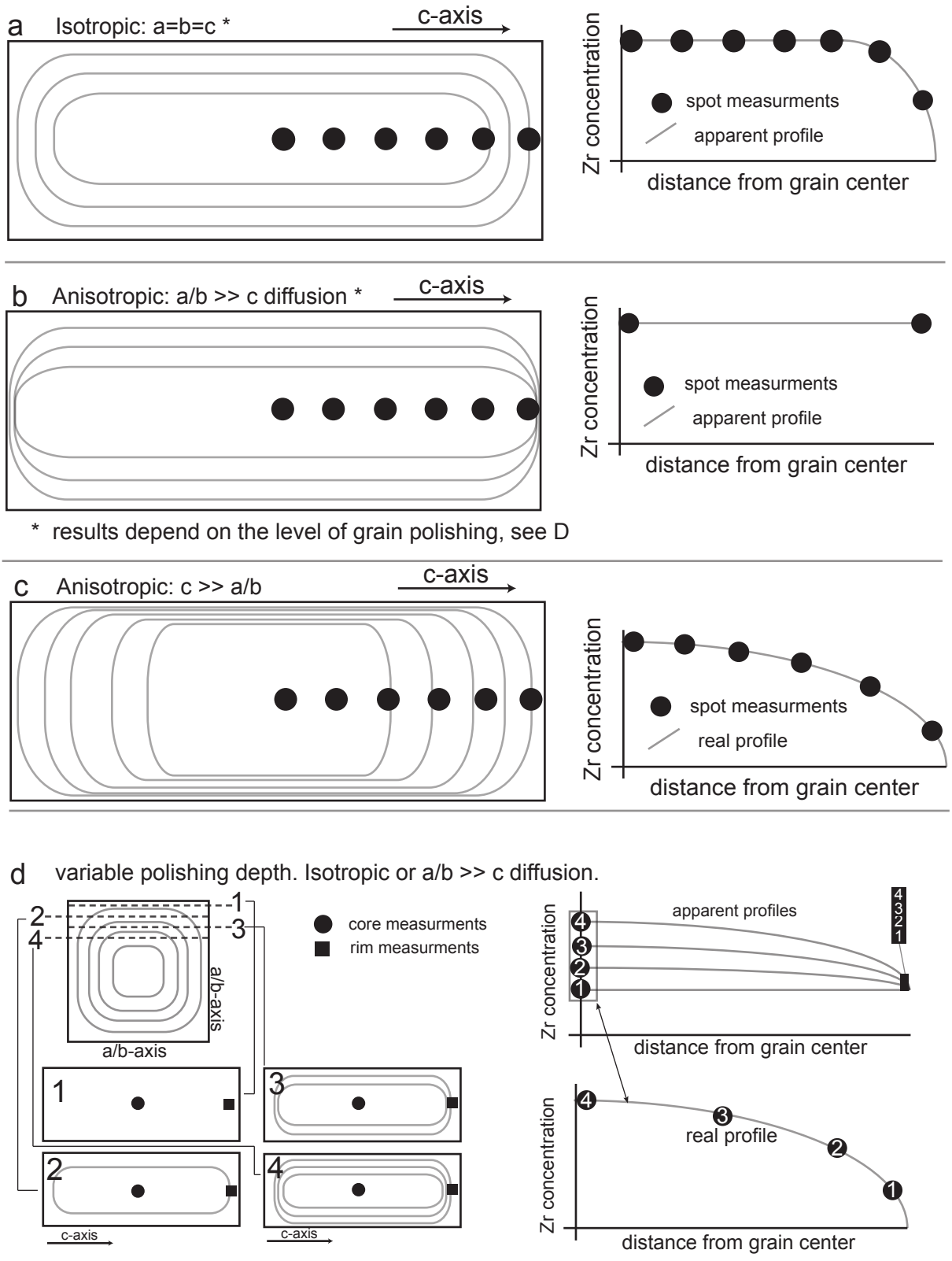
a Isotropic: a=b=c *
c-axis
Zr concentration
spot measurments
apparent profile
distance from grain center
b Anisotropic: a/b >> c diffusion *
c-axis
Zr concentration
spot measurments
apparent profile
distance from grain center
* results depend on the level of grain polishing, see D
c Anisotropic: c >> a/b
c-axis
Zr concentration
spot measurments
real profile
distance from grain center
d variable polishing depth. Isotropic or a/b >> c diffusion.
1
2
3
4
a/b-axis
a/b-axis
core measurments
rim measurments
1
2
3
4
c-axis
c-axis
apparent profiles
4
3
2
1
Zr concentration
distance from grain center
Zr concentration
real profile
distance from grain center

Figure 4.4

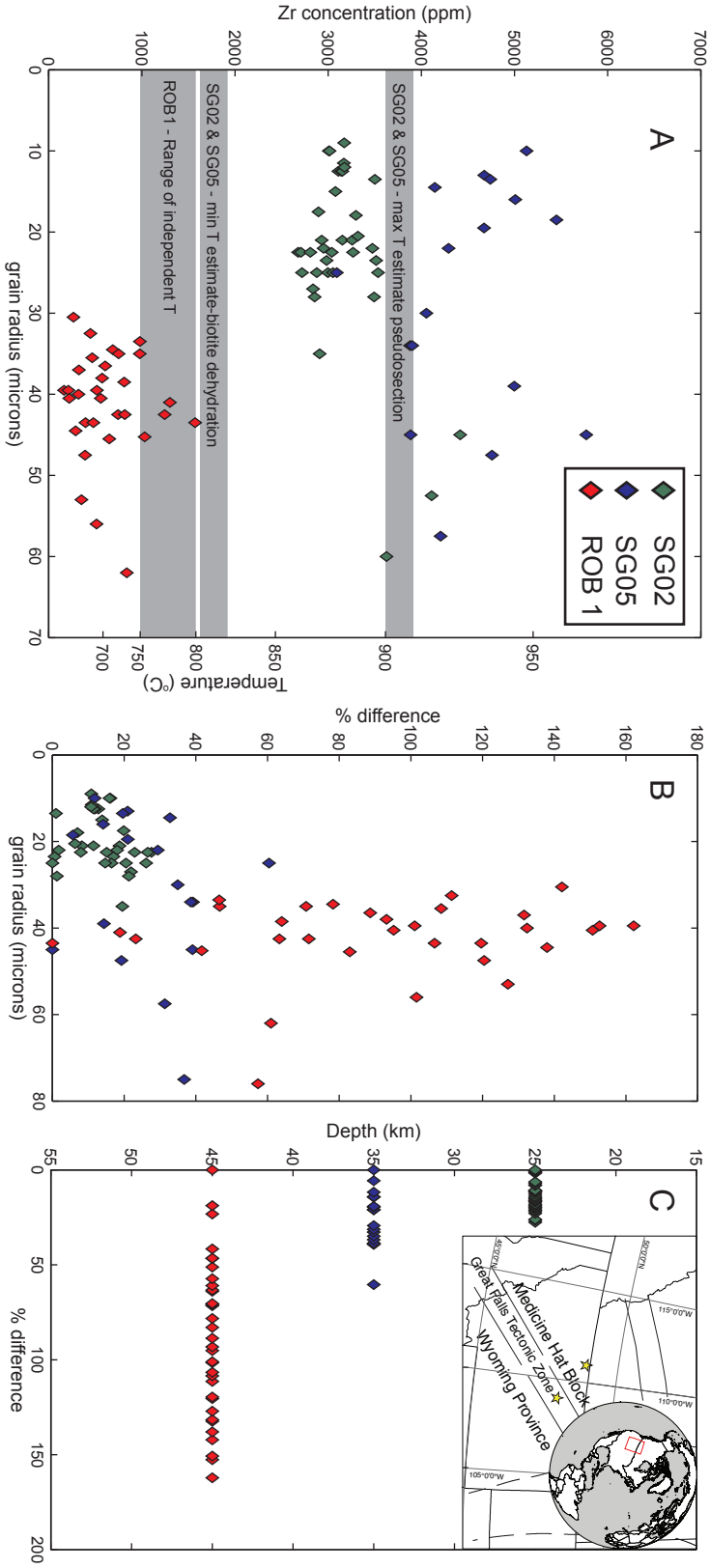
A
Zr concentration (ppm)
Temperature (°C)
grain radius (microns)
SG02
SG05
ROB 1
SG02 & SG05 - max T estimate pseudosection
SG02 & SG05 - min T estimate-biotite dehydration
ROB1 - Range of independent T
B
% difference
grain radius (microns)
C
Depth (km)
% difference
Medicine Hat Block
Great Falls Tectonic Zone
Wyoming Province

Figure 4.5

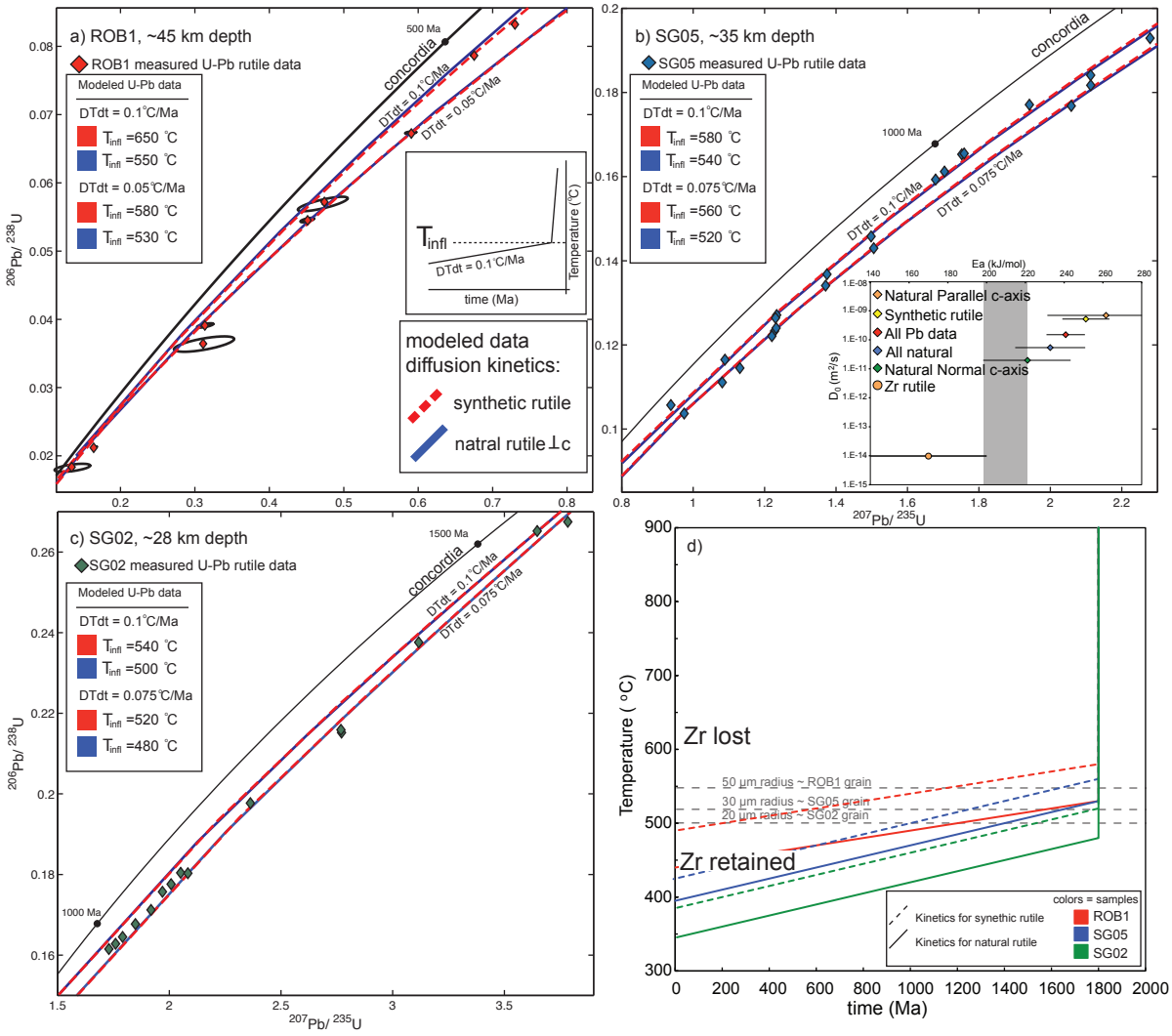
a) ROB1, ~45 km depth
ROB1 measured U-Pb rutile data
Modeled U-Pb data
DTdt = 0.1°C/Ma
Tinfl =650 °C
Tinfl =550 °C
DTdt = 0.05°C/Ma
Tinfl =580 °C
Tinfl =530 °C
500 Ma
concordia
DTdt = 0.1°C/Ma
DTdt = 0.05°C/Ma
Tinfl
DTdt = 0.1°C/Ma
time (Ma)
Temperature (°C)
modeled data
diffusion kinetics:
synthetic rutile
natral rutile ⊥c
206Pb/ 238U
b) SG05, ~35 km depth
SG05 measured U-Pb rutile data
Modeled U-Pb data
DTdt = 0.1°C/Ma
Tinfl =580 °C
Tinfl =540 °C
DTdt = 0.075°C/Ma
Tinfl =560 °C
Tinfl =520 °C
1000 Ma
concordia
DTdt = 0.1°C/Ma
DTdt = 0.075°C/Ma
Ea (kJ/mol)
Natural Parallel c-axis
Synthetic rutile
All Pb data
All natural
Natural Normal c-axis
Zr rutile
D0 (m2/s)
207Pb/ 235U
c) SG02, ~28 km depth
SG02 measured U-Pb rutile data
Modeled U-Pb data
DTdt = 0.1°C/Ma
Tinfl =540 °C
Tinfl =500 °C
DTdt = 0.075°C/Ma
Tinfl =520 °C
Tinfl =480 °C
1500 Ma
concordia
DTdt = 0.1°C/Ma
DTdt = 0.075°C/Ma
1000 Ma
206Pb/ 238U
207Pb/ 235U
d)
Zr lost
Zr retained
50 µm radius ~ ROB1 grain
30 µm radius ~ SG05 grain
20 µm radius ~ SG02 grain
Temperature (°C)
time (Ma)
colors = samples
Kinetics for synethic rutile
Kinetics for natural rutile
ROB1
SG05
SG02

Figure 4.6

Chapter 5: Sink to survive: The preservation of ancient mountain belts through crustal density changes

Abstract: Mountain belts form when collisions between continents thicken the Earth's crust, which buoyantly rises to remain in isostatic equilibrium with the underlying asthenosphere. Just as isostasy leads to the birth of mountains, it contributes to their destruction by uplifting them in response to erosion, maintaining high elevations and promoting further erosion, a process that could result in the destruction of the mountain belt. And yet the ancient roots of Earth's oldest mountains have persisted for billions of years, remaining far thicker than the mountain belt surficial relief. One previous explanation (Fischer, 2002) for this preservation proposes that the magnitude of isostatic rebound during mountain belt erosion decreases shortly after formation in response to an increased in crustal density that accompanies lithosphere cooling. The implications of this hypothesis are that the surficial erosion rate within a mountain belt is linked to the thermal and density evolution of the lithosphere. Here we test this hypothesis using a global survey of erosion rates in mountain belts with formation ages ranging from 0 to 2 billion years. We compare this data set with a model for the thermal, erosional, and density history of an idealized mountain belt. Measured and modeled data indicate that erosion is fastest in young, hot, low-density, and topographically high mountain belts, and that erosion rates decrease dramatically after several hundred million years, consistent with the timing of metamorphic garnet growth (Scherer et al., 2000; van Calsteren et al., 1986) and densification of the lower crust (Jull and Kelemen, 2001) that accompany lithospheric cooling (Blackburn et al., 2012; Schmitz and Bowring, 2003). Though erosion rates may vary within active mountain belts with different tectonic (Dadson et al., 2003) or climatic setting (Peizhen et al., 2001) settings it is isostasy coupled to the thermal and density evolution of the crust that dominantly controls the long-term erosional history of the lithosphere and ultimately leads to the preservation of Earth's ancient mountain roots.

5.1 Introduction

The elevation of Earth's surface, from the summits of the tallest mountains to the depths of the ocean's abyssal plains, is dominantly controlled by isostasy, the principle that the buoyant

lithosphere floats on the denser underlying asthenosphere at a height determined by the density and thickness of the lithosphere and the density of the asthenosphere (Fig. 1). The collision of continents at tectonic plate boundaries results in the mechanical thickening of continental crust and the formation of mountain belts or collisional "orogens". To compensate for this excess mass and maintain isostatic equilibrium, the lithosphere in this thickened region will buoyantly rise, producing the extreme relief and high elevations observed in the world's highest mountain ranges. Isostasy also controls the response within mountain belts to the erosion of their upper surfaces: as rocks are eroded from the top of a mountain belt and transported away, the lithosphere will buoyantly rebound. If the continental crust consisted of a single, constant density layer (Fig. 1b), the erosive removal of mass followed by isostatic rebound could continue until the crust was completely eroded, ending only when a state of neutral buoyancy between the remaining lithosphere and the underlying asthenosphere was attained. This simple scenario, however, is inconsistent with the observation that mountain belts have avoided complete destruction, maintaining crusts 30-50 km thick even after billions of years of erosion (Christensen and Mooney, 1995).

For mountain belts and continental crust to persist, erosion rates must attenuate more quickly than the uniform crustal density model would predict. A second, layered model with a dense lower crust underlying a light upper crust (Fig. 1b) would result in such attenuation. In this scenario, as the low-density cap erodes away, the mean crustal density increases, causing the crust to float lower, slowing erosion and working to preserve the crust. A third model1 proposes that ancient mountain belts can be preserved if the lower crust increases in density as the crust undergoes metamorphic phase changes that accompany lithosphere cooling (Fig 1). These three scenarios – constant, layered or temperature-dependent crustal density – predict distinct erosional histories that can be evaluated through comparisons with reconstructed erosional histories of decaying mountain belts. Here we present such a reconstruction using a global compilation of previously published apatite fission track (AFT) and cosmogenic ^{10}Be measurements of erosion rates in mountain belts ranging in formation age from ~2 billion years ago to the present and compare this data to predictions made from a model designed to simulate the thermal, density and erosional history of a decaying mountain belt (Fig 2a, Table S1). This approach assumes that the erosion rates observed within modern and ancient mountain belts are representative of the erosional decay of a single, idealized mountain belt.

5.2 Results

Concentrations of cosmogenic 10Be in minerals at the Earth's surface provide measures of erosion rates over relatively short timescales (103-105 years) (Portenga and Bierman, 2011). Longer timescale (10^6-10^8 years) erosion rates from AFT data are calculated here by assuming that the measured AFT date corresponds to the time at which the 120 ± 10 °C isotherm (Gleadow and Duddy, 1981) and corresponding closure depth (assuming a geothermal gradient of 25 ± 10 °C/km) were attained. Although the AFT derived erosion record may be complicated by additional factors (Methods), the agreement between the apparent erosion rates derived from AFT and 10Be derived erosion rates suggests that this simplified approach is suitable for resolving the drastically different erosion rates observed in modern and ancient orogens (Supplementary material, Fig. S1, S2). The compiled erosion rates plotted as a function of mountain belt formation age (Fig. 2a) define a trend in which young orogens erode rapidly, whereas orogens older than ~300 million years (Ma) erode at far slower rates.

We combine these erosion rate measurements with previously compiled seismic and surface relief data documenting the preservation of mountain roots (Fischer, 2002; French et al., 2009) (Fig. 2b). In a global survey of mountain belts, Fischer(Fischer, 2002) observed that the ratio (*R*) between mountain belt surface relief and root thickness decreases with orogen age. To explain the dramatic decrease in *R* early in an orogen's evolution (<300 Ma) and the coincident increase in crustal root density, Fischer (Fischer, 2002) proposed that lithospheric cooling and metamorphic phase changes(Jull and Kelemen, 2001) could increase the density of the lower crust, and thereby induce a waning isostatic response to ongoing erosion (Fig 2b, Table S2).

To evaluate which of the crustal density scenarios – constant, layered or temperature-dependent crustal density – will result in the erosional rate and R-values most consistent with the observed secular trends (Fig. 2), we've built a numerical model that describes the thermal, density and erosional history of a decaying mountain belt (Methods). Model tests were performed to find whether secular changes in erosion rate are consistent with an erosion law where erosion rate is proportional to elevation(Pinet and Souriau, 1988) or relief (Ahnert, 1970; Summerfield and Hulton, 1994); concluding that relief produced the model results most consistent with measured data (Fig. S3). Each model scenario will results in 2 erosional histories: 1) the true model erosion rate input into the model at each time step (Fig. 2a dashed lines) and 2) the apparent erosion rate generated by the interpretation of AFT data (Fig 2a, solid lines)

(Methods). The sensitivity of AFT data to heat loss through conduction will result in the overestimation of true erosion in the oldest orogens (Fig S2). Additional model-biases result from initial conditions, where rapid cooling through conduction and erosion results in the apparently high erosion rates at 0 Ma that far exceed the true erosion rate. Scenarios using a uniform, non-temperature dependent densities yield apparent erosion rates that underestimate the erosion rates observed in the oldest mountain belts. The simplest uniform density model is incapable of reproducing the secular changes in *R*-values, resulting in a decrease proportional to the model chosen erosion constant (Fig 2b). While a tiered, constant density model is capable of mimicking the erosional histories recorded by the measured data, yet cannot simultaneously match R-values of both moderate and oldest orogens (Fig. 2b). Each of these constant density models results in the over-thinning of continental crust and elevations near sea level. A model employing temperature-dependent density for the middle and lower crust yields erosion rates and *R*-values that are consistent with measured data (Fig 2). By increasing density, decreasing relief and along with it erosion, this scenario preserves more low-density upper crust than other scenarios, a result that produces long-term elevations consistent with those observed in stable continents (~500 m). Because the initial *R*-value for each model is controlled by the crustal thickness and density, no single model run can match every data point for present day orogens, which differ from one another in these quantities. For example, the Tibetan plateau and Alps have different crustal thicknesses and elevations and thus different *R*-values. The increase in lower crustal density makes the lithosphere sink lower in the asthenosphere, decreasing elevation, relief, and erosion rate, and permitting the preservation of low-density upper crust. Interestingly, the near neutral buoyancy and stability are attained rapidly, within ~ 300 million years (My) following orogenesis, suggesting that the slow present-day erosion rates(Wilkinson and McElroy, 2007) and minimal gravity anomalies(Shapiro et al., 1999) observed in Earth's most stable regions were attained relatively quickly following mountain belt formation.

Additional constraints on the timing of crustal density increase and the correlated change in mountain range erosion are provided by lower crust thermal histories and direct dating of garnet growth, both measured from volcanically exhumed fragments of the lower crust (xenoliths). High-temperature U-Pb thermochronologic analyses of xenoliths can be used to reconstruct the thermal history of the lower crust, including the time at which temperatures consistent with lower crustal densification (i.e., garnet growth) were attained. In the two available examples

(Blackburn et al., 2012; Schmitz and Bowring, 2003), titanite U-Pb data for lower crustal xenoliths record cooling to temperatures of ~650 ºC within 200-300 My after regional orogenesis, roughly the same time duration as the period of rapid erosion observed in the measured and modeled erosion histories (Fig. 2a). Additional support for this timeline is provided by dating of lower crustal garnet growth from the same orogens, where Sm-Nd and/or Lu-Hf garnet-whole rock isochron dates are consistent with garnet growth within 300-450 My following orogenesis (van Calsteren et al., 1986),(Scherer et al., 2000). Though there is some uncertainty as to whether these dates record the time of garnet growth and/or crustal cooling, the fact that the reported closure temperatures for these systems (~600-800 ºC (Dutch and Hand, 2009; Mezger et al., 1992; Scherer et al., 2000; Skora et al., 2008; Tirone et al., 2005; Van Orman et al., 2002)) are at least as high as temperatures of lower crustal garnet growth suggests that these systems applied to lower crustal depths provide a direct date for crustal densification.

Thus, geochronologic data at various timescales, from geologically recent erosion rates to ancient thermal histories recorded in lower crustal xenoliths, are consistent with an isostatic model that links the erosional decay of a collisional orogen to its thermal and density evolution. Given the geologic and climatic diversity of mountain ranges around the world, it is striking that their erosion rates are generally consistent with a single, relatively simple model. Regional geologic and geomorphologic studies have long recognized complexities in present day mountain belt erosion, having linked climate(Peizhen et al., 2001), tectonics(Dadson et al., 2003), topographic relief(Ahnert, 1970; Summerfield and Hulton, 1994) or elevation(Pinet and Souriau, 1988) to the erosion rate or spatial pattern within a specific young mountain belt or region. The assumed linear relationship between erosion rate and elevation may indirectly simulate how at high elevations, glacial erosion, precipitation, relief and slope could all contribute towards enhancing erosion in young mountain belts. Similar variability in erosion rates can occur among the Earth's most stable, ancient orogens. Even when laterally protected from destructive plate margins within the interiors of continental masses, ancient mountain belts are still susceptible to long-wavelength, low-amplitude uplift or burial driven by dynamic or far-field crustal loading(Braun, 2010). Despite the potential for such effects to influence erosion rates in young and old orogens, the secular trends in erosion rate presented here argue that the long-term erosional history of mountain belts is *dominantly* controlled by isostasy, which in turn is controlled by the thermal and density evolution of the lithosphere.

The scenario in which fast erosion rates only occur in young, hot, low-density orogens while older, colder, denser orogens erode for billions of years at extremely low rates provides an explanation for the preservation of Earth's oldest mountain belts, a pattern that has long puzzled geologists. The importance of this process is compounded by the fact that continental landmasses are constructed almost entirely through mountain building processes: like jigsaw puzzles with many pieces, continents are amalgamations of ancient mountain belts assembled over geologic time(Hoffman, 1988). Temperature-dependent densities play a global role in the long-term evolution of mountain belts and continents, influencing the preservation of all continental lithosphere throughout geologic time.

5.3 Methodology

Methods employed in this study include: 1) the treatment of measured apatite fission track data (AFT) for reconstructing erosional histories and 2) the thermal, density and isostatic model designed to simulate the erosional decay of a mountain belt. 1) The method employed here for calculating erosion rates using Apatite fission track data assumes both a constant geothermal gradient and 1-D geometry, neglecting the role that secular cooling through conduction and surface topography have in influencing measured AFT dates. Because both conductive heat transfer and surface topography will undoubtedly play a role in cooling the lithosphere, the rates presented here place a maximum estimate on the true erosion (Fig. S2). Model generated AFT data will also be biased the same way, assuming a constant geothermal gradient and a 1-D model geometry, permitting us to generate a modeled apparent erosion rate for comparison to measured data. The ancient mountain belts studied here include those that were laterally armored from subsequent thermal or tectonic events by surrounding terranes. 2) We constructed a forward model that describes the thermal, density and erosional history of a decaying mountain belt. The thermal evolution of the mountain belt is described by a numerical model quantifying heat transfer through conduction, advection and heat production(Blackburn et al., 2012). Initial model conditions include orogen (Beck et al., 1996; Gebrande et al., 2006; Hirn, 1988; Hirn et al., 1984) and lithosphere thicknesses, internal crustal layer thicknesses (Christensen and Mooney, 1995), crust and asthenosphere densities (Jull and Kelemen, 2001; Kelly et al., 2003), heat producing element concentrations (Rudnick et al., 2003; Rudnick et al., 1998), and an initial geothermal gradient (Supplementary material, Table S3). Mountain belt relief and elevation are

calculated assuming isostatic equilibrium relative to reference continental and oceanic crustal columns, respectively (Fig. 1). Surface erosion rates are assumed to be linearly proportional to elevation. For the proposed third mountain belt scenario (Fig 1b), modeled temperature and pressure dependent densities (Jull and Kelemen, 2001) for common middle and lower crust compositions are used to simulate the densification of the crust (Fig S4). As the lithosphere cools through conductive and advective heat loss, particularly as lower crustal (~1GPa) temperatures drop below ~800 °C, the model simulates garnet growth resulting in an increase in mean crustal density (Fig. S4). The thermal histories of rocks brought to the surface are used to generate synthetic AFT data, which in turn are used to calculate modeled erosion rates using the same methods applied to the measured AFT database (Fig 2a). The ratio (*R*) between mountain belt relief and root thickness through time is also calculated for comparison to measured data (Fig 2b).

5.4 Figure captions

Figure 1. Schematic illustration of density profiles for three mountain belt scenarios and reference continental and oceanic crust (inset). (**A**) Mountain belt relief (*h*) is the elevation difference between the mountain belt and reference continental crust. Root thickness (*m*) is the difference in depth of the base of the crust between the mountain belt and reference crust. (**B**) Close-up of crustal density structures for reference columns and mountain belt scenarios. Numbers are density values in kg/m^3. Isostasy calculations include full columns shown in upper inset. Modeled temperature- and pressure-dependent densities are used for middle to lower crust and mantle. Reference continental crust thickness and internal layer thickness are based on the idealized "shield and platform" model from Christensen and Mooney. The crustal thickness of Earth's youngest orogens ranges from 55 to 80 km and controls the relief and elevation attained. Oceanic and continental lithosphere densities are distinct.

Figure 2. Measured (points) and modeled (curves) mountain belt characteristics as a function of formation age in millions of years before the present (Ma). (**a**) Erosion rate (m/Ma) from apatite fission track data (diamonds, upper case labels) and cosmogenic ^{10}Be measurements (circles, lower case labels). (**b**) Ratio (*R*) of mountain belt relief to root thickness. Inset map shows locations of mountain belts. Abbreviations: EA, Eastern Alps; WA, Western Alps; TP, Tibetan Plateau; TS, Tian Shan; AN, Andean Plateau; BR, Brooks Range; LL, Lachlan orogen; AP, Appalachian Plateau; SA, Southern Appalachians; NU, Northern Urals; SU, Southern Urals; CN, Cantabrian Mountains; CR, Carpathian Mountains; GA, Grenville Orogen; SF, Svecofennian Orogen; TH, Trans-Hudson Orogen; PR, Pyrenees Mountains; VK, Verkhoyansk Mountains; AS, Alice Springs Orogen;IO, Isan Orogony; DO, Delamerian Orogen; VR, Variscan Orogen.

5.5 References:

Ahnert, F., 1970. Functional relationships between denudation, relief, and uplift in large, mid-latitude drainage basins. American Journal of Science 268, 243-263.
Beck, S.L., Zandt, G., Myers, S.C., Wallace, T.C., Silver, P.G., Drake, L., 1996. Crustal-thickness variations in the central Andes. Geology 24, 407-410.
Blackburn, T.J., Bowring, S.A., Perron, J.T., Mahan, K.H., Dudas, F.O., Barnhart, K.R., 2012. An Exhumation History of Continents over Billion-Year Time Scales. Science 335, 73-76.
Braun, J., 2010. The many surface expressions of mantle dynamics. Nature Geosci 3, 825-833.
Christensen, N.I., Mooney, W.D., 1995. Seismic velocity structure and composition of the continental crust: A global view. J. Geophys. Res. 100, 9761-9788.
Dadson, S.J., Hovius, N., Chen, H., Dade, W.B., Hsieh, M.-L., Willett, S.D., Hu, J.-C., Horng, M.-J., Chen, M.-C., Stark, C.P., Lague, D., Lin, J.-C., 2003. Links between erosion, runoff variability and seismicity in the Taiwan orogen. Nature 426, 648-651.
Dutch, R., Hand, M., 2009. Retention of Sm–Nd isotopic ages in garnets subjected to high-grade thermal reworking: implications for diffusion rates of major and rare earth elements and the Sm–Nd closure temperature in garnet. Contributions to Mineralogy and Petrology 159, 93-112.
Fischer, K.M., 2002. Waning buoyancy in the crustal roots of old mountains. Nature 417, 933-936.
French, S., Fischer, K., Syracuse, E., Wysession, M., 2009. Crustal structure beneath the Florida-to-Edmonton broadband seismometer array. Geophysical Research letters 36, L08309.
Gebrande, H., Castellarin, A., Luschen, E., Millahn, K., Neubauer, F., Nicolich, R., 2006. TRANSALP,A transect through a young collisional orogen: Introduction. Tectonophysics 414, 1-7.
Gleadow, A.J.W., Duddy, I.R., 1981. A natural long-term track annealing experiment for apatite. Nuclear Tracks 5, 169-174.
Hirn, A., 1988. Features of the Crust--Mantle Structure of Himalayas--Tibet: A Comparison with Seismic Traverses of Alpine, Pyrenean and Variscan Orogenic Belts. Philosophical Transactions of the Royal Society of London. Series A, Mathematical and Physical Sciences 326, 17-32.
Hirn, A., Lepine, J.-C., Jobert, G., Sapin, M., Wittlinger, G., Zhong Xin, X., En Yuan, G., Xiang Jing, W., Ji Wen, T., Shao Bai, X., Pandey, M.R., Tater, J.M., 1984. Crustal structure and variability of the Himalayan border of Tibet. Nature 307, 23-25.
Hoffman, P.F., 1988. United Plates of America, The Birth of a Craton: Early Proterozoic Assembly and Growth of Laurentia. Annual Review of Earth and Planetary Sciences 16, 543-603.
Jull, M., Kelemen, P.B., 2001. On the conditions for lower crustal convective instability. J. Geophys. Res. 106, 6423-6446.
Kelly, R.K., Kelemen, P.B., Jull, M., 2003. Buoyancy of the continental upper mantle. Geochem. Geophys. Geosyst. 4, 1017.
Mezger, K., Essene, E.J., Halliday, A.N., 1992. Closure temperatures of the Sm-Nd system in metamorphic garnets. Earth and Planetary Science Letters 113, 397-409.
Peizhen, Z., Molnar, P., Downs, W.R., 2001. Increased sedimentation rates and grain sizes 2-4 Myr ago due to the influence of climate change on erosion rates. Nature 410, 891-897.
Pinet, P., Souriau, M., 1988. Continental erosion and large-scale relief. Tectonics 7, 563-582.

Portenga, E.W., Bierman, P.R., 2011. Understanding Earth's eroding surface with 10Be. GSA Today 21, 4-10.
Rudnick, R.L., Gao, S., Heinrich, D.H., Karl, K.T., 2003. Composition of the Continental Crust, Treatise on Geochemistry. Pergamon, Oxford, pp. 1-64.
Rudnick, R.L., McDonough, W.F., O'Connell, R.J., 1998. Thermal structure, thickness and composition of continental lithosphere. Chemical Geology 145, 395-411.
Scherer, E.E., Cameron, K.L., Blichert-Toft, J., 2000. Lu-Hf garnet geochronology: closure temperature relative to the Sm,ÄìNd system and the effects of trace mineral inclusions. Geochimica et Cosmochimica Acta 64, 3413-3432.
Schmitz, M.D., Bowring, S.A., 2003. Constraints on the thermal evolution of continental lithosphere from U-Pb accessory mineral thermochronometry of lower crustal xenoliths, southern Africa. Contributions to Mineralogy and Petrology 144, 592-618.
Shapiro, S.S., Hager, B.H., Jordan, T.H., 1999. The continental tectosphere and Earth's long-wavelength gravity field. Developments in Geotectonics 24, 135-152.
Skora, #160, Susanne, Baumgartner, P., L., Mahlen, J., N., Lapen, J., T., Johnson, M., C., Bussy, Fran, #231, ois, 2008. Estimation of a maximum Lu diffusion rate in a natural eclogite garnet. Springer, Heidelberg, ALLEMAGNE.
Summerfield, M.A., Hulton, N.J., 1994. Natural controls of fluvial denudation rates in major world drainage basins. J. Geophys. Res. 99, 13871-13883.
Tirone, M., Ganguly, J., Dohmen, R., Langenhorst, F., Hervig, R., Becker, H.-W., 2005. Rare earth diffusion kinetics in garnet: Experimental studies and applications. Geochimica et Cosmochimica Acta 69, 2385-2398.
van Calsteren, P.W.C., Harris, N.B.W., Hawkesworth, C.J., Menzies, M.A., Rogers, N.W., 1986. Xenoliths from southern Africa: a perspective on the lower crust. Geological Society, London, Special Publications 24, 351-362.
Van Orman, J., Grove, T., Shimizu, N., Layne, G., 2002. Rare earth element diffusion in a natural pyrope single crystal at 2.8 GPa. Contributions to Mineralogy and Petrology 142, 416-424.
Wilkinson, B.H., McElroy, B.J., 2007. The impact of humans on continental erosion and sedimentation. Geological Society of America Bulletin 119, 140-156.

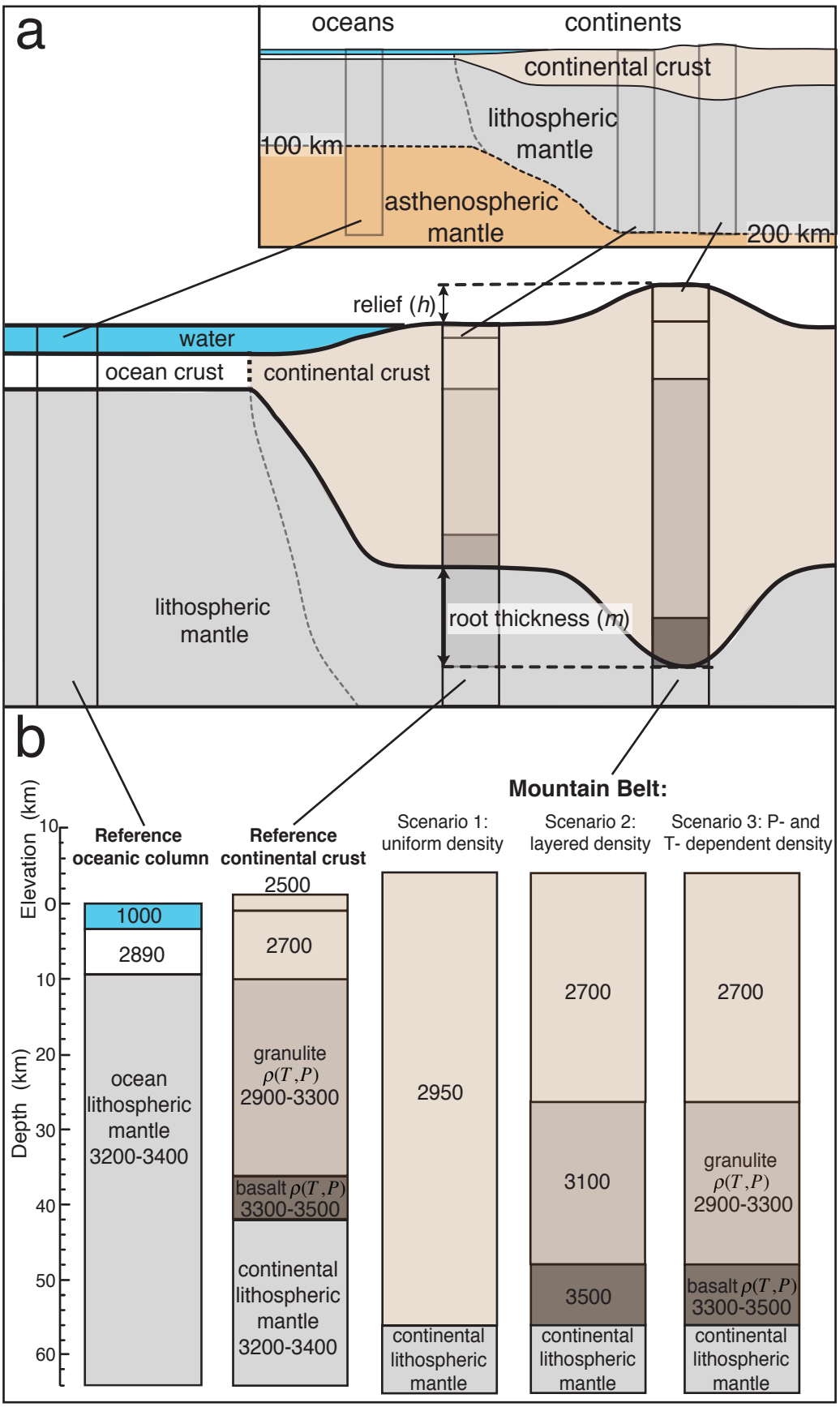
a
oceans
continents
continental crust
lithospheric mantle
100 km
asthenospheric mantle
200 km
relief (h)
water
ocean crust
continental crust
lithospheric mantle
root thickness (m)
b
Mountain Belt:
Elevation (km)
Depth (km)
Reference oceanic column
Reference continental crust
Scenario 1: uniform density
Scenario 2: layered density
Scenario 3: P- and T- dependent density
1000
2890
ocean lithospheric mantle 3200-3400
2500
2700
granulite ρ(T,P) 2900-3300
basalt ρ(T,P) 3300-3500
continental lithospheric mantle 3200-3400
2950
continental lithospheric mantle
2700
3100
3500
continental lithospheric mantle
2700
granulite ρ(T,P) 2900-3300
basalt ρ(T,P) 3300-3500
continental lithospheric mantle

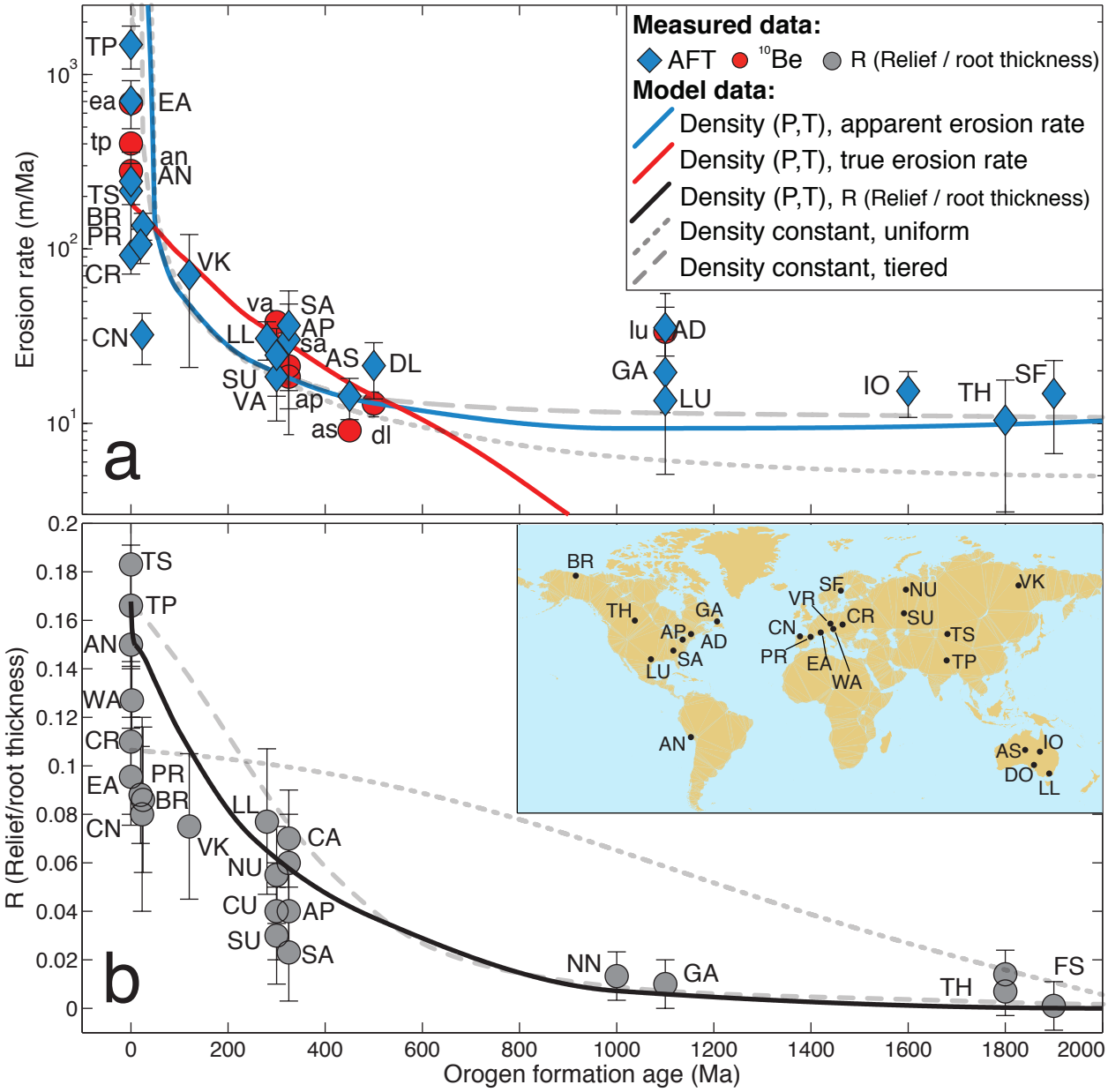
Measured data:
AFT
10Be
R (Relief / root thickness)
Model data:
Density (P,T), apparent erosion rate
Density (P,T), true erosion rate
Density (P,T), R (Relief / root thickness)
Density constant, uniform
Density constant, tiered
Erosion rate (m/Ma)
a
TP
ea
EA
tp
an
AN
TS
BR
PR
CR
VK
CN
va
SA
AP
LL
sa
AS
DL
SU
VA
ap
as
dl
lu
AD
GA
LU
IO
TH
SF
R (Relief/root thickness)
b
TS
TP
AN
WA
CR
EA
PR
BR
CN
VK
LL
CA
NU
CU
AP
SU
SA
NN
GA
TH
FS
Orogen formation age (Ma)
0
200
400
600
800
1000
1200
1400
1600
1800
2000
BR
TH
GA
AP
AD
SA
LU
AN
SF
VR
CR
CN
PR
EA
WA
NU
SU
TS
TP
VK
AS
IO
DO
LL

Figure 5.2

Chapter 6: High-precision U-Pb zircon geochronological constraints on the End-Triassic Mass Extinction and the late Triassic Astronomical Time Scale

Abstract: The apparent temporal coincidence of the end Triassic extinction event (ETE) and emplacement of the Central Atlantic Magmatic Province (CAMP) has often been used as evidence to suggest a causal relationship between the two major events. Here we present high precision geochronologic data for eight CAMP flows and sills from both the eastern U.S. and Morocco using zircon U-Pb ID-TIMS geochronology. These data are used to first, test the astronomical time scale for sediment accumulation within the Triassic-Jurassic rift basins along the eastern North America, and second, are combined with the stratigraphic and astronomical datum to constrain the onset and duration of the CAMP, while clarifying the relationship in time between the magmatic province and the ETE. Basalt flows, such as the North Mountain and Preakness basalts provide the best stratigraphic constraints with which to test astronomical calibrations, and the difference in weighted mean ^{238}U-^{206}Pb dates between these flows (285 ± 50 ky) overlaps within uncertainty with the duration of time predicted by astrochronology (250 ± 20 ky). Combining the astrochronologic and geochronologic datum for the Newark Basin places an absolute date on the ETE of 201.56 ± 0.024 Ma. Though CAMP lies stratigraphically above the ETE in eastern North America, the absolute time constraint on the ETE allows for any CAMP intrusion to be dated by geochronology and evaluated as potential trigger to the late Triassic extinction. We use this time-constraint to clarify the relationship between the ETE and the stratigarphically oldest known CAMP unit, the Tasquint Basalt in Morocco. A combination of geochronologic and stratigraphic data permits this CAMP unit to pre-date or erupt synchronously with the ETE.

6.1 Introduction

The Central Atlantic magmatic Province (CAMP) is a large igneous province (LIP) comprised mostly of basaltic thoeliites, gabbroic sills and dikes (Fig. 1). The eruption of CAMP comes late in the history of Triassic rifting within the Pangean supercontinent and based on stratigraphic and geochronologic constraints appears coincident in time with the end-Triassic extinction (ETE) event and the closely following Triassic-Jurassic boundary (TJB). The seeming coincidence of CAMP with the ETE and the apparent short duration of the CAMP has lead to the

hypothesis that flood basalt magmatism or associated intrusion caused or contributed to the extinction (Marzoli et al., 1999; Rampino and Stothers, 1988) plausibly via a methane- or CO_2-driven super-greenhouse (Marzoli et al., 1999; McElwain et al., 1999; Schaller et al.). However, both the tectonic setting and magmatic source of CAMP and its potential role in the cause of the ETE remain highly contentious. The geographic extent of the magmatism is significant, with CAMP related volcanics and intrusives spread along the Atlantic margins of North America, Africa, southwestern Europe, as well as the interior South America (Fig. 1) with an estimated volume of between 3 and 11 x 10^6 km^3 (Marzoli et al., 1999; McHone, 2003). Strata of the Triassic-Jurassic rift basins of the Eastern North America, the Newark Supergroup, are the best-preserved and studied terrestrial sections from this time period. The integration of paleomagnetic and astrochronological tuning has revealed a high-resolution record for the duration of large igneous province volcanism within these basins, estimated at 610 ky (Kent and Olsen, 1999; Olsen et al., 1996; Olsen and Kent, 1996; Olsen et al., 2003; Whiteside et al., 2007). This short duration combined with large volumes implies very high eruptive rates capable of causing rapid global fluctuations in the composition of the Earth's atmosphere and hydrosphere that could have led to the end-Triassic biotic crisis. However, significant ambiguity in evaluating the causal relationship between CAMP and the ETE an TJB exists because CAMP volcanism is preserved almost entirely in continental sedimentary sequences within Triassic-Jurassic rift basins located along the Central Atlantic margins, while the record of the invertebrate extinctions of the ETE, and the TJB, as defined by the first appearance of the Jurassic ammonite *Psiloceras spelae*, are preserved only in marine sedimentary sequences where CAMP is absent (Hillebrandt et al., 2007; Morton, 2008; Whiteside et al., 2007). Previous work linking these stratigraphic sections through paleomagnetic and paleontological data has remained contentious with several different models brought fourth for the relative timing of CAMP and the TJB in Eastern North America (Cirilli et al., 2009; Knight et al., 2004; Marzoli et al., 2004; Whiteside et al., 2007). Until recently, radioisotope geochronology has added very little to this debate, with most dates on the time period having associated uncertainties up to an order of magnitude larger than the total CAMP duration (610 ky constrained by astrochronology) largely because of the inherent difficulty in dating mafic basalt and gabbroic rocks.

Recent analyses of stable carbon isotopes from continental organic matter have provided a link between the carbon isotopic excursion originally observed with marine sequences and the

terrestrial sedimentary sequences containing CAMP (Whiteside et al., 2010). These new data confirm previous stratigraphic and palynological data suggesting the CAMP slightly post-dates the ETE in the eastern US (Olsen and Kent, 1996; Olsen et al., 2003; Whiteside et al., 2007), while still permitting the possibility that CAMP magmas in Morocco could be synchronous with the ETE (Fig. 2) (Deenen et al., 2010). High precision absolute dates for the CAMP magmas collected from the Argana basin, Morocco will provide a means to test the trans-Atlantic correlation between the Argana and Newark basins (Deenen et al., 2010). Combining this geochronologic data with stratigraphic, magnetostratigraphic and cyclostratigraphic data for the Argana basin will permit estimates to the absolute timing of the geochronologically undated lower basaltic unit in the Argana basin. This absolute time constraint on what has been suspected to be the stratigraphically oldest known CAMP magma can be used to test the hypothesis that it's eruption coincides with the palynological turnover and vertebrae extinctions recorded in the Newark terrestrial sections (Deenen et al., 2010).

Results of our U-Pb analyses of CAMP extrusives and intrusives accomplish two goals: first to test the astrochronological time scale developed within the eastern North American, Triassic-Jurassic rift basins and interbedded CAMP using U-Pb geochronology; second, to use these geochronologic and astronomical data to constrain the onset and duration of the CAMP and clarify the relationship in time between the magmatic province and the ETE.

6.2 Methods

Testing the temporal estimates on CAMP provided by astrochronology requires that at least two individual horizons within the sedimentary sequence be dated by radioisotope geochronology. The difference in time between the two horizons determined by geochronology and astrochronology can then be compared. The astrochronologic models yield estimates on the duration between the older two major CAMP lava formations in eastern North America of ~250 ky (Whiteside et al., 2007). A resolvable difference in radioisotopic dates for individual horizons requires analytical uncertainties an order of magnitude smaller than the time difference. Thus the goal is to produce a resolvable difference in geochronologic dates for each horizon of comparable precision. Though there are several accessory phases found in mafic rocks amenable to U-Pb dating (zircon, baddelyite, zirconolite, titanite), only zircon is capable of yielding the level of precision and accuracy required to test the duration of CAMP. Zircon ($ZrSi0_4$), a

refractory mineral, is not as common in mafic rocks as intermediate to felsic rocks. Despite this, primary zircon is found in coarse-grained mafic gabbroite, pegmatoidal or granophyric separations within both gabbroic sills and thick thoeliitic flows of CAMP. In the study presented here, 8 CAMP zircon-bearing bodies are dated using U-Pb methods.

Zircons were separated using standard rock crushing and mineral separation techniques. Single grain zircon analyses were dated using the Chemical Abrasion or CA-TIMS method (Mattinson, 2005). Zircon analyses were conducted using the isotopic tracer solution ET2535 containing ^{202}Pb, ^{205}Pb, ^{233}U and ^{235}U. Use of the ^{202}Pb-^{205}Pb tracer solution allows for accurate measure of Pb mass-dependent fractionation within the mass spectrometer during a Pb-analysis. The measured ^{233}U/^{235}U permits correction of uranium fractionation. The decreased uncertainty from using the ^{202}Pb-^{205}Pb tracer leads to a lower propagated uncertainty on an individual date with total uncertainties on mean error-weighted dates improved by up to 20 ky (0.01%) for the CAMP data presented here. All dates are calculated using an isotopic composition of uranium (^{238}U/^{235}U) of 137.818 (Hiess et al., 2012). For the zircon U-Pb CAMP data, the variation in uranium isotopic composition (^{238}U/^{235}U) required to change a ^{238}U-^{206}Pb date by just 1 ky, are on the order of +0.05/-0.13. This range in uranium isotopic compositions is outside the observed range for uranium in zircons (Hiess et al., 2012). Uranium was analyzed as an oxide, assuming and ^{16}O/^{18}O composition of 0.00205. Use of EARTHTIME tracer solutions allows a datum produced by this study to be compared to data from other labs using EARTHTIME tracers without propagating the ca 0.1% uncertainty derived from tracer calibration. All U-Pb data were reduced using *Tripoli* and *U-Pb redux* software (Bowring et al.; McLean et al.).

6.3 Samples

Basalts and gabbroic portions of sills from the CAMP were sampled in eastern North America from North Carolina to Nova Scotia and within the Argana basin, Morocco. Sample collection focused on identifying coarse-grained layers or segregations within basalts and gabbros. Zirconium is a refractory element and will remain within the crystallizing melts. As these large intrusive and extrusive bodies undergo fractional crystallization, the remaining residual liquid is physically isolated into layers or lenses within the magmatic body through either the compaction of crystals or buoyancy driven separation (Philpotts et al., 1996; Puffer and Horter, 1993; Puffer et al., 2009). This physical concentration of the remaining liquid in turn

concentrates the refractory elements, including zirconium, allowing igneous zircons to crystallize from the once wholly mafic magma. The zircons that crystallize from these coarse grain segregations are morphologically distinct from typical upper crustal zircons. Typical characteristics for zircons from this study include: a blocky aspect ratio, often un-terminated crystals, a weak metamict discoloration and occasionally melt or baddelyite inclusions oriented parallel with the c-axis (Fig. 3).

The 8 CAMP bodies sampled for autochthonous zircons are from gabbroids from intrusions and flows that are from north to south: 1) the East Ferry Member of the North Mountain Basalt (flow) of the Fundy basin, Nova Scotia; 2) the Palisade sill (intrusive) of the Newark basin, New Jersey; 3) the "second flow" (following Tollo and Gottfried, (1992)) of the Preakness Basalt of the Newark basin in New Jersey; 4) the Rossville Diabase, Rossville Pennsylvania; 5) the York Haven Diabase, York Haven, Pennsylvania; 6) the Rapidan sheet (intrusive) of the Culpepper Basin in Virginia; 7) the Butner olvine diabase sheet (intrusive) of the Deep River basin, North Carolina; and 8) the Alemena sill found to feed the Alemizi basalt (i.e. the upper Argana Basalt), Argana Basin, Morocco (Fig. 1).

The two basalt flows, the Preakness basalt and the previously dated North Mountain basalt and the intrusive Palisade sill, via its feeder relationship with the Orange Mountain Basalt of the Newark basin, provide stratigraphic constraints that can be used to test the astrochronological time-scale (Fig. 2). Samples from the North Mountain basalt, include material the granophyric layer within the basal East Ferry member of the flow, the very same unit at the same locality previously dated by Schoene and others (2006; 2010) as well as a second sample of North Mountain basalt from core AV-C- 2 from about 50 km west, southwest on Brier Island, Nova Scotia.

The North Mountain Basalt, constitutes the basal eruption of CAMP within the Fundy basin and is correlative with the Orange Mountain basalt at the base of the Newark basin CAMP sequence (Olsen et al., 2003)based on major and trace element geochemistry (Puffer, 1994; Deenen et al., 2010). The Preakness Basalt is the second basalt flow formation in the Newark sedimentary sequence. The difference in stratigraphic placement between the Preakness basalt and the onset of CAMP magmatism marked by the North and Orange Mountain basalts allows us to test the previously established astrochronological time constraints placed on the sedimentary sequence between these flows (Olsen and Kent, 1996; Olsen et al., 2003; Whiteside et al., 2007).

Below we will examine the evidence permitting the correlation between the Fundy and Newark basins and the basal Orange and North Mountain basalts. Geochronologic data from the remaining CAMP sills and gabbroites are used to explore the potential range of dates for the CAMP magmatic event.

Outside the eastern US, samples were collected from the coarse grain gabbroic Alemena sill, found to feed the upper Argana basalt, Argana basin, Morocco. Both the dated sill and the upper Argana basalt (Alemizi fm) flow are identical in composition and have previously been correlated based on basalt composition to the lower basalts in the Fundy (North Mountain) and Newark (Orange Mountain) basins (Deenen et al., 2010)(Fig. 2). The sill cross cuts the stratigraphically lower Argana basalt (Tasguint fm) as well as the lacustrine sediments intercalated between upper and lower Argana basalts (Fig 2). The sill does not reach the younger sediments deposited on top of the upper Argana basalt, placing a maximum depositional age for the sill. Carbon isotopic data for Triassic sediments in the Argana basin morocco reveal a negative carbon isotopic excursion at the base of this lower most basalt, which has previously been interpreted to mark the ETE (Deenen et al., 2010). It remains possible however, that the carbon isotopic data is altered during the emplacement of the overlying basalt (Whiteside et al., 2010). Cylostratigraphic models for the Newark and Argana basins, place the compositionally "intermediate" basalts ~40 ky above the top of the magnetic reversal E23r (Deenen et al., 2010; Olsen et al., 2002a; Olsen et al., 2002b). High precision zircon U-Pb dates permit testing of the magnetostratgraphic and basalt chemistry correlation between the Newark and Argana basins (Deenen et al., 2010). Further, the absolute time constraint provided by the geochronology presented here combined with the astrochronologic time-scale for the Argana basin (Deenen et al., 2010), will clarifying this relationship between the stratigaphically oldest known CAMP basalts (lower Argana basalt) and its emplacement relative to the ETE (Fig. 2).

There have been several previous geochronologic studies of CAMP, using both $^{40}Ar/^{39}Ar$ and U-Pb techniques and applied to samples from a significant geographic distribution. The great majority of work has applied $^{40}Ar/^{39}Ar$ dating of groundmass plagioclase separates from CAMP basalts and sills. Calculated plateau, mini-plateau and isochron dates are typically cited with analytical uncertainties on the order of ~1-2 My. Analyses of ground mass plagioclase are often susceptible to Ar-recoil (Jourdan et al., 2007) or excess Ar (Kelley, 2002; Seidemann, 1988), however, the low parent to daughter ratio is likely the key contributor to the high uncertainty

reported on measured dates. A comparison between CAMP $^{40}Ar/^{39}Ar$ and U-Pb data from Eastern North America inevitably reveals a 1-1.5% age bias, linked to the uncertainties on the age of neutron flux monitoring standards and the decay constants for ^{40}K (Renne et al., 2010). Two new methods for the independent re-determination of the Fish Canyon Tuff (FCT) standard date (Kuiper et al., 2008; Renne et al., 2010) and ^{40}K decay constants (Min et al., 2000; Renne et al., 2010) allow for recalculated CAMP $^{40}Ar/^{39}Ar$ data sets to be compared with U-Pb data. Though each of these revised decay constant and FCT values yield dates that are no longer systematically biased 1-1.5% younger than U-Pb dates, the level of uncertainty on each individual date is still over 1 Ma larger than the analytical uncertainty associated with a single grain U-Pb zircon date and over a full order of magnitude larger than the error-weighted mean date of the U-Pb zircon data (Fig. 4). Evaluating the accuracy of astrochronological constraints on CAMP requires precision on individual dates less than the total duration of CAMP. For these reasons we will restrict our study to utilizing higher precision U-Pb data.

Previous U-Pb geochronologic data form CAMP include a study by Dunning and Hodych (1990), where zircon and baddelyite U-Pb analyses produced a ^{238}U-^{206}Pb date for the Gettysburg and Palisades sill of 201±1 Ma (Fig. 4). Similar coarse grain material was sampled from the North Mountain Basalt in the Fundy Basin, Nova Scotia first by Hodych and Dunning (1992) and obtained an age of ^{238}U-^{206}Pb age of 202±1 Ma. The same unit was analyzed by Schoene et al. (2006), where air abraded zircons were dated using ID-TIMS yielding a non-thorium corrected ^{238}U-^{206}Pb age of 201.27±0.03 Ma. More recently Schoene and others (2010),published a new date for the North Mountain basalt, from zircons dated by CA-TIMS (Mattinson, 2005) 201.38± 0.02 Ma (Fig. 4). We present here, new North Mountain basalt zircon analyses reduced using a revised tracer calibration.

6.3.1 Feeder relationship between the Palisade sill and the Orange Mountain basalt

A discordant arm of the Palisade sill connects directly with basalt flows at the northeast terminus of the Newark basin in Ladentown, New York suggesting a feeder relationship (Ratcliffe, 1988) that allows the Palisade sill date to effectively date the Orange Mountain Basalt (Fig. 2). The detailed major and trace element chemistry of the flows is identical to the adjacent arm of the Palisade sill (Puffer et al., 2009). In addition, at least a portion of the intrusive Palisade intrudes the locally lowest flow at Ladentown. However, Ratcliffe (1988) argued that

while the Palisade sill did feed the Ladentown flows they did so after extrusion of the Orange Mountain Basalt. Ratcliffe's argument is based on the presence of basalt clasts below the Union Hill basalt in Suffern, New York and basalt clasts in metamorphosed conglomerate in contact with the Palisade sill close to the Ladentown flows. Because the Orange Mountain Basalt is the oldest known flow in the basin, these conglomerates must postdate it and thus both the local discordant arm of the sill and the Ladentown flows must postdate the Orange Mountain Basalt, providing a minimum age estimate on the flow, despite having identical chemistry.

6.3.2 Correlation between the Fundy and Newark basin basalts

The base of the CAMP in the Fundy and Newark basins, along with their basal CAMP flows, the North Mountain and Orange Mountain basalts respectively, have been temporally correlated using geochemical data, as well as paleomagnetic and palynological data from just below the basalts. The CAMP in eastern North America consists of 4 geochemically distinct tholiites based on major element chemistry: High Titanium Quartz Normative (HTQ), High Iron Quartz Normative (HFQ), Low Titanium Quartz Normalitive (LTQ) and High Iron High Titanium Quartz Normative (HFTQ) basalts (Puffer, 1992). Each of these compositions marks a distinct horizon, for example within the Newark basin, the Orange mountain basalt (HTQ) is chemically distinct from the stratigraphically higher Preakness basalt (HFQ/LTQ) and the even higher Hook Mountain basalt (HFTQ) (Fig. 2). The North Mountain basalt and Orange Mountain basalt are both High Titanium Quartz Normative Basalts (HTQ: Puffer, 1992) and share indistinguishable incompatible trace element patterns (Deenen et al., 2010; Puffer et al., 2009), suggesting a shared reservoir and potentially a shared eruption time for the two units.

Second, preserved within meters below each CAMP eruption within both the Newark and Fundy basins are key stratigraphic markers including: 1) the last occurrence of several Triassic sporomorph taxa, marking a major palynological turnover event marking the base of the ETE (Cirilli et al., 2009; Fowell and Traverse, 1995; Kent and Olsen, 1999; Olsen et al., 2002a; Olsen et al., 2002b; Whiteside et al., 2007), 2) the very short magnetic reversal E23r, and 3) several small iridium anomalies (280-300 ppt: (Olsen et al., 2002a; Tanner and Kyte, 2005; Tanner et al., 2008). Though the origin of the small iridium anomalies and their relationship to the ETE remain controversial, their presence in the same relative position relative to the basalt and the ETE in both the Fundy and Newark basins strongly suggests a temporal correlation (Fig 2).

Below both the palynological transition making the base of the ETE and the iridium markers lies the short magnetic reversal (E23r), first observed within the Newark basin (Kent and Olsen, 1999) and recently found within the Partridge island section of the Fundy basin, as well as in Morocco (Deenen et al., 2010). This magnetic reversal has been estimated by cyclostratigraphy to have a duration of <20 kyr (Olsen et al., 2003; Whiteside et al., 2007), providing a short term and thus high confidence correlation between the Fundy to Newark basin.

The significance of the ETE and its correlations to marine sequences has recently been demonstrated by correlation of terrestrial and marine carbon isotopic records (Whiteside et al., 2010). The presence of this transition beneath the North and Orange mountain basalts further strengthens a correlation between these two basal basalt units (Fig. 2).

6.4 Results

We report U-Pb zircon data for eight CAMP bodies, which are from oldest to youngest: the Amelal sill, the North Mountain Basalt, the Palisade sill, the York Haven Diabase, the Rapidan sheet in the Jet Mist quarry, the Preakness Basalt, the Rossville Diabase and the Butner olivine gabbroites. All reported dates are ^{238}U-^{206}Pb thorium-corrected mean error-weighted values. Testing the age sensitivity to this Th-correction is presented below in the following section. The date uncertainties reported within the text are analytical uncertainties alone. For the purpose of calculating a difference in time between two layers dated using the same tracer solution and same radiogenic system, only the analytical uncertainties need be propagated. Uncertainties that include tracer calibration and decay constant uncertainty are included in figure 1.

Starting with the sills and gabbroic bodies (Fig. 1), zircon analyses from a thick pegmatitic layer within the Palisade sill yield a mean date of 201.520±0.034 Ma . Zircon analyses from the Jet mist gabbroite in the Rapidan sheet gave a mean date of 201.501±0.032 Ma. Zircon U-Pb analyses from the he gabbroic sill feeding the upper Argana basalt within the Argana basin, Morocco, yield a mean date of 201.573±0.053 Ma. These oldest diabase intrusions are all compositionally similar (HTQ) and similar in chemistry to the North and Orange Mountain basalts. The emplacement of the Rossville diabase, a compositionally distinct HFQ intrusion can be placed to 201.279±0.044 Ma. The youngest date comes from the intrusive Butner olivine normative gabbroite at 200.932±0.076 Ma, a result that challenges previous

petrologic models (Ragland et al., 1992), but is consistent with trace element geochemistry (Deenen et al., 2010).

Several samples from the basaltic flows (Fig 1) of the North Mountain and Preakness basalt were dated. Over ten single grain analyses from North Mountain Basalt, sample NMB0301, were dated yielding an age of 201.575±0.033 Ma. Sample AV-C-1-2 from Brier Island contained small, metamict zircon grains yielding lower precision analyses. This secondary sample from the North Mountain basalt was dated to 201.527±0.058 Ma and is with uncertainty of sample NMB03-01 suggesting a uniform emplacement time for this CAMP unit. The Preakness Basalt was dated comparable precision as North Mountain Basalt, yielding a statistically distinguishable date of 201.282±0.031 Ma. This relatively younger CAMP intrusion age agrees within uncertainty to the Rossville Diabase dike, an HFQ sill which shares the sample geochemical signature as the Preakness basalt (Smith et al., 1975). The difference in time between the North Mountain Basalt and Preakness basalt is 285±50 kyr and the Palisades sill and the Preakness basalt is 240±60 kyr (Fig 1). Both values are within uncertainty of the astrochronologic estimate (250±20ky) on the duration of deposition of intercalated sediments between these two stratigraphic markers (assuming the feeder relationship between the Orange mountain and Preakness basalt).

6.4.1 ^{238}U-^{206}Pb age correction for initial ^{230}Th disequilibrium

The U-Pb dates reported here are the Thorium-corrected, mean error-weighted ^{238}U-^{206}Pb date. The Thorium correction, accounts for the preferential exclusion of intermediate daughter product ^{230}Th from the zircon crystal and the eventual deficiency in ^{206}Pb radiogenic daughter. The zircon Th/U value is calculated from the measured $^{208}Pb/^{206}Pb$ ratio further assuming concordance between the ^{232}Th-^{208}Pb and the ^{238}U-^{206}Pb systems. The distribution coefficients for Th and U of zircon within magma are calculated from using this known Th/U withint he zircon and an assumed or estimated magma Th/U. Key to an accurate correction for the exclusion of intermediate daughter products is a reliable estimate for the Th/U ratio of the magma from which the zircon crystallized. A compilation of Th/U measurements from CAMP rocks worldwide yields an average Th/U of 4.2 ± 0.7 (1σ) (Bertrand et al., 1982; Cebria et al., 2003; Heier and Rogers, 1963). This average for CAMP rocks is supported by the median value of 3.7 from over 15,000 Th/U measurements from basalts, diabases and tholites compiled in the Earthchem

database (Fig. 5 inset). The physical and chemical processes required to concentrate refractory elements leading to the crystallization of zircon suggest that a whole rock measurement of Th/U is unlikely to represent the composition of melts from which the zircon crystallized. One can however, utilize this whole rock composition as a starting Th/U composition. This initial condition combined with petrologic descriptions (Kontak, 2008; Puffer and Horter, 1993; Puffer and Volkert, 2001) can be used to develop a crystallization sequence for CAMP magmas, which in turn can be used as an input into a model describing the Th/U evolution within a crystallizing magma. The mass balance equation capable of describing the Th/U ratio of an evolving magma is:

$$\frac{Th}{U}_{magma} = \frac{Th}{U}_{initial} \cdot \frac{F + D_{bulk}^{U} \cdot (1-F)}{F + D_{bulk}^{Th} \cdot (1-F)}, \qquad (1)$$

where F is the fraction of crystals in the magma, $Th/U_{initial}$ is the initial or whole rock measurement. The bulk partition coefficient (D_{bulk}) for either uranium or thorium given by:

$$D_{bulk}^{element_a} = D_{mineral_i}^{element_a} \cdot x_{mineral_i} + D_{mineral_j}^{element_a} \cdot x_{mineral_j}, \qquad (2)$$

where $D_{mineral}$ describes the partition coefficient for a specific mineral in a basaltic liquid and $x_{mineral}$ describes the fraction of that mineral within the rock. Experimentally and empirically determined partition coefficients for uranium and thorium of minerals quartz, plagioclase, pyroxene, ilmenite, magnetite and apatite are used to predict the potential fractionation of Th from U during the crystallization sequence of a CAMP magma (Table 2) (Adam and Green, 2006; Beattie, 1993; Benjamin et al., 1978; Bindeman and Davis, 2000; Dostal et al., 1983; Hauri et al., 1994; Klemme et al., 2002; LaTourrette and Burnett, 1992; Lemarchand et al., 1987; Luhr et al., 1984; Matsui et al., 1977; McKenzie and O'Nions, 1991; Onuma et al., 1968; Villemant et al., 1981; Wood and Trigila, 2001; Zack and Brumm, 1998). Modal abundances of these minerals reported for a variety of CAMP flows and sills are input for the fraction of a mineral ($x_{mineral}$) (Table 2) (Philpotts et al., 1996; Puffer and Volkert, 2001) (Fig. 5). In major phases plagioclase, pyroxene and Fe-Ti oxides, both uranium and thorium are highly

incompatible and do not fractionate until low remaining melt fractions (F<0.2). Pyroxene, feldspars and Fe-Ti however, constitute up to 70% or more of the coarse grain segregation sheets or granophyres (Philpotts et al., 1996), concentrating the remaining U and Th (unfractionated) within the interstitial mesostasis. This remaining interstitial magma or mesostasis crystallizes as fine grain pyroxene, feldspars, quartz, magnetite, apatite and glass (Kontak, 2008; Philpotts et al., 1996; Puffer and Horter, 1993; Puffer and Volkert, 2001). In these remaining trace phases thorium is either not fractionated (glass, magnetite, pyroxene) or preferentially incorporated into the solid over uranium (apatite), increasing the melt Th/U from which zircon can crystallize from (Fig 5). This permits the initial value to act as a *minimum* estimate to the Th/U from which a zircon will crystallize. A high Th/U magma composition is consistent with the observation that the Th/U values for CAMP zircons are some of the highest ever reported. The magnitude of the ^{238}U-^{206}Pb Th-correction is correlated with the difference in a zircon Th/U value from the whole rock value (Fig 6a). The large difference in Th/U between CAMP whole rock data (>4.2) and CAMP zircons (1.3-2.5) results in a correction that is insensitive to the value of the melt composition at Th/U values above ~3.5. The extreme fractional crystallization histories that permit the crystallization of zircon in these magmatic bodies are accompanied by a fractionation in Th/U that will only increase the initial whole rock value. The fact that whole rock Th/U values serve as a minimum value ensures that the magnitude of Th/U correction is nearly constant yielding the ^{238}U-^{206}Pb Thorium corrected age plateau observed in figure 6a. Tabulated data and data reported in figure 1 are calculated assuming a Th/U of 4.0.

6.5 Discussion

6.5.1 Estimating Zircon-magma residence times

The U-Pb system in zircons is chemically and physically robust chronometer that behaves as a closed system in nearly all cases (i.e. U and Pb are retained). The chronometer thus delivers a temporal record since zircon crystallization that is resistant to thermally activated diffusive loss of Pb even at the high temperatures found within magmatic bodies (Cherniak, 2010). As a result, the system is prone to recording the time spent within a magma chamber in addition to the time since magma ejection and/or cooling. We can evaluate the time-scales of magma chamber residence recorded by the U-Pb in zircon system by utilizing a thermal half-space model to simulate the cooling history of any CAMP magmatic body. Contrary to the suggestion by

Jourdan and others (2009) that zircons derived from CAMP bodies have experienced prolonged magma residence, zircons within the CAMP gabbros and basalts are the result of *in-situ* fractional crystallization, and not any pre-emplacement magmatic processes (i.e. zircon crystallization at depth). This assumption is supported by petrologic observations for the physical concentration of refractory elements within CAMP bodies (Puffer and Horter, 1993) as well as field observations for the physical separation of residual melts within these magmatic bodies (Philpotts et al., 1996; Puffer and Horter, 1993). This assumption allows the measured dimensions of the CAMP flows, sills and dikes to be input directly into a thermal model to estimate the time-scales of zircon residence. Results for thermal calculations consider both a sub-ariel flow and shallow depth dike (Fig. 6 a,b respectively). Model input parameters are chosen to deliver the longest potential residence times. These parameters include a maximum intrusive temperature of 1300 °C and a maximum flow or sill thickness as measured from the thickest dated bodies, the Preakness basalt flow (200 m) and Palisades sill (300 m). A country rock temperature of 200 °C is used for the intrusive body calculation, determined assuming at depth estimate of emplacement of 3-5 km and a higher rift-setting geothermal gradient of 40 °C/km. Calculations for cooling assume conduction alone, a simplification that will yield cooling time-scales longer than a more realistic model that considers advective heat transfer at the rock-air boundary as well as within the center of the magmatic bodies. This model further assumes instantaneous magma emplacement and that the time-scale of cooling begins once the magmatic addition within a flow has stopped. Though these model parameters may not accurately reflect the setting of emplacement, the over-estimation of each condition, however, yields a reliable maximum constraint on the time-scales of zircon residence. The time-temperature path from magmatic temperatures (1300 °C) to complete cooling (0 °C for flow, 200 °C for dike) does not need to be considered for our goal of estimating zircon residence. Instead we can examine the segment of the t-T path from magmatic temperatures to the minimum temperatures anticipated for crystallization of zircon(~900 and 600 °C (Valley et al., 2006)). Results from the thermal modeling indicate that cooling from the intrusive temperatures below the temperatures anticipated for zircon crystallization occurs within 100 years for a basalt flow and 2000 years within the sills. These results suggest that the magma residence time of zircons within the basaltic flows and dikes are insignificant and far below the resolution of the U-Pb data.

6.5.2 The timing of CAMP and the Late Triassic Extinction

The high-precision zircon U-Pb dates reveal statistically valid differences between the different CAMP magmatic bodies. The difference in time between the North Mountain Basalt or Palisades Sill and Preakness Basalts (285±50/240±60 kyr) and as constrained by geochronology are in agreement with the previously published constraints placed by cyclostratigraphy (250±20 kyr) (Olsen et al., 2003; Whiteside et al., 2007). This geochronologic test of previously published astrochronologic data corroborates the astronomical tuning model for the Newark Basin section. Further integration of these two geochronologic data sets can be used to clarify the relationship between CAMP and the ETE.

Recent stable carbon isotopic data from bulk organic carbon, wood, and n-alkanes allow for a means of comparison between the terrestrial and marine sections (Whiteside et al., 2010). The palynological base of the ETE is coincident with the base of the ^{13}C excursion in the Newark basin. This strongly suggests that the ETE and biotic crisis do predate the CAMP in Eastern North America and further implies that using that the geochronologic data presented in this study can be used to anchor the high fidelity cyclostratigraphic record to the absolute time scale. If the cyclostratigraphic constraints place the ETE within 14±30 kyr beneath the basal CAMP unit (Orange Mountain Basalt/Palisades Sill). Following the Meyers et al., (2011) a mean-error weighted date on the ETE can be calculated by combining the geochronologic data with the cyclostratigraphic measurements for the differences in time between the geochronologically constrained units and the ETE. Restricting the analysis to the cyclostratigraphically constrained Newark Basin, the differences in time between the ETE and Preakness basalt (Δt = 264±30 ky) and Orange Mountain/Palisades Sill (Δt = 14±30 ky) combined with the date for each unit yields an estimate for the ETE of 201.54 ± 0.031 Ma. Utilizing all the stratigraphically constrained units (NMB,PB,AM,PS) and assuming the stratigraphic correlation at the base of the HTQ units is reliable the ETE date is refined to 201.56 ± 0.024 Ma. This absolute time constraint on the timing of the ETE provides a tie-point on the absolute time-scale with which to compare any stratigraphically uncontrolled CAMP units with the boundary and evaluate a potential causal relationship.

Defining the ETE in absolute time on a <100 ky level (201.56 ± 0.024 Ma) provides an opportunity to test hypothesis that CAMP magmatism in Morocco either pre-date the ETE as suggested by Knight et al. (2004) or is synchronous with the ETE as suggested by Deenen et al.,

(2010). Knight and others (2004), correlated paleomagnetic reversals observed within the intermediate composition upper Argana basalts of Morocco, with E23r, placing the eruption of these basalts prior to the ETE by 20ky and supporting for a causal relationship between CAMP and the biotic crisis at the ETE. The geochronologic data presented here, however, permits a high confidence correlation between the upper Argana basalt, the Alemizi formation (Fig. 2), and the contemporaneous lower most units in eastern North America; placing all these units at least ~40 ky after E23r. This result refutes the hypothesis by Knight and others(2004) that these Alemizi formation predates the ETE by 20ky. Within the Argana basin, Deenan others have documented E23r within the sediments below the Tasguint formation (Fig. 2), pacing E23r below CAMP just as in North America. A recent attempt by Font and others (2011) to test and improve the paleomagnetic results with a high-fidelity study of the Argana section, could not reproduce the reversals reported by Knight and others, suggesting that all of CAMP lie in a single normal chron (E24n) and are thus remain consistent with the stratigraphy across the Atlantic.

An alternative model suggested by Deenan et al (2010) speculates that the ETE is coincident with the emplacement of the Tasguint formation, the lower Argana basalt. This model is supported by carbon isotopic data, which places the onset of isotopic excursion just below the basalt. It remains unclear, however, how or if the emplacement of the basalt could perturb the carbon isotopic system in the underlying sediments (Whiteside et al., 2010). Triassic spores, however, are found up to the base of the lower-most Argana basalt, leaving open the possibility that this Tasguint formation is correlative or pre-dates the ETE. A similar sediment thickness between the magnetic reversal E23r and the ~201.5 HTQ basalts suggests the time interval between E23r and the lower Argana basalt is the same as in North America (14 ± 30 ky) thus placing this lower-most eruption within uncertainty of the ETE (Fig. 2) (Deenen et al., 2010).

6.6 Conclusions

The previously reported cyclostratigraphic models for the Newark basin place the duration of CAMP in the eastern US at ~610 kyr (Whiteside et al., 2007). High precision zircon U-Pb on two horizons within these astronomically tuned sections provides an opportunity to test this estimate and the application of astrochronology. Zircons were recovered from 8 CAMP magmatic bodies including basalt flows, the Preakness and North Mountain Basalts as well as 6

sills or gabbroic bodies, including the Palisades sill, which is interpreted to have a feeder relationship with the stratigraphically placed Organge Mountain basalt. New U-Pb data from the Preakness and North Mountain basalts yields a difference in time of 285±50 kyr, while the difference in time between the Preakness and Palisades sill/Orange Mountain basalt is 240±60 kyr. These durations are consistent with the astrochronologic constraints on the cyclic sedimentary interval between these two flows of 250±20 kyr. The total range in U-Pb dates for the 8 dated CAMP bodies exceeds ~630 ky, a result placing the youngest and mostly southerly intrusion, the Butner quarry sill, just outside the cyclostratigraphic constraints (618 ky) for CAMP duration in the Newark basin. The *in situ* fractional crystallization that occurs to produce zircons within these mafic bodies allows us to employ a simple thermal model to place a maximum zircon residence times at the 100-1000 year timescale.

In the eastern US, carbon isotope and palynological data place the ETE boundary prior to the onset of CAMP volcanism, with cyclostratigraphic estimates on the intervening duration at ~20 ky (Olsen et al., 2003; Olsen et al., 2002b). Using the U-Pb data to anchor the astochronologic data to the absolute time scale places an estimate on the ETE between 201.5-201.6 Ma, an absolute time constrain on the TJB that can be used to evaluate other CAMP magmatic bodies as potential triggers to the extinction. Geochronologic dates for basalts collected from the Triassic Argana basin, Morocco, provide a high-confidence trans-Atlantic correlation between the Newark and Argana basins, that agrees with previous correlations relying on magnetostratgrahy and basalt chemistry (Deenen et al., 2010; Font et al., 2011). A combination of absolute dates on the Alemizi formation basalt in the Argana basin and both stratigraphic and astrochronologic data from the underlying sediments suggests the stratigraphically oldest CAMP magma, the Tasguint formation, erupted either before or coincidently with the end Triassic extinction event, permitting a causal relationship between CAMP and the late Triassic biotic crisis.

6.7 Figure Captions

Fig. 1 Map showing the distribution of the Central Atlantic Magmatic Province (CAMP) modified from. Zircon ^{238}U-^{206}Pb data for CAMP sills and gabbroic intrusives (a) and basalt flows (b). Horizontal bars represent the ^{238}U-^{206}Pb Th-corrected date for a single crystal zircon analyses at 2σ. The color of each bar indicates geochemical group, pattern indicates the volcanic body geometry. Lightly shaded analyses are outliers and excluded from mean calculations. Solid vertical line marks the mean error weighted date. The inner and outer vertical boxes surrounding

the mean display the uncertainty on this mean at 65% and 95% confidence intervals, respectively. All values dates calculated using a Th/U of 4.0. Numbers on map correlate to numbered data on right column. Mean Square Weighted Deviation (MSWD) provides a measure of data coherence, where a value above 1 indicates scatter beyond what can be anticipated by analytical uncertainties alone, while a value below one is consistent with scatter from analytical uncertainties alone.

Fig. 2 Schematic stratigraphic sections for the Newark, Fundy and Argana basins showing the astrochronological ages and U-Pb dates from the eastern US and Argana basins pinned to the Palisade sill date (PS), which is a feeder to the Orange Mountain Basalt, and hence also provides a date for the basalt. Astrochronologic estimates for the time interval between the Late Triassic extinction (ETE) and magnetic reversal E23r in the Newark basin, permits constraints to be placed on the placment of the ETE with respect to the stratigraphically oldest CAMP unit the Tasguint basalt (Argana basin). Astrochronology from Whiteside et al. (2007).

Fig. 3 Cathode Luminesence (CL) (A) and transmitted light (B) images of zircons from the Palisades sill (A) and Rapidan Sheet (B). CL images reveal a simple single stage crystallization history (i.e. no zircon cores, embayments or reabsorbtion). Transmitted light images highlight the characteristics of nearly all "basaltic zircons" dated in this study; block aspect ration, un-terminated, slightly metamict.

Fig. 4 Comparison between ^{40}Ar-^{39}Ar (previously published) and U-Pb zircon data (previously published and data presented here) for CAMP related basalt flows and intrusions from the Eastern US and Morocco. The ability to evaluate the cyclostratigraphic model for sediment accumulation in the Newark basin or to evaluate a potential causal relationship between the Late Triassic extinction event and CAMP requires geochronologic data with uncertainties smaller estimates for flood basalt duration (~620kyr). The large uncertainties associated with ^{40}Ar-^{39}Ar or SIMS U-Pb data forces us to rely on U-Pb zircon ID-TIMS data alone for evaluating the astrochronologic time-scale and clarifying the relationship between CAMP and the ETE.

Fig. 5 Model results for Th/U evolution of CAMP magma. Petrologic descriptions and modal abundances provide a probably crystallization sequence for CAMP magmas (Table 2). Combined with partition coefficients for thorium and uranium for each mineral (Table 2) the Th/U evolution of a typical CAMP magma can be estimated. Shown are magmas with average reported initial Th/U (4.0) and minimal reported values at 1σ (3.3). The Th/U evolution of a system always results in fractionation of Th/U to higher values. Horizontal dashed lines marked the modal estimates for % Mesostasis or quenched interstitial magma found in the North Mountain and Preakness Basalts. As zircon crystallization likely occurred before the mesostatis was quenched, the intersection of the modeled Th/U evolution curves and the % mesostatis lines places a maximum constrain on Th/U values. For this reason the average CAMP Th/U value of 4.0 provides a minimum estimate for the composition that zircons crystallized from. Inset shows a compilation of over 15,000 Th/U measurements from volcanic rocks defined by the Earthchem database to be "basalts", "diabase" or "tholeiite". The data sets modal value of 4 supports the use of this Th/U value to model CAMP U-Pb zircon data.

Fig. 6 (A) Model Th-corrected ^{238}U-^{206}Pb error-weighted mean dates for North Mountain (blue) and Preakness basalts (green) for a range of Th/U magma compositions. (B) Difference in time between stratigraphic markers North Mountain Basalt and Preakness basalt for the same range of Th/U compositions. Minimum estimate on the Th/U of CAMP magmas of 4.0 suggests a difference between the North Mountain and Preakness basalts near ~250 ky, that is insensitive to the likely range in the Th/U of the magmas (Fig. 7).

Fig. 7 Results of simple thermal conduction model for basaltic flows (a) and sills (b) intended to evaluate the potential time-scale of zircon residence. Petrologic and geochemical evidence suggests that zircon crystallized within the fractional crystallizing and cooling basalt. The tested model conditions are intended to place a maximum estimate on the cooling time-scales for a sub-aerially cooling (a) and shallow intrusion (b). The temperature range in which zircon is likely to crystallize us highlighted in blue.

Table 6.1 Tabulated zircon U-Pb data for CAMP basalt flows and intrusives dated by this study
Table 6.2 Summary of Modal abundances and distribution coefficients used to model the Th/U evolution of CAMP magmas.

6.8 References

Adam, J., Green, T., 2006. Trace element partitioning between mica- and amphibole-bearing garnet lherzolite and hydrous basanitic melt: 1. Experimental results and the investigation of controls on partitioning behaviour. Contributions to Mineralogy and Petrology 152, 1-17.

Beattie, P., 1993. The generation of uranium series disequilibria by partial melting of spinel peridotite: constraints from partitioning studies. Earth and Planetary Science Letters 117, 379-391.

Benjamin, T.M., Heuser, W.R., Burnett, D.S., 1978. Laboratory Studies of Actinide Partitioning Relevant to 244 PU Chronometry, in: Merrill, R.B. (Ed.), Proceedings of the Lunar and Planetary Science Conference. Pergamon, pp. 393-391,406.

Bertrand, H., Dostal, J., Dupuy, C., 1982. Geochemistry of early mesozoic tholeiites from Morocco. Earth and Planetary Science Letters 58, 225-239.

Bindeman, I.N., Davis, A.M., 2000. Trace element partitioning between plagioclase and melt: investigation of dopant influence on partition behavior. Geochimica et Cosmochimica Acta 64, 2863-2878.

Bowring, J.F., McLean, N.M., Bowring, S.A., Engineering cyber infrastructure for U-Pb geochronology: Tripoli and U-Pb_Redux. Geochem. Geophys. Geosyst. 12, Q0AA19.

Cebria, J.M., Lopez-Ruiz, J., Doblas, M., Martins, L.T., Munha, J., 2003. Geochemistry of the Early Jurassic Messejana,ÄìPlasencia dyke (Portugal,ÄìSpain); Implications on the Origin of the Central Atlantic Magmatic Province. Journal of Petrology 44, 547-568.

Cherniak, D.J., 2010. Diffusion in Accessory Minerals: Zircon, Titanite, Apatite, Monazite and Xenotime. Reviews in Mineralogy and Geochemistry 72, 827-869.

Cirilli, S., Marzoli, A., Tanner, L., Bertrand, H., Buratti, N., Jourdan, F., Bellieni, G., Kontak, D., Renne, P.R., 2009. Latest Triassic onset of the Central Atlantic Magmatic Province (CAMP) volcanism in the Fundy Basin (Nova Scotia): New stratigraphic constraints. Earth and Planetary Science Letters 286, 514-525.

Deenen, M.H.L., Ruhl, M., Bonis, N.R., Krijgsman, W., Kuerschner, W.M., Reitsma, M., van Bergen, M.J., 2010. A new chronology for the end-Triassic mass extinction. Earth and Planetary Science Letters 291, 113-125.
Dostal, J., Dupuy, C., Carron, J.P., Le Guen de Kerneizon, M., Maury, R.C., 1983. Partition coefficients of trace elements: Application to volcanic rocks of St. Vincent, West Indies. Geochimica et Cosmochimica Acta 47, 525-533.
Dunning, G.R., Hodych, J.P., 1990. U/Pb zircon and baddeleyite ages for the Palisades and Gettysburg sills of the northeastern United States: Implications for the age of the Triassic/Jurassic boundary. Geology 18, 795-798.
Font, E., Youbi, N., Fernandes, S., El Hachimi, H., Kratinov, Z., Hamim, Y., 2011. Revisiting the magnetostratigraphy of the Central Atlantic Magmatic Province (CAMP) in Morocco. Earth and Planetary Science Letters 309, 302-317.
Fowell, S.J., Traverse, A., 1995. Palynology and age of the upper Blomidon Formation, Fundy Basin, Nova Scotia. Review of Palaeobotany and Palynology 86, 211-233.
Hauri, E.H., Wagner, T.P., Grove, T.L., 1994. Experimental and natural partitioning of Th, U, Pb and other trace elements between garnet, clinopyroxene and basaltic melts. Chemical Geology 117, 149-166.
Heier, K.S., Rogers, J.J.W., 1963. Radiometric determination of thorium, uranium and potassium in basalts and in two magmatic differentiation series. Geochimica et Cosmochimica Acta 27, 137-154.
Hiess, J., Condon, D.J., McLean, N., Noble, S.R., 2012. 238U/235U Systematics in Terrestrial Uranium-Bearing Minerals. Science 335, 1610-1614.
Hillebrandt, A.v., Krystyn, L., K√°rschner, W.M., 2007. A candidate GSSP for the base of the Jurassic in the Northern Calcareous Alps (Kuhjoch section, Karwendel Mountains, Tyrol, Autria).
Hodych, J.P., Dunning, G.R., 1992. Did the Manicouagan impact trigger end-of-Triassic mass extinction? Geology 20, 51-54.
Jourdan, F., Marzoli, A., Bertrand, H., Cirilli, S., Tanner, L.H., Kontak, D.J., McHone, G., Renne, P.R., Bellieni, G., 2009. 40Ar/39Ar ages of CAMP in North America: Implications for the Triassic-Jurassic boundary and the 40K decay constant bias. Lithos 110, 167-180.
Jourdan, F., Matzel, J.P., Renne, P.R., 2007. 39Ar and 37Ar recoil loss during neutron irradiation of sanidine and plagioclase. Geochimica et Cosmochimica Acta 71, 2791-2808.
Kelley, S., 2002. Excess argon in K-Ar and Ar-Ar geochronology. Chemical Geology 188, 1-22.
Kent, D.V., Olsen, P.E., 1999. Astronomically tuned geomagnetic polarity timescale for the Late Triassic. J. Geophys. Res. 104, 12831-12841.
Klemme, S., Blundy, J.D., Wood, B.J., 2002. Experimental constraints on major and trace element partitioning during partial melting of eclogite. Geochimica et Cosmochimica Acta 66, 3109-3123.
Knight, K.B., Nomade, S., Renne, P.R., Marzoli, A., Bertrand, H., Youbi, N., 2004. The Central Atlantic Magmatic Province at the Triassic-Jurassic boundary: paleomagnetic and 40Ar/39Ar evidence from Morocco for brief, episodic volcanism. Earth and Planetary Science Letters 228, 143-160.
Kontak, D.J., 2008. On the edge of CAMP: Geology and volcanology of the Jurassic North Mountain Basalt, Nova Scotia. Lithos 101, 74-101.
Kuiper, K.F., Deino, A., Hilgen, F.J., Krijgsman, W., Renne, P.R., Wijbrans, J.R., 2008. Synchronizing Rock Clocks of Earth History. Science 320, 500-504.

LaTourrette, T.Z., Burnett, D.S., 1992. Experimental determination of U and Th partitioning between clinopyroxene and natural and synthetic basaltic liquid. Earth and Planetary Science Letters 110, 227-244.
Lemarchand, F., Villemant, B.Æ., Calas, G., 1987. Trace element distribution coefficients in alkaline series. Geochimica et Cosmochimica Acta 51, 1071-1081.
Luhr, J.F., Carmichael, I.S.E., Varekamp, J.C., 1984. The 1982 eruptions of El Chich√≥n Volcano, Chiapas, Mexico: Mineralogy and petrology of the anhydritebearing pumices. Journal of Volcanology and Geothermal Research 23, 69-108.
Marzoli, A., Bertrand, H., Knight, K.B., Cirilli, S., Buratti, N., Verati, C., Nomade, S., Renne, P.R., Youbi, N., Martini, R., Allenbach, K., Neuwerth, R., Rapaille, C., Zaninetti, L., Bellieni, G., 2004. Synchrony of the Central Atlantic magmatic province and the Triassic-Jurassic boundary climatic and biotic crisis. Geology 32, 973-976.
Marzoli, A., Renne, P.R., Piccirillo, E.M., Ernesto, M., Bellieni, G., Min, A.D., 1999. Extensive 200-Million-Year-Old Continental Flood Basalts of the Central Atlantic Magmatic Province. Science 284, 616-618.
Matsui, Y., Onuma, N., Nagasawa, H., Higuchi, H., Banno, S., 1977. Crystal structure control in trace element partition between crystal and magma. Tectonics 100, 315-324.
Mattinson, J.M., 2005. Zircon U-Pb chemical abrastion ("CA-TIMS") method: combined annealing and multi-step partial dissolution analysis for improved precision and accuracy of zircon ages. Chemical Geology 220, 47-66.
McElwain, J.C., Beerling, D.J., Woodward, F.I., 1999. Fossil Plants and Global Warming at the Triassic-Jurassic Boundary. Science 285, 1386-1390.
McHone, G., J., 2003. Volatile emissions from Central atlantic magmatic Province basalts: Mass assumptions and environmental consequences. American Geophysical Union, Washington, DC, ETATS-UNIS.
McKenzie, D.A.N., O'Nions, R.K., 1991. Partial Melt Distributions from Inversion of Rare Earth Element Concentrations. Journal of Petrology 32, 1021-1091.
McLean, N.M., Bowring, J.F., Bowring, S.A., An algorithm for U-Pb isotope dilution data reduction and uncertainty propagation. Geochem. Geophys. Geosyst. 12, Q0AA18.
Min, K., Mundil, R., Renne, P.R., Ludwig, K.R., 2000. A test for systematic errors in 40Ar/39Ar geochronology through comparison with U/Pb analysis of a 1.1-Ga rhyolite. Geochimica et Cosmochimica Acta 64, 73-98.
Morton, N., 2008. Details of voting on proposed GSSP and ASSP for the base of the Hettangian Stage and Jurassic System. Int Subcomm Jurassic Stratigr Newslett 35, 74.
Olsen, P., E, Schlische, R., W., Fedosh, M., S., 1996. 580 ky duration of the Early Jurassic flood basalt event in eastern North America estimated using Milankovitch cyclostratigraphy, in: Morales, M. (Ed.), The Continental Jurassic. Museum of Northern Arizona Bulletin, pp. 11-22.
Olsen, P.E., Kent, D.V., 1996. Milankovitch climate forcing in the tropics of Pangaea during the Late Triassic. Palaeogeography, Palaeoclimatology, Palaeoecology 122, 1-26.
Olsen, P.E., Kent, D.V., Et-Touhami, M., PUFFER, J.H., 2003. Cyclo-, magneto-, and bio-stratigraphic constraints on the duration of the CAMP event and its relationship to the Triassic-Jurassic boundary, in: Hames, W.E., McHone, G., Renne, P.R., Ruppel, C. (Eds.), The Central Atlantic Magmatic Province: Insights from Fragments of Pangea. Geophysical Monograph Series, pp. 7-32.

Olsen, P.E., Kent, D.V., Sues, H.D., Koeberl, C., Huber, H., Montanari, A., Rainforth, E.C., Fowell, S.J., Szajna, M.J., Hartline, B.W., 2002a. Ascent of Dinosaurs Linked to an Iridium Anomaly at the Triassic-Jurassic Boundary. Science 296, 1305-1307.
Olsen, P.E., Koeberl, C., Huber, H., Montanari, A., Fowell, S.J., Et-Touhami, M., Kent, D.V., 2002b. Continental Triassic–Jurassic boundary in central Pangea: recent progress and discussion of an Ir anomaly, in: Koeberl, C., MacLeod, K.G. (Eds.), Catastrophic Events and Mass Extinctions: Impacts and Beyond. Gelogical Society of America Special Paper, Boulder, Colorado, pp. 505-522.
Onuma, N., Higuchi, H., Wakita, H., Nagasawa, H., 1968. Trace element partition between two pyroxenes and the host lava. Earth and Planetary Science Letters 5, 47-51.
Philpotts, A.R., Carroll, M., Hill, J.M., 1996. Crystal-Mush Compaction and the Origin of Pegmatitic Segregation Sheets in a Thick Flood-Basalt Flow in the Mesozoic Hartford Basin, Connecticut. Journal of Petrology 37, 811-836.
Puffer, J., 1992. Eastern North American flood basalts in the context of the incipient breakup of Pangea, in: Puffer, J., Ragland, P. (Eds.), Eastern North American Mesozoic magmatism. Geol. Soc. Amer. Spec. Paper pp. 95-118.
Puffer, J., H., Horter, D., L., 1993. Origin of pegmatitic segregation veins within flood basalts. Geological Society of America Bulletin 105, 738-748.
Puffer, J.H., Block, K.A., Steiner, J.C., 2009. Transmission of Flood Basalts through a Shallow Crustal Sill and the Correlation of Sill Layers with Extrusive Flows: The Palisades Intrusive System and the Basalts of the Newark Basin, New Jersey, U.S.A. The Journal of Geology 117, 139-155.
Puffer, J.H., Volkert, R.A., 2001. Pegmatoid and Gabbroid Layers in Jurassic Preakness and Hook Mountain Basalts, Newark Basin, New Jersey. The Journal of Geology 109, 585-601.
Ragland, P.C., Cummins, L.E., Arthur, J.D., 1992. Compositional patterns for early Mesozoic diabases from South Carolina to central Virginia, in: Puffer, J.H., Ragland, R.C. (Eds.), Eastern North American Mesozoic magmatism. Geol. Soc. Am. Spec. Pap. , pp. 309–332.
Rampino, M.R., Stothers, R.B., 1988. Flood Basalt Volcanism During the Past 250 Million Years. Science 241, 663-668.
Ratcliffe, N.M., 1988. Reinterpretation of the relationship of the western extension of the Palisades sill to the lava flows at Ladentown, New York, based on new core data, in: Froelich, A.J., Robinson, G.R., Jr. (Eds.), Studies of the Early Mesozoic basins of the eastern United States. United States. U.S. Geol. Surv. Bull. , pp. 113–140.
Renne, P.R., Mundil, R., Balco, G., Min, K., Ludwig, K.R., 2010. Joint determination of 40K decay constants and 40Ar*/40K for the Fish Canyon sanidine standard, and improved accuracy for 40Ar/39Ar geochronology. Geochimica et Cosmochimica Acta 74, 5349-5367.
Schaller, M.F., Wright, J.D., Kent, D.V., Atmospheric Pco2 Perturbations Associated with the Central Atlantic Magmatic Province. Science 331, 1404-1409.
Schoene, B., Crowley, J.L., Condon, D.J., Schmitz, M.D., Bowring, S.A., 2006. Reassessing the uranium decay constants for geochronology using ID-TIMS U-Pb data. Geochimica et Cosmochimica Acta 70, 426-445.
Schoene, B., Guex, J., Bartolini, A., Schaltegger, U., Blackburn, T.J., 2010. Correlating the end-Triassic mass extinction and flood basalt volcanism at the 100 ka level. Geology 38, 387-390.
Seidemann, D.E., 1988. The hydrothermal addition of excess 40Ar at the lava flows from the early Jurassic in the Hartford Basin (Northeastern U.S.A.): Implications for the time scale. Chemical Geology: Isotope Geoscience section 72, 37-45.

Smith, R.C., Rose, A.W., Lanning, R.M., 1975. Geology and Geochemistry of Triassic Diabase in Pennsylvania. Geological Society of America Bulletin 86, 943-955.
Tanner, L.H., Kyte, F.T., 2005. Anomalous iridium enrichment at the Triassic,ÄìJurassic boundary, Blomidon Formation, Fundy basin, Canada. Earth and Planetary Science Letters 240, 634-641.
Tanner, L.H., Kyte, F.T., Walker, A.E., 2008. Multiple Ir anomalies in uppermost Triassic to Jurassic-age strata of the Blomidon Formation, Fundy basin, eastern Canada. Earth and Planetary Science Letters 274, 103-111.
Tollo, R.P., Gottfried, D., 1992. Petrochemistry of Jurassic Basalt from Eight Cores, Newark Basin, New Jersey. SPECIAL PAPERS- GEOLOGICAL SOCIETY OF AMERICA, 233.
Valley, J.W., Cavosie, A.J., Fu, B., Peck, W.H., Wilde, S.A., 2006. Comment on "Heterogeneous Hadean Hafnium: Evidence of Continental Crust at 4.4 to 4.5 Ga". Science 312, 1139a.
Villemant, B.Æ., Jaffrezic, H., Joron, J.-L., Treuil, M., 1981. Distribution coefficients of major and trace elements; fractional crystallization in the alkali basalt series of Cha√Æne des Puys (Massif Central, France). Geochimica et Cosmochimica Acta 45, 1997-2016.
Whiteside, J.H., Olsen, P.E., Eglinton, T., Brookfield, M.E., Sambrotto, R.N., 2010. Compound-specific carbon isotopes from Earth,Äôs largest flood basalt eruptions directly linked to the end-Triassic mass extinction. Proceedings of the National Academy of Sciences 107, 6721-6725.
Whiteside, J.H., Olsen, P.E., Kent, D.V., Fowell, S.J., Et-Touhami, M., 2007. Synchrony between the Central Atlantic magmatic province and the Triassic-Jurassic mass-extinction event? Palaeogeography, Palaeoclimatology, Palaeoecology 244, 345-367.
Wood, B.J., Trigila, R., 2001. Experimental determination of aluminous clinopyroxene,Äìmelt partition coefficients for potassic liquids, with application to the evolution of the Roman province potassic magmas. Chemical Geology 172, 213-223.
Zack, T., Brumm, R., 1998. Ilmenite/liquid partition coefficients of 26 trace elements determined through ilmenite/clinopyroxene partitioning in garnet pyroxene, in: Gurney, J.J., Gurney, J.L., Pascoe, M.D., Richardson, S.H. (Eds.), 7th International Kimberlite Conference, Cape Town, pp. 986-988.

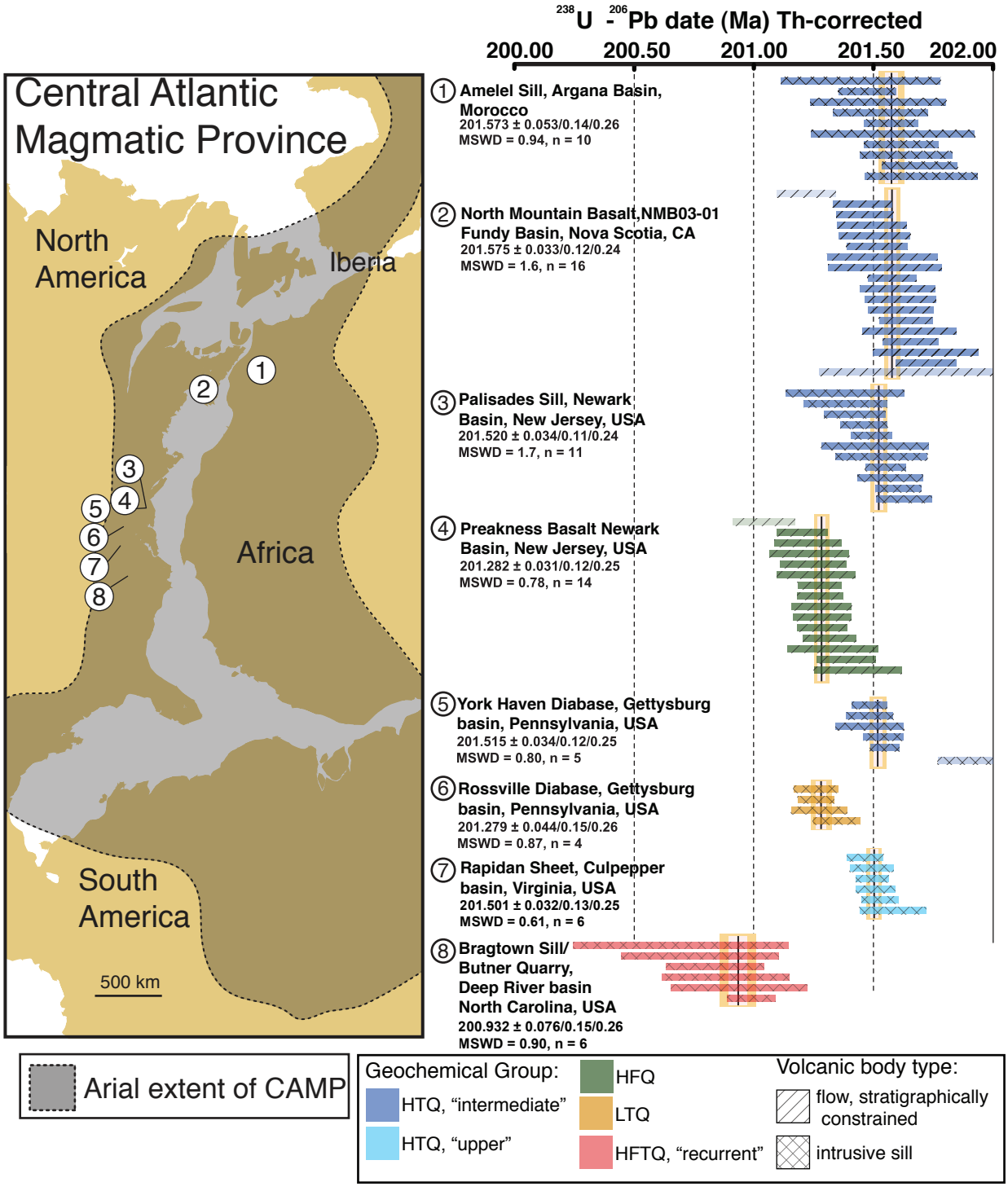
Central Atlantic Magmatic Province
North America
Iberia
Africa
South America
500 km
1
2
3
4
5
6
7
8
238U - 206Pb date (Ma) Th-corrected
200.00
200.50
201.00
201.50
202.00
① Amelel Sill, Argana Basin, Morocco
201.573 ± 0.053/0.14/0.26
MSWD = 0.94, n = 10
② North Mountain Basalt,NMB03-01 Fundy Basin, Nova Scotia, CA
201.575 ± 0.033/0.12/0.24
MSWD = 1.6, n = 16
③ Palisades Sill, Newark Basin, New Jersey, USA
201.520 ± 0.034/0.11/0.24
MSWD = 1.7, n = 11
④ Preakness Basalt Newark Basin, New Jersey, USA
201.282 ± 0.031/0.12/0.25
MSWD = 0.78, n = 14
⑤ York Haven Diabase, Gettysburg basin, Pennsylvania, USA
201.515 ± 0.034/0.12/0.25
MSWD = 0.80, n = 5
⑥ Rossville Diabase, Gettysburg basin, Pennsylvania, USA
201.279 ± 0.044/0.15/0.26
MSWD = 0.87, n = 4
⑦ Rapidan Sheet, Culpepper basin, Virginia, USA
201.501 ± 0.032/0.13/0.25
MSWD = 0.61, n = 6
⑧ Bragtown Sill/ Butner Quarry, Deep River basin North Carolina, USA
200.932 ± 0.076/0.15/0.26
MSWD = 0.90, n = 6
Arial extent of CAMP
Geochemical Group:
HTQ, "intermediate"
HTQ, "upper"
HFQ
LTQ
HFTQ, "recurrent"
Volcanic body type:
flow, stratigraphically constrained
intrusive sill

Figure 6.1

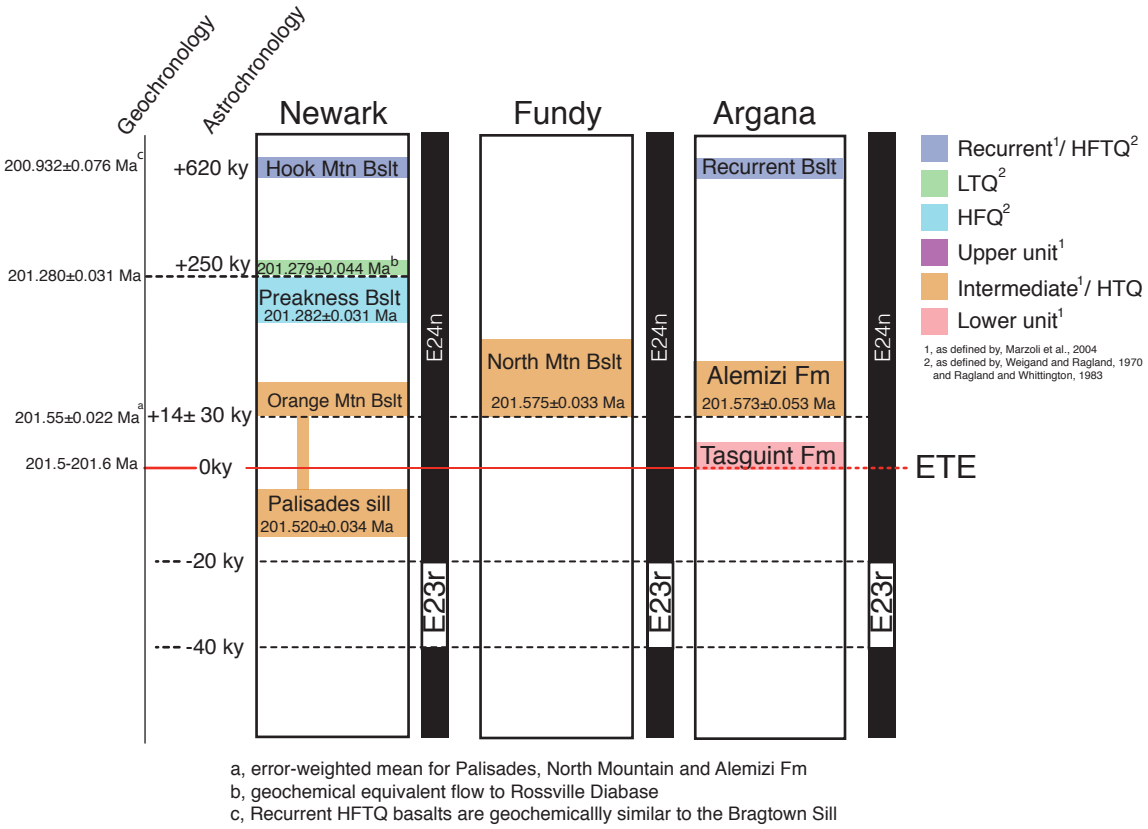

a, error-weighted mean for Palisades, North Mountain and Alemizi Fm
b, geochemical equivalent flow to Rossville Diabase
c, Recurrent HFTQ basalts are geochemicallly similar to the Bragtown Sill

Figure 6.2

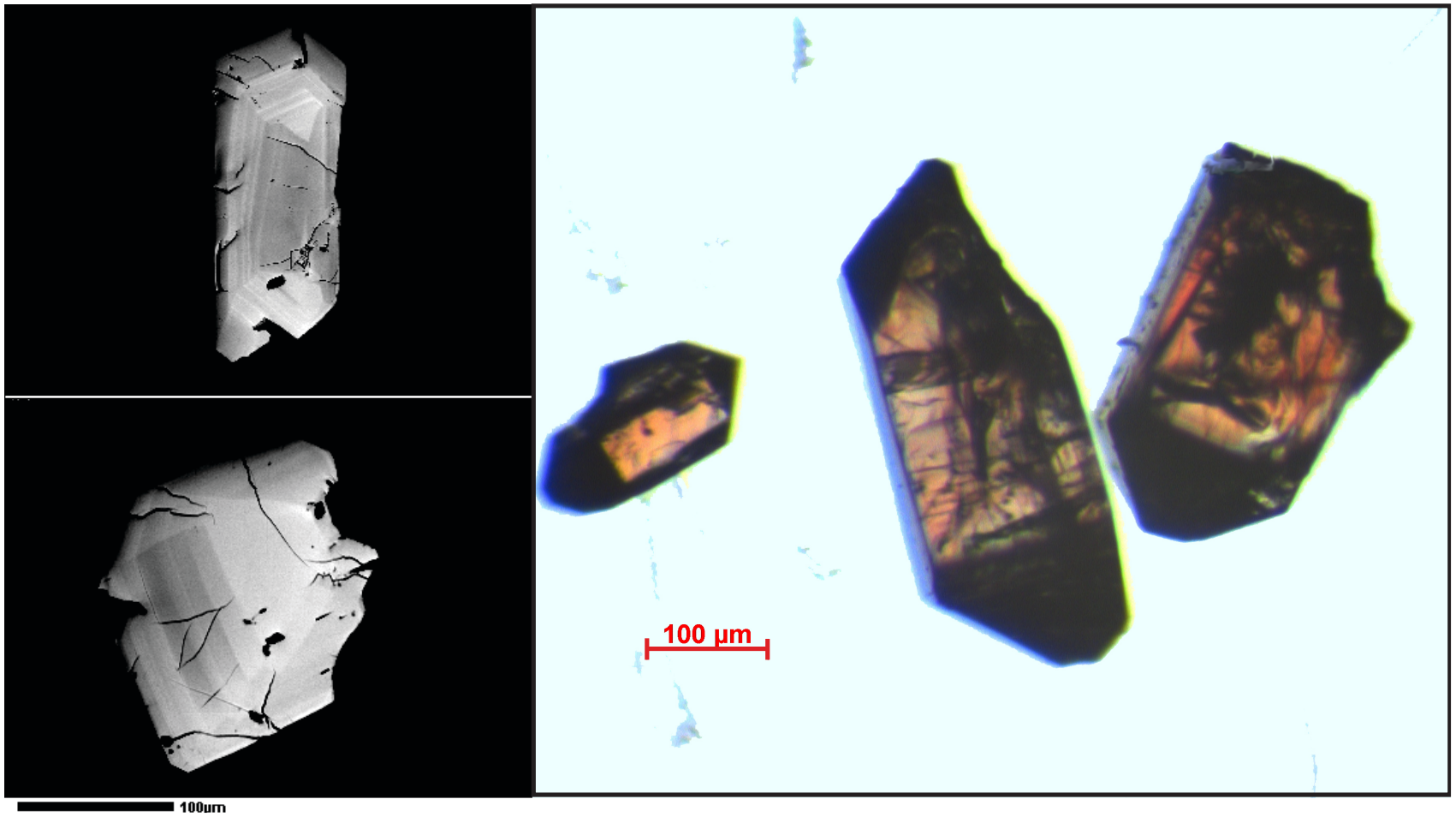

Figure 6.3

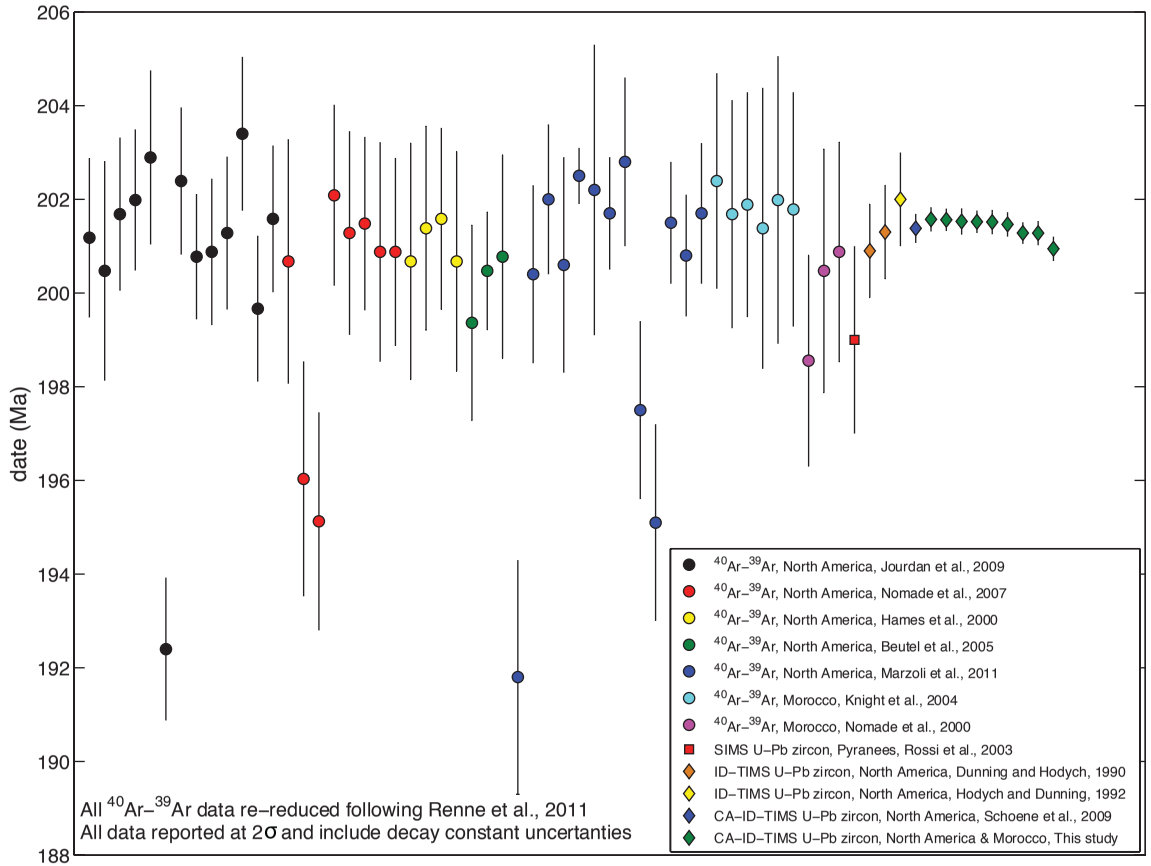
206
204
202
200
198
196
194
192
190
188
date (Ma)
All 40Ar–39Ar data re–reduced following Renne et al., 2011
All data reported at 2σ and include decay constant uncertanties
40Ar–39Ar, North America, Jourdan et al., 2009
40Ar–39Ar, North America, Nomade et al., 2007
40Ar–39Ar, North America, Hames et al., 2000
40Ar–39Ar, North America, Beutel et al., 2005
40Ar–39Ar, North America, Marzoli et al., 2011
40Ar–39Ar, Morocco, Knight et al., 2004
40Ar–39Ar, Morocco, Nomade et al., 2000
SIMS U–Pb zircon, Pyranees, Rossi et al., 2003
ID–TIMS U–Pb zircon, North America, Dunning and Hodych, 1990
ID–TIMS U–Pb zircon, North America, Hodych and Dunning, 1992
CA–ID–TIMS U–Pb zircon, North America, Schoene et al., 2009
CA–ID–TIMS U–Pb zircon, North America & Morocco, This study

Figure 6.4

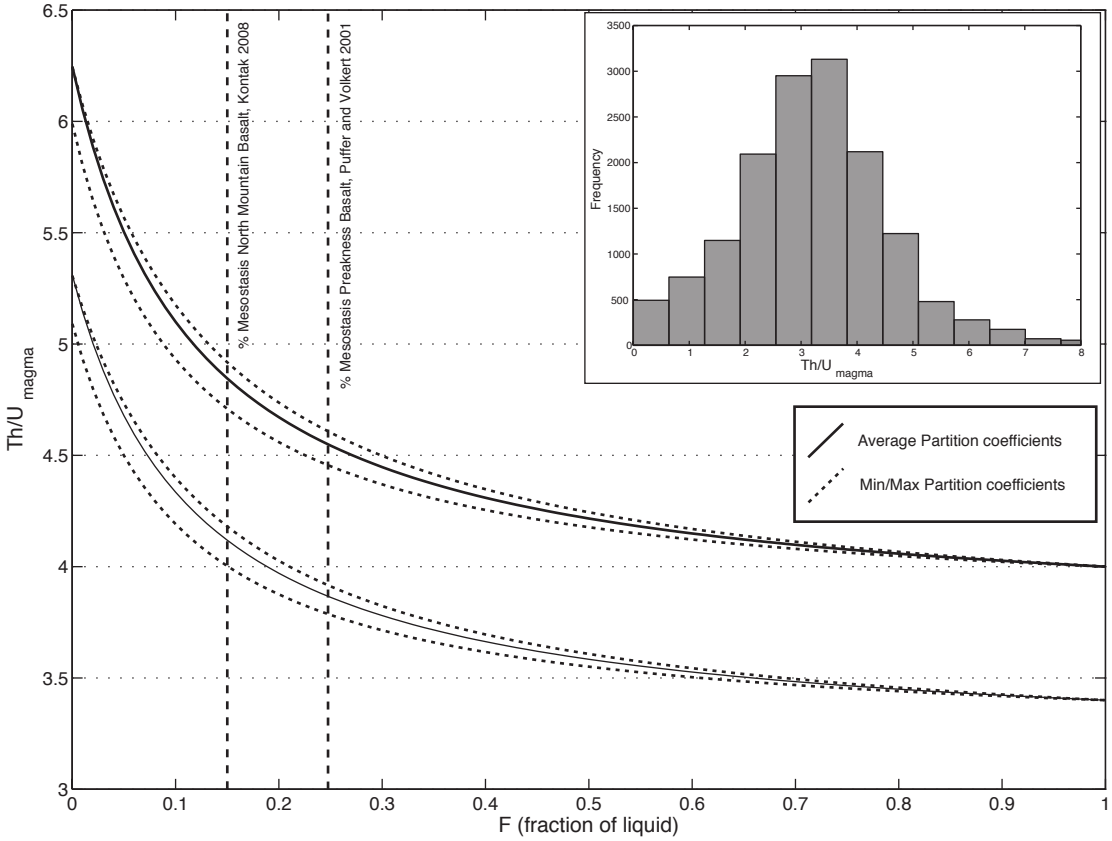
% Mesostasis North Mountain Basalt, Kontak 2008
% Mesostasis Preakness Basalt, Puffer and Volkert 2001
Th/U magma
F (fraction of liquid)
Frequency
Th/U magma
Average Partition coefficients
Min/Max Partition coefficients

Figure 6.5

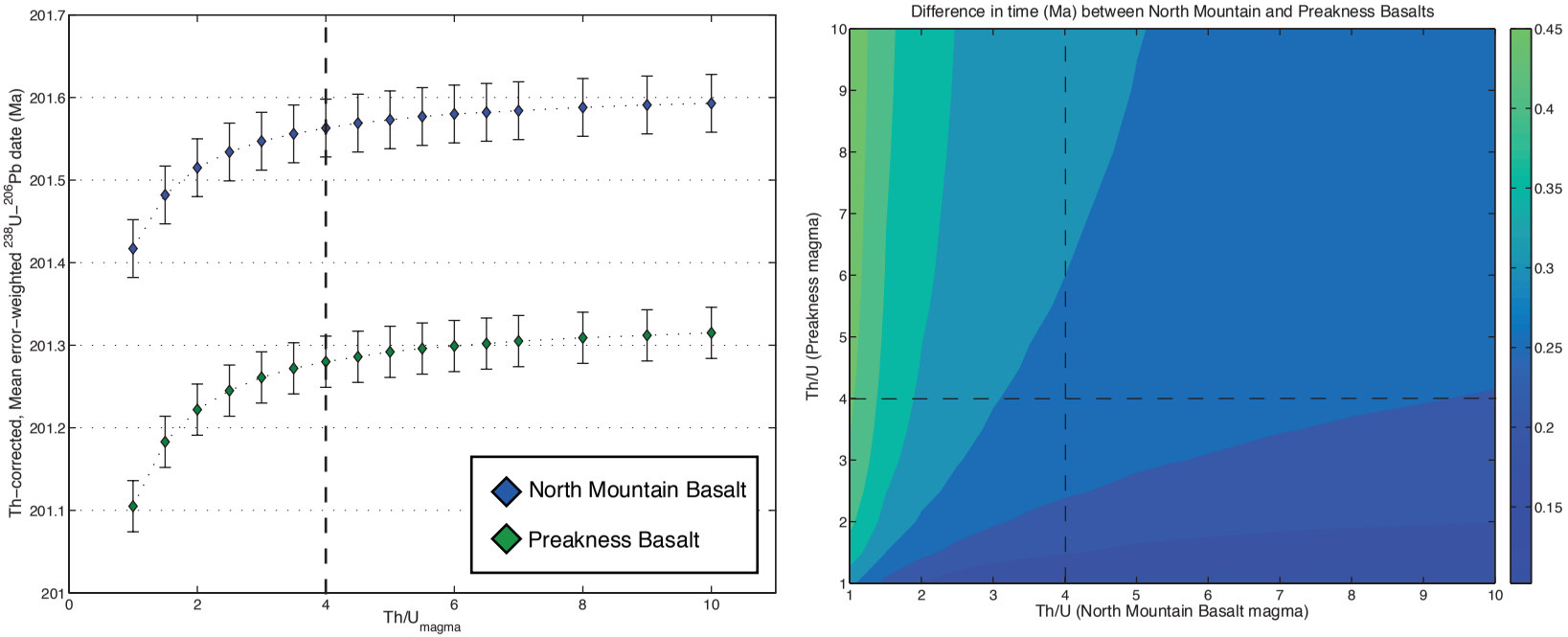
Th–corrected, Mean error–weighted $^{238}U-^{206}Pb$ date (Ma)
Th/U$_{magma}$
North Mountain Basalt
Preakness Basalt
Difference in time (Ma) between North Mountain and Preakness Basalts
Th/U (Preakness magma)
Th/U (North Mountain Basalt magma)

Figure 6.6

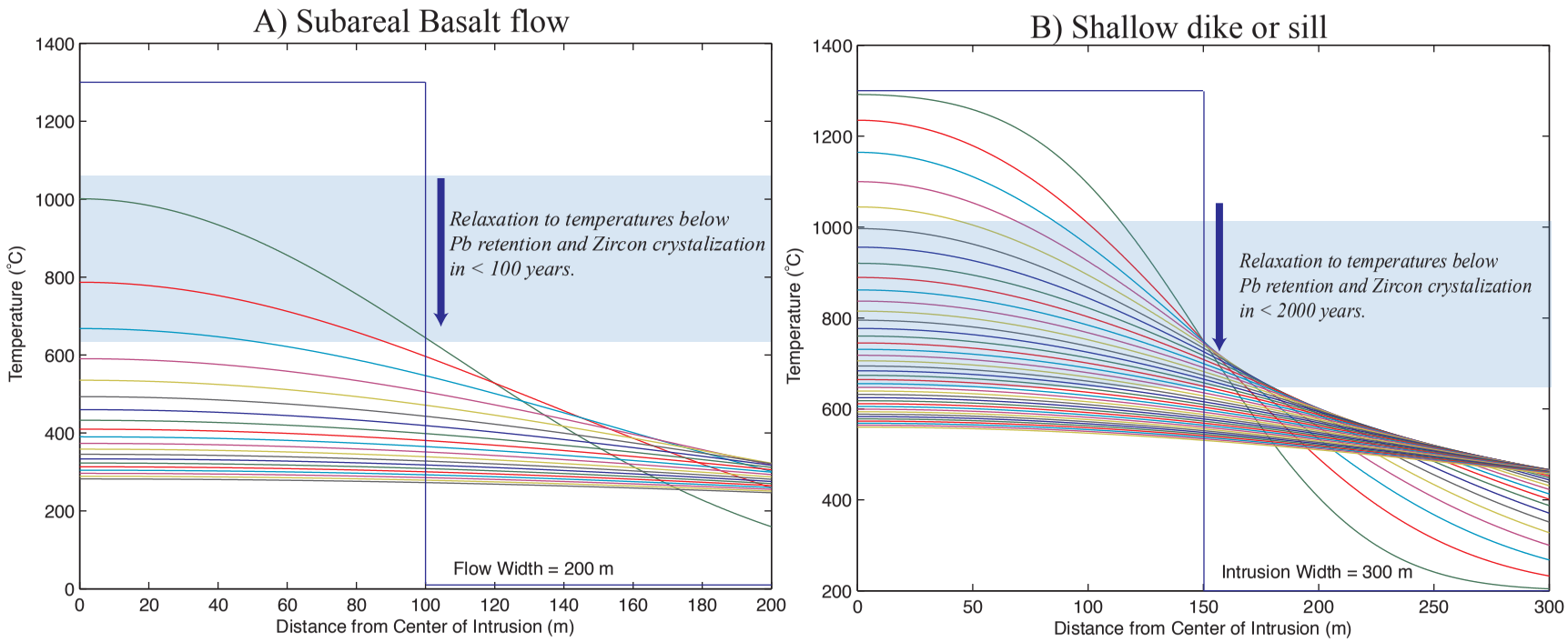
A) Subareal Basalt flow
Temperature (°C)
Distance from Center of Intrusion (m)
Relaxation to temperatures below
Pb retention and Zircon crystalization
in < 100 years.
Flow Width = 200 m
B) Shallow dike or sill
Temperature (°C)
Distance from Center of Intrusion (m)
Relaxation to temperatures below
Pb retention and Zircon crystalization
in < 2000 years.
Intrusion Width = 300 m

Figure 6.7

Table 6.1

	Dates (Ma)		Isotopic Ratios						Composition					Fraction
Fraction	206Pb/ 238U <Th> a	±2σ abs	206Pb/ 238U b	±2σ %	207Pb/ 235U b	±2σ %	207Pb/ 206Pb b	±2σ %	Corr. coef.	Th/ U c	Pb* (pg) d	Pbc (pg) e	Pb*/ Pbc f	Fraction
Alemizi Fm, Argana Basin, Morocco: MOR														
z1	201.615	0.151	0.031762	0.075924	0.219846	0.247743	0.050223	0.234204	0.2996	2.18	43.7	0.38	114.7	z1
z2	201.697	0.231	0.031774	0.116392	0.219881	0.720571	0.050212	0.664624	0.5367	1.90	33.9	1.38	24.5	z2
z4	201.572	0.108	0.031754	0.054208	0.219996	0.275983	0.050270	0.253756	0.4577	1.88	20.1	0.36	56.0	z4
z5	201.634	0.188	0.031764	0.094647	0.220027	0.628550	0.050261	0.562376	0.7291	1.97	15.5	0.34	45.7	z5
z6	201.445	0.328	0.031734	0.165416	0.219896	1.421102	0.050279	1.325434	0.6149	2.02	5.1	0.42	12.1	z6
z7	201.527	0.193	0.031746	0.097464	0.220250	0.783135	0.050341	0.745191	0.4354	1.76	7.8	0.31	25.6	z7
z8	201.518	0.279	0.031745	0.140630	0.222375	1.402761	0.050829	1.316046	0.6451	1.77	8.4	0.71	11.8	z8
z13	201.691	0.153	0.031773	0.077099	0.220434	0.779956	0.050340	0.732643	0.6360	1.94	16.6	0.78	21.2	z13
z14	201.471	0.115	0.031738	0.057875	0.220354	0.287011	0.050378	0.246901	0.7147	1.91	31.0	0.37	83.9	z14
z15	201.580	0.336	0.031755	0.169552	0.216355	1.873431	0.049437	1.869213	0.0685	1.79	9.4	0.64	14.7	z15
York Haven Diabase, York Haven, Pennsylvania, USA: YHFGRS														
z1	201.481	0.068	0.031738	0.034461	0.219844	0.153342	0.050261	0.137709	0.4464	1.55	91.8	0.79	115.8	z1
z2	201.544	0.056	0.031749	0.028368	0.219913	0.152712	0.050259	0.138796	0.4434	1.77	77.5	0.82	94.5	z2
z3	201.482	0.094	0.031739	0.047293	0.219877	0.158036	0.050267	0.143314	0.3782	1.70	72.7	0.81	89.3	z3
z6	201.540	0.079	0.031752	0.040044	0.219360	0.249747	0.050128	0.233393	0.4242	2.59	46.1	0.60	76.8	z6
z7	201.483	0.138	0.031739	0.069578	0.219081	0.252548	0.050085	0.248610	0.1649	1.77	41.6	0.30	139.9	z7
Rapidan Sheet, Jet Mist Quarry, Virginia, USA: 030507-2														
z2	201.508	0.496	0.031744	0.249841	0.219417	0.278471	0.050154	0.060718	0.9721	1.88	1850.5	1.07	1721.6	z2
z3	201.407	0.104	0.031730	0.052631	0.219272	0.122102	0.050143	0.081407	0.7806	2.47	136.8	0.57	241.0	z3
z4	201.499	0.119	0.031744	0.060137	0.219414	0.113042	0.050153	0.062006	0.8481	2.28	192.3	0.52	367.0	z4
z5	201.469	0.173	0.031745	0.086994	0.219185	0.191431	0.050100	0.130392	0.7864	3.58	105.2	0.64	163.2	z5
z6	201.467	0.107	0.031738	0.053944	0.219498	0.118101	0.050182	0.097417	0.4982	2.11	192.2	0.58	333.0	z6
z10	201.361	0.136	0.031720	0.068424	0.219695	0.338433	0.050255	0.297885	0.6362	1.87	99.6	2.00	49.7	z10
z11	201.603	0.118	0.031757	0.059585	0.220393	0.234398	0.050356	0.206738	0.5338	1.41	61.5	1.18	52.1	z11
z12	201.398	0.142	0.031725	0.071637	0.219544	0.177608	0.050213	0.124183	0.7952	1.59	411.7	2.95	139.5	z12
z13	201.615	0.127	0.031760	0.063881	0.220960	0.476307	0.050482	0.442302	0.5665	1.62	49.2	1.76	27.9	z13
z17	201.407	0.120	0.031727	0.060585	0.219789	0.237449	0.050266	0.204775	0.5943	1.78	170.0	1.29	131.3	z17
z18	201.519	0.116	0.031744	0.058353	0.220026	0.196365	0.050292	0.155422	0.7326	1.67	125.0	1.26	99.5	z18
z20	201.441	0.138	0.031732	0.069445	0.220677	0.298418	0.050461	0.275560	0.4083	1.67	47.8	0.52	92.5	z20
z21	201.441	0.153	0.031733	0.076950	0.220077	0.367145	0.050322	0.313404	0.7340	1.83	36.5	0.70	52.0	z21
z24	201.496	0.194	0.031741	0.097705	0.220445	0.336214	0.050393	0.272065	0.7237	1.72	71.7	0.98	72.9	z24
Rossville Diabase, Pennsylvania, USA: ROSSGPH														
z2	201.271	0.111	0.031703	0.056186	0.218966	0.153762	0.050116	0.144934	0.2763	1.24	134.9	0.91	148.6	z2
z3	201.257	0.089	0.031702	0.044803	0.219111	0.236910	0.050150	0.213151	0.5503	1.53	114.9	1.84	62.4	z3
z5	201.258	0.072	0.031700	0.036165	0.219241	0.160705	0.050183	0.144231	0.4570	1.04	100.7	0.80	126.5	z5
z6	201.344	0.093	0.031719	0.046937	0.219389	0.076042	0.050187	0.058613	0.4946	2.24	191.8	0.58	332.3	z6
Butner Diabase, Deep River Basin, North Carolina, USA: BQDB-1														
z2	200.976	0.200	0.031654	0.101006	0.218948	0.493034	0.050189	0.438531	0.6020	0.82	19.9	0.77	25.7	z2
z3	201.023	0.140	0.031662	0.070815	0.218594	0.277834	0.050094	0.235907	0.6489	1.07	32.1	0.54	59.9	z3
z4	200.910	0.352	0.031656	0.177927	0.218063	1.562901	0.049983	1.455212	0.6395	3.77	9.7	0.71	13.6	z4
z9	200.970	0.352	0.031654	0.178206	0.218973	1.353186	0.050194	1.247008	0.6362	1.12	5.3	0.54	9.8	z9
z10	200.824	0.301	0.031640	0.152225	0.218675	1.585030	0.050149	1.543616	0.3144	3.17	9.6	0.82	11.8	z10
z11	200.779	0.158	0.031641	0.079724	0.218358	0.379233	0.050074	0.314943	0.8263	5.23	60.6	0.81	75.1	z11
z12	200.707	0.179	0.031624	0.090554	0.217519	0.461311	0.049908	0.440159	0.3142	3.97	20.5	0.42	48.6	z12
z14	201.101	0.160	0.031675	0.080891	0.219712	0.492582	0.050330	0.435352	0.7357	1.08	14.9	0.55	27.0	z14
z15	201.210	0.246	0.031696	0.124064	0.219957	1.049679	0.050352	0.972325	0.6557	2.03	8.3	0.56	14.6	z15
North Mountain Basalt, Fundy Basin, Nova Scotia, CA :AVC-1-2														
AVC_z2	201.542	0.151	0.031757	0.075908	0.220544	0.315668	0.050391	0.269969	0.6562	3.68	74.1	0.70	105.2	AVC_z2
AVC_z3	201.663	0.201	0.031772	0.101281	0.221651	0.933165	0.050620	0.869065	0.6597	2.64	14.8	0.79	18.6	AVC_z3
AVC_z4	201.387	0.293	0.031727	0.147844	0.221991	1.575405	0.050769	1.477732	0.6848	2.52	9.6	0.99	9.7	AVC_z4
AVC_z5	201.498	0.152	0.031748	0.076650	0.220461	0.502851	0.050386	0.443135	0.7951	3.35	36.8	0.80	46.0	AVC_z5
AVC_z7	201.513	0.197	0.031749	0.099579	0.220263	0.652741	0.050339	0.584720	0.7155	3.01	20.8	0.78	26.7	AVC_z7
AVC_z9	201.537	0.232	0.031748	0.117133	0.222357	1.102919	0.050819	1.035696	0.6054	1.83	12.1	0.96	12.6	AVC_z9
AVC_z10	201.449	0.149	0.031741	0.075356	0.220592	0.719515	0.050427	0.679673	0.5565	3.42	23.0	0.83	27.8	AVC_z10
AVC_z11	201.611	0.165	0.031768	0.083096	0.220525	0.525069	0.050369	0.477670	0.6115	3.67	22.4	0.51	44.2	AVC_z11
North Mountain Basalt, Fundy Basin, Nova Scotia, CA :NMB-03-01														
202_z1	201.502	0.145	0.031743	0.072969	0.220083	0.529852	0.050308	0.493549	0.5361	1.90	19.1	0.44	43.1	202_z1
202_z3	201.462	0.113	0.031740	0.057176	0.219579	0.391530	0.050197	0.369642	0.4224	2.75	31.3	0.52	59.8	202_z3
202_z5	201.716	0.215	0.031776	0.108246	0.220523	0.962231	0.050356	0.902965	0.5820	1.60	34.8	2.22	15.7	202_z5
202_z7	201.613	0.132	0.031762	0.066543	0.220206	0.217287	0.050305	0.199405	0.3756	2.29	48.6	0.39	123.0	202_z7
202_z8	201.609	0.144	0.031759	0.072565	0.220598	0.219919	0.050399	0.211056	0.2527	1.77	34.2	0.32	105.7	202_z8
202_z9	201.575	0.097	0.031752	0.048926	0.219854	0.291707	0.050242	0.279685	0.2888	1.23	26.9	0.42	64.1	202_z9
202_z11	201.534	0.226	0.031749	0.113810	0.220467	1.088706	0.050386	1.020739	0.6267	2.05	9.3	0.56	16.6	202_z11
202_z12	201.232	0.118	0.031699	0.059350	0.218189	0.370567	0.049944	0.345458	0.4656	1.84	20.8	0.41	50.3	202_z12
202_z20	201.633	0.107	0.031767	0.053927	0.219752	0.100859	0.050195	0.079800	0.5234	2.59	293.3	0.55	534.7	202_z20
202_z21	201.490	0.141	0.031740	0.071045	0.220077	0.304292	0.050312	0.276949	0.4607	1.60	120.5	2.38	50.6	202_z21
202_z22	201.718	0.121	0.031776	0.061128	0.220007	0.095931	0.050237	0.060608	0.7032	1.69	395.3	0.39	1002.3	202_z22
202_z23	201.546	0.232	0.031752	0.117000	0.219909	0.198500	0.050253	0.159141	0.5758	2.43	106.9	0.61	174.0	202_z23
202_z24	201.829	0.561	0.031794	0.282503	0.227703	2.739623	0.051966	2.568426	0.6380	1.61	3.5	0.54	6.4	202_z24
202_z26	201.647	0.192	0.031764	0.096945	0.220279	0.159327	0.050318	0.120907	0.6198	1.54	186.3	0.55	335.8	202_z26
202_z27	201.512	0.122	0.031743	0.061449	0.219687	0.189483	0.050217	0.178790	0.2875	1.63	44.9	0.32	140.2	202_z27
202_z28	201.451	0.119	0.031733	0.060097	0.219576	0.245313	0.050207	0.227216	0.3779	1.62	112.5	1.80	62.3	202_z28

Table 6.1 (cont)

202_z30	201.599	0.152	0.031757	0.076499	0.219235	0.284631	0.050092	0.264833	0.3608	1.53	48.8	0.82	59.4	202_z30
202_z31	201.654	0.111	0.031764	0.055812	0.219812	0.132315	0.050212	0.112518	0.4701	1.28	121.0	0.50	244.2	202_z31
Palisades Sill, Newark Basin, New Jersey, USA: NB08-13														
202_z16	201.419	0.124	0.031726	0.062618	0.221017	0.369812	0.050549	0.344437	0.4540	0.97	23.0	0.46	50.0	202_z16
202_z17	201.380	0.169	0.031721	0.085518	0.219020	0.597372	0.050099	0.595302	0.0858	1.43	20.9	0.95	22.0	202_z17
202_z18	201.566	0.131	0.031748	0.066231	0.219541	0.584579	0.050175	0.552727	0.5113	0.78	12.7	0.61	20.7	202_z18
202_z21	201.532	0.186	0.031748	0.093912	0.221374	0.923946	0.050595	0.922413	0.0613	2.00	13.1	0.67	19.6	202_z21
202_z22	201.504	0.219	0.031739	0.110467	0.219489	0.959450	0.050178	0.906007	0.5231	1.02	6.4	0.43	14.9	202_z22
202_z23	201.458	0.093	0.031735	0.046857	0.220267	0.277120	0.050362	0.261365	0.3720	1.68	20.0	0.34	58.7	202_z23
202_z26	201.380	0.243	0.031721	0.122534	0.218453	0.645661	0.049969	0.593778	0.4949	1.48	14.5	0.57	25.5	202_z26
202_z28	201.548	0.080	0.031747	0.040112	0.219628	0.093318	0.050198	0.076199	0.4664	1.12	83.7	0.31	272.7	202_z28
202_z30	201.489	0.081	0.031737	0.040943	0.219597	0.098523	0.050206	0.080652	0.4783	1.05	87.2	0.33	263.5	202_z30
202_z35c	201.601	0.091	0.031756	0.045649	0.219783	0.099742	0.050218	0.077126	0.5562	1.35	182.0	0.50	366.0	202_z35c
202_z36x	201.626	0.111	0.031759	0.056079	0.220291	0.133125	0.050330	0.104972	0.5913	0.99	83.4	0.72	116.1	202_z36x
Preakness basalt, Newark Basin, New Jersey, USA: NB08-12														
202_z1	201.247	0.134	0.031706	0.067765	0.219293	0.182917	0.050185	0.123836	0.8752	2.92	49.0	0.30	162.0	202_z1
202_z2	201.040	0.125	0.031668	0.063307	0.219493	0.227538	0.050291	0.194739	0.5845	1.73	32.6	0.40	82.4	202_z2
202_z3	201.281	0.120	0.031707	0.060481	0.219314	0.308809	0.050188	0.260502	0.8069	1.89	48.4	0.51	94.1	202_z3
202_z4	201.276	0.091	0.031713	0.046176	0.218951	0.206524	0.050096	0.188989	0.4220	3.35	48.7	0.46	105.7	202_z4
202_z5	201.201	0.102	0.031694	0.051544	0.219855	0.150685	0.050333	0.128173	0.5095	1.78	49.6	0.84	59.2	202_z5
202_z6	201.329	0.185	0.031717	0.093346	0.219848	0.560771	0.050295	0.475439	0.9181	2.35	13.2	0.34	38.6	202_z6
202_z7	201.385	0.350	0.031726	0.176368	0.218660	1.037605	0.050009	0.955062	0.5316	2.39	17.2	0.46	37.8	202_z7
202_z8	201.230	0.162	0.031698	0.081663	0.220073	0.441876	0.050376	0.384896	0.7310	1.72	14.8	0.63	23.3	202_z8
202_z9	201.433	0.178	0.031733	0.089870	0.220472	0.580514	0.050412	0.504515	0.8579	2.19	16.2	0.55	29.3	202_z9
202_z11	201.319	0.489	0.031715	0.246759	0.220765	1.607981	0.050508	1.492013	0.5285	2.19	6.6	0.55	12.1	202_z11
202_z15	201.272	0.086	0.031706	0.043493	0.219644	0.090953	0.050266	0.072785	0.4863	1.88	39.9	0.30	132.8	202_z15
202_z17	201.285	0.101	0.031707	0.050742	0.219597	0.327698	0.050253	0.303046	0.5143	1.65	20.0	0.41	48.9	202_z17
202_z18	201.383	0.117	0.031722	0.059267	0.218968	0.457988	0.050086	0.405723	0.8775	1.51	12.4	0.26	48.4	202_z18
202_z19	201.313	0.106	0.031713	0.053630	0.220743	0.385596	0.050505	0.382531	0.1018	2.12	20.9	0.52	40.4	202_z19
202_z20	201.258	0.159	0.031703	0.080149	0.220629	0.600024	0.050495	0.519896	0.9892	1.82	19.4	0.54	35.8	202_z20
202_z21	201.283	0.116	0.031711	0.058577	0.219189	0.443489	0.050153	0.421489	0.4127	2.70	17.6	0.32	54.4	202_z21
202_z22	201.225	0.136	0.031698	0.068658	0.220498	0.699662	0.050473	0.653894	0.6833	1.90	9.3	0.45	20.8	202_z22

a Corrected for initial Th/U disequilibrium using radiogenic 208Pb and Th/U[magma] = 4.
b Measured ratios corrected for fractionation, tracer and blank.
c Th contents calculated from radiogenic 208Pb and the 207Pb/206Pb date of the sample, assuming concordance between U-Th and Pb systems.
d Total mass of radiogenic Pb.
e Total mass of common Pb.
f Ratio of radiogenic Pb (including 208Pb) to common Pb.

	Puffer and Volkert 2001		Mineral-Element partition coeficients		
	Modal/Gabbroid	Modal/Pegmatoid	D_{Th}	D_U	Partition coeficient References
Plagioclase	35.6	34.1	0.05+/-0.025	0.07+/- 0.05	1-5
Pyroxene	34.4	31.6	0.01+/-0.02	0.007+/-0.02	1,2,6-15
Fe-Ti oxide	8.1	8.3	0.1	0.11	4
Mesostatis	21.5	25.4	-	-	quenced magma does not fractionate Th/U
Apatite*	0.40%	0.40%	17.1	1.82	16

*Maximum estimate from reported P_20_5 concentrations

References: 1: Villemant et al., 1981; 2: McKenzie & O'Nions 1991; 3: Bindeman & Davis, 2000; 4: Lemarchand et al., 1987; 5: Dostal et al., 1983; 6: Latourrette & Burnett 1992; 7: Beattie, 1993; 8: Matsui et al., 1977; 9: Hauri et al., 1994; 10: Benjamin et al., 1978; 11 Zack & Brumm, 1998;12: Onuma et al., 1968; 13:Klemme & Bundy 2002; 14: Wood & Trigila 2001; 15: Adam & Green 2006; 16: Luhr et al., 1984

Table 6.2

Chapter 7: U-Pb geochronologic and thermochronologic time-temperature constraints of $^{40}Ar/^{39}Ar$ hornblende standard HB3gr

Abstract: HB3gr hornblende has served as irradiation standard in $^{40}Ar/^{39}Ar$ studies for decades. In order to compare the apparent age bias that currently exists between the U-Pb and $^{40}Ar/^{39}Ar$ systems, zircon and titanite from the same rock from which the hornblende $^{40}Ar/^{39}Ar$ standard HB3gr was derived, were dated by high-precision Isotope Dilution Thermal Ionization Mass Spectrometry (ID-TIMS). Radiogenic Pb is retained within zircon at high temperatures over geologic time, often providing an age for initial crystallization. Radiogenic Pb in titanite obeys temperature dependent volume diffusion, with a nominal closure temperature of ~600 °C. Together, the zircon and titanite permit constraints to be placed upon the timing of initial crystallization of the rock as well as the rate of any subsequent thermal relaxation. Reconstruction of the time-temperature path for the host rock of the hornblende $^{40}Ar/^{39}Ar$ standard HB3gr will allow for an evaluation of the closed/open system behavior of the hornblende $^{40}Ar/^{39}Ar$ system in this sample. Zircon U-Pb data indicate initial crystallization at 1090.10±0.16 Ma, a date that is 1.7% older than the accepted K-Ar date (1072±11) for Hb3gr; an offset that exceeds the typical 0.5-1% bias between the two systems (though remaining within uncertainty due to the large uncertainties in the ^{40}K decay constant). Single grain titanite analyses range between 1082±0.75 and 1086±0.81 Ma and are interpreted to record the subsequent cooling following crystallization at rates between 30-50 °C/Ma. This is supported by the observation that hornblende $^{40}Ar/^{39}Ar$ dates corrected for decay constant bias are more consistent with titanite U-Pb dates than zircon, permitting the conclusion that both titanite U-Pb and hornblende $^{40}Ar/^{39}Ar$ systems provide a record of cooling. Future use of the HB3gr should evaluate whether the cooling history is manifested in hornblende grain size-date relationships.

7.1 Introduction

Significant advancements in radioisotopic geochronology have provided unprecedented levels of precision. This has in turn highlighted the resolution of a systematic bias between the two most commonly applied chronometers, the U-Pb and $^{40}Ar/^{39}Ar$ systems. The EARTHTIME initiative has encouraged the development of a high-precision absolute time line for Earth's history that can use geochronologic data from any radioisotopic system. In order to accomplish this goal, several recent studies have focused on reducing the systematic uncertainties and/or inaccuracies that contribute to the biases between different radiometric systems (Kuiper et al.,

2008; Min et al., 2000; Renne et al., 2010). Calculated dates for samples using both U-Pb and $^{40}Ar/^{39}Ar$ reveals a systematic, 0.5-1.5 % age bias, where the U-Pb yields the older date. This systematic age discrepancy has typically been attributed to uncertainties and/or inaccuracies associated with the ^{40}K decay constants and/or the "true" age of neutron flux standards used in $^{40}Ar/^{39}Ar$ studies (Renne et al., 2010). There have been several different approaches aimed at reducing or minimizing these uncertainties. These include: Intra-system comparisons, where $^{40}Ar/^{39}Ar$ standards are co-irradiated and analyzed in order to reevaluate the true age of standards through calibration with other independently known standards (Jourdan and Renne, 2007). Second, determination of a $^{40}Ar/^{39}Ar$ standard's true age using an independent chronological technique such as astrochronology (Kuiper et al., 2008). Lastly, the redetermination of ^{40}K decay constants and age of $^{40}Ar/^{39}Ar$ standards through inter-system comparison with the U-Pb system (Kwon et al., 2002; Min et al., 2000; Renne et al., 2010). Correct use of this inter-system comparison requires that important criterions be met. First, the precision and reproducibility of data produced by both the $^{40}Ar/^{39}Ar$ and U-Pb systems must be high. Second, both systems must have remained closed throughout the sample's history. This requires that both chronometers record the same geologic event and that no slow cooling, thermal reheating, or chemical/physical alteration of the radioisotopic systems violate closed system behavior. $^{40}Ar/^{39}Ar$ standards derived from plutonic rocks have typically been excluded from these inter-comparison studies because of the potential geologic bias that slow cooling will induce on the different chronometers. Exceptions to the bias between the $^{40}Ar/^{39}Ar$ and U-Pb systems in plutonic rocks include the McClure Mountain Syenite a ~520 Ma intrusive where the hornblende $^{40}Ar/^{39}Ar$ and K-Ar data overlap within uncertainty with the zircon, titanite and apatite U-Pb dates, indicating rapid cooling of this plutonic rock and its potential usefulness in inter-calibration studies (Schoene and Bowring, 2006).

To further contribute to the inter-calibraiton of the $^{40}Ar/^{39}Ar$ and U-Pb systems, we present here U-Pb zircon and titanite data from a sample of granite pluton that is the source of the $^{40}Ar/^{39}Ar$ hornblende standard HB3gr. Zircon and titanite U-Pb geo/thermochronology have the potential to constrain the thermal evolution of the sample, which in turn can be used to evaluate whether this sample should be used as a primary standard and for inter-calibration studies. Evidence for protracted cooling or reheating can then be used to model the expected effects of volume diffusion of Ar in hornblende for this thermal history. Titanite is a U-rich

accessory phase with a nominal Pb closure temperature of ~600 °C that has been both empirically (Mezger et al., 1991) and experimentally (Cherniak, 2010) calibrated. The zircon U-Pb system has a high experimentally measured closure temperature of ~850-1000 °C (Cherniak, 2010) and has been shown to retain Pb at even higher temperatures over long periods of geologic time. In the case of sample HB3gr, zircon is anticipated to yield the age of crystallization within a granitic magma. A combination of U-Pb titanite and zircon data allows construction of a time-temperature path from magmatic crystallization through the closure of the U-Pb titanite system. The geologic significance of the hornblende $^{40}Ar/^{39}Ar$ data can then be evaluated by comparison to the time-temperature history based on U-Pb systematics.

7.2 3gr Sample Overview

The Lone Grove batholith is one of several syn- to post-tectonic granites that intrude metasedimentary and metaigneous rocks of Grenville origin and are collectively known as the Town Mountain Granite. The host rock for the standard hornblende was collected from the Petrick quarry (3gr) described by Zartman (1964) as a grayish-pink, coarse-grained porphyritic granite. This intrusive complex seems to have a simple history including: intrusion into the shallow crust, post-dating the Grenville orogony, followed by thermal relaxation with no apparent deformation. This simplicity made it an attractive case study area for Zartman's (1964) seminal paper that compared the K-Ar and Rb-Sr systematics of a variety of different mineral phases, examined the effects of weathering, and produced the first K-Ar date for what would later become the HB3gr hornblende standard of 1050±20 Ma (Fig. 1). Turner and others, (1971) used Hb3gr as a neutron flux monitor in an $^{40}Ar/^{39}Ar$ study of lunar rocks. The characteristics of HB3gr, including its relative antiquity and high K/Ca ratio, makes it an attractive standard for studying older rocks. Turner and others (1971), purified the original hornblende separate material from Zartman's 1964 study, publishing a new K-Ar date of 1060 ± 20 Ma (Fig. 1). This K-Ar was later recalculated by Roddick (1983) using the decay constants from Steiger and Jager (1977) yielding what has become the accepted date for Hb3gr of 1072±11 Ma (Fig. 1) (2σ including decay constant uncertainties). The overall reproducibility and apparent homogeneity of the 3gr Hornblende led to the development and use of the sample as a neutron flux monitor in several studies (Jourdan et al., 2004; Nomade et al., 2001; Renne, 2000; Verati et al., 2005). A recent effort by Jourdan and others (2006) to evaluate the reproducibility of Hb3gr at the single

grain level produced a large data set of single grain UV laser analyses on 125-200 μm material. In this study, over 70 single grain analyses from 3 different irradiation batches yield a mean date that lies within analytical uncertainties of the previously published K-Ar date (Fig. 1). The error-weighted mean date of a similar number of single grain analyses from just a single irradiation agree with the published K-Ar dates as well (Renne, 2000). Each of these studies used the sanidine separated from the Fish Canyon Tuff (FCs) standard as a neutron flux monitor, while more recently, Schwartz and Treiloff (2007) report data for HB3gr inter-calibrated and co-irradiated with 3 different K-Ar standards, yielding an age of 1073.6 ±9.2/ x Ma (2σ excluding decay constants). For a range of different irradiation procedures, laboratories, and external standards, the HB3gr standard yields a highly reproducible mean date that is in good agreement with the accepted K-Ar date (Fig. 1). Despite the overall agreement in mean age, single crystal UV laser analyses reveal a slight "$^{40}Ar/^{39}Ar$ age heterogeneity" as suggested by Jourdan and others (2006). The reported mean error-weighted date from this single grain study has an unreported MSWD = 4.6, a value that indicates that the scatter in the data cannot be explained by analytical uncertainties alone. The cause of single grain date variability has been suspected to be the result of alteration, variation in K/Ca ratios and/or variation in neutron flux or flux gradients, although these provide no definitive explanation for the variation observed in Hb3gr (Jourdan et al., 2006). A source of heterogeneity that has not been considered is that slow cooling could induce rounded ^{40}Ar diffusion profiles and heterogeneity in calculated dates between grains as well as within single grains. Constraining the thermal history using U-Pb geo/thermochronology permits testing of the hypothesis that slow cooling and volume diffusion as the cause of variable dates in Hb3gr.

7.3 U-Pb Methodology

Zircon grains were separated from 3gr using standard crushing and mineral separation techniques. All reported zircon U-Pb analyses are either single grain or fragments of single grains and the Chemical Abrasion method (CA-TIMS) (Mattinson, 2005) was applied to all. Prior to analysis several grains were imaged using CL and backscatter techniques (fig 2). Zircon images reveal a relatively simple texture suggesting a relatively single stage growth history. Over 10 single grain analyses were measured using the EARTHTIME tracer ET2525 (^{202}Pb, ^{205}Pb, ^{235}U, ^{233}U), allowing for the internal fractionation correction using the measured $^{202}Pb/^{205}Pb$. Mass

dependent fractionation of uranium isotopes were corrected for using the measured $^{233}U/^{235}U$ ratio. Both titanite data and an additional >10 zircon analyses are conducted using the EARTHTIME tracer solution ET535 (^{205}Pb, ^{235}U, ^{233}U) and externally correct for Pb-fractionation using fractionation coefficients determined from long-term measurements of isotopic standard NBS-981. Zircon dates are calculated using an isotopic composition of uranium ($^{238}U/^{235}U$) of 137.818 (Hiess et al., 2012). Uranium and lead data for both zircon and titanite were analyzed and U-Pb dates calculated using the programs *Tripoli* and *U-Pb Redux*, respectively (Bowring et al., 2011; McLean et al., 2011).

Individual titanite grains were dated following procedures similar to those of Schoene and Bowring (2006). This includes grain size measurement, a cleaning step in weak HNO_3, followed by U-Pb tracer addition and a 2 step dissolution procedures (HF/HCL). Separates of Pb and U are isolated and purified using HBr ion chromotogrpahy followed by measurement using the VG Sector Thermal Ionization Mass Spectrometer at MIT. Single grain titanite U-Pb data from grains of variable diffusion domain size allows evaluation of the granite's cooling rate through the titanite closure window for Pb diffusion. Numerical solutions to the diffusion/production equation allow forward modeling of the U-Pb system and an ability to match grain size vs. U-Pb date relationships derived from laboratory measurements with the forward modeled results for any time-temperature path. Diffusion kinetics for Pb in titanite from Cherniak (2010) are used and all modeled cooling paths are linear. Important initial conditions include the initial temperature, previously estimated at 750-850 °C (Smith et al., 2010), and start time, which is provided from by the zircon crystallization age. All numerical solutions assume a spherical grain geometry.

7.4 Results

7.4.1 U-Pb geo/thermochronologic data

U-Pb zircon dates are reported as thorium corrected $^{206}Pb/^{238}U$ dates ± uncertainty (Th/U_{Magma}= 4). Reported uncertainties are: analytical/analytical + tracer calibration/all uncertainties including decay constants. The mean error-weighted ^{238}U-^{206}Pb date using isotopic tracer ET2535 is 1090.10 ± 0.16/0.71/1.4 Ma, with an MSWD of 4.2 (n=9) (Fig 3). An additional zircon data set using isotopic tracer solution ET535, yields a statistically uniform population due to larger individual analysis uncertainties associated with Pb-fractionation, with a mean date of

1090.17 ± 0.20/0.47/1.3 Ma and an MSWD of 1.7 (Fig. 3 inset). The mean error-weighted value including decay constant uncertainties will be used to compare to the available K-Ar and $^{40}Ar/^{39}Ar$ data. Titanite yield a range of ^{238}U-^{206}Pb dates between 1082.2±0.75 and 1086.3±0.81 Ma over a range of grain sizes between ~30 and 110 microns. There is an ~ 6 My difference between the zircon and titanite U-Pb dates (Fig 3). No statistically significant mean data could be assigned to the titanite U-Pb data because of volume diffusion effects. For comparison to $^{40}Ar/^{39}Ar$ data the youngest date (of 1082.2±0.75 Ma) is used, corresponding to the smallest crystal and thus the closest effective closure temperature to Ar in hornblende. Results for both zircon and titanite U-Pb measurements are tabulated in table 1.

Several recent U-Pb zircon studies have worked to constrain the time-scales of granite pluton construction have revealed, tens to hundred of thousand year assembly times within a single granitic body (Schaltegger et al., 2009) . These studies have typically focused on younger granitic bodies, where the percentage uncertainty any U-Pb date (<0.05%) can easily resolve the prolonged pluton assembly in these younger granitoids. In the case of sample 3gr, U-Pb zircon data generated using single Pb isotopic tracer ET535 show a homogenous population of grains, leading to the interpretation of a single stage formation of the granitic body. Use of a Pb double spike ET2535 (^{205}Pb, ^{202}Pb) however, allows for the internal fractionation of Pb within the mass spectrometer a reduction in the uncertainty associated with Pb fractionation correction (the dominant source of uncertainty for the ^{205}Pb analyses), resulting in a far more precise individual analysis (Fig. 3 inset). The resulting data from several single grain measurements using this technique, provides sufficient precision to rule-out an instantaneous formation and cooling of the granite body, suggesting a slightly prolonged period of pluton assembly. This may be one of the first examples of ~1 Ga pluton assembly being resolved at the <1 Ma level.

7.4.2 Numerical Modeling of Titanite U-Pb and Hornblende $^{40}Ar/^{39}Ar$ systems

Numerical solutions to the diffusion equation allows for forward modeling of the titanite U-Pb system. Using a model start time of 1090 Ma and initial temperatures of 750-850 °C(Smith et al., 2010), the forward calculation can produce synthetic titanite U-Pb data for any tested time-temperature path. The measured grain size age relationship can be reasonably well fit by modeled data for a range of cooling rates between 30-50 °C/Ma (Fig 4). A single titanite analysis (T14) remains an outlier to these modeled grain size vs. age curves. All other measured titanite

dates are in good agreement with modeled results. The large range of estimates on start temperature/granite crystallization temperature are the dominant source of uncertainty contributing to the range of estimated cooling rates.

The cooling rates determined for the titanite U-Pb system can then be used as a maximum estimate of the cooling rate for the rock as the hornblende cooled through the Ar Partial Retention Zone (PRZ). Igneous rocks emplaced in the upper crust are assumed to follow exponential cooling paths and thus it is likely that cooling rate slowed through the lower bound of the ^{40}Ar Hornblende PRZ; resolution of this is not possible given the relatively large uncertainties on ^{40}Ar/^{39}Ar measurements. Forward modeling of the ^{40}Ar hornblende system allows us to predict the variation in measured date with grain size that could result from the upper bound on this cooling rate. The influence that slow cooling and diffusive loss of ^{40}Ar for the grain sizes analyzed in previous studies (Jourdan et al., 2006) can then be evaluated as a potential source of ^{40}Ar/^{39}Ar age heterogeneity observed on the single grain scale. Using the range of cooling rates constrained by the titanite U-Pb data, the total range in ^{40}Ar/^{39}Ar dates induced by volume diffusion is less than 1 My for the reported grain size range. However, if we assume that these grains did not obey as a single domain, and that the effective diffusion dimension may be as low as 1 μm, forward model calculations will produce a spread in dates no greater than ~6 my, just a small percentage of the observed range in ^{40}Ar-^{39}Ar dates (>20 Ma), suggesting that volume diffusion cannot account for all of the observed age heterogeneity revealed by single grain ^{40}Ar/^{39}Ar studies. The values of modeled ^{40}Ar/^{39}Ar dates for these cooling rates lies between ~1078.0-1081.5 Ma, a value that agrees within uncertainty (including decay constants) with the average of the previously published ^{40}Ar/^{39}Ar data.

7.5 Discussion

7.5.1 U-Pb ^{40}Ar/^{39}Ar comparison

The available ^{40}Ar/^{39}Ar and K-Ar data for Hb3gr must be recalculated using revised decay constant and FCs values to permit a systematic comparison with the U-Pb data presented here. The previously published ^{40}Ar/^{39}Ar and K-Ar dates and associated uncertainties for Hb3gr have been recalculated using three different data reduction methods: 1) Renne and others (1998) used decay constants from Steiger and Jager (1977) and a FCs value of 28.02 Ma; 2) Kuiper and others (2008) used decay constants from Min and others (2000) and an orbitally tuned date for

the FCs of 28.201 Ma; 3) decay constants and FCs values defined in Renne and others (Renne et al., 2011; Renne et al., 2010). All recalculated data are reported at the 2σ level with uncertainties that include decay constants. Presented in Table 2 are the comparisons between the zircon and titanite dates for 3gr reported here and the previously published K-Ar (Turner et al., 1971) and $^{40}Ar/^{39}Ar$ dates (Jourdan et al., 2006; Renne, 2000).

In all nearly all comparisons between the recalculated K-Ar/$^{40}Ar/^{39}Ar$ and U-Pb data, the large uncertainties on ^{40}K prevent the ability to resolve any difference between the older U-Pb zircon date and the hornblende K-Ar/Ar-Ar date. The singular acceptation to this, the re-reduction of data from Jourdan and others (2006) using decay constants and FCs values from Renne and others (2011), results in a resolvable difference of ~7 ± 5 My (0.5 ± 0.4 %). The persistence of a bias between the $^{40}Ar/^{39}Ar$ hornblende and zircon U-Pb systems even after using the most recent estimates of decay constants and FCs suggests that slow cooling and the diffusive loss of Ar from hornblende may be contributing to the difference between U-Pb zircon and $^{40}Ar/^{39}Ar$ hornblende dates. This is supported by the observation that the recalculated $^{40}Ar/^{39}Ar$ dates and the U-Pb titanite dates overlap within uncertainties. This allows us to make a strong case for the hypothesis that the Ar in hornblende system is recording the cooling of the Lone Grove pluton.

7.5.2 Time-temperature path for Hb3gr

Geo/thermochronologic data from sample 3gr collected from the Lone Grove Pluton, can be used to reconstruct its time-temperature history. U-Pb zircon dates are interpreted to record crystallization of the granitic pluton at a 1090.10 ± 0.16 Ma. The dispersion in single grain zircon U-Pb dates results in a relatively high MSWD of 4.2, and suggests that the zircon U-Pb dates may record a prolonged crystallization history. Subsequent to crystallization, both U-Pb titanite and $^{40}Ar/^{39}Ar$ hornblende thermochronometers record the sample's cooling path. The resolvable difference in time of ~5± my revealed by the zircon and titanite data sets indicates cooling at rates between 30-50 °C/my. This cooling rate is consistent with the modeled grain size vs. date relationships derived from numerical modeling of titanite U-Pb data (Fig 4). The dates produced using the decay constants from Min and others (2000) and Renne and others (2010) fall on or very near the time temperature paths predicted from the titanite U-Pb data (Fig. 5). Construction of this time-temperature path strongly suggests that both the titanite U-Pb system

and hornblende $^{40}Ar/^{39}Ar$ system have *not* remained closed to radiogenic daughter throughout the history of the sample and records the cooling history of the HB3gr host rock. This indicates that this $^{40}Ar/^{39}Ar$ standard is not suitable for intersystem comparison studies and the refinement of the $^{40}Ar/^{39}Ar$ system.

7.6 Conclusions

The reduction of intersystem biases between the $^{40}Ar/^{39}Ar$ and U-Pb system by intercomparision requires: 1) precise and accurate dates for a single sample using both systems, and 2) a sample where the $^{40}Ar/^{39}Ar$ and U-Pb systems are closed to parent/daughter loss over the entire history of the sample. For sample HB3gr, new high-precision U-Pb zircon dates using CA-TIMS are presented here. A Th-corrected ^{238}U-^{206}Pb mean error weighted date of 1090.10± 1.4 Ma (2σ including decay constants) remains ~7 My older than the K-Ar or $^{40}Ar/^{39}Ar$ dates, recalculated using new decay constants. Single grain titanite U-Pb dates for the HB3gr yield a range of ^{238}U-^{206}Pb dates between 1082.2±0.75 and 1086.3±0.81 Ma, approximately 6 ± 2 my younger than the zircon date. This difference in dates and forward models used to predict the grain size vs. age relationship in the U-Pb titanite system indicates that the sample experienced protracted cooling after initial crystallization at 1090 Ma. The reconstruction of a time-temperature path for the host rock of the hornblende $^{40}Ar/^{39}Ar$ standard HB3gr reveals that cooling at rates between 30-50 °C/Ma have also likely influenced the $^{40}Ar/^{39}Ar$ and K-Ar data. The implication of this history is that HB3gr is not an acceptable sample for intersystem comparison studies. It also suggests that any future use of this standard in $^{40}Ar/^{39}Ar$ studies must consider the effects of Ar-loss through volume diffusion.

7.7 Figure Captions

Fig. 1 Summary of K-Ar and ^{40}Ar-^{39}Ar dates for standard HB3gr plotted against the year of publication for each data point. All uncertainties are at the one sigma level and do not include the decay constant uncertainties.

Fig. 2 Photomicrograph of zircon grains from Hb3gr using transmitted (A) and cathode luminescence(B). Transmitted light images reveal zircon grains contain melt or apatite inclusions, either of which could contribute to common Pb to a zircon analysis. Use of Mattinson's (2005) chemical abrasion technique removes these inclusions from the analyzed

zircon. Lack of multiple growth histories, embayed grains or inherited cores shown in the Cathode luminescence images(B) suggests a single stage growth history for zircons from Hb3gr.

Fig. 3 U-Pb Concordia diagram displaying both zircon U-Pb analyses and titanite U-Pb analyses. Only the zircon grains dated using double Pb tracer ET2535 are shown on condordia. The figure inset plots the Th-corrected ^{238}U-^{206}Pb dates for titanite and zircons dated using both single and double Pb tracers. A resolvable difference of ~5 my between zircon and titanite data is apparent in both diagrams.

Fig. 4 Titanite ^{238}U-^{206}Pb date (Ma) plotted (black diamonds) against the diameter for each analyses (μm). Grain size vs. age correlations can be utilized to determine a cooling rate (°C/Ma) through the titanite Pb partial retention zone. Forward calculated U-Pb dates for the same range of grain sizes and over a range of potential thermal histories are plotted for comparison with the real data. A range of system start temperatures between 750- 850 ° C and cooling rates between 25-50 °C/Ma are tested. Diffusion kinetics for titanite are from Cherniak (2010).

Fig. 5 Plot of a reconstructed time-temperature path for 3gr. Zircon U-Pb analyses and estimates of initial temperature between 750-850 °C (Smith et al., 2010) constrain the initial conditions. Cooling rates between 30-50 °C/Ma from this range of temperatures are consistent with the measured titanite U-Pb data. For comparison, the ^{40}Ar-^{39}Ar data from Jourdan and others (2006) is plotted using the decay constant and fish canyon tuff monitor ages described in the text. The uncertainties are reported at the 2σ level and include those from decay constants.

7.8 References:

Bowring, J.F., McLean, N.M., Bowring, S.A., 2011. Engineering cyber infrastructure for U-Pb geochronology: Tripoli and U-Pb_Redux. Geochem. Geophys. Geosyst. 12, Q0AA19.

Cherniak, D.J., 2010. Diffusion in Accessory Minerals: Zircon, Titanite, Apatite, Monazite and Xenotime. Reviews in Mineralogy and Geochemistry 72, 827-869.

Hiess, J., Condon, D.J., McLean, N., Noble, S.R., 2012. 238U/235U Systematics in Terrestrial Uranium-Bearing Minerals. Science 335, 1610-1614.

Jourdan, F., FÈraud, G., Bertrand, H., Kampunzu, A.B., Tshoso, G., Le Gall, B., Tiercelin, J.J., Capiez, P., 2004. The Karoo triple junction questioned: evidence from Jurassic and Proterozoic 40Ar/39Ar ages and geochemistry of the giant Okavango dyke swarm (Botswana). Earth and Planetary Science Letters 222, 989-1006.

Jourdan, F., Renne, P.R., 2007. Age calibration of the Fish Canyon sanidine 40Ar/39Ar dating standard using primary K-Ar standards. Geochimica et Cosmochimica Acta 71, 387-402.

Jourdan, F., Verati, C., FÈraud, G., 2006. Intercalibration of the Hb3gr 40Ar/39Ar dating standard. Chemical Geology 231, 177-189.

Kuiper, K.F., Deino, A., Hilgen, F.J., Krijgsman, W., Renne, P.R., Wijbrans, J.R., 2008. Synchronizing Rock Clocks of Earth History. Science 320, 500-504.

Kwon, J., Min, K., Bickel, P.J., Renne, P.R., 2002. Statistical Methods for Jointly Estimating the Decay Constant of ^40K and the Age of a Dating Standard. Mathematical Geology 34, 457-474.

Mattinson, J.M., 2005. Zircon U-Pb chemical abrasion ("CA-TIMS") method: Combined annealing and multi-step partial dissolution analysis for improved precision and accuracy of zircon ages. Chemical Geology 220, 47-66.

McLean, N.M., Bowring, J.F., Bowring, S.A., 2011. An algorithm for U-Pb isotope dilution data reduction and uncertainty propagation. Geochem. Geophys. Geosyst. 12, Q0AA18.
Mezger, K., Rawnsley, C.M., Bohlen, S.R., Hanson, G.N., 1991. U-Pb Garnet, Sphene, Monazite, and Rutile Ages: Implications for the Duration of High-Grade Metamorphism and Cooling Histories, Adirondack Mts., New York. The Journal of Geology 99, 415-428.
Min, K., Mundil, R., Renne, P.R., Ludwig, K.R., 2000. A test for systematic errors in 40Ar/39Ar geochronology through comparison with U/Pb analysis of a 1.1-Ga rhyolite. Geochimica et Cosmochimica Acta 64, 73-98.
Nomade, S., Chen, Y., FÈraud, G., Pouclet, A., ThÈveniaut, H., 2001. First paleomagnetic and 40Ar/39Ar study of Paleoproterozoic rocks from the French Guyana (Camopi and Oyapok rivers), northeastern Guyana Shield. Precambrian Research 109, 239-256.
Renne, P.R., 2000. 40Ar/39Ar age of plagioclase from Acapulco meteorite and the problem of systematic errors in cosmochronology. Earth and Planetary Science Letters 175, 13-26.
Renne, P.R., Balco, G., Ludwig, K.R., Mundil, R., Min, K., 2011. Response to the comment by W.H. Schwarz et al. on ‚ÄúJoint determination of 40K decay constants and 40Ar‚àó/40K for the Fish Canyon sanidine standard, and improved accuracy for 40Ar/39Ar geochronology‚Äù by P.R. Renne et al. (2010). Geochimica et Cosmochimica Acta 75, 5097-5100.
Renne, P.R., Mundil, R., Balco, G., Min, K., Ludwig, K.R., 2010. Joint determination of 40K decay constants and 40Ar*/40K for the Fish Canyon sanidine standard, and improved accuracy for 40Ar/39Ar geochronology. Geochimica et Cosmochimica Acta 74, 5349-5367.
Renne, P.R., Swisher, C.C., Deino, A.L., Karner, D.B., Owens, T.L., DePaolo, D.J., 1998. Intercalibration of standards, absolute ages and uncertainties in 40Ar/39Ar dating. Chemical Geology 145, 117-152.
Roddick, J.C., 1983. High precision intercalibration of 40Ar-39Ar standards. Geochimica et Cosmochimica Acta 47, 887-898.
Schaltegger, U., Brack, P., Ovtcharova, M., Peytcheva, I., Schoene, B., Stracke, A., Marocchi, M., Bargossi, G.M., 2009. Zircon and titanite recording 1.5 million years of magma accretion, crystallization and initial cooling in a composite pluton (southern Adamello batholith, northern Italy). Earth and Planetary Science Letters 286, 208-218.
Schoene, B., Bowring, S., 2006. U–Pb systematics of the McClure Mountain syenite: thermochronological constraints on the age of the 40Ar/39Ar standard MMhb. Contributions to Mineralogy and Petrology 151, 615-630.
Schwarz, W.H., Trieloff, M., 2007. Intercalibration of 40Ar-39Ar age standards NL-25, HB3gr hornblende, GA1550, SB-3, HD-B1 biotite and BMus/2 muscovite. Chemical Geology 242, 218-231.
Smith, R.K., Gray, W., Gibbs, T., Gallegos, M.A., 2010. Petrogenesis of Mesoproterozoic granitic plutons, eastern Llano Uplift, central Texas, USA. Lithos 118, 238-254.
Steiger, R.H., Jager, E., 1977. Subcommission of geochronology: convention on the use of decay constants in geo- and cosmochronology. Earth and Planetary Science Letters 6, 359-362.
Turner, G., Huneke, J.C., Podosek, F.A., Wasserburg, G.J., 1971. 40Ar-39Ar ages and cosmic ray exposure ages of Apollo 14 samples. Earth and Planetary Science Letters 12, 19-35.
Verati, C., Bertrand, H., FÈraud, G., 2005. The farthest record of the Central Atlantic Magmatic Province into West Africa craton: Precise 40Ar/39Ar dating and geochemistry of Taoudenni basin intrusives (northern Mali). Earth and Planetary Science Letters 235, 391-407.
Zartman, R.E., 1964. A Geochronologie Study of the Lone Grove Pluton from the Llano Uplift, Texas. Journal of Petrology 5, 359-409.

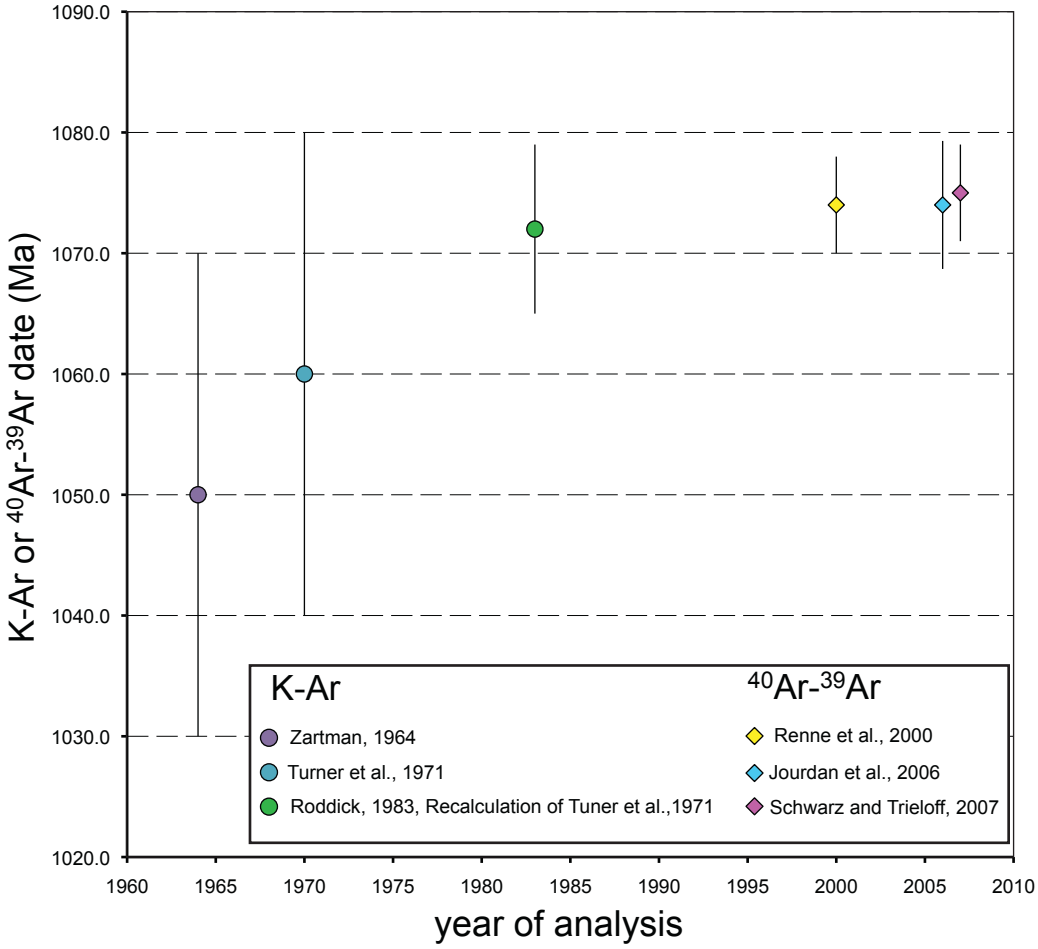
1090.0
1080.0
1070.0
1060.0
1050.0
1040.0
1030.0
1020.0
K-Ar or 40Ar-39Ar date (Ma)
1960
1965
1970
1975
1980
1985
1990
1995
2000
2005
2010
year of analysis
K-Ar
Zartman, 1964
Turner et al., 1971
Roddick, 1983, Recalculation of Tuner et al.,1971
40Ar-39Ar
Renne et al., 2000
Jourdan et al., 2006
Schwarz and Trieloff, 2007

Figure 7.1

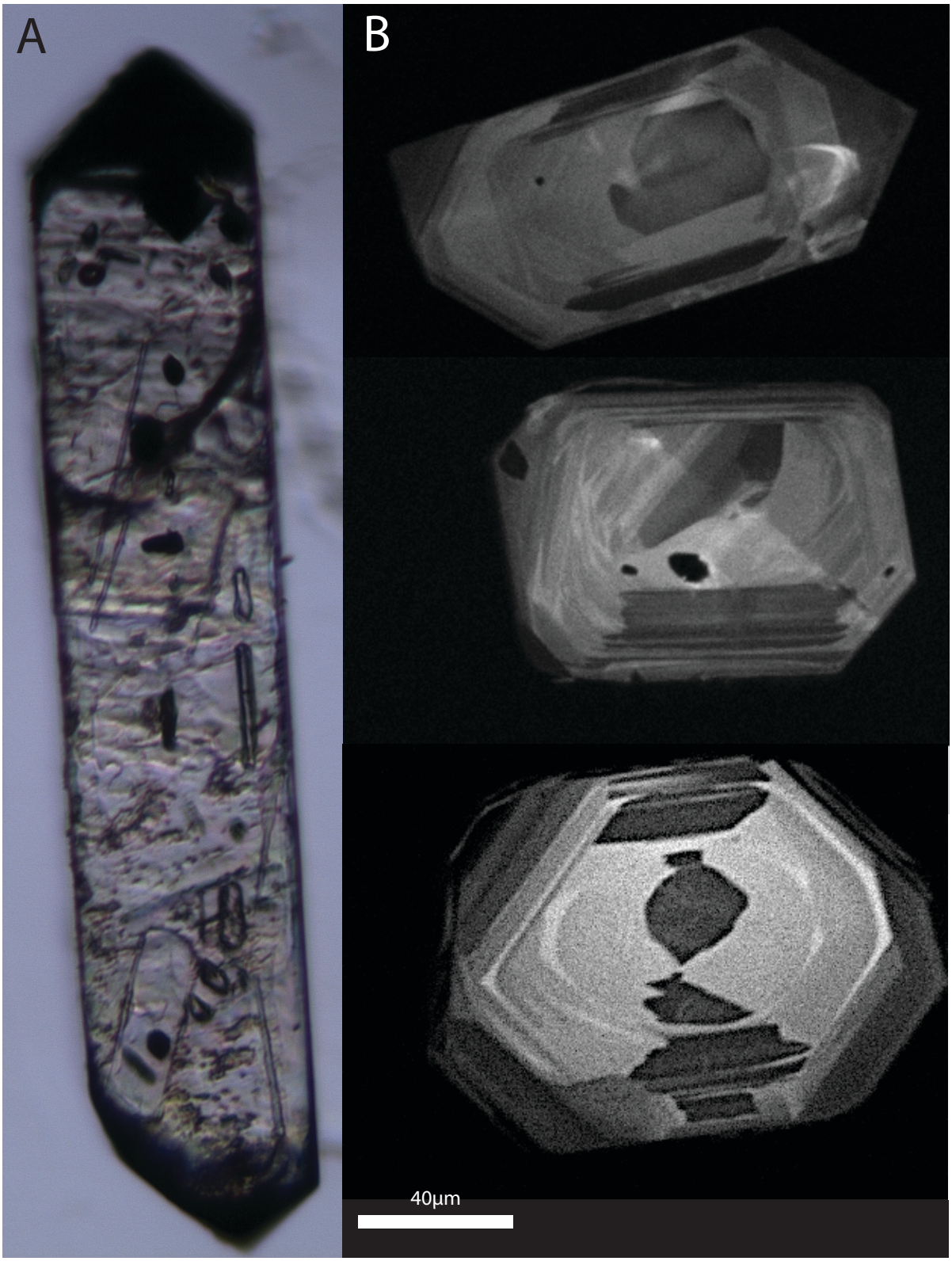

Figure 7.2

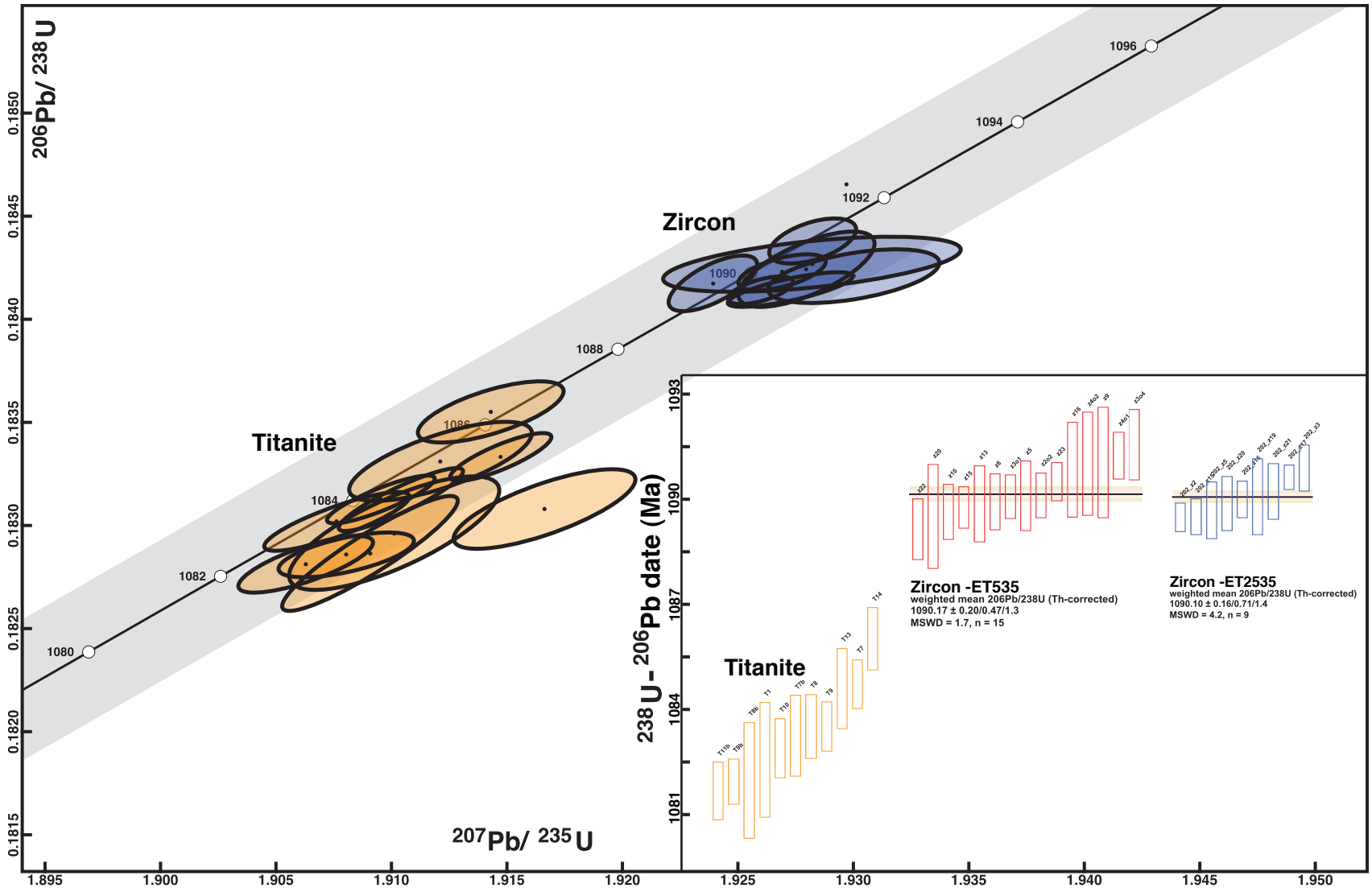
206Pb/ 238U
207Pb/ 235U
Zircon
Titanite
1080
1082
1084
1086
1088
1090
1092
1094
1096
0.1815
0.1820
0.1825
0.1830
0.1835
0.1840
0.1845
0.1850
1.895
1.900
1.905
1.910
1.915
1.920
1.925
1.930
1.935
1.940
1.945
1.950
238U-206Pb date (Ma)
1081
1084
1087
1090
1093
Titanite
Zircon -ET535
weighted mean 206Pb/238U (Th-corrected)
1090.17 ± 0.20/0.47/1.3
MSWD = 1.7, n = 15
Zircon -ET2535
weighted mean 206Pb/238U (Th-corrected)
1090.10 ± 0.16/0.71/1.4
MSWD = 4.2, n = 9

Figure 7.3

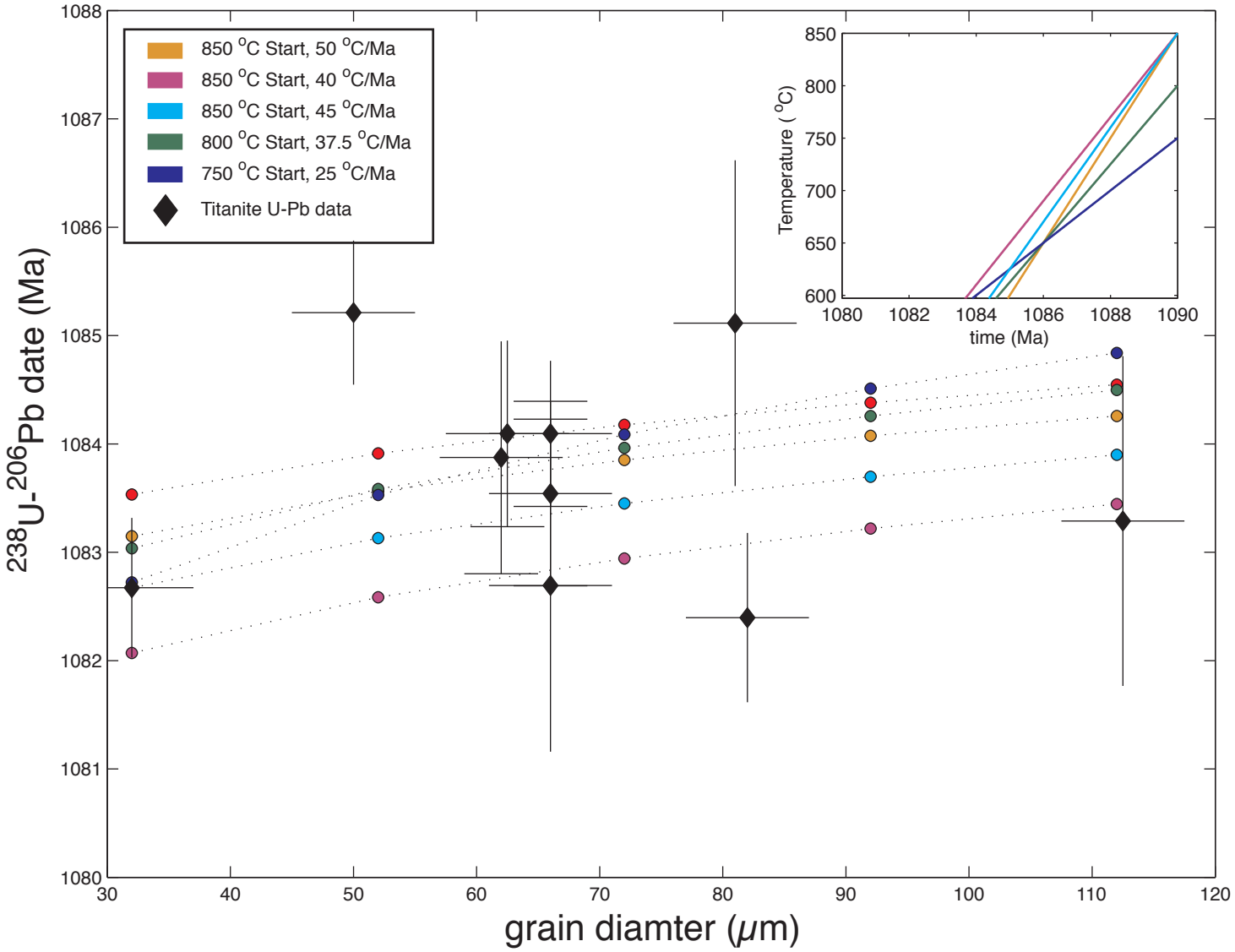
850 °C Start, 50 °C/Ma
850 °C Start, 40 °C/Ma
850 °C Start, 45 °C/Ma
800 °C Start, 37.5 °C/Ma
750 °C Start, 25 °C/Ma
Titanite U-Pb data
238U-206Pb date (Ma)
grain diamter (μm)
Temperature (°C)
time (Ma)

Figure 7. 4

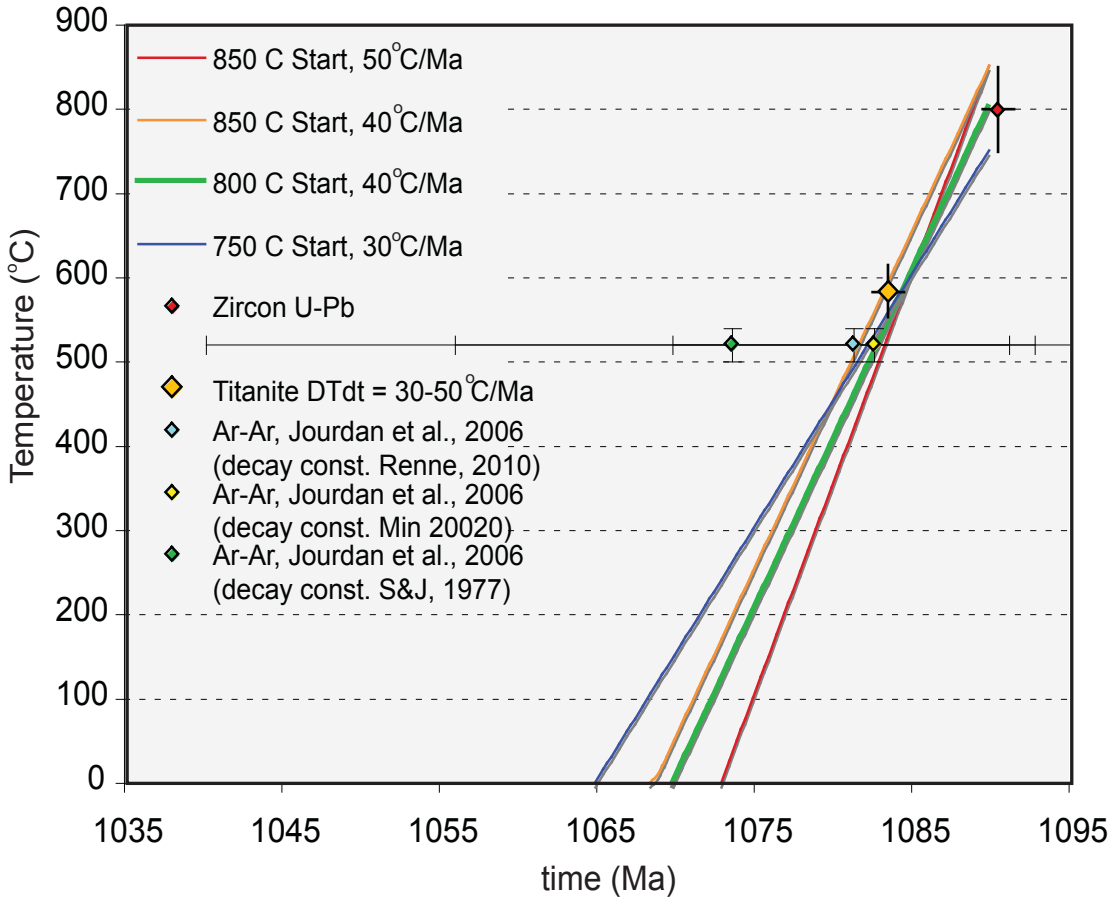
900
800
700
600
500
400
300
200
100
0
Temperature (°C)
1035
1045
1055
1065
1075
1085
1095
time (Ma)
850 C Start, 50°C/Ma
850 C Start, 40°C/Ma
800 C Start, 40°C/Ma
750 C Start, 30°C/Ma
Zircon U-Pb
Titanite DTdt = 30-50°C/Ma
Ar-Ar, Jourdan et al., 2006
(decay const. Renne, 2010)
Ar-Ar, Jourdan et al., 2006
(decay const. Min 20020)
Ar-Ar, Jourdan et al., 2006
(decay const. S&J, 1977)

Figure 7.5

3gr

	Dates (Ma)									Composition				Isotopic Ratios								Correlation Coefficients	
Fraction	206Pb/ 238U a	±2σ abs	206Pb/ 238U <Th> b	±2σ abs	207Pb/ 235U a	±2σ abs	207Pb/ 206Pb a	±2σ abs	Corr. coef.	% disc c	Th/ U d	Pb* (pg) e	Pbc (pg) f	Pb*/ Pbc g	206Pb/ 204Pb h	206Pb/ 238U i	±2σ %	207Pb/ 235U i	±2σ %	207Pb/ 206Pb i	±2σ %	206Pb/238U - 207Pb/235U	Fraction
Titanite																							
T1	1083.10	1.50	1083.10	1.50	1084.60	1.60	1087.80	3.20	0.8	0.43	0.48	84	4.5	19	1141	0.18295	0.15	1.9101	0.24	0.07572	0.16	0.75	T1
T7	1085.07	0.63	1085.15	0.63	1086.23	0.76	1088.60	1.40	0.8	0.32	0.42	594	20.55	29	1786	0.18332	0.063	1.9147	0.11	0.075754	0.069	0.83	T7
T7b	1083.70	1.10	1083.80	1.10	1086.90	1.40	1093.30	2.90	0.7	0.88	0.47	207	8.13	25	1550	0.18306	0.11	1.9166	0.21	0.07593	0.14	0.74	T7b
T8	1083.95	0.83	1084.03	0.83	1084.73	0.94	1086.30	1.50	0.9	0.22	0.47	441	16	28	1684	0.18311	0.083	1.9104	0.14	0.075668	0.074	0.9	T8
T8b	1082.50	1.50	1082.60	1.50	1084.30	1.30	1087.80	1.70	0.9	0.48	0.5	242	9.59	25	1528	0.18285	0.15	1.9091	0.2	0.075723	0.084	0.92	T8b
T9	1083.95	0.63	1084.03	0.63	1084.42	0.81	1085.40	1.50	0.9	0.13	0.63	599	22.16	27	1587	0.18311	0.063	1.9095	0.12	0.075633	0.073	0.87	T9
T9b	1082.48	0.59	1082.57	0.59	1083.90	1.00	1086.80	2.50	0.6	0.39	0.39	165	7.99	21	1288	0.18284	0.059	1.908	0.15	0.075685	0.12	0.62	T9b
T10	1083.37	0.78	1083.45	0.78	1083.80	1.10	1084.50	2.20	0.8	0.11	0.62	257	15.04	17	1011	0.18301	0.078	1.9076	0.16	0.075602	0.11	0.84	T10
T11b	1082.24	0.75	1082.32	0.75	1083.30	1.00	1085.40	2.10	0.8	0.29	0.51	339	13.14	26	1561	0.1828	0.075	1.9063	0.15	0.075634	0.11	0.77	T11b
T13	1085.00	1.00	1085.00	1.00	1085.30	1.40	1086.10	3.00	0.7	0.1	0.52	413	16.97	24	1469	0.1833	0.1	1.9121	0.21	0.07566	0.15	0.71	T13
T14	1086.26	0.81	1086.34	0.81	1086.10	1.10	1085.70	2.50	0.7	-0.05	0.5	149	5.77	26	1562	0.18354	0.081	1.9143	0.16	0.075646	0.12	0.68	T14
zircon --ET535																							
z2o2	1090.07	0.58	1090.15	0.58	1090.33	0.82	1090.90	1.60	0.8	0.07	0.45	68	0.52	131	7885	0.18423	0.058	1.9265	0.12	0.075874	0.081	0.82	z2o2
z3o1	1090.02	0.57	1090.10	0.57	1090.03	0.79	1090.10	1.60	0.8	0	0.6	72.4	0.4	182	10539	0.18423	0.057	1.9257	0.12	0.075844	0.077	0.82	z3o1
z3o4	1091.40	0.91	1091.48	0.91	1089.40	2.00	1085.30	5.00	0.7	-0.57	0.68	23.1	0.69	33	1915	0.18448	0.091	1.9237	0.3	0.07566	0.25	0.65	z3o4
z4o1	1091.11	0.61	1091.19	0.61	1091.40	1.10	1091.90	2.50	0.8	0.07	0.66	31.7	0.42	76	4372	0.18443	0.061	1.9295	0.17	0.075914	0.12	0.78	z4o1
z4o2	1090.90	1.40	1091.00	1.40	1091.00	1.60	1091.10	3.60	0.7	0.02	0.66	23.9	0.37	64	3660	0.18439	0.13	1.9283	0.24	0.07588	0.18	0.7	z4o2
z5	1090.05	0.91	1090.13	0.91	1090.80	2.00	1092.30	4.90	0.6	0.2	0.59	72	2.44	30	1731	0.18423	0.09	1.9278	0.29	0.07593	0.25	0.64	z5
z6	1089.88	0.73	1089.97	0.73	1090.80	1.10	1092.70	2.50	0.8	0.26	0.47	68.3	0.87	79	4722	0.1842	0.073	1.928	0.17	0.075945	0.12	0.78	z6
z9	1090.90	1.50	1091.00	1.50	1091.40	1.60	1092.00	0.00	1.4	0.13	0.59	32.5	0.43	76	4423	0.18439	0.14	1.9296	0.24	0	0	1.4	z9
z10	1089.62	0.71	1089.71	0.71	1089.45	0.87	1089.10	2.10	0.6	-0.05	0.45	92	0.64	144	8684	0.18415	0.071	1.924	0.13	0.075808	0.1	0.6	z10
z13	1089.80	1.00	1089.90	1.00	1090.20	1.60	1090.80	4.60	0.3	0.09	0.54	32.1	0.53	61	3572	0.18419	0.099	1.926	0.24	0.07587	0.23	0.33	z13
z15	1089.74	0.53	1089.82	0.53	1090.34	0.87	1091.50	1.90	0.8	0.16	0.63	68.6	0.38	179	10313	0.184175	0.053	1.9266	0.13	0.0759	0.092	0.79	z15
z16	1090.70	1.20	1090.80	1.20	1091.70	2.20	1093.70	5.40	0.7	0.28	0.43	9.4	0.32	29	1780	0.18436	0.12	1.9306	0.33	0.07598	0.27	0.65	z16
z20	1089.50	1.40	1089.60	1.40	1090.60	1.80	1092.80	4.80	0.5	0.3	0.51	48.6	0.86	56	3359	0.18413	0.14	1.9273	0.28	0.07595	0.24	0.51	z20
z22	1089.16	0.78	1089.24	0.78	1089.50	1.40	1090.10	3.00	0.9	0.09	0.45	62.6	1.13	55	3336	0.18407	0.078	1.9241	0.21	0.07585	0.15	0.86	z22
z23	1090.42	0.50	1090.50	0.50	1090.70	1.30	1091.30	2.80	1.1	0.08	0.44	37.7	0.55	69	4154	0.184299	0.05	1.9276	0.2	0.07589	0.14	1.1	z23
zircon ET2535																							
202_z2	1089.47	0.36	1089.55	0.36	1090.15	0.48	1091.50	1.20	0.6	0.18	0.5	71.2	0.24	295	17515	0.184126	0.036	1.926	0.073	0.075898	0.049	0.61	202_z2
202_z3	1090.78	0.60	1090.86	0.60	1090.93	0.65	1091.20	1.70	0.5	0.04	0.59	55.5	0.36	153	8900	0.18437	0.059	1.9282	0.098	0.075888	0.078	0.51	202_z3
202_z4	1092.27	0.82	1092.35	0.82	1091.43	0.95	1089.80	2.40	0.5	-0.23	0.54	18.1	0.25	74	4353	0.18464	0.082	1.9297	0.14	0.075832	0.12	0.52	202_z4
202_z5	1089.66	0.74	1089.74	0.74	1089.43	0.67	1089.00	1.50	0.7	-0.06	0.54	37.9	0.19	197	11557	0.18416	0.073	1.9239	0.1	0.075803	0.067	0.67	202_z5
202_z15	1089.50	0.46	1089.58	0.46	1090.59	0.94	1092.80	2.20	0.8	0.3	0.6	45.1	0.64	71	4109	0.18413	0.046	1.9273	0.14	0.075947	0.1	0.77	202_z15
202_z16	1089.95	0.48	1090.03	0.48	1090.47	0.66	1091.50	1.60	0.6	0.14	0.37	70.6	0.42	166	10209	0.184213	0.047	1.9269	0.098	0.075899	0.074	0.58	202_z16
202_z17	1090.54	0.31	1090.62	0.31	1090.54	0.39	1090.50	2.70	-4.0	0	0.59	39.5	0.44	89	5175	0.184321	0.031	1.9271	0.058	0.07586	0.13	-4	202_z17
202_z19	1090.00	1.00	1090.10	1.00	1090.80	1.00	1092.40	2.30	0.7	0.22	0.51	25.5	0.34	75	4434	0.18423	0.099	1.928	0.15	0.075934	0.11	0.68	202_z19
202_z20	1089.85	0.71	1089.93	0.71	1091.50	1.30	1094.90	3.40	0.5	0.46	0.48	28.4	0.63	45	2702	0.18419	0.071	1.93	0.19	0.07603	0.17	0.5	202_z20
202_z21	1090.16	0.73	1090.24	0.73	1090.90	2.20	1092.40	6.00	0.5	0.21	0.43	26.3	1.3	20	1238	0.18425	0.072	1.9282	0.33	0.07593	0.3	0.53	202_z21

a Isotopic dates calculated using the decay constants λ238 = 1.55125E-10 and λ235 = 9.8485E-10 (Jaffey et al. 1971).
b Corrected for initial Th/U disequilibrium using radiogenic 208Pb and Th/U[magma] = 4.
c % discordance = 100 - (100 * (206Pb/238U date) / (207Pb/206Pb date))
d Th contents calculated from radiogenic 208Pb and the 207Pb/206Pb date of the sample, assuming concordance between U-Th and Pb systems.
e Total mass of radiogenic Pb.
f Total mass of common Pb.
g Ratio of radiogenic Pb (including 208Pb) to common Pb.
h Measured ratio corrected for fractionation and spike contribution only.
i Measured ratios corrected for fractionation, tracer, blank and, where applicable, initial common Pb.

Table 7.1

Decay Constants/	Fish Canyon Tuff Ar- data source	abs dif zircon	unc	abs dif titanite	unc
1/-	K-Ar (Turner et al., 1971)	18.1	20.0	10.2	18.1
1/a	Ar-Ar (Jourdan et al. 2006)	16.5	17.7	8.6	16.5
1/a	Ar-Ar (Renne 2000)	16.1	16.1	8.2	16.1
2/-	K-Ar (Turner et al., 1971)	13.2	24.0	5.3	24.0
2/b	Ar-Ar (Jourdan et al. 2006)	6.6	42.6	-1.3	42.6
2/b	Ar-Ar (Renne 2000)	8.1	43.2	0.2	43.2
3/-	K-Ar (Turner et al., 1971)	11.2	12.8	3.4	12.8
3/c	Ar-Ar (Jourdan et al. 2006)	7.4	5.3	-0.5	5.2
3/c	Ar-Ar (Renne 2000)	8.4	11.2	0.5	11.1

Decay constants: 1 = Steiger and Jager, 1971, 2= Min et al., 2000, 3=Renne et al., 2010

FCT values : a = Renne et al., 1998, b = Kuiper et al., 2008, c = Renne et al., 2010

Table 7.2

Appendix:

A.1 Chapter 3 appendix

Methods

Lithosphere thermal models

The thermal processes operating in the lithosphere include heat conduction, heat producing element decay, exhumation or burial and lithosphere thickness. To model this setting we employed a thermal model consisting of a one-dimensional, conductive depth profile in a reference frame fixed with respect to Earth's surface. Source and advection terms are included to account for heat production and advection. A 1-D thermal model is suitable for studying the deep lithosphere, as lateral variations in isotherms at depths corresponding to 400 °C or higher cannot be induced by surface topography and are unlikely within the stable continental interior. Lithosphere exhumation is simulated using a semi-lagrangian method to quantify the effects of sample cooling/warming by uplift/burial through the conductive column towards/away the heat-loss surface. A source term accounts for the heat contributed from the decay of heat producing elements (HPE). Total lithosphere HPE concentrations are allocated between the upper, middle and lower crusts and the mantle lithosphere. Compiled data sets of HPE concentrations from (*12, 13*) were used (appendix Table 2). A model for temperature dependent thermal diffusivity is employed for the crust (*30*) and an average value for olivine thermal diffusivity is used for the mantle (*31-33*). Input parameters that match the regional setting for the lithosphere are used, including a tested range of lithosphere thicknesses between 200-250 km, consistent with seismologic (*34*) and mantle xenolith data (*16*), and upper, middle and lower crustal thicknesses derived from seismic velocity models for the regions crust (*14*). The initial geothermal gradient was chosen by assuming the maximum temperature condition associated with each lithosphere layer; crust at 700 °C, lower crust 900 °C, and mantle lithosphere 1450 °C. Varying these initial temperature conditions has a negligible effect on the lower temperature U-Pb thermochronometric data, as these variations in initial geothermal gradient only effect the rate and magnitude of the initial relaxation from high temperatures and does not effect the rate of long-term slow cooling or absolute temperatures experienced by lower crustal samples, the later of which is controlled by lithosphere thickness and sample depth. Surface temperature is fixed to 10 °C, while the basal boundary condition employs a dirichlet boundary condition that changes with our estimate of the absolute temperature and secular cooling rate of the mantle. A complied literature summary of mantle secular cooling rates and absolute mantle temperatures is provided by (*35*) and references therein. These values are supported by more recent work by (*36, 37*) The mantle secular cooling rate and absolute temperature at 2.0 Ga used for this study is 0.05 ºC/Ma and 1450 ºC respectively. Varying these each of these parameters over a broader range of reported values (*35*) has little to no effect on the lower crustal thermal histories (<3% difference in maximum Δ U-Pb) and this study's conclusion that lithosphere exhumation is low (Fig S1). In addition to exhumation, both lithosphere thickness and HPE distribution and concentration play a secondary role in controlling the rate of heat loss and the topology of U-Pb data. Exploring a minimum to maximum range of compiled HPE concentrations from compiled databases for the upper, middle and lower crust (*12*) as well as the mantle lithosphere (*13*) yields a <20% variation in the maximum Δ U-Pb when compared to the nominal HPE values (Fig S1) (*12, 13*). Varying the lithosphere thickness ±25 km about 225 km yields variations in Δ U-Pb of <15 % (Fig S1). If in reality the HPE concentration were lower than the nominal values and lithosphere thickness were 25 km less than the modeled value any comparison between modeled and measured data would overestimate exhumation by up to 0.0025 km/Ma. A maximum exhumation rate of 0.0025 km/Ma for a lithosphere thickness of 250 km and HPE concentrations at a minimum is consistent with both the

modeled data for 0.00 km/Ma and the measured U-Pb data presented in the main text. For this reason the 0.0025-0.005 km/Ma can serve as a maximum range in exhumation rate.

Diffusion models for the U-Pb system

Resulting time-temperature paths from the thermal model at lower crustal depths are then exported to a forward model to calculate the U-Pb data that would result for this thermal history. The spherical form of the production-diffusion equation is solved using a Crank-Nicholson scheme resulting in a singular internal Pb diffusion profiles for the tested t-T path. Assuming the grain boundary acts as infinite reservoir to Pb diffusion, the end of each grain radius is held at zero. The grain center boundary is set to have center symmetry. The solution is carried out for multiple grains of varying size and repeated for time-temperature paths for any sample depth. Diffusion kinetics for rutile used values reported for natural rutile with normal to c-axis diffusion (*38*). Convergence tests evaluating the accuracy of both the internal Pb diffusion profile, and the whole grain U-Pb date were conducted over a range time and spatial increments (Fig S2). Internal Pb diffusion profiles were evaluated by comparison to analytical solutions for spherical diffusion from Crank (Fig S2a) (*39*). Whole grain U-Pb dates were evaluated by analytical solutions for whole grains that includes a Pb source from Tilton (Fig S2b) (*40*).

Analytical methods

Reported U-Pb rutile and titanite data are whole-crystal analyses using Isotope Dilution-Thermal Ionization Mass Spectrometry (ID-TIMS) following methods by (*9*). Dissolution of an entire crystal provides an integrated measure of the internal Pb-diffusion profile. The internal diffusion profile of a grain can be inferred by U-Pb analysis of multiple grains over a range of grain sizes. Exploiting diffusion's length-scale dependency, where the largest crystals retain Pb at the highest temperatures and oldest times and the smallest crystals at lower temperatures and a younger time. Similarly, measuring multiple xenoliths, each from a different depth, provides a measure on the long-term cooling of the lithosphere where the shallowest samples cool first and the deepest last. By measuring multiple grains of varying sizes the thermal record from one xenolith extends up to 500 Ma or more, typically overlapping with the history recorded by shallower/deeper samples. The overlap in thermal histories increase the likelihood that a unique thermal setting for the lithosphere can be achieved by finding a modeled thermal history that matches the measured data at all depths.

Multi-domain behavior in U-Pb accessory phases

Dispersion in measured U-Pb data cane result from multi-domain behavior, where an analyzed single crystal effectively behaves as two or more isolated diffusion domains. The whole grain integration of these domains using the analytical procedures employed here will yield a mixture of the two (or more) domains resulting in delta U-Pb value that will always overestimate the true value. Single domain behavior (or near to) is thus required to yield a reliable exhumation history. Correlations between measured grain size and U-Pb age were used to test whether samples exhibit single domain behavior and evaluate accuracy. Here we present the how the reduction of a crystals effective diffusion grain radius to a size smaller than the grain itself will effect the U-Pb data from slow cooling lower crustal rocks. Reduction of the effective diffusion dimension could result from fast diffusion pathways including cracks or grain defects. The whole-grain analysis of a single crystal experiencing multi-grain behavior will result in a mixture of the total Pb and U from each diffusion domain. Mixtures of different diffusion domains will result in a secondary trajectory on a delta U-Pb vs. time plot (Appendix fig 3a), multi-domain behavior will systematically shift analyses to higher delta-U-Pb values. For example, a mixture between a 25-micron grain and any number of 1-micron sub-domains will result in a data point lying along a secondary curvilinear trajectory that yields higher delta U-Pb values than the main array.

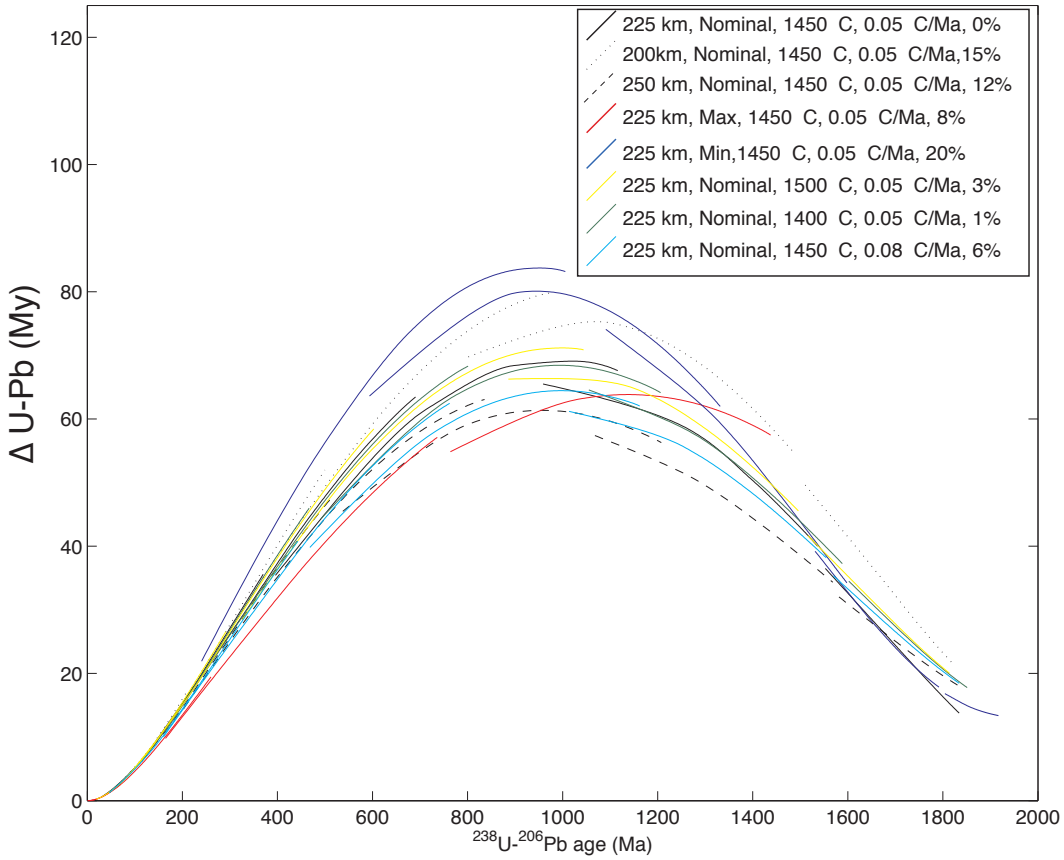

Fig. S1.

Sensitivity testing of thermal model parameters. Modeled U-Pb thermochronologic data are presented for constant exhumation (0.00km/Ma) while varying additional thermal model parameters, including Heat Producing Elements (HPE), lithosphere thickness and basal temperature boundary conditions. Legend reports lithosphere thickness, heat producing element concentration, Initial mantle temperature, mantle secular cooling rate and percent different in maximum Δ U-Pb value from data calculated using a lithosphere thickness of 225 km, and nominal HPE concentrations (black). The largest deveiation from thes middle values is achieved by combining HPE concentrations at a minimum and a lithopshere thickness of 250 km. This deviation in maximum Δ U-Pb can be compensated for (decrease Δ U-Pb) by emplying an exhumation rate of 0.0025 km/Ma.

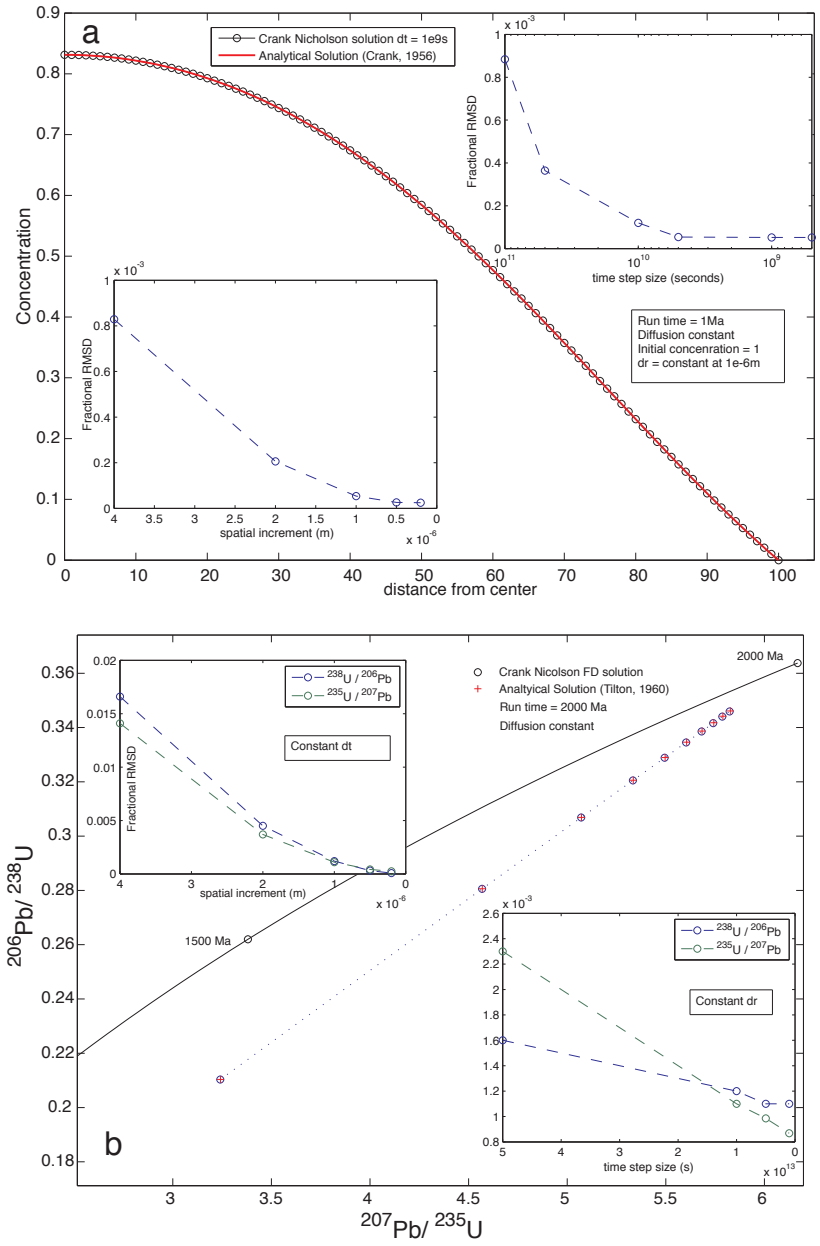

Fig. S2

Convergence tests for U-Pb production diffusion models. Accuracy of U-Pb production/diffusion models are evaluated through comparison with analytical solutions for the (a) internal diffusion profile and (b) whole grain U-Pb date. Convergence is observed with both decreasing spatial increment and time step increment.

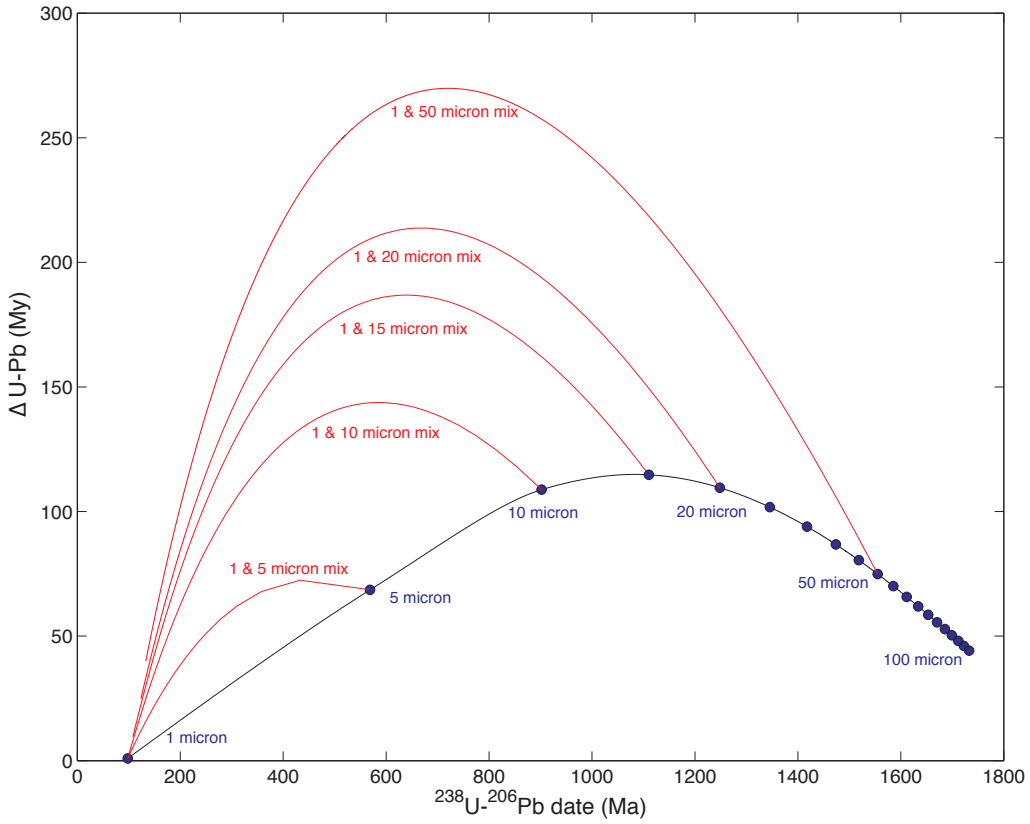

Fig. S3

Modeled effects of multi-domain behavior. Modeled U-Pb thermochronologic data from a single sample, experiencing a simple thermal history are plotted in blue. Variations in ^{238}U-^{206}Pb age and Δ U-Pb are the result of volume diffusion behavior, where different sized crystals retain Pb at different temperatures and thus different times. Mixing domains of different size, as would a whole crystal analysis of a grain with cracks or other fast diffusion pathways, will result in deviations (red) from the array of data shown in blue. Secondary trajectories shown in red are mixtures between different domain sizes and a 1 micron domain, where the number of 1 micron domains varies from 1 (plotting near the larger domain) to many thousands 1 micron domains (plotting closer to 1 micron).

	Dates (Ma)										Composition												
Fraction	206Pb/ 238U a	±2σ abs	207Pb/ 235U a	±2σ abs	207Pb/ 206Pb a	±2σ abs	Delta (Ma)	U-Pb	±2σ abs	Corr. coef.	% disc b	Th/ U c	Pb* (pg) d	Pbc (pg) e	Pb*/ Pbc f	206Pb/ 238U h	±2σ %	207Pb/ 235U h	±2σ %	207Pb/ 206Pb h	±2σ %
Great Falls Tectonic Zone: ROB = Robinson Ranch, LSC = Little Sand Creek																					
ROB5																					
5r16	53.063894	0.706407	58.617949	10.653137	291.843798	403.029619	5.55	11.36	0.80446862	81.82	0.10	0.74	1.34	0.55	0.008266	1.336725	0.059429	18.703482	0.052147	17.645995	
5r9	80.163615	0.532772	89.264241	7.550283	339.955217	189.023614	9.10	8.08	0.74765692	76.42	0.00	0.84	0.75	1.13	0.012513	0.668747	0.091892	8.835592	0.053262	8.347409	
5r12	278.040136	1.061430	358.919504	7.338225	921.708817	45.851269	80.88	8.40	0.56354656	69.83	0.27	5.11	1.58	3.24	0.044075	0.390046	0.424017	2.427129	0.069774	2.230666	
5r11	467.705399	1.276928	517.458800	6.192648	743.639008	29.174367	49.75	7.47	0.589181041	37.11	-0.01	13.33	2.89	4.61	0.075250	0.283044	0.664657	1.527473	0.064061	1.379718	
5r10	55.859014	0.500866	57.319090	8.971192	118.760937	363.859089	1.46	9.47	0.747491599	52.97	-0.03	1.11	1.80	0.61	0.008703	0.900552	0.058074	16.097237	0.048398	15.435671	
ROB3																					
3r4	786.918006	3.547243	844.125789	9.195163	997.705960	26.705283	57.21	12.74	0.699446875	21.13	0.01	10.22	2.28	4.48	0.129834	0.478850	1.296388	1.604131	0.072418	1.314450	
3r5	585.876488	2.421630	633.099170	6.887468	805.552844	26.547259	47.22	9.31	0.566658966	27.27	0.01	5.44	1.28	4.24	0.095142	0.432402	0.865460	1.462071	0.065974	1.268041	
309r7	62.878424	2.454043	71.424019	15.166287	367.834735	467.271888	8.55	17.62	0.399469427	82.91	0.13	0.56	1.34	0.42	0.009802	3.921904	0.072875	21.989736	0.053923	20.737112	
ROB1																					
1r21	229.527418	0.991673	275.160174	31.487798	683.776580	239.664136	45.63	38.48	0.670121985	66.43	0.01	1.64	2.39	0.69	0.036247	3.100668	0.311264	13.063926	0.062281	11.224570	
1r20	115.913943	3.709563	127.104280	21.518658	341.795606	371.685962	11.19	25.23	0.560969085	66.09	-0.02	0.98	1.81	0.54	0.018144	3.229132	0.133351	18.011658	0.053305	16.419279	
1r15	419.146217	1.122293	471.170129	4.776287	733.231215	24.822606	52.02	5.90	0.43987603	42.84	0.00	8.02	1.37	5.85	0.067180	0.276556	0.590474	1.267029	0.063747	1.171907	
1r14	246.471981	1.968493	276.331852	8.468553	537.468261	65.547467	29.86	10.44	0.691733508	54.14	2.12	9.25	2.24	4.12	0.038974	0.814034	0.312778	3.500536	0.058205	2.995651	
1r5	487.839107	0.926327	523.774577	1.883446	683.674840	7.817711	35.94	2.81	0.642834583	28.64	0.00	47.54	2.17	21.92	0.078613	0.197159	0.675044	0.460275	0.062278	0.365846	
1r16	355.843007	6.447143	392.322288	23.209800	613.420362	124.878817	36.48	29.66	0.787524111	41.99	0.04	11.60	7.16	1.62	0.056752	1.862260	0.471642	7.132329	0.060274	5.780807	
1r4	515.069796	0.554812	556.476926	1.883692	729.690864	8.858540	41.41	2.44	0.316094624	29.41	0.01	34.86	1.69	20.59	0.083179	0.112076	0.729870	0.439691	0.063640	0.417763	
1r3	341.456090	1.949257	377.827341	6.465467	607.287377	37.150529	36.37	8.41	0.662569872	43.77	0.01	8.99	2.23	4.03	0.054396	0.586119	0.450783	2.049298	0.060103	1.717929	
1r7	135.157563	0.475887	154.249523	1.998750	458.636179	25.308346	19.09	2.47	0.779975962	70.53	0.00	39.34	4.76	8.27	0.021188	0.355802	0.164059	1.396705	0.056158	1.141030	
LSC18																					
18r3	886.092272	1.903737	948.563107	3.890767	1096.486509	12.455876	62.47	5.79	0.220408607	19.19	0.01	11.81	1.25	9.44	0.147350	0.229950	1.545157	0.631171	0.076054	0.622145	
18r5	852.284639	2.303664	922.896160	5.573667	1095.679211	18.205204	70.61	7.88	0.19125038	22.21	0.01	10.64	1.49	7.16	0.141349	0.288554	1.481627	0.919409	0.076023	0.909334	
18r6	917.479435	3.901725	978.352336	11.065037	1117.621486	35.540384	60.87	14.97	0.0871653	17.91	0.02	8.25	2.01	4.11	0.152950	0.456246	1.620933	1.762032	0.076862	1.781168	
18r8	1130.350238	2.688856	1152.986287	4.166990	1195.796290	10.242095	22.64	6.86	0.821767349	5.47	0.00	37.74	2.06	18.36	0.191658	0.259053	2.112787	0.609017	0.079952	0.519027	
18r9	1170.627049	3.768341	1195.987572	6.148374	1242.108309	16.366060	25.36	9.92	0.311398726	5.75	0.04	88.31	6.66	13.27	0.199127	0.352020	2.247444	0.874950	0.081857	0.835119	
18r15	737.445617	2.552543	785.573740	7.337008	924.792311	26.556596	48.13	9.89	0.267242799	20.26	0.00	32.17	3.50	9.19	0.121196	0.366309	1.167712	1.341390	0.069879	1.292545	
1809r1	722.752527	18.040308	802.714692	28.787736	1031.567240	84.445800	79.96	46.83	0.599964415	29.94	0.01	0.94	0.61	1.56	0.118644	2.638595	1.204616	5.188739	0.072638	4.178132	
1809r2	854.313647	6.589459	898.189818	17.340646	1007.755810	52.631889	43.88	23.93	0.502362594	15.23	0.00	2.45	0.91	2.70	0.141708	0.823554	1.421972	2.908797	0.072777	2.594660	
1809r3	842.746357	3.864391	885.170478	10.317762	992.749578	29.373445	42.42	14.18	0.703732471	15.11	0.00	3.56	0.50	7.17	0.139661	0.489173	1.391116	1.746598	0.072241	1.444701	
1809r4	962.297856	3.992538	1007.090608	5.733694	1105.874908	14.724273	44.79	9.73	0.576801727	12.98	0.00	6.41	0.70	9.11	0.160994	0.446634	1.696173	0.897599	0.076412	0.736531	
1809r5	759.250690	1.719522	820.473716	2.681126	990.267821	7.758751	61.22	4.40	0.60793445	23.33	0.00	12.36	0.58	21.33	0.124995	0.240075	1.243514	0.476393	0.072153	0.381204	
1810r2	716.494742	8.358282	771.955755	14.676892	935.948981	48.082152	55.46	23.04	0.506937794	23.45	-0.06	7.43	1.21	6.15	0.117558	1.232581	1.138834	2.714694	0.072093	2.344376	
1810r10	1171.334188	0.945802	1205.806653	1.999605	34.472465	2.945407	34.47	2.95	1268.087387	1.74	0.56	8.34	0.00	54.46	50.197800	3362.570801	0.199258	0.080746	2.279001	0.165831	
1810r11	1030.914487	2.645707	1063.817957	3.735213	32.903470	6.380920	32.90	6.38	1131.937408	2.57	0.76	9.66	0.00	51.65	19.121300	1249.905029	0.173418	0.256637	1.851089	0.351114	
ROB 9 Titanite																					
T2	1465.221873	8.051433	1476.380847	11.640363	1492.457765	20.218213	11.16	19.69	0.801923655	1.82	2.06	313.86	35.01	8.96	0.255197	0.614315	3.280260	1.495886	0.093225	1.068176	
T3	1433.076525	8.932487	1451.066314	13.141122	1477.516017	23.120266	17.99	22.07	0.800118781	3.01	1.66	424.88	57.28	7.42	0.248953	0.695156	3.174868	1.701843	0.092492	1.219076	
T4	1366.113313	17.584417	1386.544751	27.343172	1418.130412	50.023906	20.43	44.93	0.800361056	3.67	2.39	208.32	51.10	4.08	0.236047	1.428389	2.917833	3.615801	0.089652	2.616627	
T5	1382.299436	7.364075	1395.103808	11.383692	1414.740082	20.778018	12.81	18.75	0.800977101	2.29	1.56	274.20	32.34	8.48	0.239154	0.591900	2.950997	1.501036	0.089493	1.086263	
T6	1288.491995	9.971877	1319.259662	16.351722	1369.598959	31.082814	30.77	26.32	0.799655568	5.92	2.24	74.54	11.54	6.46	0.221253	0.853838	2.666630	2.214307	0.087412	1.615003	
T7	1398.829685	8.812146	1421.816124	13.299066	1456.409250	23.770205	22.99	22.11	0.800628528	3.95	2.42	109.75	13.44	8.17	0.242336	0.700785	3.056318	1.738300	0.091470	1.249786	
Northern Wyoming Province, Homestead Kimberlite																					
HS01 Titanite																					
T2	1789.101692	1.053042	1818.180919	1.144433	1851.664809	1.412229	29.08	2.20	0.918052944	3.38	0.61	368.32	4.65	79.28	0.319872	0.067404	4.993260	0.135282	0.113216	0.076756	
T3	1707.853574	1.024835	1743.307791	1.059976	1786.101498	1.428837	35.45	2.08	0.846247005	4.38	0.35	340.34	4.12	82.68	0.303341	0.068307	4.567225	0.127248	0.109199	0.077049	
T4	1753.712460	1.631911	1780.783829	1.231296	1812.660687	1.193773	27.07	2.86	0.913726864	3.25	0.69	849.98	5.34	159.31	0.312646	0.106285	4.776540	0.146652	0.110805	0.064098	
T6	1793.999784	1.399259	1820.562892	2.096177	1851.092695	3.846339	26.56	3.50	0.543759757	3.08	0.58	756.56	32.94	22.97	0.320875	0.089352	5.007336	0.247670	0.113180	0.212243	
T8	1816.934062	1.833568	1838.072358	4.814643	1862.092615	9.431768	21.14	6.65	0.471886794	2.43	0.50	361.31	38.80	9.31	0.325582	0.115804	5.111826	0.566930	0.113871	0.522157	
T9	1763.840129	1.809924	1793.182450	2.095266	1827.485922	3.543801	29.34	3.91	0.642561819	3.48	0.49	767.24	28.89	26.56	0.314709	0.117290	4.847509	0.248921	0.111714	0.194905	
T10	1750.605291	2.226820	1776.096968	1.658987	1806.191981	2.003195	25.49	3.89	0.83670121	3.08	0.65	232.15	4.07	57.03	0.312013	0.145255	4.749938	0.197783	0.110411	0.109232	
T13	1640.690661	0.964376	1674.331127	0.917205	1716.756523	0.877294	33.64	1.88	0.984578903	4.43	0.33	188.63	0.63	301.47	0.289832	0.066576	4.201593	0.111830	0.105140	0.045466	
T16	1820.159786	1.152943	1841.848719	1.061097	1866.441836	1.203179	21.69	2.21	0.904962393	2.48	0.69	501.10	2.77	181.09	0.326246	0.072706	5.134599	0.124855	0.114146	0.065073	
T17	1756.345172	1.246821	1791.570799	1.423595	1832.835049	2.210626	35.23	2.67	0.740352765	4.17	0.59	222.12	5.10	43.54	0.313182	0.081099	4.838235	0.169181	0.112044	0.121132	
HS02 rutile																					
r1	820.157996	1.698362	878.935527	5.713423	1030.013199	17.580757	58.78	7.41	0.551046866	20.37	0.04	14.94	2.80	5.33	0.135675	0.220530	1.376478	0.971474	0.073582	0.869524	
r4	957.882455	2.284360	1045.099093	4.514900	1232.240321	12.558861	87.22	6.80	0.379682324	22.26	0.02	3.04	0.40	7.62	0.160199	0.256637	1.799010	0.691814	0.081447	0.639873	
r5	639.567149	0.739930	693.970111	4.538146	874.476447	18.059879	54.40	5.28	0.314036415	26.86	0.01	3.20	0.86	3.70	0.104301	0.121526	0.980712	0.902669	0.068195	0.872050	
r6	751.260977	5.130342	847.834644	7.483483	1109.812255	21.501295	96.57	12.61	0.562552799	32.31	0.00	2.60	0.53	4.93	0.123602	0.723462	1.304791	1.301861	0.076562	1.076267	
r7	871.151319	1.972467	946.681967	5.179717	1126.716146	15.388294	75.53	7.15	0.417241686	22.68	0.00	3.06	0.79	3.89	0.144694	0.242064	1.540446	0.841278	0.077214	0.772138	
r9	480.094403	2.848595	521.081524	12.360409	705.025490	51.236332	40.99	15.21	1.011414563	31.90	0.00	14.70	2.15	6.85	0.077318	0.615709	0.670607	3.032558	0.062905	2.407970	

a Isotopic dates calculated using the decay constants λ238 = 1.55125E-10 and λ235 = 9.8485E-10 (Jaffey et al. 1971).
b % discordance = 100 - (100 * (206Pb/238U date) / (207Pb/206Pb date))
c Th contents calculated from radiogenic 208Pb and the 207Pb/206Pb date of the sample, assuming concordance between U-Th and Pb systems.
d Total mass of radiogenic Pb.
e Total mass of common Pb.
f Ratio of radiogenic Pb (including 208Pb) to common Pb.
g Measured ratio corrected for fractionation and spike contribution only.
h Measured ratios corrected for fractionation, tracer, blank and initial common Pb.

Table S1.

Tabulated U-Pb rutile and titanite data. Each analysis is a single, whole crystal measurement using isotope dilution and thermal ionization mass spectrometry techniques.

Heat producing elment (HPE) concentrations

	U (ppm)	Th (ppm)	K20 (wt%)
UC suggested*	2.7	10.5	2.8
UC Min/Max*	1.5/2.8	8.6/10.7	2.68/4.13
MC suggested*	1.3	6.5	2.3
MC Min/Max*	0.9/2.2	6.1/8.4	2.07/3.36
LC suggested*	0.2	1.2	0.6
LC Min/Max*	0.05/1.38	0.42/5.74	0.17/3.41
MLsuggested**[a]	0.0	0.1	0.0
ML Min/Max**[b]	0.009/0.138	0.034/.537	0.01/0.166

[a]alkali basalt hosted xenoliths
[b]mins = median off-craton massif, max = kimberlite hosted xenoliths

UC = upper crust
MC = Middle crust
LC = Lower crust
ML = Mantle Lithosphere

Table S2.

Compiled Heat Producing Element concentrations for crust and mantle lithosphere values used in thermal model. Symbols (*) data from (*12*) and (**) from (*13*).

A.2 Chapter 4 appendix

		Grain Size (microns)				Calculated Temperatures (C)		
Grain #	Core/Rim	Width 1	Height	spherical diameter	Zr conc (ppm)	Watson et al. 2007	Zack et al. 2004	Tomkins et al., 2007
Sample : SG02		-	-	-	-	-	-	-
Sb-7	C	45	195	30	3038	878	1015	871
Sb-7	R	45	195	30	3267	887	1024	880
Sb-7*	C	45	190	30	3322	889	1026	882
Sb-8	C	70	150	43	2908	872	1009	866
Sb-8	R	70	150	43	2853	870	1007	863
Sb-12	C	50	152	32	2997	876	1013	869
Sb-12	R	50	160	32	3051	878	1015	872
Sb-12	R	50	160	32	2718	864	1001	857
Sb-13	C	45	165	30	2706	863	1000	857
Sb-13	R	45	165	30	2678	862	999	856
Sb-13	R	45	165	30	2808	868	1005	861
Sb-13*	C	45	165	30	3516	896	1033	890
Sb-10	C	50	200	33	2877	871	1008	864
Sb-18	C	50	190	33	3535	897	1034	890
Sb-18*	C	50	190	33	3813	907	1044	900
L-3	C	120	345	77	3626	900	1037	894
L-4	C	90	191	55	4641	934	1069	927
L-5	C	105	190	62	4111	917	1053	910
L-5	R	105	190	62	4116	917	1054	910
L-7	C	90	230	56	4417	927	1063	920
L-7	C	90	230	56	4417	927	1063	920
L-7	R	90	230	56	4501	930	1065	922
LS-9	C	23	127	16	3168	883	1020	876
LS-9	R	23	127	16	3461	894	1031	888
LS-12	C	24	163	17	3174	883	1020	877
LS-12	R	24	163	17	3380	891	1028	885
LS-13	C	27	130	18	3501	896	1033	889
LS-13	R	27	130	18	3853	908	1045	902
LS-14	C	25	114	17	3140	882	1019	875
LS-14	R	25	114	17	3100	880	1017	874
LS-16	C	18	100	12	3172	883	1020	877
LS-16	R	18	100	12	3267	887	1024	880
LS-19	C	30	180	21	3078	879	1016	873
LS-19	R	30	180	21	3439	893	1031	887
LS-28	C	32	173	22	1033	755	877	751
LS-28	R	32	173	22	343	654	736	651
LS-29	C	25	189	18	3110	880	1018	874
LS-29	R	25	189	18	2980	875	1012	869
LS-30	C	33	170	23	188	607	659	604
LS-30	R	33	170	23	135	583	617	581
		Grain Size (microns)				Calculated Temperatures (C)		
Grain #	Core/Rim	Width 1	Height	spherical diameter	Zr conc (ppm)	Watson et al. 2007	Zack et al. 2004	Tomkins et al., 2007
LS-30	R	33	170	23	182	605	655	602
LS-31	C	25	93	17	3152	882	1020	876
LS-31	R	25	93	17	3397	892	1029	885
S R10	C	54	158	35	2837	869	1006	863
S R11	C	56	224	37	2854	870	1007	863
S R12	C	47	288	33	2982	875	1012	869
S R13	C	42	180	28	2930	873	1010	867
S R14	C	47	263	32	3515	896	1033	890
S R15	C	41	191	28	3320	889	1026	882
S R16	C	56	130	35	3492	895	1033	889
S R17	C	36	147	24	3298	888	1025	881
S R19	C	42	187	28	3257	886	1024	880

Table 4.1

S R20	C	44	112	28	3475	895	1032	888
S R21	C	44	148	29	2950	874	1011	867
S R22	C	42	155	28	3153	882	1020	876
S R23	C	35	180	24	2896	871	1009	865
Sample: SG05		-	-	-	-	-	-	
Sb-1	C	68	133	41	3902	910	1047	914
Sb-1	R	68	133	41	3895	910	1047	914
Sb-1	R	68	133	41	3837	908	1045	912
Sb-1 pst	C	68	133	41	3879	909	1046	913
Sb-2	C	90	170	53	3885	910	1046	914
Sb-2	R	90	160	53	3912	911	1047	914
Sb-2	R	90	160	53	3885	910	1046	914
Sb-2	R	90	160	53	3912	911	1047	914
Sb-2	R	90	160	53	3885	910	1046	914
Sb-5	C	60	125	36	4054	915	1052	919
Sb-5	R	60	125	36	4008	914	1050	918
Sb-5	R	60	125	36	4085	916	1053	920
XL-6	C	115	270	71	4673	935	1070	939
XL-6	R	115	270	71	4207	920	1056	924
XL-2	C	150	210	83	3979	913	1049	917
XL-3	C	106	260	66	3615	900	1037	904
XL-3	R	106	260	66	3316	889	1026	893
XL-3	R	106	260	66	3698	903	1040	907
XL-3	R	106	260	66	3658	902	1039	906
XL-3	R	106	260	66	3628	900	1038	904
XL-3	R	106	260	66	3612	900	1037	904
L-1	C	95	270	61	4758	937	1072	941
L-1	R	95	270	61	4750	937	1072	941
L-1	R	95	270	61	4553	931	1067	935
		Grain Size (microns)				**Calculated Temperatures (C)**		
Grain # Core/Rim		**Width 1**	**Height**	**spherical diameter**	**Zr conc (ppm)**	**Watson et al. 2007**	**Zack et al. 2004**	**Tomkins et al., 2007**
L-2	C	90	310	59	5770	965	1097	969
L-2	R	90	310	59	6504	983	1112	986
L-2	R	90	310	59	5980	970	1101	974
S 32	C	26	78	17	4676	935	1070	939
S 32	R	26	78	17	4527	930	1066	934
S 33	C	39	175	26	4673	935	1070	939
S 33	R	39	175	26	4632	934	1069	937
S 34	C	37	102	23	5451	957	1090	960
S 34	R	37	102	23	5311	953	1086	957
S 35	C	32	63	19	5009	945	1079	948
S 35	R	32	63	19	5344	954	1087	958
S 36	C	27	140	18	4740	937	1072	941
S 36	R	27	140	18	5032	945	1079	949
S 41	C	29	112	19	4145	918	1055	922
S 41	R	29	112	19	4148	918	1055	922
S 42	C	20	102	14	5130	948	1082	952
S 42	R	20	102	14	4995	944	1078	948
S R6	C	78	137	46	4997	944	1078	948
S R4	C	44	205	30	4292	923	1059	927
S R4	R	44	205	30	4280	923	1059	927
S R4	R	44	205	30	4270	922	1058	926
S R2	C	50	122	31	3093	880	1017	884

***** Analyses taken in the center of the grain, after grain was ground down to remove material

Table 4.1

A.3 Chapter 5 appendix

Model

This finite difference calculation separately determines the temperature as function of depth, temperature and pressure dependent density profile, elevation, relief and erosion rate at each time step. Beginning with temperature, the thermal processes operating in the mountain belt include heat conduction, heat producing element decay, advection (i.e. erosion). To model this setting we employed a one-dimensional thermal model consisting of a conductive depth profile in a fixed reference frame with respect to orogen surface using a Crank-Nicholson solution to the 1-D diffusion equation:

$$T_i^{n+1} = T_i^n + \frac{dt \bullet \alpha}{2(dz)^2}\left[(T_{i-1}^{n+1} - 2T_i^{n+1} + T_{i+1}^{n+1}) + (T_{i-1}^n - 2T_i^n + T_{i+1}^n)\right] \quad (1),$$

where α is the thermal diffusivity (Table S3), and *dt* and *dz* are the time and spatial increments respectively. A temperature dependent thermal diffusivity of the upper and middle crust following Whittington(2009) is used, while a constant value of 0.8e-6 m^2/s is used for the mafic lower crust and mantle lithosphere. Both upper and lower thermal boundaries employ a fixed boundary condition where the upper boundary is fixed to 10 °C, while the basal temperature is fixed by a model describing the secular cooling of the underlying mantle (Grigne et al., 2005).A source term accounts for the heat contributed from the decay of heat producing elements (HPE). At each time step the heat produced (*H*) through decay of HPE's is calculated following Turcotte and Schubert,(Turcotte and Schubert, 2001)

$$H(t) = R_{238} \bullet C_U \bullet H_{U238} \bullet e^{\lambda_{238} \bullet t} + R_{235} \bullet C_U \bullet H_{U235} \bullet e^{\lambda_{235} \bullet t} + 1 \bullet C_{Th} \bullet H_{Th232} \bullet e^{\lambda_{232} \bullet t} + R_{K40} \bullet C_K \bullet H_{K40} \bullet e^{\lambda_{40} \bullet t} \quad (2)$$

where: C is the total present day concentration of U, Th or K; R is the isotopic ratio of each radioactive nuclide to total U, Th or K; H the heat production constant (W/kg) ; λ to the decay constants for each radionuclide (1/time); and t is time before the present (Ma) (Table S2). Compiled data sets of HPE concentrations for the crust and mantle lithosphere are used(Rudnick et al., 2003; Rudnick et al., 1998). The minimum and maximum HPE concentrations and their effect on the lithosphere erosional history is presented in the supplementary figure S4. Continental lithosphere structure including the upper, middle, lower crustal and mantle lithosphere thicknesses use generalized models based off of present day crustal sections from Chistensen and Mooney(Christensen and Mooney, 1995) (Fig. 2). We explore variations in mountain belt thickness and individual layer thickness and determine their influence on the erosional history. The initial temperature profile assumes a high geothermal gradient, consistent with conditions during the onset of orogen formation (Fig. 2). Lithosphere exhumation is simulated using a semi-lagrangian method to quantify the effects of sample cooling by uplift through the conductive column towards the heat-loss surface and to advect the different crustal densities upwards according to the level of erosion. As heat is lost at the lithosphere surface by both conductive and advective heat loss, this high geothermal gradient will relax.

Temperature and pressure dependent density models for idealized lower crust compositions from Jull and Kelemen(Jull and Kelemen, 2001) are used. Upper crustal layers are fixed at a constant density. At each time step, the temperature profile is used to calculate the corresponding density profile. The integrated lithosphere density is used to calculate the height to which the lithosphere isostatically floats in the underlying asthenosphere. The asthenosphere mantle density is calculated using the pyrolite mantle composition with modeled temperature and pressure dependent densities from Kelly and others (Kelly et al., 2003) (Table 2). The asthenosphere density increases as the mantle/lithosphere basal boundary condition cools with time. The lithospheric mantle plays a critical role by thermally insulating the lower crust from the convecting asthenosphere, permitting the lower crust to reach temperatures consistent with garnet growth. The density of the mantle lithosphere is set equal to the convecting mantle (i.e. "isopycnic"(Jordan, 1988)) (Fig. 1) , while the density of the oceanic lithosphere is 40 kg/m^3 less than the convecting mantle(Afonso et al., 2007). Assuming isostatic equilibrium is maintained, the elevation (E) of the orogen relative to an "old" ocean column is calculated following,

$$E = (1-\frac{\rho_l}{\rho_a})\bullet z_l - (1-\frac{\rho_w}{\rho_a})\bullet z_w - (1-\frac{\rho_{oc}}{\rho_a})\bullet z_{oc} - (1-\frac{\rho_{ol}}{\rho_a})\bullet z_{ol} \quad (3)$$

where density of each reservoir is denoted as ρ and the thickness by z. The indices for the continental lithosphere, asthenosphere, ocean water, oceanic crust(Carlson and Raskin, 1984), and oceanic lithosphere are denoted as *l, a, w, oc and ol* respectively (Table 2). To calculate mountain belt relief (h) the height of the orogen is calculated instead to a reference column of continental crust,

$$h = (1-\frac{\rho_l}{\rho_a})\bullet z_o - (1-\frac{\rho_{cc}}{\rho_a})\bullet z_{cc} \quad (4)$$

The surficial erosion rate at each time step is determined assuming a linear relationship between erosion rate and orogen relief, related by an erosional constant (E_k = 0.06 (1/My)). Where again the density of each reservoir is denoted as ρ and the thickness by z, while the indices for the

reference column of continental crust is denoted as *cc* (Fig. 2, Table S2). The root thickness of the mount belt (*m*) is defined as the difference between the total orogen thickness and the thickness of the reference column of continental crust and the regional relief (Fig. 2, Table S2). To conserve mass during density changes, the amount of contraction (ΔH) at each point through the lithosphere (z) is calculated from the ratio between the density from the present (t) and previous time step ($t\text{-}1$) using,

$$\Delta H(z) = dz \bullet (1 - (\frac{\rho(z)_{t-1}}{\rho(z)_t}) \quad (5).$$

Initial values and constants used are reported in supplementary table S3, and figure 2. The influence of varying these variables on the model-generated data are explore in figure S3.

Survey of erosion rates in mountain belts ranging in age from 2000 Ma to the present

This exhumation rate is an integrated measure over the time between the present day (0 Ma) and the time at which the sample reached the 120 ± 10 °C isotherm (AFT date) (Fig. S1). This method of erosion rate calculation assumes that the geothermal gradient has remained constant between the time recorded by the AFT system and the present day, neglecting secular cooling by conductive heat transfer over this duration of time. This method assumes a 1-D geometry, neglecting the effects of surface topography on lithosphere cooling. Because both conductive heat transfer and surface topography will undoubtedly play a role in cooling the lithosphere, the rates presented here place a maximum estimate on the true erosion (Fig. S2). Model generated data will also be biased the same way, assuming a constant geothermal gradient and a 1-D model geometry, permitting us to generate a modeled apparent erosion rate. Using the method of exhumation rate calculation employed here, the average exhumation rate for time-temperature paths (t-T) A, B and C are equal. Despite the potential for producing an overestimation of erosion rates using the AFT data (Fig. S1, S2), the good agreement between AFT and ^{10}Be data suggests the simplistic method of erosion rate calculation using the AFT data employed here is suitable for resolving the drastically different erosion rates observed in modern and ancient orogens. All ^{10}Be cosmogenic nuclide data was collected from a global database of measurements(Bierman, 1994), restricting the data to collisional orogens. The tabulated and plotted erosion rates (table S3, Figure 1b) use the cited "CHRONUS" erosion rate and uncertainty.

Additional complications to this AFT erosional record arise from partial resetting of the AFT system during burial induced heating. A phenomenon likely restricted to the oldest orogens, burial within a foreland(Lorencak et al., 2004) or a dynamically driven(Flowers et al., 2012) basin can be included as a period of negative exhumation (burial) within the integrated measure of erosion rate between the time of AFT closure and the present day. Though the resulting thermal insulation would have been sufficient to perturb the low-temperature AFT system, it is unlikely to cause significant changes in lower crustal density. As such, after the cessation of subsidence driving forces, the subsequent erosion of sediments would likely occur at rates controlled by the temperature and density of the crust, meaning that the cold, dense state of these orogens will require that subsequent erosion rates be representative of long-term orogen decay even after regional deposition.

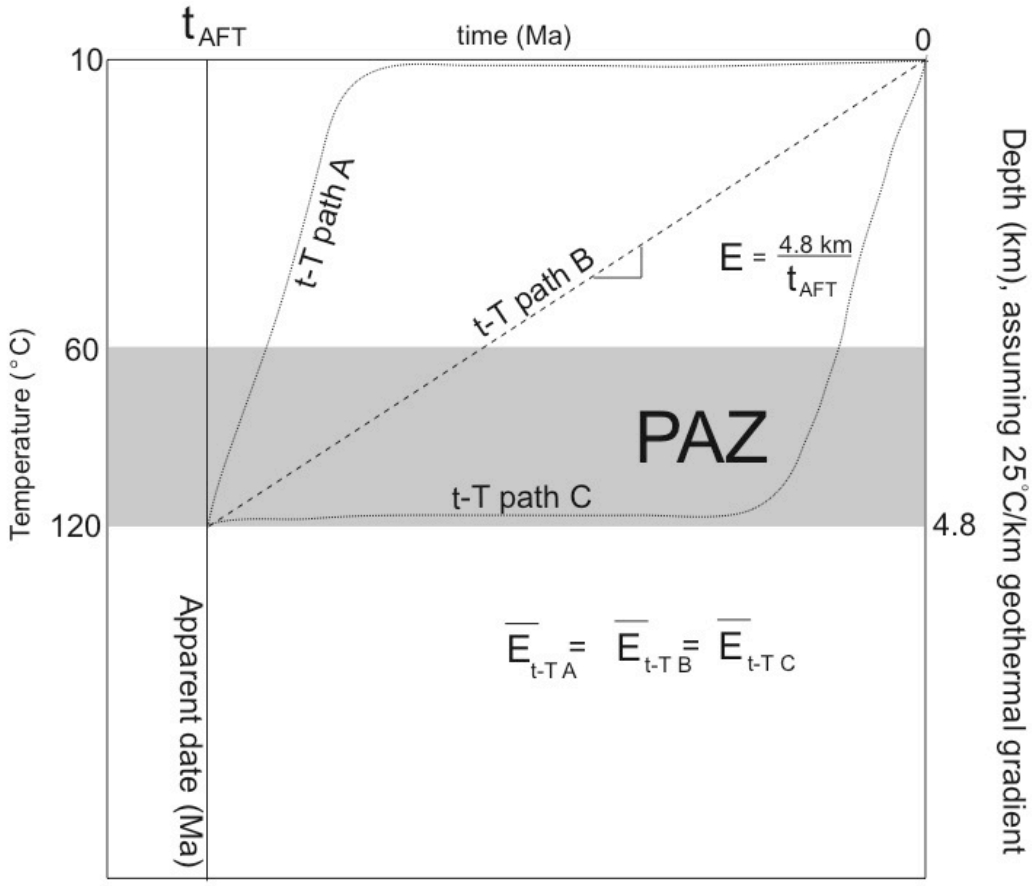

Supplementary Figure S1. Schematic illustration of how integrated exhumation rates are calculated from apatite fission track data.

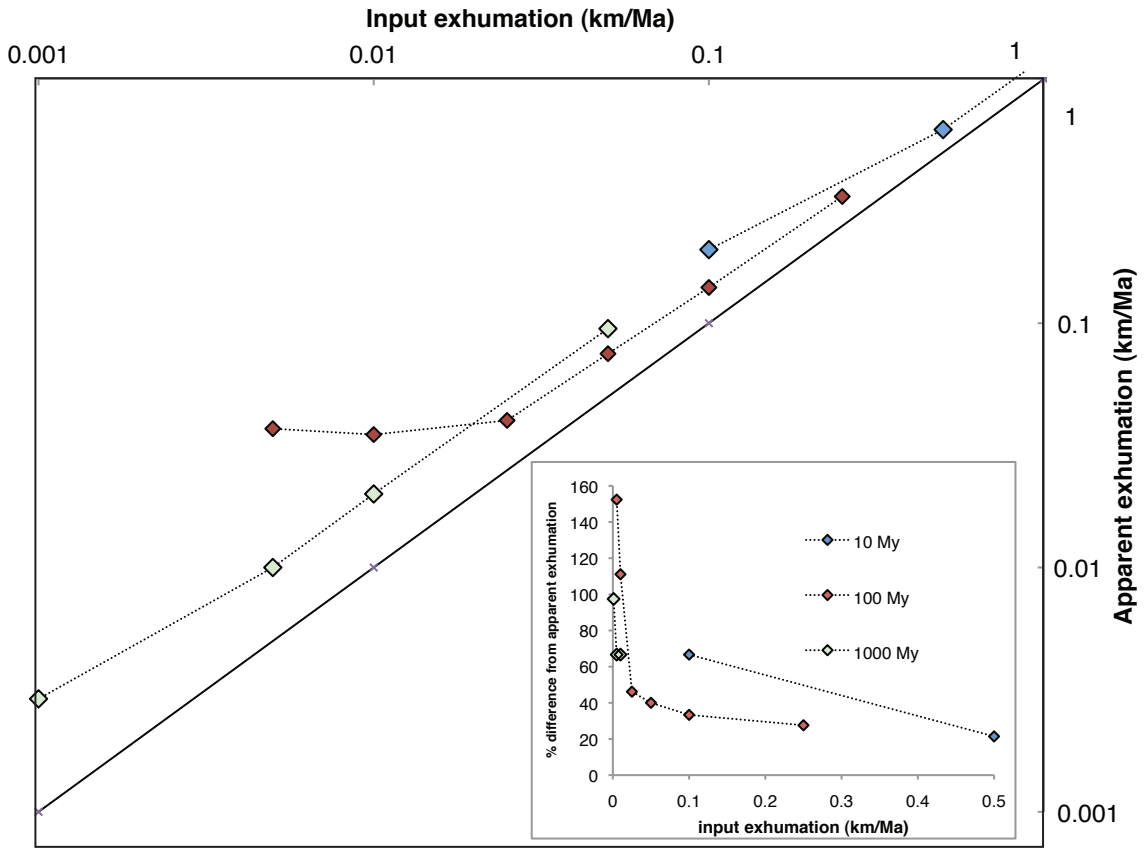

Supplementary Figure S2. Modeled output from thermal model where the input exhumation (km/Ma) is plotted against the apparent exhumation rate calculated from modeled apatite fission track data. At low exhumation rates and/or long model runs the apparent exhumation may overestimate the true exhumation rate by as much as 100%. This occurs because the AFT data provides a record in response to lithosphere cooling and is not solely the result of exhumation. Calculating a surface-AFT isotherm exhumation rate (see text), assumes that the geothermal gradient has remained constant between the timing recorded by the AFT system and the present day; i.e. conductive heat transfer has not contributed to secular cooling within the orogen. The exhumation rates shown here demonstrate that this assumption has not been meet, leading to an overestimate in exhumation/erosion rate.

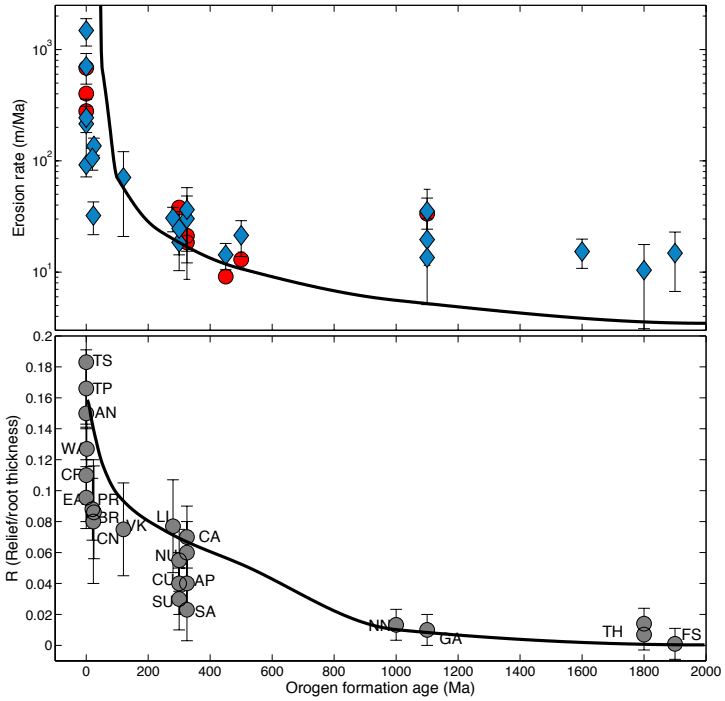

Supplementary Figure S3. Plot of model generated (**A**) erosion rate and (**B**) *R*-value i.e. ratio between orogen relief and root thickness, exploring the effects of erosion law, relating erosion rate to elevation instead of relief.

			Exh rate (m/Ma)		
Orogen	**orogen age**	**AFT**	**2s unc**	**Be10***	**unc**
TS	0	215	143.3	-	-
TP	0	1485	409.2	402.3	15.9
CR	0	92	4.3	-	-
AN	0	244	64.7	279.4	11.8
EA	0	705	216.2	684.4	47.5
PR	25	136	23.8	-	-
VK	120	70.9	50.0	-	-
BR	20	106	23.6	-	-
LL	280	30.6	7.6	-	-
SU	300	18.5	8.2	-	-
VA	300	24.6	10.3	38.0	1.2
AP	325	30.2	18.1	21.2	12.6
SA	325	36.4	21.0	18.5	0.2
CN	23	32.2	10.5	-	-
AS	450	14.3	3.8	9.1	0.9
DL	500	21.4	7.6	13.0	2.1
AD	1100	35.3	11.0	-	-
GA	1100	19.6	14.5	-	-
LU	1100	13.5	16.7	33.5	22.0
IO	1600	15.3	4.5	-	-
TH	1800	10.4	7.3	-	-
SF	1900	14.8	8.1	-	-

Supplementary Table S1. Summary of orogen erosion rate data from Apatite fission track (AFT) (Anders et al., 2002; Barnes et al., 2006; Barnes et al., 2008; Benjamin et al., 1987; Blackmer et al., 1994; Blythe et al., 1998; Blythe et al., 1997; Boettcher and Milliken, 1994; Bogdanoff et al., 2000; Bullen et al., 2003; Cederbom et al., 2000; Crough, 1983; Danišík et al., 2009; Ege et al., 2007; Fitzgerald et al., 1999; Flowers et al., 2012; Gibson et al., 2007; Glasmacher et al., 2002; Grobe et al.; Gunnell et al., 2009; Hejl, 1997; Hendriks et al., 1993; Hendrix et al., 1994; Huigen and Andriessen, 2004; Jolivet et al., 2001; Kohn et al., 2002; Leech and Stockli, 2000; Martin et al., 1998; Moser et al., 2005; Murrell and Andriessen, 2004; O'Sullivan et al., 1995; Osadetz et al., 2002; Perilli, 2000; Reinecker et al., 2008; Roden, 1991; Roden and Miller, 1989; Seward and Mancktelow, 1994; Seward et al., 1997; Sinclair et al., 2005; Spotila et al., 2004; Toro et al., 2004; Wagner et al., 1979) and cosmogenic nuclide ^{10}Be data (Bierman, 1994).

Orogen	formation age (Ma)	R	R error
S. Appalachians (34N)**	320	0.023	0.02
S. Appalachians (36N)	320	0.07	0.02
C. Appalachians (38.5N)	320	0.06	0.02
Appalachian Plateau (41.5N)	320	0.04	0.02
Central Andes	0	0.15	0.03
S. Urals	300	0.03	0.02
C. Urals	300	0.04	0.02
N. Urals	300	0.055	0.02
E. Alps	0	0.0955	0.02
W. Alps	2	0.127	0.02
Carpathians	0	0.11	0.03
C. Pyrenees	25	0.086	0.03
Tibetan Plateau	0	0.166	0.025
Tien Shan	0	0.183	0.04
Brooks Range	170	0.088	0.02
Verkhoyansk Mtns	150	0.075	0.03
Lachlan Orogen	280	0.077	0.03
Cantabrian Mtns	350	0.08	0.04
Sveco-Fennian Orogen	1900	0.001	0.01
N. Trans-Hudson (54-55N)*	1800	0.014	0.01
Namaqua-Natal Orogen	1000	0.0133	0.01
NW Grenville Orogen	1100	0.01	0.01
U.S. Trans-Hudson (45-48N)**	1800	0.007	0.01

*White et al. (2005)
**French et al. (2009)
Other references in Fischer (2002)

Supplementary Table S2. Summary of orogen R-value (mountain belt relief divided by root thickness) and orogen formation age, plotted in figure 2b. (Fischer, 2002; French et al., 2009; White et al., 2005)

variable	value	units	ref
ρ_l	2750-3200 [a]	kg/m^3	7
ρ_a	3300-3400 [a]	kg/m^3	8
ρ_{cc}	2950	kg/m^2	
ρ_{oc}	2890	kg/m^3	11
ρ_w	1000	kg/m^3	
ρ_{ol}	ρ_a - 40	kg/m^3	10
z_l	200	km	
z_{cc}	40	km	6
z_{oc}	6	km	3
z_{ol}	100	km	3,10
z_w	3.8	km	
Ek	0.07-0.1	1/Ma	
H_{U238}	9.46E-05	W/kg	3
H_{U235}	5.69E-04	W/kg	3
H_{Th}	2.64E-05	W/kg	3
H_K	2.92E-05	W/kg	3

[a] Temperature dependent

Supplementary Table S3. Tabulated values for model constants, initial and boundary conditions. (Carlson and Raskin, 1984)

References:

Afonso, J.C., Ranalli, G., Fern‡ndez, M., 2007. Density structure and buoyancy of the oceanic lithosphere revisited. Geophys. Res. Lett. 34, L10302.
Anders, M.H., Gregory,ÄêWodzicki, K.M., Spiegelman, M., 2002. A Critical Evaluation of Late Tertiary Accelerated Uplift Rates for the Eastern Cordillera, Central Andes of Bolivia. The Journal of Geology 110, 89-100.
Barnes, J.B., Ehlers, T.A., McQuarrie, N., O'Sullivan, P.B., Pelletier, J.D., 2006. Eocene to recent variations in erosion across the central Andean fold-thrust belt, northern Bolivia: Implications for plateau evolution. Earth and Planetary Science Letters 248, 118-133.

Barnes, J.B., Ehlers, T.A., McQuarrie, N., O'Sullivan, P.B., Tawackoli, S., 2008. Thermochronometer record of central Andean Plateau growth, Bolivia (19.5∞S). Tectonics 27, TC3003.
Benjamin, M.T., Johnson, N.M., Naeser, C.W., 1987. Recent rapid uplift in the Bolivian Andes: Evidence from fission-track dating. Geology 15, 680-683.
Bierman, P.R., 1994. Using in situ produced cosmogenic isotopes to estimate rates of landscape evolution: A review from the geomorphic perspective. J. Geophys. Res. 99, 13885-13896.
Blackmer, G.C., Omar, G.I., Gold, D.P., 1994. Post-Alleghanian unroofing history of the Appalachian Basin, Pennsylvania, from apatite fission track analysis and thermal models. Tectonics 13, 1259-1276.
Blythe, A.E., Bird, J.M., Omar, G.I., 1998. Constraints on the cooling history of the central Brooks Range, Alaska, from fission-track and 40Ar/39Ar analyses. Geological Society of America Special Papers 324, 163-177.
Blythe, A.E., Murphy, J., O'Sullivan, P.B., 1997. Tertiary Cooling and Deformation in the South,ÄêCentral Brooks Range: Evidence from Zircon and Apatite Fission,ÄêTrack Analyses. The Journal of Geology 105, 583-600.
Boettcher, S.S., Milliken, K.L., 1994. Mesozoic-Cenozoic Unroofing of the Southern Appalachian Basin: Apatite Fission Track Evidence from Middle Pennsylvanian Sandstones. The Journal of Geology 102, 655-668.
Bogdanoff, S., Michard, A., Mansour, M., Poupeau, G., 2000. Apatite fission track analysis in the Argentera massif: evidence of contrasting denudation rates in the External Crystalline Massifs of the Western Alps. Terra Nova 12, 117-125.
Bullen, M., Burbank, D., Garver, J., 2003. Building the northern Tien Shan: Integrated thermal, structural, and topographic constraints. The Journal of Geology 111, 149-165.
Carlson, R.L., Raskin, G.S., 1984. Density of the ocean crust. Nature 311, 555-558.
Cederbom, C., Larson, S.Ö., Tullborg, E.-L., Stiberg, J.-P., 2000. Fission track thermochronology applied to Phanerozoic thermotectonic events in central and southern Sweden. Tectonophysics 316, 153-167.
Christensen, N.I., Mooney, W.D., 1995. Seismic velocity structure and composition of the continental crust: A global view. J. Geophys. Res. 100, 9761-9788.
Crough, S.T., 1983. Apatite fission-track dating of erosion in the eastern Andes, Bolivia. Earth and Planetary Science Letters 64, 396-397.
Danišík, M., Kohút, M., Dunkl, I., Hraško, L.u., Frisch, W., Froitzheim, N., Schmid, S.M., 2009. Apatite fission track and (U-Th)/He thermochronology of the Rochovce granite (Slovakia) — implications for the thermal evolution of the Western Carpathian-Pannonian region

Orogenic Processes in the Alpine Collision Zone. Birkhäuser Basel, pp. S225-S233.
Ege, H., Sobel, E.R., Scheuber, E., Jacobshagen, V., 2007. Exhumation history of the southern Altiplano plateau (southern Bolivia) constrained by apatite fission track thermochronology. Tectonics 26, TC1004.
Fischer, K.M., 2002. Waning buoyancy in the crustal roots of old mountains. Nature 417, 933-936.
Fitzgerald, P.G., Mu√±oz, J.A., Coney, P.J., Baldwin, S.L., 1999. Asymmetric exhumation across the Pyrenean orogen: implications for the tectonic evolution of a collisional orogen. Earth and Planetary Science Letters 173, 157-170.
Flowers, R.M., Ault, A.K., Kelley, S.A., Zhang, N., Zhong, S., 2012. Epeirogeny or eustasy? Paleozoic-Mesozoic vertical motion of the North American continental interior from

thermochronometry and implications for mantle dynamics. Earth and Planetary Science Letters 317,Äì318, 436-445.
French, S., Fischer, K., Syracuse, E., Wysession, M., 2009. Crustal structure beneath the Florida-to-Edmonton broadband seismometer array. Geophysical Research letters 36, L08309.
Gibson, M., Sinclair, H.D., Lynn, G.J., Stuart, F.M., 2007. Late- to post-orogenic exhumation of the Central Pyrenees revealed through combined thermochronological data and modelling. Basin Research 19, 323-334.
Glasmacher, U.A., Wagner, G.A., Puchkov, V.N., 2002. Thermotectonic evolution of the western fold-and-thrust belt, southern Uralides, Russia, as revealed by apatite fission track data. Tectonophysics 354, 25-48.
Grigne, C., Labrosse, S., Tackley, P.J., 2005. Convective heat transfer as a function of wavelength: Implications for the cooling of the Earth. J. Geophys. Res. 110, B03409.
Grobe, R.W., Alvarez-Marr√≥n, J., Glasmacher, U.A., Men√©ndez-Duarte, R., Low-temperature exhumation history of Variscan-age rocks in the western Cantabrian Mountains (NW Spain) recorded by apatite fission-track data. Tectonophysics 489, 76-90.
Gunnell, Y., Calvet, M., Brichau, S., Carter, A., Aguilar, J.P., Zeyen, H., 2009. Low long-term erosion rates in high-energy mountain belts: Insights from thermo- and biochronology in the Eastern Pyrenees. Earth and Planetary Science Letters 278, 208-218.
Hejl, E., 1997. Cold spots during the Cenozoic evolution of the Eastern Alps: thermochronological interpretation of apatite fission-track data. Tectonophysics 272, 159-173.
Hendriks, M., Jamieson, R.A., Willett, S.D., Zentilli, M., 1993. Burial and exhumation of the Long Range Inlier and its surroundings, western Newfoundland: results of an apatite fission-track study. Canadian Journal of Earth Sciences 30, 1594-1606.
Hendrix, M.S., Dumitru, T.A., Graham, S.A., 1994. Late Oligocene-early Miocene unroofing in the Chinese Tian Shan: An early effect of the India-Asia collision. Geology 22, 487-490.
Huigen, Y., Andriessen, P., 2004. Thermal effects of Caledonian foreland basin formation, based on fission track analyses applied on basement rocks in central Sweden. Physics and Chemistry of the Earth, Parts A/B/C 29, 683-694.
Jolivet, M., Brunel, M., Seward, D., Xu, Z., Yang, J., Roger, F., Tapponnier, P., Malavieille, J., Arnaud, N., Wu, C., 2001. Mesozoic and Cenozoic tectonics of the northern edge of the Tibetan plateau: fission-track constraints. Tectonophysics 343, 111-134.
Jordan, T.H., 1988. Structure and Formation of the Continental Tectosphere. Journal of Petrology Special_Volume, 11-37.
Jull, M., Kelemen, P.B., 2001. On the conditions for lower crustal convective instability. J. Geophys. Res. 106, 6423-6446.
Kelly, R.K., Kelemen, P.B., Jull, M., 2003. Buoyancy of the continental upper mantle. Geochem. Geophys. Geosyst. 4, 1017.
Kohn, B.P., Gleadow, A.J.W., Brown, R.W., Gallagher, K., O'Sullivan, P.B., Foster, D.A., 2002. Shaping the Australian crust over the last 300 million years: insights from fission track thermotectonic imaging and denudation studies of key terranes. Australian Journal of Earth Sciences 49, 697-717.
Leech, M.L., Stockli, D.F., 2000. The late exhumation history of the ultrahigh-pressure Maksyutov Complex, south Ural Mountains, from new apatite fission track data. Tectonics 19, 153-167.

Lorencak, M., Kohn, B.P., Osadetz, K.G., Gleadow, A.J.W., 2004. Combined apatite fission track and (U,ÄìTh)/He thermochronometry in a slowly cooled terrane: results from a 3440-m-deep drill hole in the southern Canadian Shield. Earth and Planetary Science Letters 227, 87-104.
Martin, S., Bigazzi, G., Zattin, M., Viola, G., Balestrieri, M.L., 1998. Neogene kinematics of the Giudicarie fault (Central-Eastern Alps, Italy): new apatite fission-track data. Terra Nova 10, 217-221.
Moser, F., Hann, H.P., Dunkl, I., Frisch, W., 2005. Exhumation and relief history of the Southern Carpathians (Romania) as evaluated from apatite fission track chronology in crystalline basement and intramontane sedimentary rocks. International Journal of Earth Sciences 94, 218-230.
Murrell, G.R., Andriessen, P.A.M., 2004. Unravelling a long-term multi-event thermal record in the cratonic interior of southern Finland through apatite fission track thermochronology. Physics and Chemistry of the Earth, Parts A/B/C 29, 695-706.
O'Sullivan, P.B., Hanks, C.L., Wallace, W.K., Green, P.F., 1995. Multiple episodes of Cenozoic denudation in the northeastern Brooks Range: fission-track data from the Okpilak batholith, Alaska. Canadian Journal of Earth Sciences 32, 1106-1118.
Osadetz, K.G., Kohn, B.P., Feinstein, S., O'Sullivan, P.B., 2002. Thermal history of Canadian Williston basin from apatite fission-track thermochronology,Äîimplications for petroleum systems and geodynamic history. Tectonophysics 349, 221-249.
Perilli, S.L., 2000. 40Ar/39Ar and Fission-track thermochronology of the central Trans-Hudson orogen, Manitoba, Canada, Department of Earth and Environmental Science. New Mexico Tech, Socorro.
Reinecker, J., Dani, Ìk, M., Schmid, C., Glotzbach, C., Rahn, M., Frisch, W., Spiegel, C., 2008. Tectonic control on the late stage exhumation of the Aar Massif (Switzerland): Constraints from apatite fission track and (U-Th)/He data. Tectonics 27, TC6009.
Roden, M.K., 1991. Apatite Fission-Track Thermochronology of the Southern Appalachian Basin: Maryland, West Virginia, and Virginia. The Journal of Geology 99, 41-53.
Roden, M.K., Miller, D.S., 1989. Apatite fission-track thermochronology of the Pennsylvania Appalachian Basin. Geomorphology 2, 39-51.
Rudnick, R.L., Gao, S., Heinrich, D.H., Karl, K.T., 2003. Composition of the Continental Crust, Treatise on Geochemistry. Pergamon, Oxford, pp. 1-64.
Rudnick, R.L., McDonough, W.F., O'Connell, R.J., 1998. Thermal structure, thickness and composition of continental lithosphere. Chemical Geology 145, 395-411.
Seward, D., Mancktelow, N.S., 1994. Neogene kinematics of the central and western Alps: Evidence from fission-track dating. Geology 22, 803-806.
Seward, D., P√©rez-Esta√ñn, A., Puchkov, V., 1997. Preliminary fission-track results from the southern Urals ,Äî Sterlitamak to Magnitogorsk. Tectonophysics 276, 281-290.
Sinclair, H.D., Gibson, M., Naylor, M., Morris, R.G., 2005. Asymmetric growth of the Pyrenees revealed through measurement and modeling of orogenic fluxes. American Journal of Science 305, 369-406.
Spotila, J.A., Bank, G.C., Reiners, P.W., Naeser, C.W., Naeser, N.D., Henika, B.S., 2004. Origin of the Blue Ridge escarpment along the passive margin of Eastern North America. Basin Research 16, 41-63.
Toro, J., Prokopiev, A., Colgan, J., Dumitru, T., Miller, E.L., 2004. Apatite Fission-Track Thermochronology of the Southern Verkhoyansk Fold-and-Thrust Belt, Russia, American Geophysical Union, Fall Meeting. AGU, San Francisco.

Turcotte, D.L., Schubert, G., 2001. Geodynamics. Cambridge, University Press, New York.
Wagner, G.n.A., Miller, D.S., J√§ger, E., 1979. Fission track ages on apatite of Bergell rocks from Central Alps and Bergell boulders in Oligocene sediments. Earth and Planetary Science Letters 45, 355-360.
White, D.J., Thomas, M.D., Jones, A.G., Hope, J., Nemeth, B., Hajnal, Z., 2005. Geophysical transect across a Paleoproterozoic continent-continent collision zone: The Trans-Hudson Orogen. Canadian Journal of Earth Sciences 42, 385-402.
Whittington, A.G., Hofmeister, A.M., Nabelek, P.I., 2009. Temperature-dependent thermal diffusivity of the Earth/'s crust and implications for magmatism. Nature 458, 319-321.